ISSN number 0971 - 9709

IGU
Promoting Earth System Sciences

The Journal of Indian Geophysical Union

A SCI Journal

Impact Factor (2026) 0.3

AN OPEN ACCESS BIMONTHLY JOURNAL OF IGU

VOLUME 30, ISSUE 4, JULY, 2026

PUBLISHED BY
Indian Geophysical Union, NGRI Campus, Uppal Road, Hyderabad- 500 007
Telephone: 91-4027012739, 27012332; Telefax:+91-04-27171564
Email: jigu1963@gmail.com, website: http://iguonline.in/journal/

The Journal with six issues in a year publishes articles covering
Solid Earth Geosciences; Marine Geosciences; and Atmospheric, Space and Planetary Sciences.

The Journal is supported by CSIR-NGRI & MoES, Govt. of India

Annual Subscription
Individual Rs -1000/- per issue and Institutional Rs- 5000/- for six issues
Payments should be sent by DD drawn in favour of "The Treasurer, Indian Geophysical Union", payable at Hyderabad,
Money Transfer/NEFT/RTGS (Inter-Bank Transfer), Treasurer, Indian Geophysical Union, State Bank of India, Habsiguda Branch,
Habsiguda, Uppal Road, Hyderabad- 500 007
A/C: 52191021424, IFSC Code: SBIN0020087, MICR Code: 500002318, SWIFT Code: SBININBBHO9.
For correspondence, please contact, Hon. Secretary, Indian Geophysical Union, NGRI Campus, Uppal Road,
Hyderabad - 500 007, India; Email: igu123@gmail.com; Ph: 040 27012332

ISSN: 0257-7968 (Clarivate Analytics)
ISSN: 0971-9709 (NISCAIR)
Approved as bimonthly ESCI journal by Clarivate Analytics
Cited in Indian Citation Index (ICI), New Delhi
Evaluated by NISCAIR, New Delhi
UGC Approved Journal

CONTENTS

Research Articles

Short Note

Obituary

J. Ind. Geophys. Union, 30(4) (2026), 241-252
https://doi.org/10.71122/JIGU.30(4)2026.0024

Shallow upper crustal structure of south Rewa Gondwana basin, Central India constrained from different geophysical studies

Sudeshna Moharana[1,2*] and Laxmidhar Behera[1,2]
[1]CSIR-National Geophysical Research Institute (CSIR-NGRI), Hyderabad - 500007, India
[2]Academy of Scientific and Innovative Research (AcSIR-NGRI), Ghaziabad -201002, India
*Corresponding author: sudeshna.ngri19a@acsir.res.in

ABSTRACT

The south Rewa basin is located in northern part of the Son-Mahanadi rift system in Central India, which has huge deposit of Gondwana rocks. The basin is affected by active tectonic activities towards north and ubiquitous presence of Deccan Traps in south, making this basin geologically complex to image the subsurface geological features. The hydrocarbon prospect of the Gondwana rocks in this sedimentary basin, has encouraged multi-disciplinary geological and geophysical investigations. The upper-crustal P-wave velocity model (V_P) of the south Rewa rift-basin is derived down to 10 km depth by using the 2-D traveltime inversion of both seismic refraction and long-offset reflection traveltime data along the 155 km long Hardi-Samatpur seismic profile. The model shows V_P variations of 3.2-3.5 km/s for the first-layer, which are mainly composed of complex mixtures of exposed upper-Gondwana rocks, basalts and dykes, as well as weathered rocks with alluviums. The second-layer mainly comprises high-velocity-layer (HVL) basalt with V_P varying from 4.9-5.1 km/s, corresponding to the Deccan volcanics that overly the low-velocity-layer (LVL) Gondwana rocks of velocity 4.0 km/s. The basement is highly undulated, forming horst and graben structures, having V_P variation from 5.9-6.1 km/s, showing significant upwarping on either side of the basin along the profile. The deep-basinal faults constrain the presence of Gondwana rocks below Deccan Traps in a graben structure that may have potential for hydrocarbon accumulation. The sub-basement, with V_P varying from 6.4-6.5 km/s, follows the basement geometry, showing significant upwarping towards the Narmada-Son-Lineament (NSL). The results obtained from the inversion of seismic data are further corroborated using residual-Bouguer-gravity anomaly, magneto-telluric (MT), well lithology, magnetic, and heat-flow studies over this region along the Hardi-Samatpur profile. The MT, magnetic, and gravity information suitably complement the seismic results corresponding to gravity-lows, conductive-zones, and low-velocity zones associated with deposition of the Gondwana rocks, confined by intra-basinal faults. Hence, with the help of suitable integration of different geophysical studies, we have obtained good constraints on the nature of subsurface geological features in the upper-crust in the south Rewa Gondwana sedimentary basin of Central India.

Keywords: Seismic refraction and long-offset reflection; Ray-trace inversion; Horsts and grabens; Gondwana rocks; Basement; Upper-crust, South Rewa basin

INTRODUCTION

The Gondwana sedimentary basins of the peninsular Indian shield have undergone multiple stages of drifting and rifting during different geological time periods, forming continuous changes in basin development. The south Rewa basin (Figure 1) is a sub-basin of the Son-Mahanadi intra-cratonic rift-basin located in Central India (Mukherjee et al., 2012; Chowdari et al., 2017). The rift-basin contains heterogeneous rocks with complex geological settings controlled by deep-basinal faults, linear belts and undulated basement. The basin came into the limelight because of the presence of hydrocarbons. The south Rewa rift-basin is classified as a Category-IV sedimentary basin in India for conventional petroleum systems. The basin contains undiscovered conventional hydrocarbon reservoirs and is currently producing unconventional coal-bed-methane (CBM). The Deccan volcanics mask the hydrocarbon-bearing Gondwana rocks by intruding into the Gondwana strata, which was corroborated by the findings from the Tihki exploratory well (Figure 2) drilled by ONGC (Kumar et al., 2005). The paleomagnetic study and $^{39}Ar/^{40}Ar$ dating of mafic dykes exposed along the Son river, near the Shahdol region, conforms with the Deccan volcanism (Lala et al., 2011, 2014; Chowdari et al., 2017). The presence of high-velocity Deccan Traps overlying the low-velocity Gondwana strata creates a challenging situation for imaging the sub-trappean geological features of interest.

The seismic wave propagations through the high-velocity basalts create significant loss of energy due to scattering, absorption, dispersion, diffraction, attenuation, mode-conversion etc., thus limiting the effectiveness of conventional near-vertical reflection techniques for imaging the sub-basalt structures (Behera et al., 2002, 2004). To overcome this challenge, the long-offset seismic refraction and reflection data are acquired, in which the energy can penetrate the high-velocity basalts to image the deep-seated targets of interest, like low-velocity sediments and basement configurations. In case of the presence of thick low-velocity rocks overlain by thin high-velocity rocks, the lowering of seismic energy is observed in the first-arrival data, resulting traveltime delay in the seismic section called “skip”, indicating the occurrence of velocity inversion in the subsurface earth (Greenhalgh, 1977; Whiteley and Greenhalgh, 1979).

The main aim of this study is to suitably integrate the results from other geophysical methods like gravity, magnetic, magneto-telluric (MT), exploratory well and heat-flow with the corresponding velocity model derived along the Hardi-Samatpur seismic profile of south Rewa basin (Figure 1).

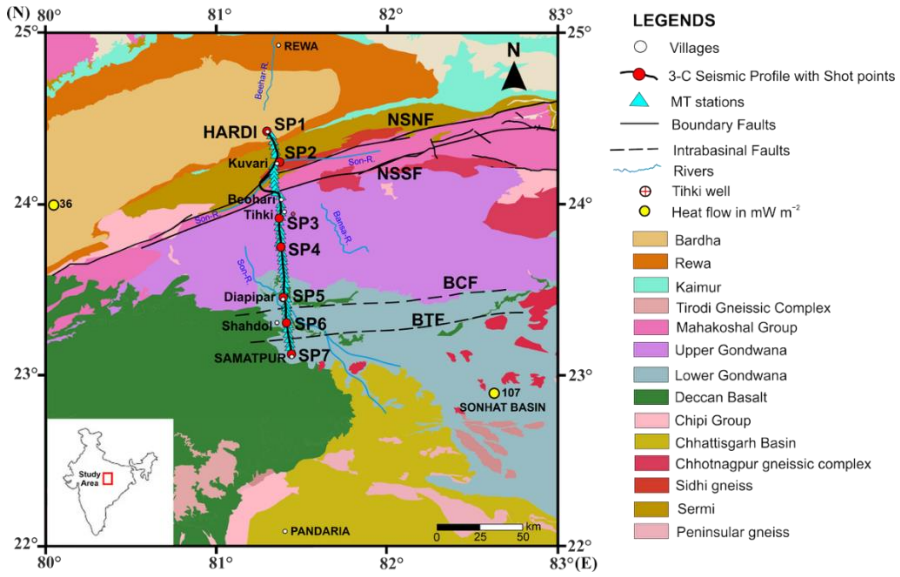

Figure 1. Geological map of the south Rewa basin in Central India showing N-S trending 155 km long 3-C seismic profile from Hardi-Samatpur with seven long-offset shot points (SPs) marked by red dots (SP1-SP7) along with MT stations (Raju et al., 2022), Tihki well (Kumar et al., 2005) and heat-flow values (Nagaraju et al., 2017) superimposed on it. Source: https://geodataindia.gov.in/

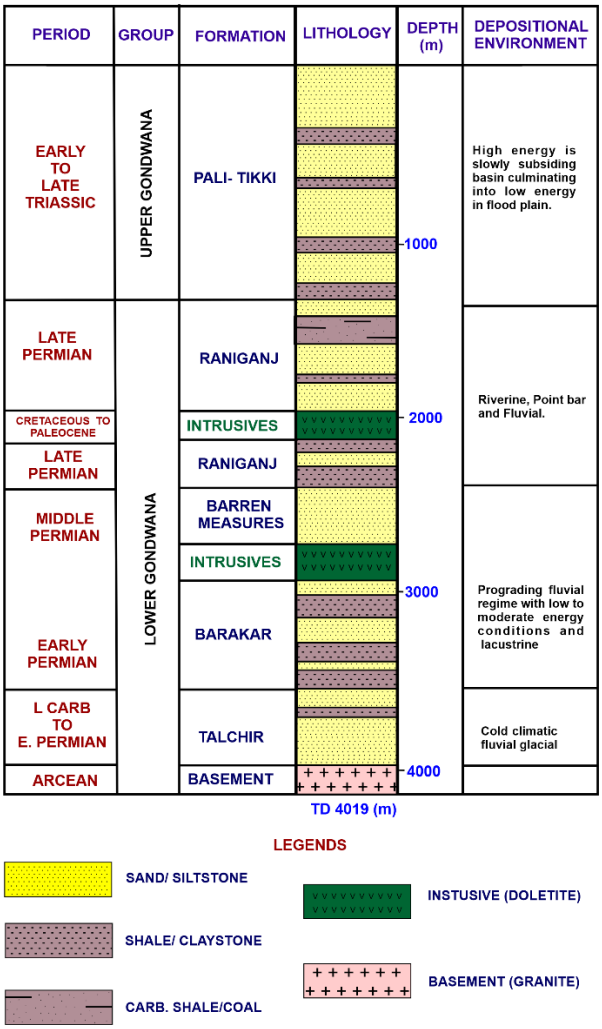

Figure 2. Litho-stratigraphy of Tihki exploratory well drilled by ONGC in the south Rewa basin (modified after Kumar et al., 2005)

With the help of this study, it is possible to resolve major geological complexities, such as imaging of sub-trappean Gondwana rocks, delineate horsts and grabens, granitic basement, upper-crustal structures, basalts/traps and deep-seated faults present in this region to understand the shallow geology and tectonic settings. The values of different parameters like density, susceptibility, conductivity, seismic velocity and rock core data from this study will provide more information about the heterogeneous rock composition and physical properties of the underlying layers.

GEOLOGY OF THE STUDY AREA

The south Rewa basin (Figure 1) is oriented in the northwest-southeast (NW-SE) direction, situated in the northern part of the Son-Mahanadi rift system of Central India (Mukherjee et al., 2012; Chowdari et al., 2017). Multiple rifting, fault re-activation near lineaments and intense magmatic activity during Deccan volcanism have shaped the intra-cratonic south Rewa basin. The accumulation of sediments is mainly controlled by the horsts and grabens, confined by deep-basinal faults within the basin. A substantial amount of hydrocarbon and coal is preserved in the Permo-Triassic Gondwana strata overlain by 65 Ma Deccan volcanics. In the north of the basin, the Narmada-Son south and north faults (NSSF and NSNF) form a linear belt that exposes the Mahakoshal group (Raju et al., 2022). There are two intra-basinal boundary faults present in the basin namely, the Balarampoor-Tattapani fault (BTF) and the Bahmin-Chilpa fault (BCF). The Upper Gondwana rocks are exposed along the south of the linear belt, whereas the Deccan basalts are exposed towards south of the basin.

Litho-stratigraphically, the Gondwana supergroup mainly contains sandstone, siltstone, limestone, shale, claystone, carbonaceous shale and coal seams. These deposits are mainly due to shallow marine environments with maximum accumulation of sediments occurred because of the presence of deep-basinal faults near Beohari region. The sediments have two groups namely: (i) Upper Gondwana consisting of the Pali, Tihki and Parsora formations, and (ii) Lower Gondwana consisting of the Raniganj, Barren Measures, Barakar and Talchir formations (Kumar et al., 2005; Behera et al., 2024). The Tihki exploratory well (Figure 2) validated the presence of an igneous intrusive body (mafic rock) within the Lower Gondwana.

SEISMIC DATA

Acquisition and pre-processing

In the south Rewa sedimentary basin, the CSS Group of CSIR-NGRI has acquired the 2-D 3-C (three-component) long-offset seismic refraction and reflection data with seven shot points (SPs) along the 155 km long N-S trending Hardi to Samatpur profile during the years 2014-2015 under aegis of the XII-V Year Plan SHORE Project of CSIR (Figure 1). The data was recorded with 30-35 km shot interval (SI) of each SPs by using explosives (minimum 100 kg to maximum of 1.8 Metric tons) as source with spread length of 24 km. The spread moves along the profile for all the SPs corresponding to the required offset covered based on the seismic field setup, so as to acquire long-offset seismic data. The receiver interval (RI) was kept as 200 m by deploying 4.5 Hz frequency geophones of 120 standalone 3-C seismic stations (Taurus) having a sampling interval of 4 ms. The 3-C seismic data was acquired in geographical coordinate system (i.e., Vertical (Z), Northing (N) and Easting (E) coordinate system), which must be rotated according to the source-receiver azimuth at each station along the seismic profile (Guevera and Stewart, 1998). After the 3-C data rotation for each spread, the vertical (Z) remains the same, whereas northing (N) and easting (E), correspond to radial (R) and transverse (T) components, respectively. The conventional pre-processing steps (Yilmaz, 2001) are applied to individual gathers of Z, R and T components for all SPs along the profile. The radial component is chosen for modeling and inversion due to its high signal-to-noise ratio (SNR) compared to Z and T components as it travels along the seismic line.

Data analysis and picking

The main purpose of data analysis is the identification of different seismic phases and picking according to the good SNR and coherence of the seismic data. Since the R-component seismic data are very strong and clear as compared to Z and T component data, we have used the R-component phases for modeling and inversion to derive the P-wave velocity model of this region. Hence, we have chosen the R-component pre-processed seismic data for phase identification and picking. We have picked the first-arrival phases (P_1, P_2, P_4, P_5) and reflection phases (P^2, P^3, P^4) of all the seven SPs for 2-D ray-trace inversion of R-component P-wave data along the profile (Figure 3). At small offsets, the first-arrival phases are clearly visible, whereas at long-offsets, the cycle-skip increases. To mitigate over-fitting or under-fitting problems during the inversion process, the picking uncertainties are considered based on the SNR and frequency content of the data. The picking uncertainties are assigned as ±25 ms for near-offset direct and refraction phases (P_1, P_2), ±50 ms for long-offset refraction (P_4, P_5) and reflection phases (P^2, P^3, P^4) for all the seven SPs along the profile (Zelt and Smith, 1992; Zelt, 1999; Behera et al., 2004).

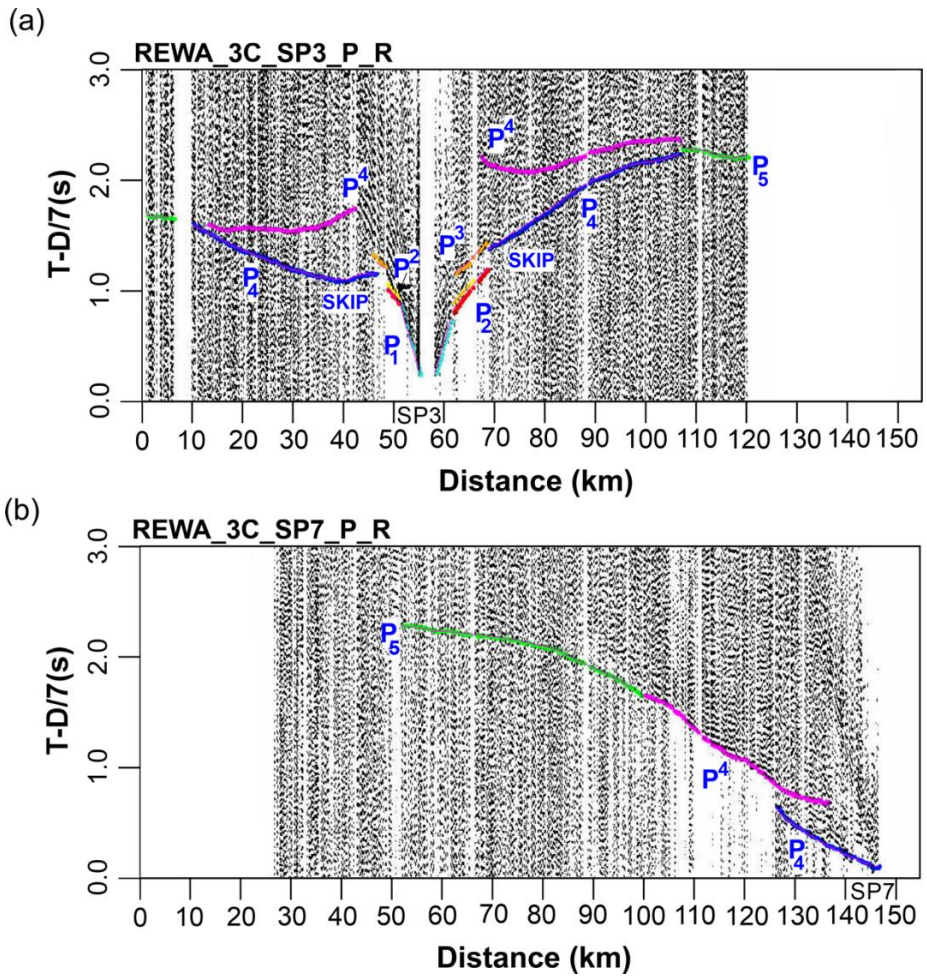

Figure 3. The example radial-component SP gathers shown for **(a)** SP3 and **(b)** SP7 with P-wave phases picked marked by colored dots for first-arrival refraction (P_1, P_2, P_4, P_5) and reflection (P^2, P^3, P^4) seismic data, respectively used for modeling and inversion.

The seismic energy is reduced in the presence of high-velocity Deccan volcanics due to attenuation and absorption along the seismic profile, resulting in the absence of P_3 phase from the first-arrivals. The energy dissipation results in the reduction of seismic amplitude, as evidenced by traveltime skip in the seismic data, signifying low-velocity Gondwana strata overlain by high-velocity Deccan basalts. Significant impedance contrast and amplitude build-up in the post-critical region, cause the reflection phases to be strong and noticeable at long-offsets (Greenhalgh, 1977; Whiteley and Greenhalgh, 1979; Behera et al., 2002, 2004; Behera and Sarkar, 2011; Behera and Sen, 2014; Behera et al., 2021; Kolluru and Behera, 2025; Chandrakala and Kumar, 2026).

METHODOLOGY

To obtain P-wave velocity model along the Hardi-Samatpur seismic profile (Figure 1), the 2-D traveltime inversion method was employed based on model parameterization and ray-trace technique as described by Zelt and Smith (1992). The model consists of an uneven grid of velocity and boundary nodes with a linear interpolation of velocity values between these points. Smooth-layer boundary constraints are implemented to provide stability and prevent scattering of rays. During ray-tracing, the traveltime and their partial-derivatives with respect to both velocity and interface depth are computed using the efficient numerical algorithm explained by Zelt and Ellis (1988). The forward response of the initial model is iteratively compared with the observed data. The model parameters are updated in each iteration by applying correction vectors obtained from the damped least-squares inversion until the normalized χ^2 value reaches close to 1.0.

2-D Ray-trace inversion

The first-arrival (P_1, P_2, P_4, P_5) and reflection (P^2, P^3, P^4) phases picked from P-wave seismic data (Figure 3) are used for the ray-trace inversion (Figure 4) by employing the method of Zelt and Smith (1992). The refraction phase (P_3) is absent due to the traveltime-skip as observed from different SPs.

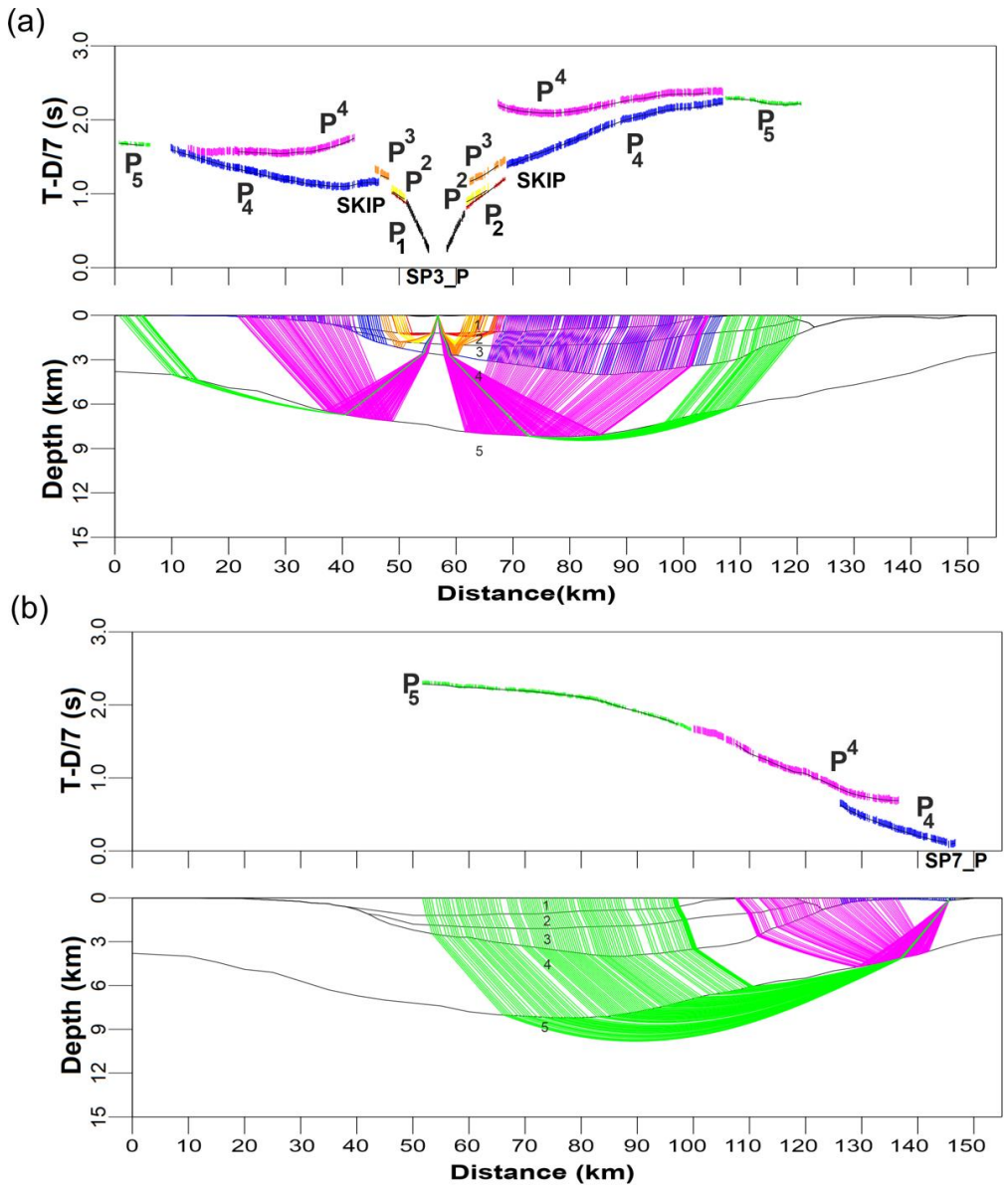

Figure 4. The top panel show the traveltime fit of the observed data (colored vertical bars) superimposed by the synthetic responses (solid black line) of **(a)** SP3 and **(b)** SP7. The bottom panel show the corresponding ray-trace inversion through different layers (1 to 5) of **(a)** SP3 and **(b)** SP7. The data are displayed in reduced-time scale with reduction-velocity of 7.0 km/s.

Individual 1-D velocity models are derived for all the seven SPs along the seismic profile. The 1-D velocity model shows five layers with different apparent velocities. The 1-D velocity models are joined smoothly to derive the pseudo 2-D velocity that acts as initial velocity model for the 2-D ray-trace inversion. Both velocity and boundary nodes are changed simultaneously during the ray-trace inversion to obtain traveltime fit of the observed data using layer-stripping method iteratively.

This iterative ray-trace inversion process is continued until optimum fit is achieved between the observed data and the corresponding computed responses through different layers of the derived P-wave velocity model (Zelt and Smith, 1992; Behera et al., 2002, 2004; Behera and Sen, 2014; Behera and Kumar, 2022; Kumar and Behera, 2024). The final P-wave velocity model obtained (Figure 5) is constrained by RMS traveltime residual of 0.046 s and the chi-square misfit of 1.151 using both the long-offset refraction and reflection traveltime data computed for all the seven SPs along the 155 km long Hardi-Samatpur seismic profile (Figure 1).

2-D P-wave velocity model

The final five layered 2-D P-wave velocity model is derived to show both lateral and vertical velocity variations along the studied profile (Figure 5).

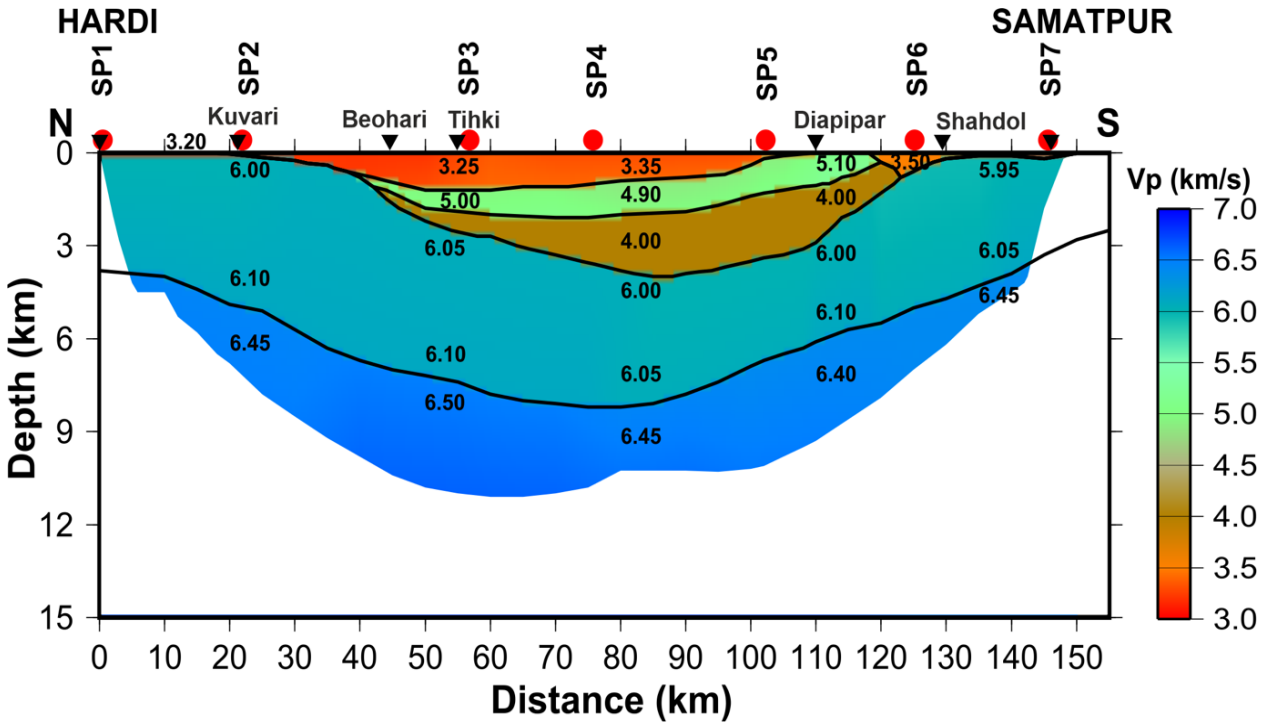

Figure 5. The shallow upper-crustal 2-D P-wave velocity model derived along the Hardi-Samatpur seismic profile in south Rewa basin. The red dots represent shot point (SP1-SP7) locations, and the inverted black triangle represents the local villages present along the profile in the study area. Velocity variations within the model are shown by color scale along with the corresponding average velocity values (5.0 km/s) indicated for each layer. The unsampled regions of ray-tracing are left blank.

The first-layer is a complex mixture of exposed Upper Gondwana rocks, basalts and weathered rocks with alluviums (~1 km) having P-wave velocity variation from 3.2-3.5 km/s horizontally within the graben. The second-layer has P-wave velocity variation from 4.9-5.1 km/s representing lateral flow of basalts/dolerites confined between Beohari to Shahdol along the profile. Near Shahdol, the basalt is thicker, and some mafic dykes are exposed on the surface. The Gondwana rocks having a P-wave velocity of 4.0 km/s lie above the basement, which extends to maximum 3.0 km depth. The basement is highly distorted forming horst and graben feature, which extends from 0.1 km to 8.0 km depth along the profile characterized by P-wave velocity 5.9-6.1 km/s. The basement is almost exposed on either side of the graben towards Kuvari in the north and Shahdol in the south forming horst structures. The sub-basement is extending from 2.8 km to 10 km depth as constrained from the 2-D ray-trace inversion (Figure 4). It shows P-wave velocity variations of 6.4-6.5 km/s (Figure 5).

INTEGRATED GEOPHYSICAL STUDIES

Gravity

The residual Bouguer gravity anomaly map for the south Rewa basin (Figure 6) has been produced using the revised Bouguer gravity anomaly map of India (NGRI, 2006).

The revised Bouguer gravity anomaly map of India has a scale of 1:2,000,000 having 5mGal contour interval (NGRI, 2006). The Hardi-Samatpur seismic profile is superimposed on the corresponding 5 mGal residual Bouguer gravity anomaly map of south Rewa basin (NGRI, 2006; Behera et al., 2024).

The residual Bouguer gravity anomaly map shows variations of gravity from -45 mGal to +50 mGal, representing gravity highs and lows (Figure 6). The presence of high-density basalts and granitic-gneissic basement up-warping, forms horst feature with gravity-high. On the other hand, the presence of low-density Gondwana rocks present within the graben show gravity-low. The gravity values increase gradually from Kuvari to Hardi in the north and from Shahdol to Samatpur in the south of the profile, which are associated with basement up-warping that forms large horst structures on either side of the graben.

The corresponding decrease of gravity values observed from Beohari (-10 mGal) to Shahdol (-35 mGal) indicate the presence of substantial low-density rock formations, which are associated with low-velocity Gondwana rocks. The sharp change of gravity values near the Kuvari and Shahdol regions may be correlated with deep-basinal faults.

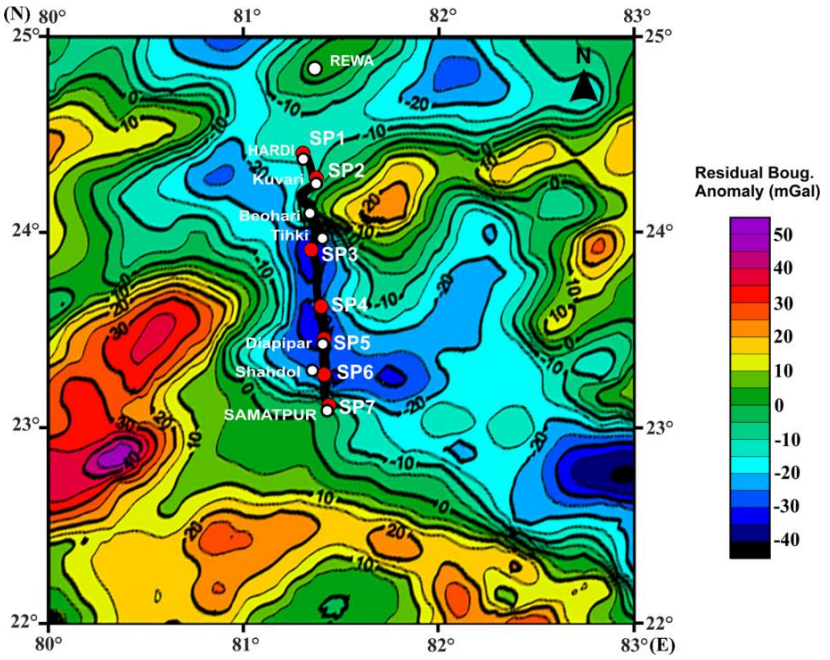

Figure 6. Residual Bouguer gravity anomaly contour map of the study area is shown with the color-scale (modified after NGRI, 2006; Behera et al., 2024). The shot points (red dots) and the village names (white dots) are shown along the seismic profile.

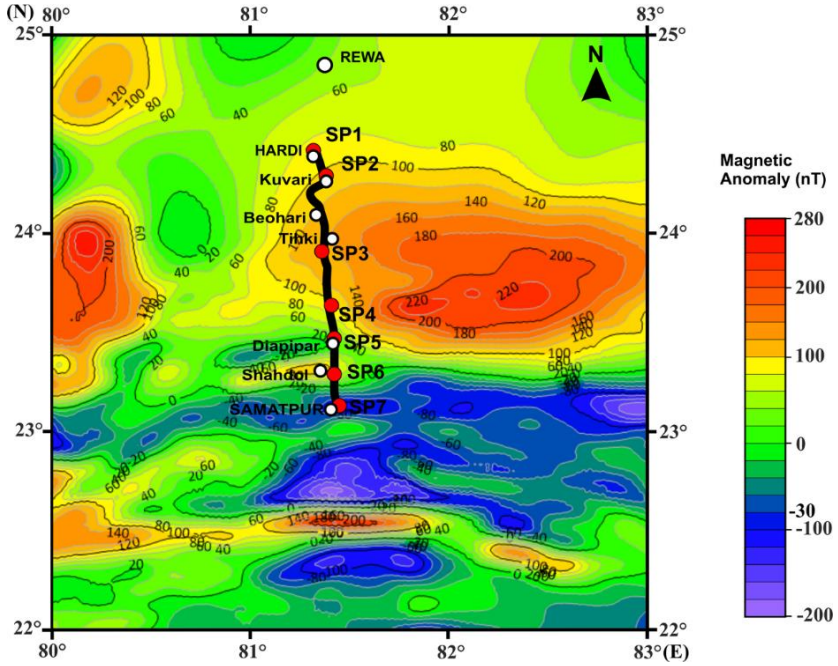

Figure 7. The EMAG2 magnetic anomaly map of the study area is shown along with the color-scale. The shot points (red dots) and the village names (white dots) are also shown along the seismic profile.

Magnetic

The Earth Magnetic Anomaly Grid (EMAG2) is being used to analyse the magnetic data. The EMAG2 provides the base grid for the World Digital Magnetic Anomaly Map (WDMAP), a compilation of crustal magnetic anomalies with 2 arc-minute resolution. This map of magnetic intensity is at an altitude of 4 km above mean-sea-level (MSL).

The EMAG2 is a compilation of multiple datasets obtained from satellite, ship/marine, aeromagnetic, and ground magnetic surveys. The EMAG2 dataset was downloaded as an ASCII grid of total magnetic intensity (http://geomag.org/models/ emag2.html) from which the magnetic anomaly map of the study area is generated with 2 km grid-spacing (Figure 7).

The EMAG2 magnetic data help to identify the presence of mafic dykes and sills. We have superimposed the seismic profile on the magnetic anomaly map generated for the study area (Figure 7). The magnetic anomaly map provides important information about the presence of subsurface mafic bodies. The magnetic anomaly map shows positive values (80 nT to 12 nT) in the north of the seismic profile due to exposed basement and Mahakoshal meta-sediments, which are mafic in nature. The magnetic anomaly map also shows negative values in the southernmost part of the seismic profile near Diapipar (0 nT to -20 nT) and Samatpur (-40 nT to -80 nT) regions, except for the Shahdol (40 nT to 80 nT) region, which show positive magnetic anomalies due to the presence of mafic dykes. The boundary-faults are indicated by sharp gradients, explaining the presence of sharp normal-faults down to the basement in the south Rewa basin (Chowdari et al. 2017).

Magneto-telluric (MT)

The magneto-telluric investigations have been carried out by Raju et al. (2022) along the 275 km long MT profile from Rewa in the north to Pandaria in the south using 69 MT stations during 2014-2016 (Figure 1). They have used the ADU-07e system (M/s Metronix, Germany) for MT data acquisition, which is a broadband magneto-telluric and electromagnetic (EM) measurement system. Three orthogonal magnetic-field components (H_x, H_y, H_z) and two horizontal electrical-field components (E_x and E_y) were recorded simultaneously over a frequency range of 65 kHz to 0.001 Hz. The station spacing was approximately 4-5 km and reduced to 0.5 km across major tectonic features. One base station was maintained remotely to record data with low S/N ratio.

The seismic and MT data have been acquired along the same profile (Figure 1). In this study, we have considered the MT data from Hardi to Samatpur seismic profile. The 2D geoelectric section derived from the inversion of MT data delineates different conductive bodies, which are marked as C3-C8 (Figure 8). In the MT model, the presence of vertically moderate conductive bodies C3 and C4, having low resistivity (50-100 Ω-m), represents the intra-basinal faults BTF and BCF respectively, which coincide with the surface expressions. The MT study delineates a conductive body (C7) in the middle of the Narmada-Son Lineament (NSL) bounded by Narmada-Son North Fault (NSNF) and Narmada-Son South Fault (NSSF) that represent sediments associated with Mahakoshal Group (MG) rocks, which is considered as a low-to-moderate resistive (10-100 Ω-m) body. There is also a presence of high resistive (>1000 Ω-m) structure below the NSL (Figure 8).

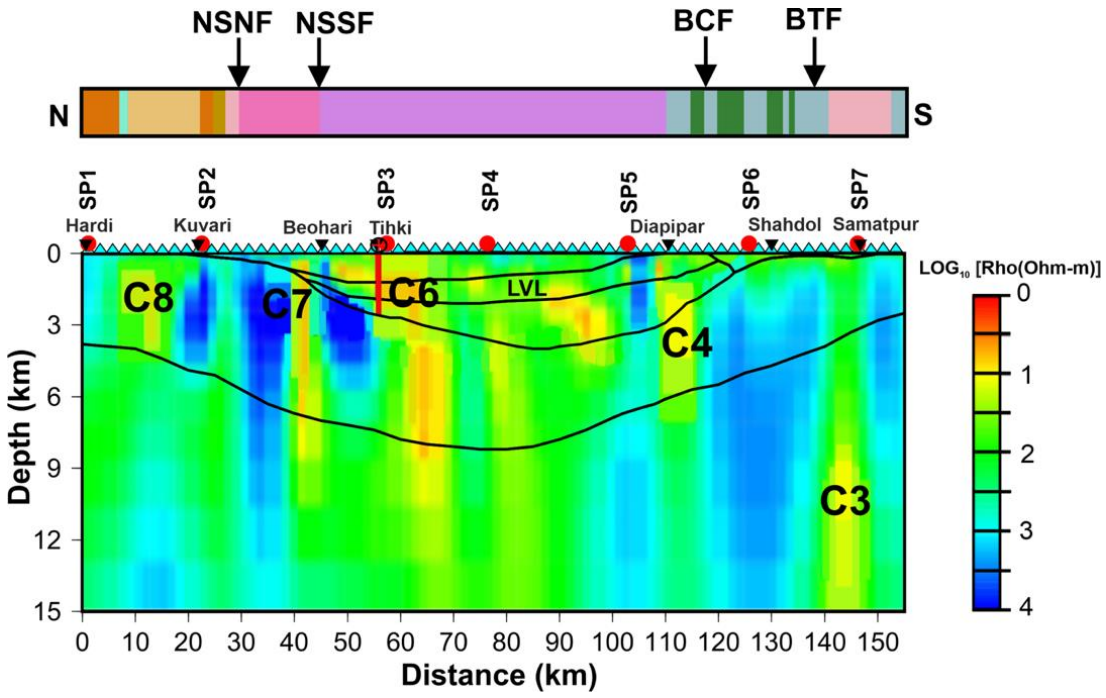

Figure 8. The shallow geoelectric section derived from the inversion of magneto-telluric (MT) data along the Hardi-Samatpur profile (modified after Raju et al., 2022). The different conductive bodies are marked as C3-C8, which coincide with the boundary of intra-basinal faults. The corresponding interface boundaries of the V_P model (Figure 5) are superimposed on the MT results along the same seismic profile.

Heat-flow

Heat-flow plays a vital role in hydrocarbon maturation. The high heat-flow in the Gondwana sedimentary basin converts organic materials into gaseous hydrocarbons. The heat-flow values are relatively high in the Gondwana sedimentary basin (46-107 mWm^{-2}) in comparison with the Vindhyan basin (50-68 mWm^{-2}) and the Deccan Volcanic Province (41-55 mWm^{-2}) of India (Rao and Rao, 1980, 1983; Nagaraju et al., 2017). The Sonhat basin, located south of the south Rewa basin, has the only available measured heat-flow value of 107 mWm^{-2} close to the seismic profile (Rao and Rao, 1983; Pandey, 2020), which is significantly high as compared to the nearby areas of the Gondwana basins (Figure 1). The high heat-flow values obtained in the Gondwana basins are due to the high radioactive heat-production in the gneissic basement rocks underlying the sedimentary cover in the Son-Mahanadi basins (Rao and Rao, 1983).

DISCUSSION

A five layered upper-crustal V_P model is derived, constrained to a depth of 10 km along the Hardi-Samatpur seismic profile in the south Rewa rift sedimentary basin. The rifting has occurred over a geological time period, led to the complex structural configuration of the basin, confined between the deep-basinal faults forming horst and graben features (Figure 5). The P-wave velocity shows significant variations along the seismic profile, indicating heterogeneous rock depositions. Towards northern part of the profile, the basement is almost exposed, having V_P variations of 6.0-6.1 km/s representing crystalline granitic-gneissic rocks that extends up to 20 km horizontally from Hardi to Kuvari along the profile. From Kuvari to Shahdol, the basement forms a large depression or graben structure in which the Gondwana rocks are deposited, which corresponds to the south Rewa Gondwana sedimentary basin, which extends laterally on either side of the profile (Figures 5 and 6). Again, the basement is almost exposed from Shahdol to Samatpur towards south of the profile having V_P variations of 5.95-6.05 km/s. Within the Gondwana graben between Kuvari to Shahdol, we have obtained three distinct layers overlying the basement. The first-layer has V_P 3.2-3.5 km/s, which corresponds to complex mixture of sediments and other rocks such as Upper Gondwana, exposed and weathered basalts, alluviums, shale and claystones extending to 100 km along the profile. The second-layer is mainly basaltic intrusives corresponds to HVL Deccan volcanics characterized by V_P 4.9-5.1 km/s, which is followed further by the LVL Gondwana rocks (third-layer) having average V_P of 4.0 km/s. It overlies the basement (fourth-layer) having V_P variations of 5.9-6.1 km/s. Below the basement, the fifth-layer is delineated having V_P variation from 6.4-6.5 km/s. It possibly corresponds to upwarped mid-crust (Figure 5).

The five-layered V_P model shows both lateral and vertical velocity variations. The HVL Deccan volcanics acts as a lid or mask for the thick (1.5-2.0 km) LVL Gondwana rocks deposited within the graben from Beohari to Diapipar, which is very important for hydrocarbon potential in this sedimentary basin. The Tihki exploratory well (Figure 2) drilled near Tihki village show the intrusives of Cretaceous to Paleocene age encountered at ~2 km depth (Kumar et al., 2005), which correlates very well with our results of the presence of Deccan volcanics at a depth of 2 km near Tihki along the profile. The Deccan basalt influences the southern part of the seismic profile, with sporadic basalt exposures near Shahdol in the form of small dykes, which are diminished gradually towards the north (Beohari village). The Gondwana sediments (1.5-2.0 km thick) contain coal, which is the primary source rock in the Raniganj and Barakar formations, with high organic matter of type-III, generating methane during coalification. The Barakar formation also contains carbonaceous shale, which on thermal maturation, generates shale gas. The low-permeable shale and clay act as a seal within the sequence and the impermeable Deccan basalt acts as an effective cap rock, making a suitable environment for hydrocarbon accumulation and a possible oil and gas reservoir in this south Rewa basin. The granitic-gneissic basement having V_P (5.9-6.1 km/s) forms horst and graben features, confined by deep-basinal faults developed due to tectonic activities during rifting, thus providing suitable site for the deposition of thick column of Gondwana sediments important for hydrocarbon accumulation. The horsts and grabens along with different geological structures prevalent within this sedimentary basin, mainly influence the formation of the structural traps for hydrocarbon exploration.

The geological features are well validated by the Tihki exploratory well, which has a total depth (TD) of 4 km (Figure 2). The presence of Gondwana sediments are mainly characterized by low-velocity, low-density and weak magnetic responses. Along the seismic profile, the residual Bouguer gravity-anomaly map shows low gravity-anomaly (-30 mGal to -35 mGal) from Beohari to Shahdol with low-to-moderate electrical resistivity (10-100 Ω-m), which mainly corresponds to the presence of Gondwana rocks deposited in this region. The low-gravity anomaly seen across the exposed Deccan volcanics in the south near the Shahdol region may result from Gondwana sediments masked by the basalts. The Deccan Traps characterized by high V_P (4.9-5.1 km/s) show high magnetic-anomaly (60 nT to 120 nT) and high resistivity (100-10,000 Ω-m) in this region. The magnetic-anomaly map

(Figure 7) reveals a decreasing magnetic response from north to south along the seismic profile, suggesting lack of mafic rocks in the southern region, except for the Shahdol area (60-100 nT), which exhibits a robust magnetic response due to the presence and exposure of mafic dykes (Figure 7).

The deep-basinal faults are the major tectonic features, which has developed the basinal structure. The geoelectrical model derived from the MT data along the seismic profile indicates low-to-moderate resistivity (10-100 Ω-m) below intra-basinal faults (BTF and BCF) and moderate-resistivity (50-100 Ω-m) below the NSNF and NSSF, because of the fluid infiltration in the weak-zones developed by faults. The sharp change in gravity anomaly and magnetic anomaly near the Kuvari and Shahdol regions, may be correlated with the deep-basinal faults.

The integration of seismic, gravity, well lithology, MT, magnetic and heat-flow studies reduces the inherent non-uniqueness persists in the modeling and provides better results for geologically plausible interpretation. This integrated interpretation has helped to delineate subsurface geological features including basinal geometry, determine thickness of Gondwana rocks important for hydrocarbon accumulation, basement configuration, deep-basinal faults and basaltic traps in the south Rewa sedimentary basin. The seismic study has obtained the average V_P variations both laterally and vertically. The interpretation from seismic, gravity, and MT results provide important information about the physical properties of the Gondwana rocks as well as conductive and resistive bodies present in the graben, which are controlled by deep-basinal faults near Kuvari in the north and Shahdol in the south along the profile (Figures 5, 6 and 8). It also revealed that the basement is upwarped due to Gondwana rifting and intense tectonic activity happened during the Deccan volcanism. The regions dominated by mafic rocks such as basalts, igneous intrusives and dykes are also constrained from the magnetic studies (Figure 7).

CONCLUSIONS

The south Rewa Gondwana sedimentary basin has undergone multiple stages of rifting since the Early Cretaceous period, making this an intra-cratonic basin with sediments deposited in a graben forming the syn-rift strata. The robust V_P model derived along the 155 km long seismic profile from Hardi-Samatpur is corroborated with gravity, well lithology, MT, magnetic, and heat-flow studies, which reveal intra-cratonic faults, basement undulations with deep-basinal faults, presence of thick column of sub-trappean Gondwana sediments, large-scale basaltic intrusions forming dykes and sills, significant compositional changes of rocks, and upper-crustal depression. The important conclusions inferred from this study are mentioned below.

(i) The top-most layer is highly heterogeneous with V_P variations of 3.2-3.5 km/s having thickness of 1.0 km near Beohari that decreases gradually towards south of the profile.

(ii) The Deccan volcanics (0.5-1.0 km thick) has a high V_P of 4.9-5.1 km/s, which influences the southern part of the seismic profile having sporadic basalt exposures near Shahdol in the form of small dykes. The thickness of the basalt increases towards Shahdol.

(iii) The low-velocity Gondwana rocks having average V_P of 4.0 km/s are masked by high-velocity Deccan basalts, which show thick (1.5-2.0 km) sequence of deposits within the graben potential for hydrocarbon.

(iv) The granitic-gneissic basement having V_P (5.9-6.1 km/s) is exposed in the north along with the metasedimentary Mahakoshal group and forms horst and graben features, confined by deep-basinal faults developed due to tectonic activities during rifting and thick column of Gondwana rocks are deposited within the graben. The undulated basement structure influences the formation of structural features for hydrocarbon accumulation.

(v) The basement below NSL is underlain by high velocity layer 6.45-6.50 km/s, possibly representing upwarped mid-level crust.

(vi) The gravity, magnetic, well lithology and MT studies in this region correlate very well with the corresponding upper-crustal velocity model derived along the seismic profile, thus provide suitable information about the basin structure and presence of different faults and mafic dykes/sills in the study area, indicating one of the geologically very complex Gondwana sedimentary basin of India.

ACKNOWLEDGEMENTS

We thank Dr. Prakash Kumar, Director, CSIR-National Geophysical Research Institute (CSIR-NGRI), Hyderabad for according permission to publish this paper. CSS staff members of CSIR-NGRI are formally recognized for their assistance in 3-C seismic data acquisition in the Rewa basin. We profusely thank Prof. Uma Shankar and an anonymous reviewer for their critical comments and suggestions to improve the quality of the paper. We sincerely thank Dr. ASSSRS Prasad, manuscript handling Editor and Dr. O. P. Panday, Chief-Editor of the Journal of Geophysical Union (JIGU) for their suggestions and encouragement to publish

this work. The Academy of Scientific and Innovative Research (AcSIR), Ghaziabad, Uttar Pradesh is thanked for granting permission to SM for carrying out her research for Ph. D. with necessary support and CSIR for granting Senior Research Fellowship (SRF). Prof. Colin A. Zelt of Rice University, USA is thanked for using the RAYINVR codes. This work relates to the scientific research contribution of CSIR-NGRI, under the XII-V Year Plan Project PSC-0205 (LB) SHORE, having Ref. No. NGRI/LIB/2026/Pub-58.

Author Credit Statement

Sudeshna Moharana: Data curation, data analysis, methodology, writing original-manuscript. Laxmidhar Behera: Conceptualization, data curation, methodology, data analysis, editing and revision of manuscript, funding acquisition, resources and supervision.

Data Availability

The seismic data and gravity used in this research can be made available by requesting to the Director, CSIR-NGRI (director.ngri@csir.res.in) as per CSIR-NGRI data policy. The magnetic data is available at EMAG2 (https://www.ncei.noaa.gov/products/earth-magnetic-model-anomaly-grid-2).

Compliance with Ethical Standards

The authors declare that they have no conflict of interest and adhere to the copyright norms.

References

Behera, L. and Sarkar, D., 2011. Tomographic imaging of large volcanic province due to intense magmatism in the Mahanadi delta of eastern India. Phys. Earth Planet. Int., 189, 142-150.

Behera, L. and Sen, M. K., 2014. Tomographic imaging of sub-basalt Mesozoic sediments and shallow basement geometry for hydrocarbon potential below the Deccan Volcanic Province (DVP) of India. Geophys. J. Int., 199, 296-314.

Behera, L. and Kumar, D., 2022. Deep crustal structure and compositions for tectonic and geodynamic implications of the Dharwar Craton (Southern India) inferred from 3-C wide-angle seismic data. J. Asian Earth Sci., 227(105092), 1-37.

Behera, L., Sain, K., Reddy, P. R., Rao, I. B. P. and Sarma, V. Y. N., 2002. Delineation of shallow structure and the Gondwana graben in the Mahanadi delta, India, using forward modeling of first arrival seismic data. J. Geodyn., 34, 127-139.

Behera, L., Sain, K. and Reddy, P. R., 2004. Evidence of underplating from seismic and gravity studies in the Mahanadi delta of eastern India and its tectonic significance. J. Geophys. Res., 109(B12311), 1-25.

Behera, L., Kolluru, R. and Singh, B., 2021. Imaging Mesozoic sediments in Deccan Volcanic Province of India: Inferences from seismic and gravity studies. J. Geol. Soc. India, 97, 1260-1273.

Behera, L., Panigrahi, S. P., Rao, G. S. P., Reddy, M. S., Karuppannan, P., Premkumar, N. and Moharana, S., 2024. Tomographic imaging of South Rewa basin, Central India: Implications of Gondwana rifting and Late Cretaceous volcanism. Tectonophysics, 880(230321), 1-23.

Chandrakala, K. and Kumar, P., 2026. Crust-mantle seismic structure along Jakhau-Mandvi DSS Profile: A geodynamic perspective. J. Indian Geophys. Union, 30(1), 6-20.

Chowdari, S., Singh, B., Rao, B. N., Kumar, N., Singh, A.P. and Chandrasekhar, D.V., 2017. Structural mapping based on potential field and remote sensing data, South Rewa Gondwana Basin, India. J. Earth Syst. Sci., 126, 1-27.

Greenhalgh, S. A., 1977. Comments on "The hidden layer problem in seismic refraction work". Geophys. Pros., 25, 179-181.

Guevara, S. E. and Stewart, R., 1998. Multicomponent seismic polarization analysis. CREWES Research Report, 10, 7-19.

Kolluru, R. and Behera, L., 2025. Imaging intra-volcanic Mesozoic sediments and shallow crustal configuration from traveltime inversion of long-offset seismic data in Saurashtra Basin, India. J. Indian Geophys. Union, 29(4), 218-235.

Kumar, D. and Behera, L., 2024. Upper-crustal structure, compositions and tectonic settings obtained from Perur-Chikmagalur 3-C seismic profile of Archean Dharwar Province, southern India. Acta Geophysica, 72, 2521-2553.

Kumar, J., Singh, P., Verma, N. K. and Negi, M. S., 2005. Modelling of igneous-prone South Rewa basin: An integrated approach. In: Proceedings of 6th International Petroleum Conference and Exhibition, 15-19th January, New Delhi, pp. 1-6.

Lala, T., Chaudhary, A. K., Patil, S. K. and Paul, D. K., 2011. Mafic dykes of Rewa basin, central India: Implications on magma dispersal and petrogenesis. In: Srivastava, R. K. (Eds.), Dyke Swarms. Springer-Verlag, Berlin, pp. 141-162.

Lala, T., Mombasawala, L. S., Pande, K. and Paul, D. K., 2014. New ^{39}Ar-^{40}Ar ages of dykes from Madhya Pradesh and Chhattisgarh: Evidence for polyphase dyke intrusion in eastern Deccan Volcanic Province. Curr. Sci., 107, 1027-1032.

Mukherjee, D., Ray, S., Chandra, S., Pal, S. and Bandyopadhyay, S., 2012. Upper Gondwana succession of the Rewa basin, India: Understanding the interrelationship of lithologic and stratigraphic variables. J. Geol. Soc. India, 79, 563-575.

Nagaraju, P., Ray, L., Singh, S. P. and Roy, S., 2017. Heat flow, heat production, and crustal temperatures in the Archaean Bundelkhand craton, north-Central India: implications for thermal regime beneath the Indian shield. J. Geophys. Res., 122, 5766-5788.

NGRI, 2006. National Geophysical Research Institute, Gravity map series of India, scale 1:20,000,00, Hyderabad, India.

Pandey, O. P., 2020. Heat flow and lithospheric thermal structure. In: Geodynamic evolution of the Indian Shield: Geophysical aspects, Springer, Switzerland, pp 291-330.

Raju, K., Patro, P. K., Borah, U. K., Srivastava, S. and Reddy, K. C., 2022. Evolution of eastern segment of the Central India Tectonic Zone: An insight from a magnetotelluric study. Geophys. J. Int., 230, 272-287.

Rao, G. V. and Rao, R. U. M., 1980. A geothermal study of the Jharia Gondwana basin (India): Heat flow results from several holes and heat production of basement rocks. Earth Planet. Sci. Lett., 48, 397-405.

Rao, G. V. and Rao, R. U. M., 1983. Heat flow in Indian Gondwana basins and heat production of their basement rocks. Tectonophysics, 91, 105-117.

Whiteley, R. J. and Greenhalgh, S. A., 1979. Velocity inversion and the shallow seismic refraction method. Geoexploration, 17, 125-141.

Yilmaz, Ö., 2001. Seismic Data Analysis. Soc. Explor. Geophys., Tulsa, OK, USA.

Zelt, C. A., 1999. Modelling strategies and model assessment for wide-angle seismic traveltime data. Geophys. J. Int., 139, 183-204.

Zelt, C. A. and Ellis, R. M., 1988. Practical and efficient ray tracing in two-dimensional media for rapid traveltime and amplitude forward modeling. Can. J. Exp. Geophys., 24, 16-31.

Zelt, C. A. and Smith, R. B., 1992. Seismic traveltime inversion for 2-D crustal velocity structure. Geophys. J. Int., 108, 16-34.

Received on: 19-05-2026; Revised on: 10-06-2026; Accepted on: 11-06-2026,

J. Ind. Geophys. Union, 30(4) (2026), 253-262
https://doi.org/10.71122/JIGU.30(4)2026.0025

Hurst Exponent-driven magnetotelluric signal noise suppression using adaptive mode decomposition methods

B. Pradeep Naick*[1], K. Naganjaneyulu[2] and I. Santi Prabha[3]
*[1]Instrumentation, Airborne & Engineering Geophysics, CSIR-National Geophysical Research Institute, Hyderabad 500 007, Telangana, India
[2]Magnetotellurics, CSIR-National Geophysical Research Institute, Hyderabad 500 007, Telangana, India
[3]Department of Electronics and Communication Engineering, JNTU Kakinada, Kakinada 533003, Andhra Pradesh, India
*Corresponding author: kholapradeep@gmail.com

Abstract

The magnetotelluric (MT) method is a passive geophysical technique used to image the electrical resistivity structure of the Earth. MT signals are usually contaminated by various types of noise. The quality of the impedance tensor estimate is degraded by noise, which in turn influences subsurface models. In this paper, we present a noise suppression scheme based on the Hurst exponent by applying adaptive mode decomposition methods to MT signals. These methods are, Empirical Mode Decomposition (EMD), Ensemble Empirical Mode Decomposition (EEMD), Complete Ensemble Empirical Mode Decomposition with Adaptive Noise (CEEMDAN), and Improved CEEMDAN (ICEEMDAN). Each method decomposes the noisy MT signal into a set of intrinsic mode functions (IMFs), also called modes or components. We then compute the Hurst exponent for each mode; modes with low Hurst exponents, are considered noise-dominant, and those with high Hurst exponents, are classified as signal-dominant. The noise-suppressed or denoised signal is reconstructed by summing only the signal-dominant modes. We tested this approach on real MT field data collected from the Dharwar Craton, Karnataka State, and compared the performance of all four methods using performance indicators, which include signal-to-noise ratio and correlation coefficient. Results show that the Hurst exponent is an effective criterion for identifying and separating signal from noise in MT data. Among the four methods, ICEEMDAN provides the best noise suppression performance. This study offers a practical, adaptive approach to remove different types of noise from the MT signal.

Keywords: Magnetotellurics, Dharwar Craton, Hurst exponent, Empirical Mode Decomposition, EEMD, CEEMDAN, ICEEMDAN, Noise suppression

INTRODUCTION

The magnetotelluric (MT) method is a geophysical exploration technique. To study the electrical resistivity of the Earth's subsurface, it uses natural variations in the electromagnetic (EM) field. The theoretical basis of the MT method was first proposed by Tikhonov (1950), and later, Cagniard (1953) developed the practical method. Since then, the MT method has been widely used in mineral exploration, geothermal studies, investigations of crustal structure, and hydrocarbon exploration.

At the Earth's surface, MT signals are measured as time series of electric and magnetic field components. The electric field is measured using grounded electrodes, and the magnetic field is measured using induction coils or fluxgate magnetometers. The impedance tensor is estimated by the ratio of electric to magnetic fields in the frequency domain. The impedance tensor is then used to calculate apparent resistivity and phase, which are the primary data used for subsurface imaging.

However, MT signals are mostly contaminated by noise from different sources. Cultural noise from power lines, electric fences, and railways is common in many areas due to urbanisation. The data also gets distorted by near-field source effects. Due to instrument vibrations, random noise from wind, and electronic circuits noise degrades signal quality (Chave and Jones, 2012). This noise is a major problem in MT data processing, which leads to biased impedance estimates and distorted apparent resistivity and phase curves. This, in turn, produces unreliable inversion models.

To handle noise in MT data, different techniques have been developed, such as the remote reference method, where a reference station is used to remove correlated noise (Gamble et al., 1979). Techniques such as robust processing, use statistical methods to downweight noisy data segments (Egbert and Booker, 1986). Fourier-based filtering methods are used to remove narrowband noise such as power line harmonics. However, these methods have limitations, while the remote reference method requires an additional station. Robust processing may not remove strong noise completely, and the Fourier-based filtering method assumes stationarity, which MT signals do not satisfy.

In recent years, data-driven decomposition methods have drawn attention in digital signal processing. Huang et al. (1998) proposed the Empirical Mode Decomposition (EMD) method, which doesn't require a predefined basis; it decomposes a signal into a set of Intrinsic Mode Functions (IMFs). This property makes it an appropriate technique for non-stationary and non-linear signals like MT data. However, there are a few shortcomings, like EMD suffers from mode mixing, which means that a single IMF may contain oscillations of very different frequencies.

To address the mode mixing problem, Wu and Huang (2009) proposed a technique, the Ensemble EMD (EEMD). In this method, before decomposition, white noise is added to the signal, and the results are averaged over many trials. Torres et al. (2011) further improved this approach with Complete Ensemble EMD with Adaptive Noise (CEEMDAN). Later, Colominas et al. (2014) proposed the Improved CEEMDAN

(ICEEMDAN). Each variant reduces the problems of the previous method by improving computational efficiency and mode separation.

A key task in using any decomposition method for noise suppression or denoising is selecting the noise-dominant modes. Several criteria have been proposed, such as energy-based methods that compare mode energies and correlation-based methods that evaluate the extent to which each mode correlates with the original signal. At the same time, when noise and signal overlap in energy or frequency, these methods may not work well.

An alternative approach, named the Hurst exponent, was originally proposed by Hurst (1951) for hydrological studies. The Hurst exponent measures the long-range dependence of a time series. This method has been used in various fields, like finance, network traffic analysis, and geophysics (Mandelbrot and Van Ness, 1968). A time series with a Hurst exponent less than 0.5, is anti-persistent and behaves like noise, and a Hurst exponent greater than 0.5, indicates persistence and long-range dependence, which is characteristic of natural signals. For separating signal from noise in decomposed MT data, this property makes the Hurst exponent a suitable criterion.

In this paper, we propose a noise suppression (denoising) scheme for MT signals. We apply different decomposition methods: EMD, EEMD, CEEMDAN, and ICEEMDAN. We use the Hurst exponent to classify the decomposed intrinsic modes into noise-dominant and signal-dominant categories. We test this scheme on real field MT data and compare the performance of these methods.

MAGNETOTELLURIC METHOD AND NOISE CHARACTERISTICS

Fundamentals of magnetotelluric signals

The MT method is based on the propagation of natural EM fields into the Earth. The fundamental equations are derived from Maxwell's equations in the quasi-static approximation. Under these conditions, displacement currents are neglected. The propagation of the electric field E into a homogeneous half-space is described by:

$$\nabla^2 \mathrm{E} = \mu\sigma \frac{\partial \mathrm{E}}{\partial \mathrm{t}} \qquad (1)$$

Where μ is the magnetic permeability, and σ is the electrical conductivity. The depth to which EM fields penetrate depends on frequency. This is described by the skin depth:

$$\delta = \sqrt{\frac{2}{\omega\mu\sigma}} \approx 03\sqrt{\frac{\rho}{\mathrm{f}}} \qquad (2)$$

Where ω is the angular frequency, ρ is the resistivity in ohm-meters, and f is the frequency in hertz. The skin depth δ is in meters. Lower frequencies penetrate deeper into the Earth. This means MT data at different frequencies provides information about different depths. In practice, we measure two horizontal electric field components (Ex, Ey) and two horizontal magnetic field components (Bx, By). The relationship between these fields in the frequency domain is given by the impedance tensor Z:

$$[\mathrm{Ex}, \mathrm{Ey}]^{\mathrm{T}} = \mathrm{Z}\,[\mathrm{Bx}, \mathrm{By}]^{\mathrm{T}} \qquad (3)$$

where Z is a 2×2 complex tensor. The apparent resistivity and phase are calculated from the impedance tensor elements. For example, the apparent resistivity for the xy component is:

$$\rho_{\mathrm{xy}} = \left(\frac{1}{\omega\mu}\right)\left|\mathrm{Z}_{\mathrm{xy}}\right|^2 \qquad (4)$$

and, the phase is:

$$\varphi_{\mathrm{xy}} = \arctan\left(\frac{\mathrm{Im}\left(\mathrm{Z}_{\mathrm{xy}}\right)}{\mathrm{Re}\left(\mathrm{Z}_{\mathrm{xy}}\right)}\right) \qquad (5)$$

These quantities serve as the basis for MT interpretation and inversion.

Sources and types of noise in MT Data

MT signals are passive measurements of natural EM field variations. These natural sources include thunderstorm activity (above 1 Hz) and solar wind interactions with the magnetosphere (below 1 Hz). Because the signals are natural, they cannot be controlled. This makes MT data vulnerable to noise contamination (Simpson and Bahr, 2005; Chave and Jones, 2012).

Cultural noise is the most common problem; power lines produce strong signals at 50 Hz or 60 Hz and their harmonics, and electric fences produce periodic impulses. Railways with DC traction produce broadband noise, and industrial machinery creates electromagnetic interference. This type of noise is especially strong in urban and semi-urban areas.

Near-field source effects occur when the EM source is close to the measurement site. The MT method assumes plane-wave sources at large distances. When sources are nearby, this assumption breaks down, and the measured fields no longer represent the true subsurface response. Random noise arises from wind-induced sensor vibration, thermal noise is generated in electronic circuits, and poor electrode contact.

These types of noise are typically broadband and unpredictable.

Impact of noise on MT data quality

In MT data processing, noise affects the data at every stage. In the time domain, generally noise corrupts the measured field components and in the frequency domain, noise biases the cross-spectral estimates, which then leads to errors in the impedance tensor. The apparent resistivity curves become scattered, and the phase curves show large deviations from smooth trends. When noisy data are used for inversion, the resulting resistivity models contain artifacts. These artifacts can be mistaken for real geological features. For this reason, effective noise suppression is essential for reliable MT interpretation.

THEORETICAL BACKGROUND OF DECOMPOSITION METHODS

Empirical Mode Decomposition (EMD)

EMD was proposed by Huang et al. (1998) as an adaptive signal decomposition method. It decomposes a signal x(t) into a finite set of Intrinsic Mode Functions (IMFs) and a residue. Each IMF satisfies two conditions. First, the number of extrema and the number of zero crossings must differ by at most one. Second, the mean of the upper and lower envelopes must be zero at every point (Garcia-Casado et al., 2010). The decomposition is performed through a sifting process. The steps are as follows.

(i) Identify all local maxima and minima of x(t).

(ii) Connect all maxima by a cubic spline to form the upper envelope $e_{max}(t)$.

(iii) Connect all minima by a cubic spline to form the lower envelope $e_{min}(t)$.

(iv) Compute the mean envelope: $m(t) = (e_{max}(t) + e_{min}(t))/2$.

(v) Subtract the mean from the signal: $h(t) = x(t) – m(t)$.

(vi) Check if h(t) satisfies the IMF conditions. If not, repeat steps 1–5 with h(t) as the new signal.

(vii) When the conditions are met, h(t) is the first IMF, $c_1(t)$.

(viii) Compute the residue: $r(t) = x(t) – c_1(t)$.

(ix) Repeat the process on r(t) to extract subsequent IMFs.

The process stops when the residue is a monotonic function or has fewer than two extrema.

The original signal can be reconstructed as:

$$x(t) = \sum c_i(t) + r_n(t), i = 1,2, \dots \dots, n \qquad (6)$$

where $c_i(t)$ are the IMFs and $r_n(t)$ is the final residue. EMD is fully data-driven; it does not require a predefined basis. However, EMD has a well-known problem called mode mixing, which occurs when oscillations of different time scales appear in the same IMF or similar oscillations are split across different IMFs.

Ensemble Empirical Mode Decomposition (EEMD)

EEMD was proposed by Wu and Huang (2009) to address mode-mixing problems. The key idea is to add white noise to the signal before decomposition. The noise fills the entire frequency space evenly. This helps the sifting process to separate different scales properly.

The EEMD algorithm works as follows.

(i) Add a realization of white Gaussian noise w(t) to the signal: $x_i(t) = x(t) + w(t)$.

(ii) Decompose $x_i(t)$ using EMD to obtain IMFs.

(iii) Repeat steps 1–2 for N trials with different noise realizations.

(iv) Average the IMFs across all trials.

The ensemble average cancels out the added noise because the noise is random and has zero mean. The number of trials N and the noise amplitude ‘ε’ are two important parameters. Typical values are N = 100 to 500 and ε = 0.1 to 0.4 times the standard deviation of the signal.

EEMD effectively reduces mode mixing, however, it has some drawbacks. The ensemble averaging does not guarantee a complete reconstruction. The sum of all averaged IMFs may not exactly equal the original signal. Also, residual noise may remain in the averaged IMFs.

Complete Ensemble Empirical Mode Decomposition with Adaptive Noise (CEEMDAN)

CEEMDAN addresses the limitations of EEMD and this method was proposed by Torres et al. (2011). In CEEMDAN, adaptive noise is added at each stage of the decomposition rather than only at the beginning. The method adds noise to the residue at each decomposition level. This produces a more complete decomposition with near-zero reconstruction error. The CEEMDAN procedure is as follows.

(i) Add white noise to the signal and decompose using EMD.

(ii) Average the first IMFs across all trials to get the first CEEMDAN mode.

(iii) Compute the residue.

(iv) Add noise to the residue and extract the next mode.

(iv) Repeat until no more modes can be extracted.

The reconstruction error in CEEMDAN is much smaller than in EEMD and the computational cost is also lower because fewer trials are needed.

Improved CEEMDAN (ICEEMDAN)

ICEEMDAN was proposed by Colominas et al. (2014) as a further improvement over CEEMDAN. It addresses two issues: First, CEEMDAN can produce spurious modes in the early decomposition stages. Second, CEEMDAN modes may contain residual noise.

In ICEEMDAN, the first residue is computed differently: instead of using the first IMF directly, it uses the local mean of the signal with added noise. This reduces noise in the first mode. The subsequent stages also use a modified approach that produces cleaner modes with better spectral separation. ICEEMDAN achieves lower reconstruction error and better mode separation than CEEMDAN.

HURST EXPONENT AS A NOISE-SIGNAL DISCRIMINATOR

Concept and definition

The Hurst exponent was introduced by Hurst (1951) during his study of the Nile River's flood patterns. The Hurst exponent is a measure of the long-range dependence of a signal time series. It takes values between 0 and 1. The interpretation is done as below (Guangxi et., 2018):

(i) $H < 0.5$: The signal time series is anti-persistent. That is, an increase is likely to be followed by a decrease and vice versa. This type of behaviour is characteristic of noise.

(ii) $H = 0.5$: The signal time series is a random walk. It indicates there is no long-range dependence. This corresponds to white noise or Brownian motion increments.

(iii) $H > 0.5$: The signal time series is persistent. That is, an increase is likely to be followed by another increase. This type of behaviour indicates long-range dependence and is typical of natural signals.

Estimation using rescaled range analysis

To estimate the Hurst exponent, we used the Rescaled Range (R/S) analysis. This is the classical method proposed by Hurst. For a signal time series of length N, the procedure is written below:

a. Divide the time series into sub-series of length n.

b. For each sub-series, compute the mean.

c. Compute the cumulative deviation from the mean.

d. Calculate the range R as the difference between the maximum and minimum of the cumulative deviation.

e. Calculate the standard deviation S.

f. Compute the ratio R/S.

g. Average R/S over all sub-series.

h. Repeat for different values of n.

The Hurst exponent is estimated from the relationship:

$$E\left[\frac{R}{S}\right] = C \cdot n^{H} \qquad (7)$$

where E[R/S] is the expected value of the rescaled range, C is a constant, n is the sub-series length, and H is the Hurst exponent. Taking the logarithm of both sides:

$$\log\left[\frac{R}{S}\right] = H \cdot \log(n) + \log(C) \qquad (8)$$

The Hurst exponent H is the slope of the line obtained by plotting log(R/S) against log(n). This slope is estimated using linear regression.

Hurst Exponent for mode classification

When we decompose an MT signal using any of the four methods, we obtain a set of modes. Some modes are dominated by noise and others contain the true MT signal. The Hurst exponent provides a natural way to distinguish between these two types.

Noise-dominant modes have low Hurst exponent values, typically below 0.5. This is because noise lacks long-range dependence. Signal-dominant modes have high Hurst exponent values, typically above 0.5. This is because natural MT signals exhibit persistence and long-range dependence due to the diffusive nature of EM wave propagation in the Earth.

We set a threshold value H_{th} to classify the modes. Modes with $H < H_{th}$ are considered noise-dominant and are discarded. Modes with $H \geq H_{th}$ are considered signal-dominant and are retained. In this study, we used $H_{th} < 0.4$ as the primary threshold. This value was chosen based on preliminary tests on the dataset, which showed that $H_{th} = 0.4$ provides clearer separation between noise-dominant and signal-dominant modes compared to the standard boundary of $H_{th} = 0.5$, while better preserving weak signal modes in real MT field data.

Compared to other mode selection criteria such as energy-based and correlation-based methods, the Hurst exponent has several advantages. It is independent of the signal amplitude, it captures the temporal structure of the mode rather than just its magnitude and it is robust to the scaling of the signal. These properties make it well suited for MT signals, which can vary greatly in amplitude across different frequency bands.

PROPOSED DENOISING APPROACH

Overall workflow

The proposed denoising approach consists of four major steps. Figure 1 shows the complete procedure in a flow chart.

Decomposition: The noisy MT signal x(t) is decomposed into a set of intrinsic modes using one of the four methods (EMD, EEMD, CEEMDAN, ICEEMDAN). Each method produces a set of modes $\{c_1(t), c_2(t), ..., c_n(t)\}$ and a residue r(t).

Hurst exponent computation: For each mode $c_i(t)$, compute the Hurst exponent H_i using the R/S analysis described in previous section.

Mode classification: Classify each mode based on its Hurst exponent. If $H_i < H_{th}$, the mode is labelled as noise-dominant. If $H_i \geq H_{th}$, the mode is labelled as signal-dominant.

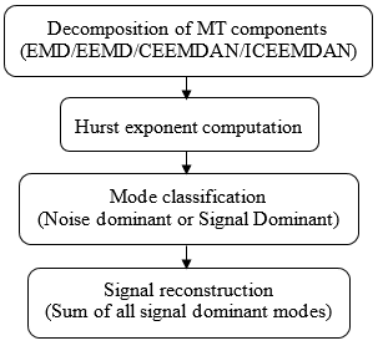

Figure 1. Flowchart of the proposed MT signals denoising approach.

Signal reconstruction: The denoised signal is then reconstructed by summing the signal-dominant modes only:

$$\hat{x}(t) = \sum_i c_i(t) + r(t), \quad \text{Where } H_i \geq H_{th} \tag{9}$$

where, $\hat{x}(t)$ represents the denoised signal and the residue r(t) is always included in the reconstruction because it represents the overall trend of the signal.

The flowchart illustrates the four steps of the proposed denoising approach. First, the noisy MT signal components are decomposed into intrinsic mode functions (IMFs) using one of the four methods (EMD, EEMD, CEEMDAN, or ICEEMDAN). Second, the Hurst exponent is computed for each IMF using rescaled range (R/S) analysis. Third, each IMF is classified as either noise-dominant ($H < H_{th}$) or signal-dominant ($H \geq H_{th}$) based on its Hurst exponent value. Finally, the denoised signal is reconstructed by summing only the signal-dominant modes along with the residue.

Implementation details

Before applying the decomposition, we performed basic pre-processing and removed linear trend from the MT time series. For EEMD, we used an ensemble size of N = 5 and a noise amplitude of $\varepsilon = 0.2$ times the standard deviation of the input signal. For CEEMDAN and ICEEMDAN, we used N = 5 trials each. The Hurst exponent is computed for each mode using R/S analysis with sub-series lengths ranging from 10 to N/4, where N is the mode length. We used at least 10 different sub-series lengths to ensure a reliable estimate of the slope in the log-log plot.

Evaluation Metrics

We used the following metrics to evaluate denoising performance. The first is the Signal-to-Noise Ratio (SNR) and Signal-to-Noise-Ratio improvement (ΔSNR):

$$\text{SNR} = 10 \log_{10}\left(\frac{P_{signal}}{P_{noise}}\right) \text{(dB)} \tag{10}$$

$$\text{and,} \quad \Delta\text{SNR} = \text{SNR}_{out} - \text{SNR}_{in} \text{ (dB)} \tag{11}$$

Where P_{signal} is the power of the signal, P_{noise} is the power of the noise component, SNR_{out} is the SNR after denoising and SNR_{in} is the SNR before denoising. A higher ΔSNR indicates better noise removal. The second metric is the correlation coefficient (CC):

$$CC = \frac{\text{Cov}(x, \hat{x})}{\sigma_x \cdot \sigma_{\hat{x}}} \tag{12}$$

where Cov denotes covariance and σ denotes standard deviation. A CC value close to 1 indicates high similarity between the original and denoised signals.

APPLICATION TO REAL MAGNETOTELLURIC FIELD DATA

Field data description

We applied the proposed approach to real MT field data. The data were collected from a survey site in the Dharwar Craton (Karnataka state, southern India). The survey used a standard five-component MT setup. We measured two horizontal electric fields (Ex, Ey) and three magnetic fields (Bx, By, Bz). High-frequency data acquired with a broadband field system were used to test the denoising approach. The sampling rate of high frequency data is 640 Hz, and the recording duration is approximately 50 minutes.

The field data contain visible noise contamination, and the time series shows signatures of cultural noise. The apparent resistivity and phase curves computed from the raw data show significant scatter and are not smooth.

Denoising results on field data

We applied all four decomposition methods to the high frequency field MT time series (Figure 2) shows an example of the intrinsic model functions (IMFs) after decomposition of the Bx component using ICEEMDAN method. The decomposition produces 20 modes. The first few modes correspond to high-frequency oscillations. The later modes contain lower-frequency components. Likewise, all five components (i.e., Ex, Ey, Bx, By, and Bz) of high-frequency MT data are decomposed to corresponding IMF modes using all four methods (i.e., EMD, EEMD, CEEMDAN, ICEEMDAN).

Tables 1(a) and 1(b) show the Hurst exponent values computed for each mode across all four methods. In all cases, the first few modes (high-frequency) have Hurst exponent values below 0.4. These correspond to noise-dominant modes. The latter modes have Hurst exponent values above 0.4, indicating signal-dominant behavior. The transition from noise to signal modes is generally sharp, which validates the effectiveness of the Hurst exponent criterion.

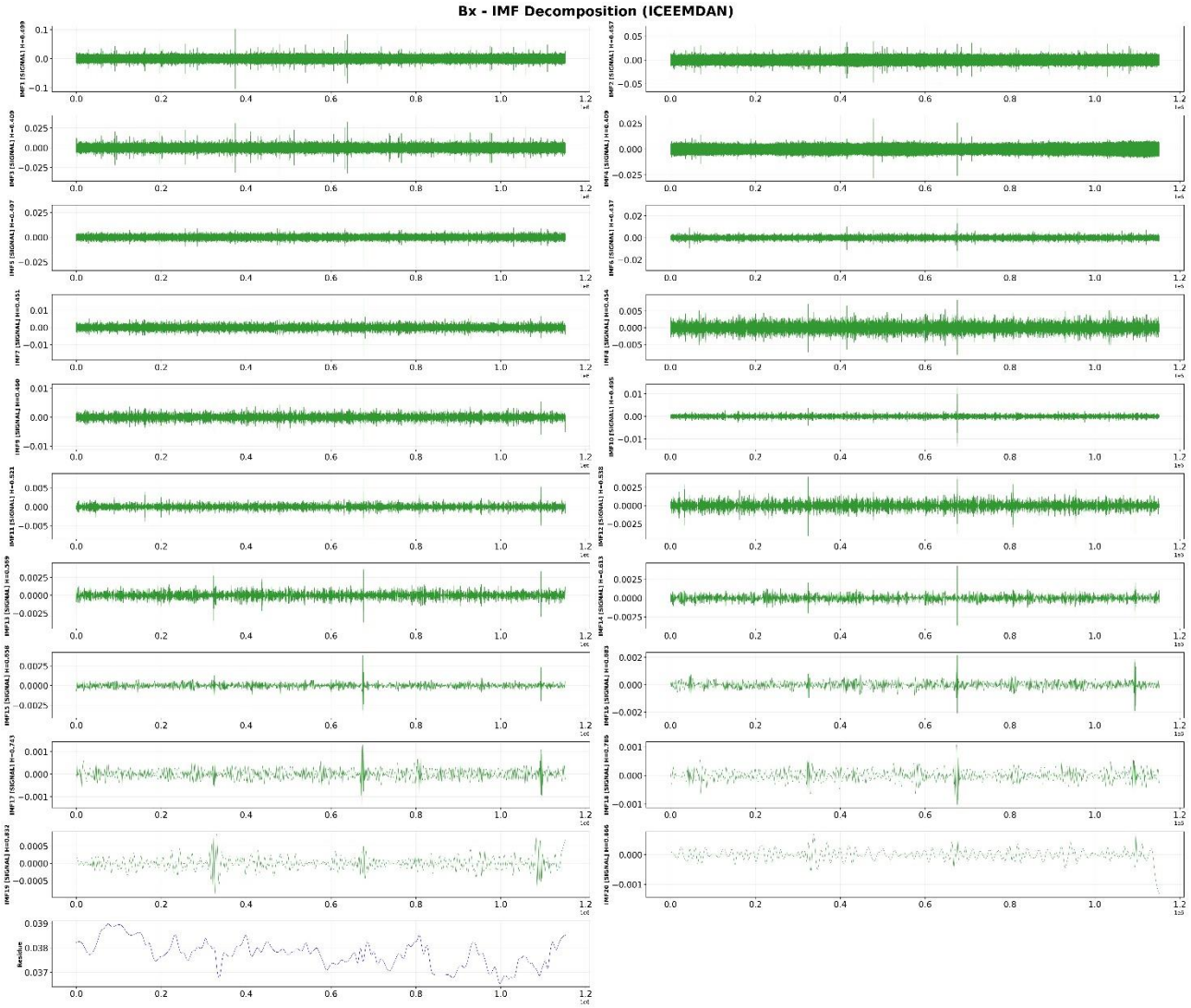

Figure 2. ICEEMDAN IMFs decomposition of the Bx component from high frequency field MT data. Each panel shows one mode from highest frequency (top) to lowest frequency (bottom). The final panel shows the residue.

Table 1(a). Hurst exponent values of modes for EMD and EEMD methods.

IMF	EMD					EEMD				
	Ex	Ey	Bx	By	Bz	Ex	Ey	Bx	By	Bz
IMF1	0.2966	0.5102	0.4905	0.2952	0.3115	0.4012	0.5035	0.4759	0.4053	0.3932
IMF2	0.3173	0.5247	0.4508	0.3264	0.4339	0.3551	0.4973	0.4369	0.3578	0.4120
IMF3	0.3642	0.4772	0.4115	0.4065	0.5650	0.3946	0.4355	0.4341	0.4092	0.4407
IMF4	0.3749	0.4225	0.4091	0.2711	0.3460	0.4024	0.4152	0.3833	0.3671	0.3852
IMF5	0.2961	0.4275	0.4003	0.3136	0.4339	0.3920	0.4105	0.4189	0.3776	0.3749
IMF6	0.5239	0.4530	0.4443	0.4933	0.4604	0.4216	0.4479	0.4270	0.4376	0.4293
IMF7	0.4407	0.4347	0.4351	0.4533	0.4374	0.4538	0.4370	0.4481	0.4328	0.4426
IMF8	0.4750	0.4462	0.4521	0.4847	0.4824	0.4474	0.4469	0.4475	0.4736	0.4426
IMF9	0.5057	0.5016	0.4845	0.4955	0.5401	0.4829	0.4786	0.4967	0.4893	0.5165
IMF10	0.5418	0.5291	0.5187	0.5224	0.5680	0.4978	0.4909	0.5167	0.5109	0.5108
IMF11	0.5668	0.5491	0.5443	0.5574	0.5596	0.5322	0.5209	0.5462	0.5531	0.5555
IMF12	0.6286	0.5934	0.5687	0.5756	0.5843	0.5577	0.5913	0.5689	0.6219	0.5792
IMF13	0.6444	0.6149	0.5961	0.6220	0.6195	0.6106	0.6169	0.5817	0.6196	0.6159
IMF14	0.6707	0.6634	0.6290	0.6642	0.6466	0.6455	0.6601	0.6483	0.6503	0.6694
IMF15	0.7252	0.6639	0.6587	0.6902	0.6767	0.6611	0.6972	0.6718	0.6874	0.6777
IMF16	0.7527	0.7531	0.6852	0.7164	0.7244	0.7059	0.7092	0.7025	0.7024	0.7252
IMF17	0.7841	0.7615	0.7395	0.7878	0.7493	0.7363	0.7675	0.7360	0.7431	0.7673
IMF18	0.8189	0.8208	0.7695	0.7995	0.7875	0.7655	0.8000	0.7704	0.7670	0.7917
IMF19	0.8569	0.8597	0.8189	0.8294	0.8685	0.8060	0.8601	0.8301	0.8275	0.8546
IMF20	0.9115	0.8666	0.8570	0.8647	0.8784	0.8666	0.8664	0.8665	0.8422	0.8812

Table 1(b). Hurst exponent values of modes for CEEMDAN and ICEEMDAN methods.

IMF	CEEMDAN					ICEEMDAN				
	Ex	Ey	Bx	By	Bz	Ex	Ey	Bx	By	Bz
IMF1	0.3933	0.5019	0.4939	0.4044	0.3855	0.4205	0.4994	0.4991	0.4317	0.4253
IMF2	0.4508	0.4828	0.4766	0.4505	0.4743	0.3835	0.4740	0.4573	0.3964	0.4100
IMF3	0.4426	0.4433	0.4518	0.4280	0.4262	0.4084	0.4446	0.4094	0.4253	0.4396
IMF4	0.4258	0.4201	0.4383	0.4475	0.4466	0.4008	0.4007	0.4085	0.3798	0.3911
IMF5	0.3992	0.3968	0.4017	0.3704	0.3638	0.4009	0.4222	0.4066	0.3955	0.3944
IMF6	0.4161	0.4235	0.4330	0.4110	0.4005	0.4113	0.4355	0.4368	0.4191	0.4257
IMF7	0.4409	0.4329	0.4341	0.4095	0.4257	0.4426	0.4414	0.4511	0.4456	0.4718
IMF8	0.4488	0.4463	0.4519	0.4367	0.4502	0.4330	0.4326	0.4543	0.4280	0.4465
IMF9	0.4256	0.4334	0.4627	0.4509	0.4355	0.4771	0.4685	0.4602	0.4581	0.4868
IMF10	0.4617	0.4772	0.4617	0.4632	0.4831	0.5118	0.5020	0.4945	0.5003	0.5084
IMF11	0.5162	0.4969	0.5141	0.4994	0.5110	0.5572	0.5438	0.5212	0.5224	0.5386
IMF12	0.5368	0.5263	0.5306	0.5218	0.5168	0.5681	0.5625	0.5380	0.5664	0.5708
IMF13	0.5599	0.5630	0.5425	0.5375	0.5561	0.6024	0.6336	0.5695	0.6389	0.6114
IMF14	0.6137	0.6028	0.5728	0.5726	0.5781	0.6401	0.6484	0.6127	0.6830	0.6478
IMF15	0.6423	0.6371	0.6078	0.6347	0.5991	0.6807	0.6782	0.6582	0.6998	0.6831
IMF16	0.6535	0.6633	0.6383	0.6504	0.6834	0.7147	0.7292	0.6830	0.7458	0.7041
IMF17	0.6844	0.6925	0.6569	0.6927	0.7302	0.7594	0.7650	0.7425	0.7528	0.7446
IMF18	0.7135	0.7045	0.7171	0.7254	0.7603	0.7960	0.8069	0.7864	0.7768	0.7818
IMF19	0.7785	0.7601	0.7582	0.7804	0.7522	0.8285	0.8494	0.8316	0.8259	0.8322
IMF20	0.8124	0.8109	0.8412	0.7849	0.7805	0.8509	0.8678	0.8658	0.8844	0.8437

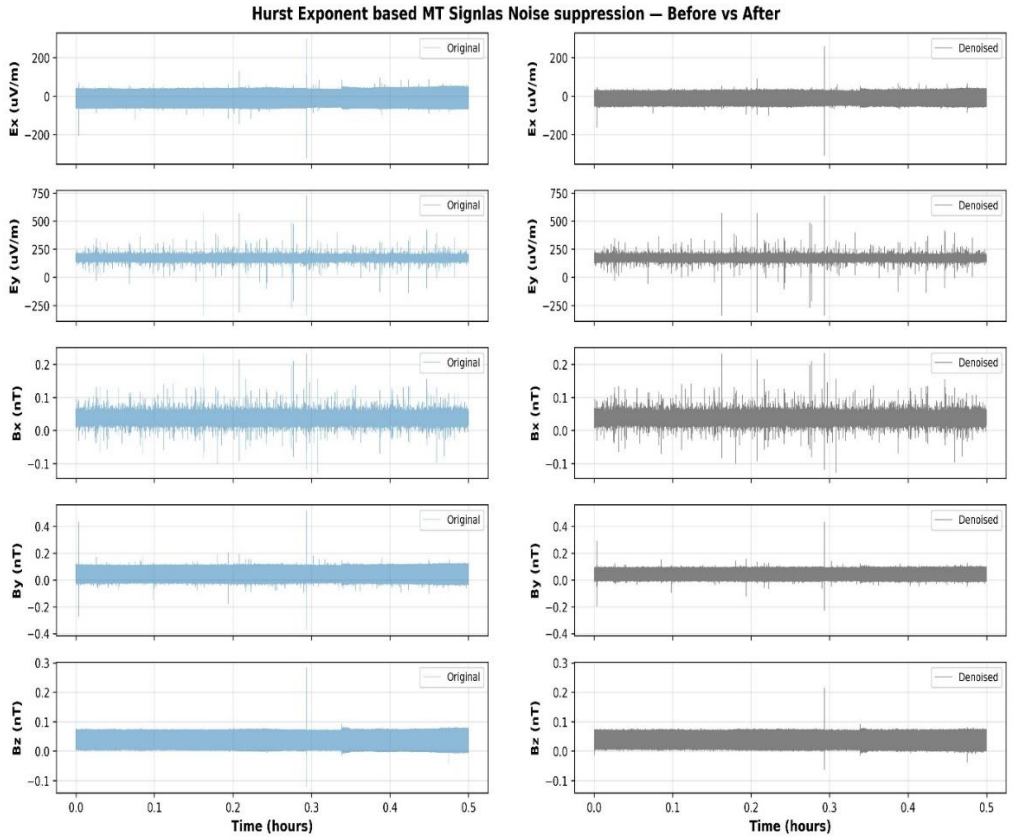

Figure 3. Comparison of original and denoised MT time series of all five components using ICEEMDAN method.

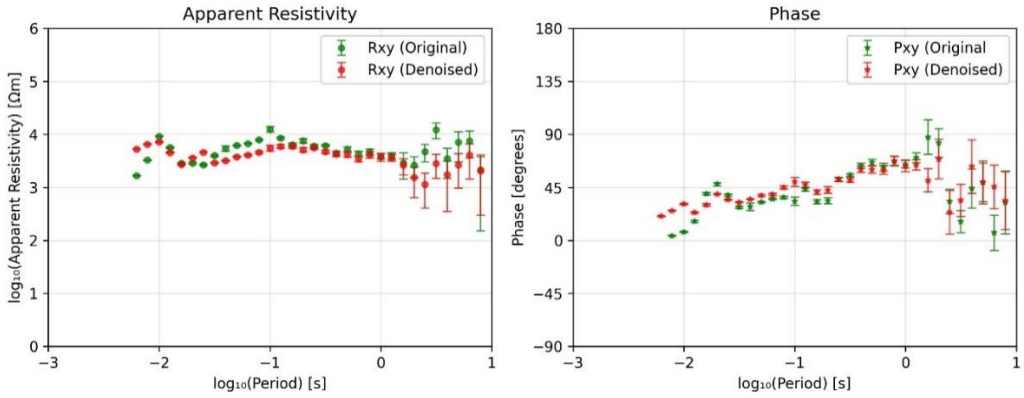

Figure 4. Apparent resistivity (left) and phase (right) curves. Green dots show original data and red dots show results after denoising with ICEEMDAN method.

Table 2. Noise suppression performance comparison of the four decomposition methods on field MT data. All the values represent the average of five MT components.

Method	ΔSNR (dB)	Correlation Coefficient
EMD	0.075	0.461
EEMD	8.967	0.775
CEEMDAN	12.89	0.726
ICEEMDAN	13.084	0.930

Figure 3 shows the denoised time series of all five components using the ICEEMDAN method compared with the original noisy signal. All methods successfully remove high-frequency noise. However, the degree of noise removal and signal preservation varies. CEEMDAN and ICEEMDAN produce the smoothest results while preserving the important signal features. EMD shows some residual noise due to mode mixing. EEMD and CEEMDAN perform better than EMD but not as well as ICEEMDAN.

Figure 4 shows the apparent resistivity and phase curves before and after denoising the MT components. The raw data curves show scatter, and after denoising with the ICEEMDAN method, the curves become much smoother. The improvement is noticeable at high frequencies where cultural noise is stronger.

Table 2 presents the quantitative comparison of all four methods. The table shows the SNR improvement, correlation coefficient. ICEEMDAN achieves the highest ΔSNR and correlation coefficient. EMD has the fastest computation but the lowest denoising performance due to mode mixing.

DISCUSSION

The results show a clear progression in Hurst exponent values from EMD to ICEEMDAN within the EMD family. EMD suffers from mode mixing. This causes some noise to be classified as signal, and some signal to be classified as noise. EEMD reduces mode mixing through ensemble averaging. However, the residual noise in EEMD is higher than in CEEMDAN and ICEEMDAN. CEEMDAN provides a near-complete reconstruction. ICEEMDAN further improves mode separation by reducing spurious modes.

In terms of computational cost, EMD is the fastest. EEMD and CEEMDAN are slower because they require multiple trials. For real-time MT processing, ICEEMDAN offers the best balance between quality and speed. All computations were performed in Python using Jupyter Notebook. The computational times for EMD, EEMD, CEEMDAN, and ICEEMDAN were approximately 3, 10, 112, and 18 hours, respectively, for a dataset consisting of 11,52,000 samples for each MT component. The long computational time is primarily due to the large dataset size and the ensemble-based nature of the methods.

The Hurst exponent proves to be an effective criterion for mode classification. Its energy lies in its capacity to capture the temporal structure of the signal. Natural MT signals arise from diffusion processes in the Earth. These signals exhibit long-range dependence, which translates to high Hurst exponent values. Noise, on the other hand, lacks this temporal structure. This fundamental physical difference makes the Hurst exponent a natural choice for MT denoising (Flandrin et al., 2004; Wu and Huang, 2004).

The threshold of $H_{th} < 0.4$ works well in this case. However, in some situations, a slightly different threshold may be needed. For example, when the noise is coloured rather than white, its Hurst exponent may be slightly above 0.5. In such cases, a higher threshold (e.g., $H_{th} = 0.55$ or 0.6) may be more appropriate. We recommend testing a range of threshold values and selecting the one that gives the best results based on the evaluation metrics.

The Hurst exponent threshold should be set to 0.5 as a starting point. If the denoised data still shows noise, the threshold can be increased. If the denoised data appears over-smoothed, the threshold can be decreased. The user should always inspect the apparent resistivity and phase curves before and after denoising to verify the quality of the results.

Further, this study has a few limitations. Firstly, we process each channel of the MT data independently. A multivariate approach that considers all channels simultaneously could improve performance. Secondly, the Hurst exponent threshold is set manually. An automatic threshold selection method based on statistical criteria would make the approach more robust. Future work should therefore explore multivariate extensions of the decomposition methods for MT denoising. Application to other geophysical signals such as seismic, ground penetrating radar, and gravity data is also a promising direction (Li et al., 2018; Neukirch and Garcia, 2014; Sungkono and Santosa, 2015).

CONCLUSIONS

We presented a denoising approach for magnetotelluric signals based on the Hurst exponent. The approach works with four different decomposition methods: EMD, EEMD, CEEMDAN, ICEEMDAN. Each method decomposes the noisy MT signal into intrinsic mode functions. The Hurst exponent of each mode is computed using rescaled range analysis. Modes with Hurst exponent values below the threshold are classified as noise and removed. The denoised signal is reconstructed from the remaining modes.

We tested the method on real field MT data and the results show that the Hurst exponent is an effective criterion for separating signal from noise. All the methods improve the data quality. However, the performance varies across methods. Within the EMD family, ICEEMDAN provides

the best results due to its superior mode separation. CEEMDAN offers a good compromise between quality and complexity. EEMD improves over basic EMD but has higher residual noise. EMD is the simplest but is limited by mode mixing.

The proposed approach is adaptive, data-driven, and easy to implement. It does not require prior knowledge of the noise characteristics. The Hurst exponent provides a physically motivated criterion that distinguishes between the persistent nature of MT signals and the anti-persistent nature of noise, which makes the apparent resistivity and phase curves smoother without losing the original characteristic features.

Acknowledgements

The authors sincerely thank Dr. O. P. Pandey for editorial handling and the anonymous reviewers for their insightful comments and valuable suggestions. The authors are thankful to the Director of CSIR-NGRI, Hyderabad, for his encouragement and permission to publish this work. The corresponding author is thankful to Dr. H.V.S. Satyanarayana, Project Leader of the Division, for his encouragement and support. The authors are also thankful to the Head of the department (ECE), JNTUK. Kakinada for the support.

Author Credit Statement

B. Pradeep Naick is credited with the data acquisition, algorithm development, data processing, and drafting of the manuscript; K. Naganjaneyulu is credited with the responsibility as a principal investigator of the LMTENDEX project, including the site selections, data acquisition, magnetotelluric data analysis, supervision, and paper draft; I. Santi Prabha is credited with overall supervision, interpretation and review.

Data availability

The data used in this study is proprietary of CSIR– National Geophysical Research Institute, Hyderabad, and governed by its data sharing policy.

Compliance with ethical standards

The authors declare no conflict of interest and adhere to copyright norms.

References

Cagniard, L., 1953. Basic theory of the magneto-telluric method of geophysical prospecting. Geophysics, 18(3), 605–635.

Chave, A.D. and Jones, A.G. (eds.), 2012. The Magnetotelluric Method: Theory and Practice. Cambridge University Press.

Colominas, M.A., Schlotthauer, G. and Torres, M.E., 2014. Improved complete ensemble EMD: A suitable tool for biomedical signal processing. Biomedical Signal Processing and Control, 14, 19–29.

Egbert, G.D. and Booker, J.R., 1986. Robust estimation of geomagnetic transfer functions. Geophys. J. Int., 87(1), 173–194.

Flandrin, P., Rilling, G. and Goncalves, P., 2004. Empirical mode decomposition as a filter bank. IEEE Signal Processing Lett., 11(2), 112–114.

Gamble, T.D., Goubau, W.M. and Clarke, J., 1979. Magnetotellurics with a remote magnetic reference. Geophysics, 44(1), 53–68.

Garcia-Casado, J, Y Ye-Lin, G Prats-Boluda, J Guimera, and J Alberola, 2010. Enhancement of Laplacian EEnG from humans by means of an EMD-based method. Annual International Conference of the IEEE Engineering in Medicine and Biology. Buenos Aires, Argentina, 943–946.

Guangxi, C., Ling-Yun He and Jie Cao, 2018. Multifractal Detrended Analysis Method and Its Application in Financial Markets. Springer.

Huang, N.E., Shen, Z., Long, S.R., Wu, M.C., Shih, H.H., Zheng, Q., Yen, N.C., Tung, C.C. and Liu, H.H., 1998. The empirical mode decomposition and the Hilbert spectrum for nonlinear and non-stationary time series analysis. Proc. Royal Soc. London A, 454(1971), 903–995.

Hurst, H.E., 1951. Long-term storage capacity of reservoirs. Trans. American Society of Civil Engineers, 116, 770–799.

Li, J., Zhang, X., Gong, J. and Tang, J., 2018. Signal–noise identification of magnetotelluric signals using fractal–entropy and clustering algorithm. Fractals, 26(2), 1840011.

Mandelbrot, B.B. and Van Ness, J.W., 1968. Fractional Brownian motions, fractional noises and applications. SIAM Review, 10(4), 422–437.

Neukirch, M. and Garcia, X., 2014. Nonstationary magnetotelluric data processing with instantaneous parameter. J. Geophys. Res., Solid Earth, 119(3), 1634–1654.

Simpson, F. and Bahr, K., 2005. Practical Magnetotellurics. Cambridge University Press.

Sungkono and Santosa, B.J., 2015. Application of EEMD and Hurst exponent for geophysical signal denoising. J. Physics: Conference Series, 633, 012053.

Tikhonov, A.N., 1950. On determining electrical characteristics of the deep layers of the Earth's crust. Doklady Akademii Nauk SSSR, 73(2), 295–297.

Torres, M.E., Colominas, M.A., Schlotthauer, G. and Flandrin, P., 2011. A complete ensemble empirical mode decomposition with adaptive noise. In IEEE Int. Conf. on Acoustics, Speech and Signal Processing (ICASSP), 4144–4147.

Wu, Z. and Huang, N.E., 2004. A study of the characteristics of white noise using the empirical mode decomposition method. Proc. Royal Soc. London A, 460(2046), 1597–1611.

Wu, Z. and Huang, N.E., 2009. Ensemble empirical mode decomposition: A noise-assisted data analysis method. Advances in Adaptive Data Analysis, 1(1), 1–41.

(Received on: 08-04-2026; Revised on: 21- 04-2026 ; Accepted on: 15-05-2026)

J. Ind. Geophys. Union, 30(4) (2026), 263-275
https://doi.org/10.71122/JIGU.30(4)2026.0026

Prediction of pre-monsoon temperature of Varanasi using machine learning and deep learning techniques

R. Bhatla[1*], Mohini Dangi[2], Aashna Verma[1]and Manjari Gupta[3]
[1] Department of Geophysics, Institute of Science, BHU, Varanasi-221005, India
[2] DST- CIMS, Institute of Science, BHU, Varanasi-221005 , India
[3] Department of Computer Science, Institute of Science, BHU, Varanasi-221005, India
*Corresponding author: rbhatla@bhu.ac.in

ABSTRACT

Accurate short-term temperature forecasting is essential for understanding climate changes and supporting agricultural planning during the pre-monsoon period in northern India, when temperatures rise sharply. Although machine learning approaches have been applied in several regions, their performance for short-lead prediction, using long historical observations in densely populated urban areas such as Varanasi, has received very limited attention. In this study, we evaluate four widely used machine learning and deep learning models, Support Vector Regression (SVR), Random Forest (RF), Multi-Layer Perceptron (MLP), and Long Short-Term Memory (LSTM), to predict daily maximum temperature using a univariate approach over Varanasi, based on 71 years of IMD observations. The purpose of adopting a univariate framework is to keep forecasting operationally simple, while capturing the short-term evolution of temperature patterns without additional climatic variables. Our results show that SVR achieved the highest R^2 score (0.801) and correlation (0.897), while LSTM produced the lowest RMSE (1.673) and MAE (1.213). Overall, LSTM is considered the best performing model because the study prioritizes minimizing short-term forecasting errors, even though SVR achieves the highest explained variance. The good performance of SVR and LSTM suggests that short-term temperature forecasts can be generated reliably with limited input information, which is useful for early warnings, heatwave preparedness, and agricultural decision making during the vulnerable pre-monsoon season in the region.

Keywords: Univariate time series; Deep learning; Long Short-Term Memory (LSTM); Temperature forecasting; Support Vector Regression.

INTRODUCTION

Temperature plays a central role in shaping human health, agriculture and local environmental conditions. Rising temperatures increase the frequency and duration of heat waves, and prolonged exposure can lead to heat stress, heatstroke and cardiovascular risks, particularly among vulnerable populations such as the elderly and those with pre-existing medical conditions. Accurate temperature forecasting is essential for anticipating extreme events and improving preparedness during high-risk periods. In addition to its direct impact, temperature fluctuations are intricately linked to broader environmental and societal challenges such as urbanization, which has become a major contributor to global warming and environmental degradation (Grimmond et al., 2007, Bhatla et al., 2016a, Gupta et al., 2019). Human activities, such as deforestation for agricultural expansion and industrialization, are driven by the growing population's demands. The consequences of these activities result in disrupting the ecosystem, increasing flood and drought frequency (Verma et al., 2022; Verma et al., 2023; Maurya et al., 2023, Bhatla et al., 2025), intensifying typhoons, reducing freshwater availability, and leading to erratic and random temperature rises (Nikam and Meshram, 2013, Kumar et al., 2024). Climate models project that temperature variability in India will increase by up to 10% ºC by the end of this decade, potentially causing soil drying and shifts in atmospheric structure (Bathiany et al., 2018). Throughout the 21st century, India is expected to experience greater seasonal variation in temperature and warming beyond the global average. However, rising temperatures could lead to a 40% decline in India's agricultural productivity by the 2080s. The threats of climate change are also affecting the quality and quantity parameters of water resources and crop productivity (Kumar et al., 2014, Bhatla et al., 2016b).

Predicting these impacts requires robust forecasting methods, as effective forecasting can help mitigate risks and adapt to changing conditions. Traditional statistical approaches such as the autoregressive integrated moving average (ARIMA) model have been widely used for weather and climate time-series forecasting because they are mathematically interpretable and effective for short memory processes. However, ARIMA assumes linearity and stationarity, which limits its ability to capture rapidly changing and non-linear temperature behaviour, especially during pre-monsoon months when short-term variability and extremes are common. More importantly, statistical models depend heavily on parameter specification and often deteriorate when long historical records contain abrupt regime shifts. These limitations have motivated the increasing use of machine learning and deep learning approaches (Shrivastava et al., 2023), which are capable of modelling non-linear relationships and learning temporal patterns directly from data without strong assumptions about underlying processes. Artificial intelligent systems have revolutionized human lifestyle in various fields like healthcare, agriculture and commerce (Gosala et al., 2023; Kural et al., 2024; Pathak et al., 2024). Precisely, Artificial Neural Networks (ANN) offer an alternative due to their high accuracy and ability to efficiently learn hidden nonlinear relationships between variables. Neural networks are increasingly becoming popular in the field of forecasting because of their practicality (Chen et al., 2018). Neural Networks have the potential to

learn the hidden complex non-linear relationship efficiently between different variables. They are particularly effective in capturing unexpected temperature fluctuations and identifying trends, even when older data proves more insightful than the recent data (Zaytar et al., 2016). In recent decades, advancement in deep learning and neural network techniques have significantly enhanced weather forecasting capabilities (Zhang et al., 2025). These methodologies are widely applied in time-series analysis and enable the prediction of spatial and temporal information (Utku and Kaya, 2022). For example, the Random Forest (RF) classification algorithm has been utilized to predict weather conditions that proved to be a low cost and portable solution (Singh et al., 2019). Additionally, Support Vector Machine (SVM) and Multi-Layer Perceptron (MLP) methods have been employed for atmospheric temperature prediction, with SVM demonstrating superior performance in forecasting daily maximum temperatures, as compared to MLP (Radhika and Shashi, 2009). Further, RF regression technique has been evaluated against Ridge Regression, SVM, MLP regression, and Extra-Tree Regression (ETR); concluding that these ML models outperformed traditional models by predicting weather features accurately enough (Jakaria et al., 2020). Data-driven approaches such as the Adaptive Network-Based Fuzzy Inference System with Fuzzy C-Means (ANFIS-FCM), grid partitioning (ANFIS-GP), and Long Short-Term Memory (LSTM) neural networks have also been applied to forecast one-day-ahead sea surface temperatures, demonstrating high accuracy and reliability (Özbek and Orcid, 2022). The objectives of the present study is to develop short-term maximum temperature forecasts during the pre-monsoon period, compare the performance of four ML/DL models, and to identify the most suitable model for operational short-term forecasting over Varanasi (Figure 1).

DATA AND METHODOLOGY

In this study, the collected data underwent pre-processing and general analysis before being organized into a relevant format. Subsequently, the model design was developed, and the input data was supplied to train the model. Following this, hyper-parameter tuning was performed to optimize the models, which were then evaluated against the test dataset to compute performance metrics. The overall workflow chart is presented in Figure 2.

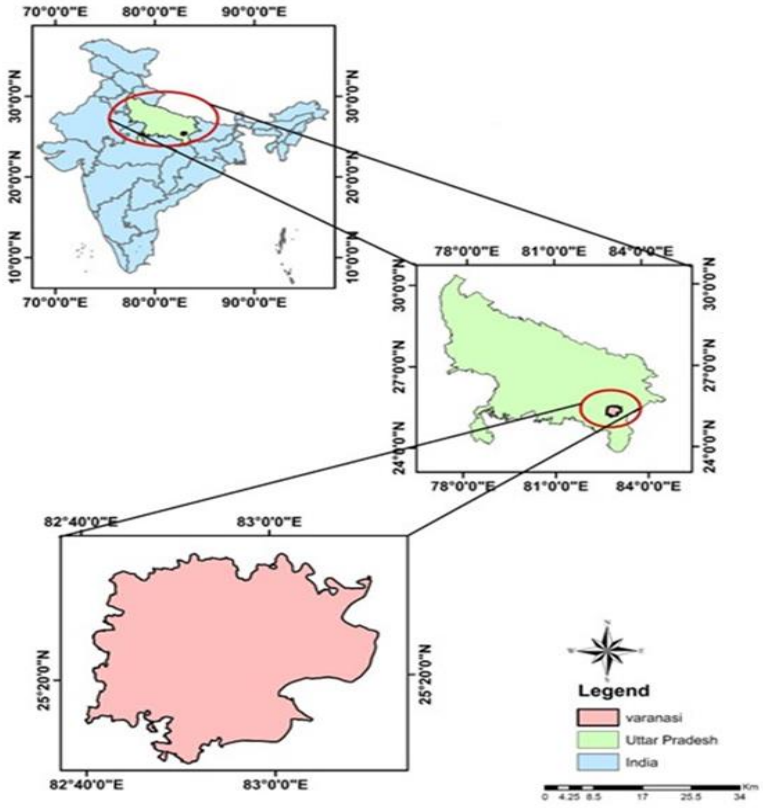

Figure 1. Location of Varanasi City in Uttar Pradesh

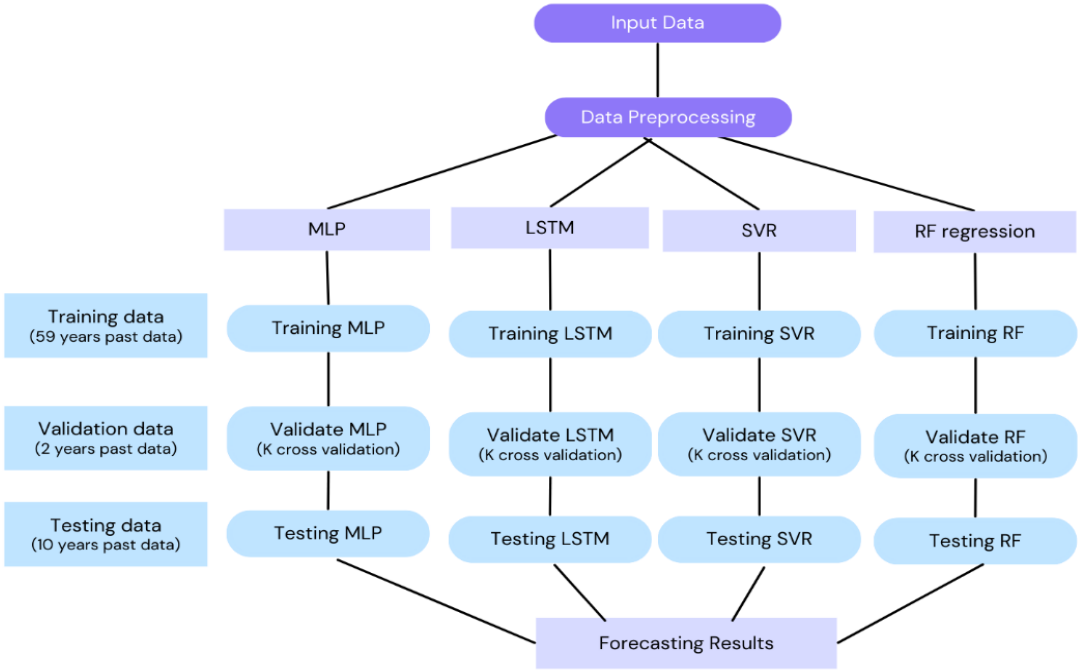

Figure 2. Workflow diagram for pre-monsoon temperature prediction, describing different models used in this study.

For the present study, 71 years (1951-2021) data of historical daily maximum (MaxT) temperature for the Varanasi city was obtained from India Meteorological Department (IMD), Pune (IMD: https://mausam.imd.gov.in/). The selected data columns include month, latitude, longitude and daily maximum temperature 1° resolution with analysis focused on the pre-monsoon season (March-May). This season is particularly important due to high temperatures and frequent heat-stress events in Varanasi, making short-lead forecasts during this period especially valuable for public health, urban planning, and agricultural decisions. While the methodology could be applied to other seasons, focusing on pre-monsoon allows for a targeted evaluation of model performance under extreme temperature conditions. The data is structured into input-target pairs, where five consecutive days temperatures formed the input (X = $[T_1, T_2, T_3, T_4, T_5]$) and the temperature of the sixth day set as the target (y = T_6) . The dataset was divided into 59 years, 2 years, 10 years for training set, validation set and testing set respectively. Any missing or erroneous temperature entries (<0.5% of total data) were identified and replaced using linear interpolation based on adjacent days to maintain temporal continuity. To improve model convergence, all temperature values were normalized using min-max scaling to the [0,1] range. After forecasting, predictions were rescaled back to the original temperature units for interpretation and evaluation.

The process of using a model to predict future values of a time series based on historical data is called time series forecasting. In the present study, a univariate time series approach is adopted, focusing solely on temperature values to simplify the modeling process and reduce the potential for overfitting associated with high-dimensional input data. While this does not guarantee avoidance of overfitting, it allows the models to focus on the primary variable of interest and improves interpretability. In time series analysis, the known past data serves as the input for the model, while the value of the same variable at the next time step is used as the output. This approach focuses on univariate modelling, capturing the underlying periodic patterns within the data. A key benefit of univariate modelling is that it relies solely on historical data points and their behaviour to forecast future values, without requiring additional information or observations.

We selected four representative models, MLP, LSTM, SVR, and RF for this study. These models provide a balance between simplicity, interpretability, and capability to handle univariate time series. MLP and SVR serve as classical ML baselines, RF captures non-linear relationships through an ensemble of decision trees, and LSTM captures temporal dependencies in sequential data. While CNN-based, hybrid, and more complex ensemble models are increasingly common in climate forecasting, they are better suited for multivariate or spatially distributed datasets. Since our study

focuses on univariate, short-lead prediction for an urban location, the chosen models offer sufficient complexity to capture relevant patterns while ensuring computational efficiency and reproducibility. Future work can explore hybrid or ensemble approaches when multiple predictors or high-resolution spatial data are available. Hyperparameters tuning of LSTM models to get best forecasting results we used k-fold cross validation with a value of k as 10 in our process. Some tuning results decided by comparing learning curves include sequence length of data series and batch size, and the optimizer. The learning curve of the above hyperparameter is shown in Table 1.

In Figure 3, we show the different learning curves for different temperature input series length. We can see the performance was similar after the model converged. And to train our model we choose input series length 5 because it shows least training and validation loss. Then, the difference caused by different optimizers, where Adam optimizer performed better compared to RMSprop. The learning rate initially is 0.01 and for regularization dropout method is used while setting dropout value 0.2.

Building on this understanding, the study incorporates four different models SVR (Support Vector Regression) (Aghelpour et al 2019); RF (Random Forest) given by Leo Breiman (2001); MLP (Multi-Layer Perceptron) (Mishra and Gupta, 2017) and LSTM (Long Short-Term Memory) introduced by Hochreiter and Schmidhuber (1997) on MaxT (Maximum Temperature) dataset of Varanasi to predict maximum temperature, using time-series data univariate modeling. While machine learning and deep learning approaches have been increasingly adopted for meteorological applications, most studies focus either on national-scale climate variability or on multivariate forecasting frameworks.

Table 1. Parameters of hyperparameter tuning of LSTM model

Hyperparameters	Values
Dropout values in LSTM	0.2
Learning rate in LSTM	0.01
Optimizer	Adam
LSTM neurons	64
Data series length	5

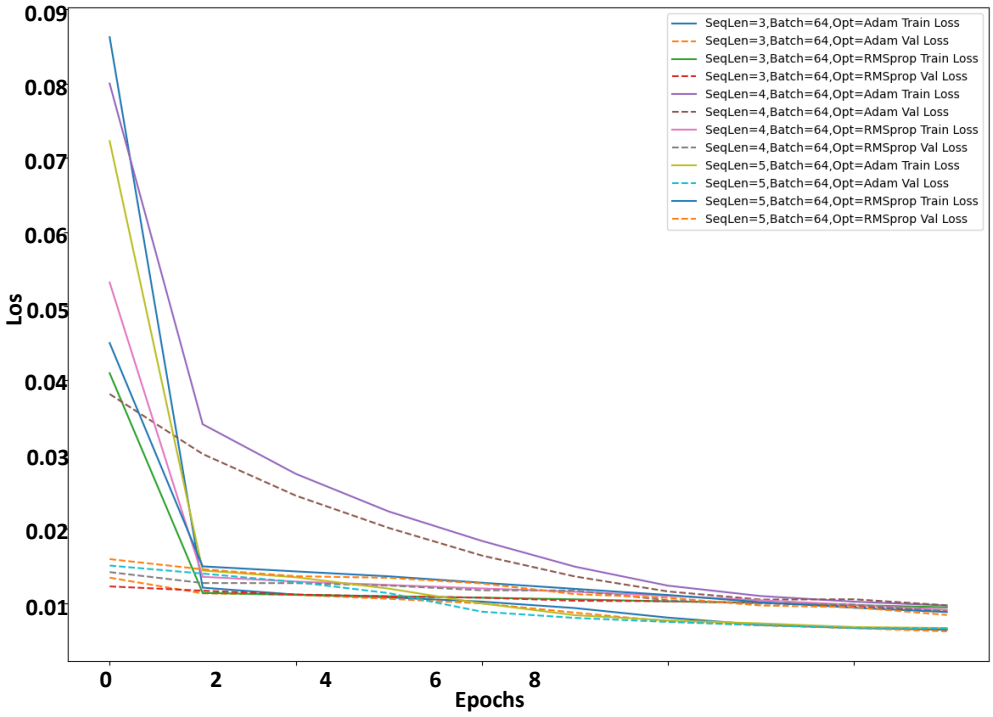

Figure 3 - Learning curves for different hyperparameters.

Performance matrix

In these experiments, the prediction results comparison criteria are mean average error (MAE), root mean square error (RMSE), coefficient of determination (R^2) and correlation coefficient. Models are evaluated by calculating the following equation of MAE, RMSE, R^2 and correlation coefficient:

$$MAE = \frac{1}{m}\sum_{i=1}^{m}\left|Y_{forecasting} - X_{actual}\right|$$

$$RMSE = \sqrt{\frac{1}{m}\sum_{i=1}^{m}(Y_{actual} - Y_{forecasting})^2}$$

$$R^2 = 1 - \frac{\sum_{i=1}^{m}(Y_{actual} - Y_{forecasting})^2}{\sum_{i=1}^{m}(Y_{actual} - Y_{mean})^2}$$

Where, m is the number of test examples in the test set. Y_{actual} and $Y_{forecasting}$ are actual temperature and predicted temperature, respectively.

RESULTS AND DISCUSSION

The SVR, RF model, LSTM, and MLP were used for training and prediction. The dataset selection of the best hyperparameters retrained in all the models. The models used daily air temperature measurements of the previous five days to forecast 1-day-ahead temperature. The prediction vs. actual plots for each model Figures 4 to 7**,** show the model outputs over March, April, and May, as well as the combined pre-monsoon period. The fitting results plots provide a visual comparison of the model's ability to forecast daily maximum temperatures by displaying how closely each model's predictions follows with the observed values. The MLP model's predictions in Figure 4 show a bias to either overestimate or underestimate during sudden shifts in temperatures, indicating sensitivity to seasonal fluctuations. The plots of MLP models capture trends in March adequately, comparatively April and May predictions became less consistent. The prediction vs actual plot for SVR (Figure 5) predicted values following the trend of actual values perfectly. SVR performs well with relatively smooth patterns by utilising the kernel transformation approach. Still SVR struggles to wholly capture temperature spikes or dips, which are more common in April and May. Overall SVR demonstrated high accuracy in steady temperature patterns, but underperformed during periods with swift temperature changes. The Random Forest model's step-like pattern prediction is visible in the prediction vs actual plots **(**Figure 6). RF comprehends general trends but deteriorates with continuous, smooth changes, leading to sudden prediction shifts. LSTM prediction vs actual plots (Figure 7) effectively track the temperature patterns in March, April, and May, showing minimum lag values to respond to changes. But the LSTM predictions are a little slow in responding to extreme values of temperatures.

RF model exhibits step-like patterns in its forecasts because it treats the lagged input temperatures as independent static features and does not explicitly model temporal dependencies. Each prediction is effectively a regression based on a fixed combination of past days' temperatures, which can lead to abrupt shifts between predicted values rather than smooth transitions. In contrast, MLP tends to over- or underestimate sudden temperature changes because, while it can learn non-linear relationships, it lacks inherent memory of sequential dynamics. As a result, MLP captures the general trend, but responds less accurately to rapid fluctuations, particularly during periods of high variability in April and May.

The analysis of individual pre-monsoon months was conducted to evaluate model performance during March, April and May. Our results showed how the models' performance varies throughout these months, also reflecting the temperature's underlying fluctuation during these periods of time. Likely due to the relatively stable temperature patterns in the month of March, all models performed proficiently throughout these months. And as temperatures fluctuated more in April and May, the challenges in forecasting during these months emphasized for all models. Lastly, the pre-monsoon heat peak had been transited in the month of April by all models.

SVR and LSTM models display residuals that are tightly centred around zero, reflecting that they have balanced predictions and minimal bias as shown in Figure 8 (a, b). The residual plots of SVR and LSTM showing the minimal deviation, that implies models grasped the temperature fluctuation without overfitting. Residual distribution of MLP and RF model in Figure 8 (c, d) display larger deviations from zero. Table 2 presents the MaxT temperature performance metrics for each model. SVR achieved the highest R^2 score (0.801), compared to the variance of other models, SVR is most accurate. The correlation coefficient (0.897) is also highest for SVR, this indicates that the model captured trends effectively. LSTM achieved the lowest RMSE (1.673) and MAE (1.213), indicating minimum average prediction errors.

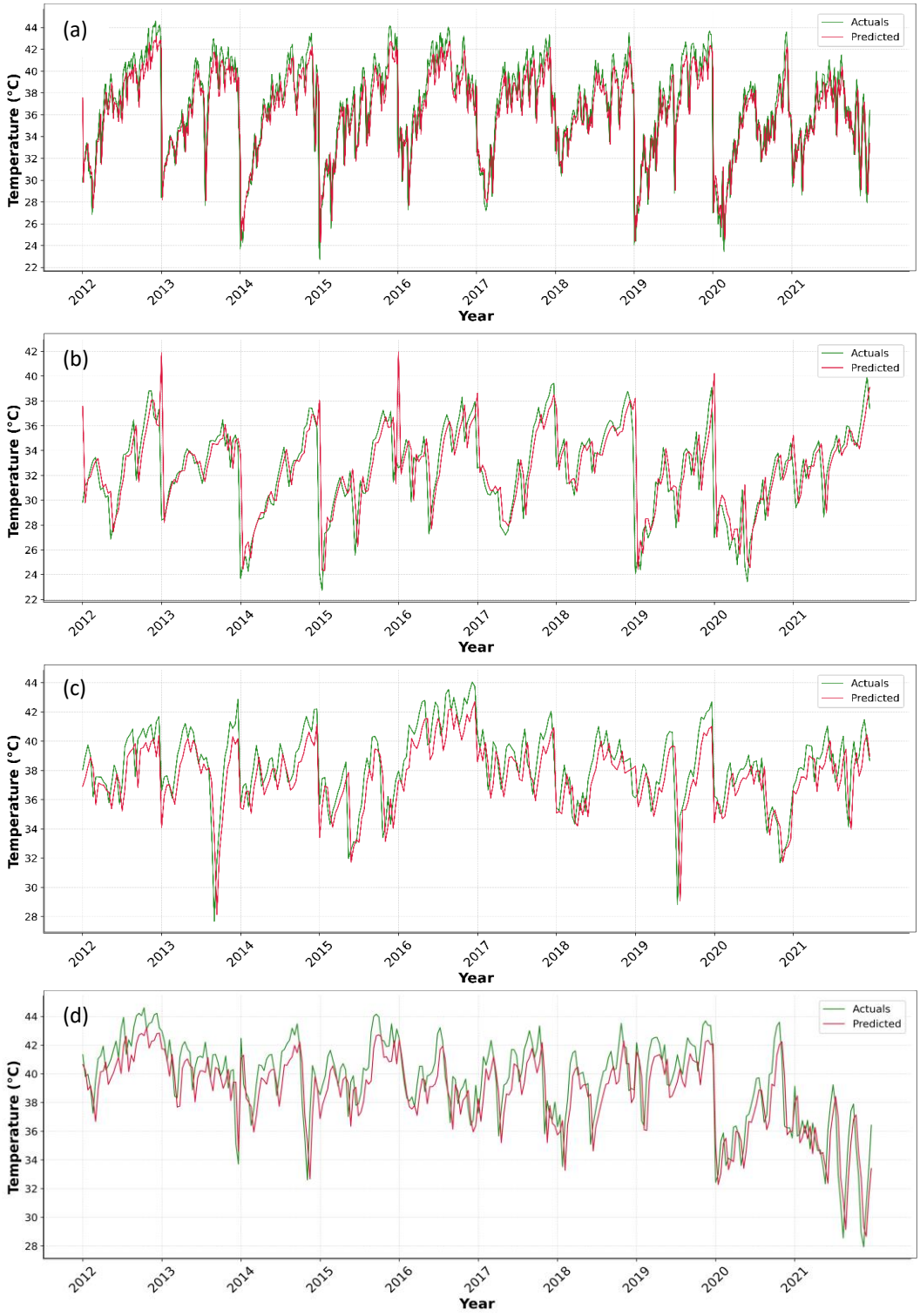

Figure 4. MLP Prediction vs. Actual of MaxT for **(a)** Pre- Monsoon, **(b**) March, **(c)** April, and **(d)** May.

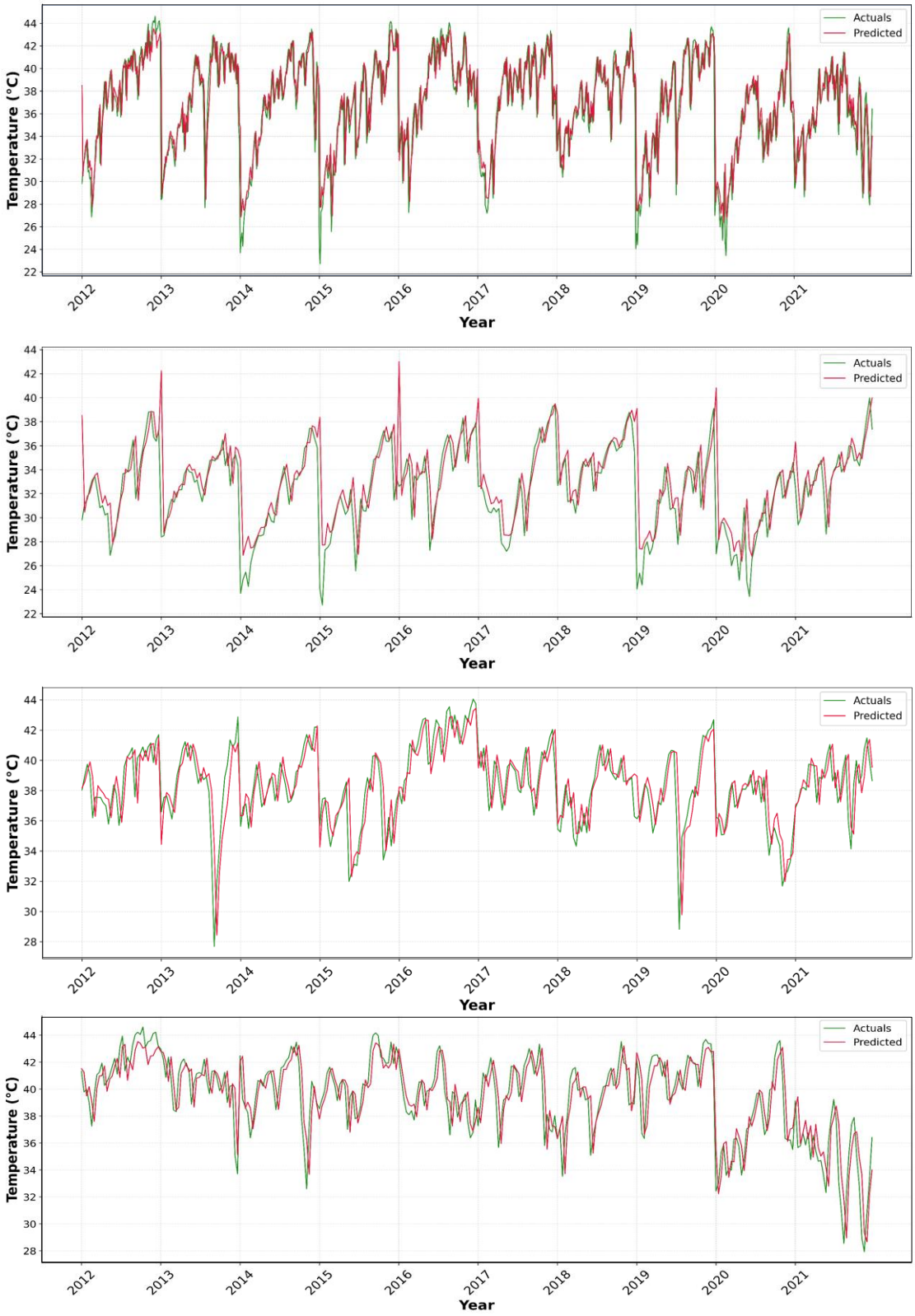

Figure 5. SVR Prediction vs. Actual MaxT for **(a)** Pre- Monsoon, **(b)** March, **(c)** April, and **(d)** May.

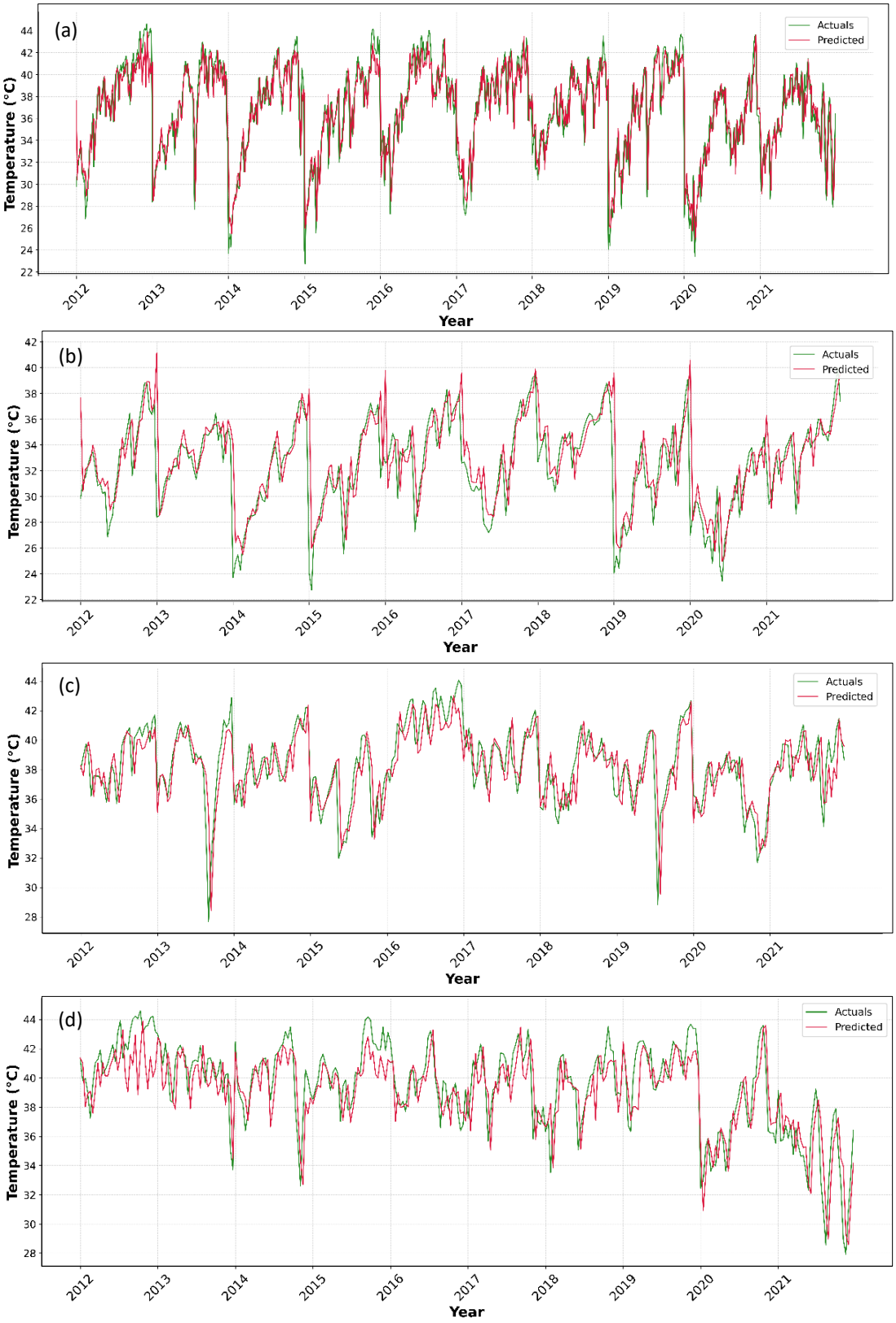

Figure 6. RF Prediction vs. Actual MaxT for **(a)** Pre- Monsoon, **(b)** March, **(c)** April, and **(d)** May.

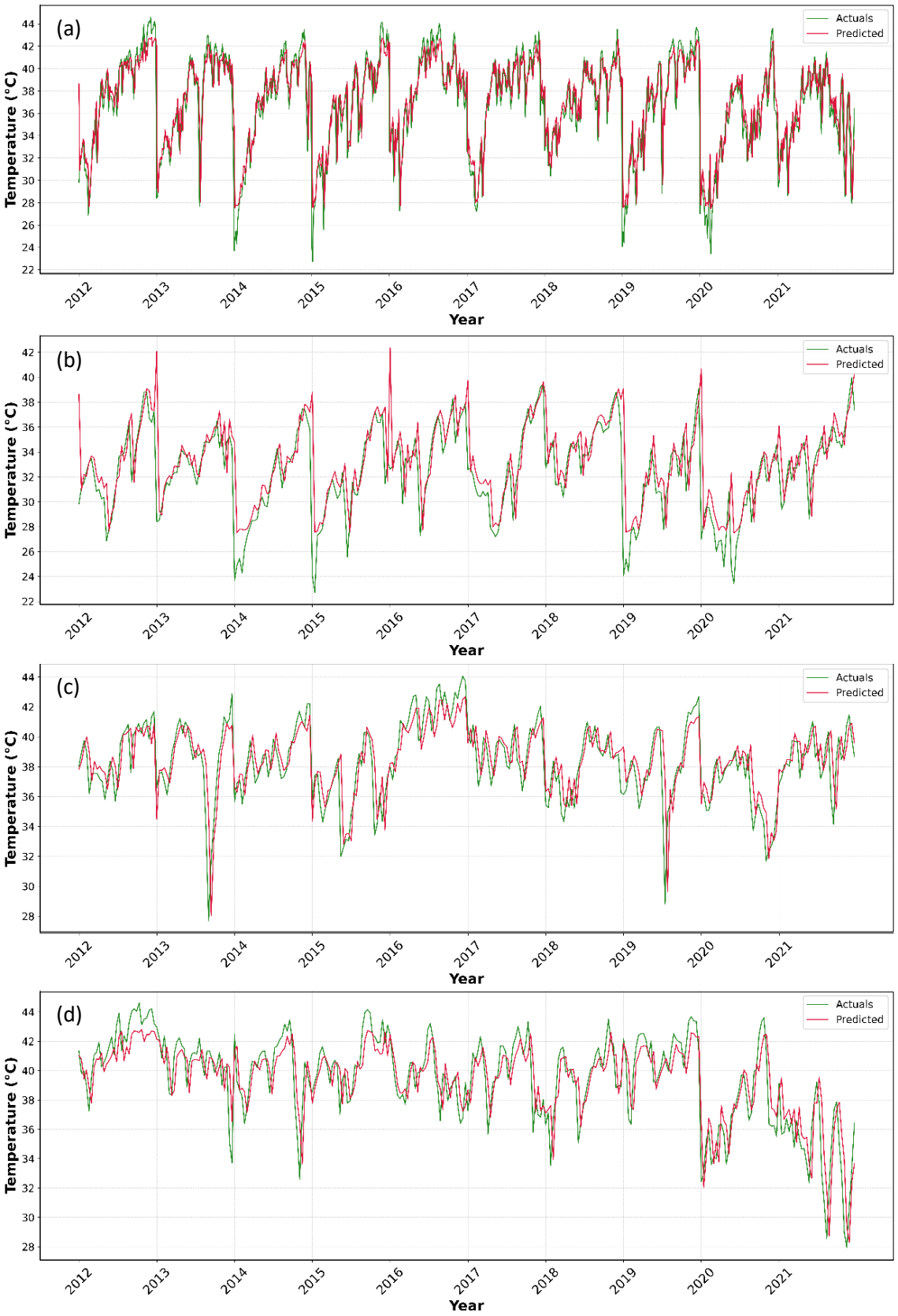

Figure. 7. LSTM Prediction vs. Actual MaxT for **(a)** Pre- Monsoon, **(b)** March, **(c)** April, and **(d)** May.

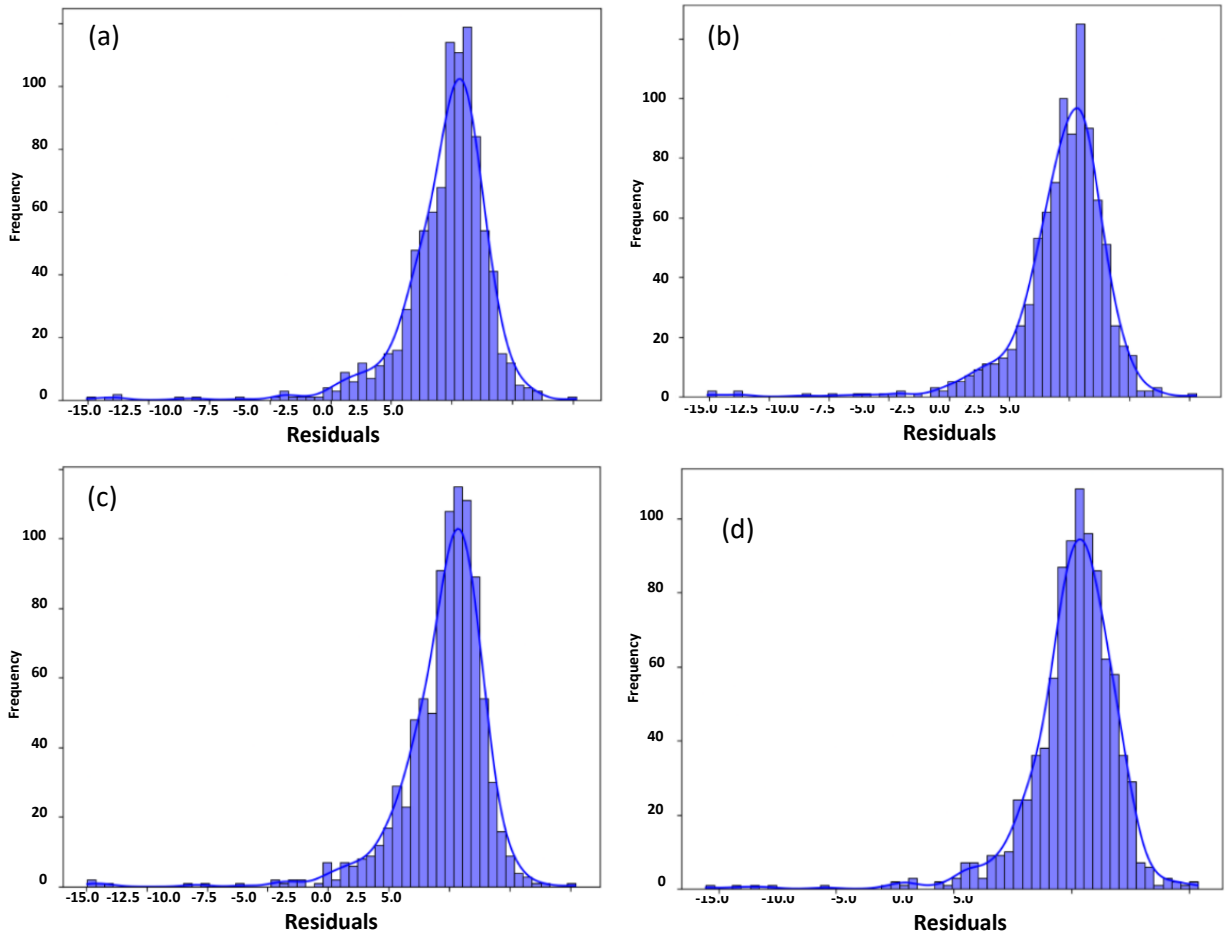

Figure 8. Residual distribution of different predicted models, **(a)** Residual distribution of SVR model for predicted values**, (b)** Residual distribution of predicted values for LSTM model, **(c)** Residual distribution of MLP model and **(d)** Residual distribution of RF model

Table 2: Performance metrics for each model for MaxT

MODEL	R^2	RMSE	MAE	Correlation
MLP	0.716	1.843	1.466	0.894
SVR	0.801	1.927	1.230	0.897
RF	0.794	1.959	1.323	0.891
LSTM	0.766	1.673	1.213	0.885

Although LSTM is specifically designed to capture temporal dependencies in sequential data, SVR outperforms LSTM in terms of R^2. This is primarily due to the short input sequence of only five lag days, which limits the extent to which LSTM can exploit its capacity for learning longer-term temporal patterns. In contrast, SVR efficiently maps these short-term inputs to the next-day target using its kernel transformation. Additionally, the pre-monsoon period exhibits relatively stable and predictable temperature patterns, especially in March, which favours SVR's smoother, trend-focused predictions. While LSTM achieves lower average errors (RMSE and MAE) by closely tracking day-to-day fluctuations, its sensitivity to small variations slightly reduces the overall variance explained, resulting in a lower R^2. This highlights that R^2 is influenced by the model's ability to capture the overall trend rather than pointwise errors, explaining why SVR can show higher R^2 despite the sequence-oriented design of LSTM. Although SVR achieves a higher R^2 by closely capturing the overall trend in temperature, LSTM demonstrates lower RMSE and MAE because it is more sensitive to day-to-day fluctuations and short-term variations.

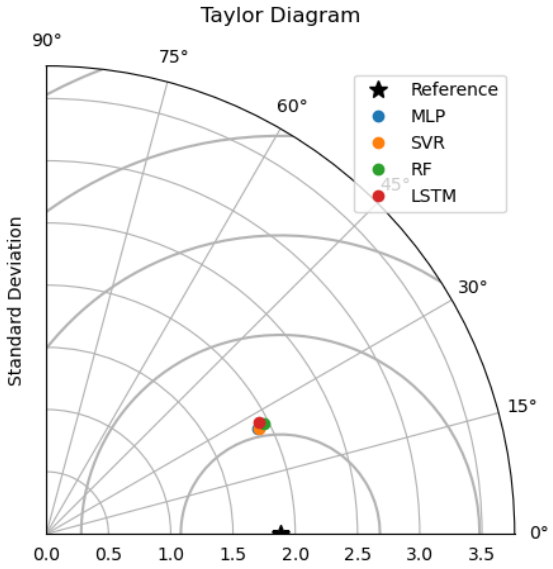

Figure 9. Taylor diagram, the four models are compared to the observed data in terms of standard deviation, correlation coefficient, and cantered root mean square error.

LSTM's recurrent architecture allows it to adapt to sudden changes in temperature, reducing pointwise prediction errors even if the overall trend is slightly under- or over-estimated. R^2 reflects how well a model captures the overall variance and trend in the data, whereas RMSE and MAE quantify the average magnitude of prediction errors. In practical terms, LSTM may be more suitable when minimizing daily forecast errors is critical, while SVR may better capture the general seasonal pattern.

A Taylor diagram is a graphical tool that summarizes how well a pattern (e.g., predicted data) matches observations in terms of three statistical metrics: the correlation coefficient, the RMSE, and the standard deviation. This is particularly useful when comparing the performance of multiple models. In the diagram, each model is plotted as a point whose distance from the origin reflects its standard deviation relative to observations, its angular position represents correlation strength, and its distance from the reference point (observed data) corresponds to RMSE. Models located closer to the observational reference point are considered more accurate.

This visualization allows simultaneous assessment of how well each model reproduces both the variability and the pattern of the observed temperature series. The diagram indicates that all models (MLP, SVR, RF and LSTM) are closely clustered with similar standard deviations and correlations values. Figure 9 visually concludes that SVR and LSTM have superior quantitative metrics (standard deviations, correlations and RMSE) compared to MLP and RF.

When considering overall performance, each model exhibits a distinct trade-off between trend fidelity and short-term accuracy. SVR achieves the highest R^2 (0.801) and correlation (0.897), indicating it best captures the overall temperature trend, especially during stable periods in March. LSTM. However, achieves the lowest RMSE (1.673) and MAE (1.213), reflecting its superior ability to track daily fluctuations and respond to short-term changes. RF shows step-like forecasts that capture general trends but fail to represent smooth transitions, while MLP can approximate non-linear relationships but tends to over- or underestimate sudden shifts.

Based on these metrics, if the objective is to accurately follow the general pre-monsoon trend, SVR is preferable, whereas for minimizing daily forecast errors, LSTM is the better choice. RF and MLP serve as intermediate baselines, useful for capturing broad trends but less reliable for extreme or rapidly changing conditions. This ranking highlights the practical trade-off between trend fidelity and responsiveness to short-term variability in temperature prediction.

CONCLUSIONS

In this study, the application of machine learning and deep learning techniques for forecasting daily maximum temperatures during the pre-monsoon season in Varanasi, India has been explored. By applying a univariate time series approach, the work demonstrates the abilities of these methods to predict temperatures. The dataset, comprising 71 years (1951–2021) of historical temperature data of Varanasi with complex climatic patterns, was pre-processed,

structured into input-target pairs, and directly comparing classical ML models (SVR, RF, MLP) and a sequence-oriented DL model (LSTM). A key novelty of this work lies in its focus on localized, urban-scale short-lead forecasting with minimal input requirements, a scenario less explored in previous studies that predominantly consider regional or multivariate datasets. The findings proves that SVR achieved the highest R^2 score (0.801) and correlation coefficient (0.897), capturing linear relationships and variance in the data. Its kernel-based technology was able to capture long-term steady temperature changes but was poor at sudden temperatures' spikes or dips. Conversely, LSTM had the least RMSE (1.673) as well as MAE (1.213) implying it was the best in terms of accuracy when predicting the outcome. LSTM's ability to learn temporal dependencies and complex patterns proved advantageous, especially in capturing fluctuations and transitions during the pre-monsoon season. RF regression displayed a step-like prediction pattern, accurately capturing general trends but struggling with continuous and smooth temperature changes, particularly during periods of high variability. MLP exhibited sensitivity to seasonal fluctuations, performing well during stable conditions but showing inconsistencies in predicting sudden temperature variations.

A key outcome is that while SVR provides the highest explained variance (R^2) and strongest linear correlation with observations, LSTM delivers the lowest RMSE and MAE. These findings underscore the importance of tailoring model selection to specific forecasting needs and data characteristics. The study also highlights the advantages of using univariate modeling for temperature forecasting. This simplicity is particularly beneficial for localized studies where resources and additional data may be limited. Moreover, timely forecasts can support mitigation strategies against heatwaves and other temperature-related extreme events, reducing their impact on vulnerable populations. Future work could explore hybrid models that combine the strengths of multiple approaches, incorporate additional climatic variables (such as humidity, wind, and solar radiation), and evaluate the models' performance under different seasonal and climatic conditions, potentially improving prediction accuracy and operational applicability across seasons and climatic conditions.

Acknowledgement

This work is part of a transdisciplinary project by IoE (6031), Banaras Hindu University. The authors wish to thank the India Meteorological Department (IMD) for providing the necessary data.

Author Credit Statement

All authors contributed to the study conception and design. R Bhatla and Manjari Gupta supervised the research, provided conceptual guidance, and critically reviewed the manuscript. All authors read and approved the final manuscript. Aashna Verma and Mohini Dangi were responsible for data collection, analysis, model implementation, and preparation of the first draft of the manuscript.

Data availability

The temperature datasets used in this study are freely available from the IMD website (IMD: https://mausam.imd.gov.in/).

Compliance with Ethical Standards The authors declare no competing interests and adhere to copyright norms.

References

Aghelpour, P., Mohammadi, B. and Biazar, S. M., 2019. Long-term monthly average temperature forecasting in some climate types of Iran, using the models SARIMA, SVR, and SVR-FA: P. Theoretical and Appl. Climatology, 138(3), 1471-1480.

Bathiany, S., Dakos, V., Scheffer, M. and Lenton, T. M., 2018. Climate models predict increasing temperature variability in poor countries. Science Advances, 4(5). https://doi.org/10.1126/SCIADV.AAR5809/SUPPL_FILE/AAR5809_SM.PDF

Bhatla R., Tabassum Swaleha and Tripathi, A., 2016a. Trend analysis and extreme events of temperature during post monsoon and winter season over Varanasi. J. Indian Geophys. Union**,** 20(1), 123-127.

Bhatla, R., Tripathi, A. and Singh, R.S., 2016b. Study of trend analysis and extreme events of temperature over Varanasi during summer monsoon season. Mausam, 67(2), 463-474.

Bhatla R., Verma, A., Vishwakarma, A. and Mall, R.K., 2025. India's Drought Challenge: Insights from CMIP6 Models on Historical and Future Climate Scenarios. Int. J. Climatology, 1-22**.** https://doi.org/10.1002/joc.70075

Chen, Y., Cheng, Q., Cheng, Y., Yang, H. and Yu, H., 2018. Applications of recurrent neural networks in environmental factor forecasting: A review. Neural Computation, 30(11), 2855–2881. https://doi.org/10.1162/NECO_A_01134

Goala, B., Dindayal Kapgate, P., Jain, P., Nath Chaurasia, R. and Gupta, M., 2023. Wavelet transforms for feature engineering in EEG data processing: An application on Schizophrenia. Bio mortality: a review and exploration of heterogeneity. J. Epid. & Comm. Health, 64(9), 753–760.

Grimmond, S. U. E., 2007. Urbanization and global environmental change: local effects of urban warming. The Geogr. J., 173(1), 83-88.

Gupta, P., Verma, S., Bhatla, R., Payra Swagata and Yadava, P. K., 2019. Long term (1984-2013) winter temperature variability and cold wave analysis over Varanasi City. J. Indian Geophys. Union, 23(4), 343-351.

Hochreiter, S. and Schmidhuber, J., 1997. Long Short-Term Memory. Neural Computation, *9*(8), 1735–1780. https://doi.org/10.1162/NECO.1997.9.8.1735

Jakaria, A. H. M., Hossain, M. M. and Rahman, M. A., 2020. Smart Weather Forecasting Using Machine Learning: A Case Study in Tennessee. https://doi.org/10.1145/nnnnnnn.nnnnnnn

Kumar, R., Singh Parmar, Y. and Raj Gautam, H., 2014. Climate Change and its Impact on Agricultural Productivity in India. J. Clim. Wea. Fore. https://doi.org/10.4172/2332-2594.1000109

Kumar, A., Kumar, S., Kumar, N., Lohan Nitin and Bhatla R., 2024. Comparison of characteristics associated with super cyclonic storm 'Amphan' using numerical model WRF-ARW analysis and ERA5 reanalysis. J. Indian Geophys. Union, 28 (2), 99-107.

Kural, S., Pathak, A. K., Singh, S., Jain, G., Yadav, M., Agarwal, S., Kumar, I., Gupta, M., Singh, Y., Kumar, U., Trivedi, S., Sankhwar, S. N., Das, P. and Kumar, L., 2024. Prospective Assessment of VI-RADS with Muscle Invasion in Urinary Bladder Cancer and Its Implication on Re-Resection/Restaging TURBT Patients. Ann. Surg. Onco., 32(1), 609–618. https://doi.org/10.1245/S10434-024-16424-0/FIGURES/4

Leo Breiman, 2001. Machine Learning. Kluwer Academic Publishers. The Netherlands, 45, 5–32

Maurya, A., Verma, S., Pant, M. and Bhatla, R., 2023. Epochal changes in the intrinsic nature/dynamics of flood and drought during Indian summer monsoon, Earth and Space Sci.**.,** 10, e2022EA002674, 1-21.

Mishra, C. and Gupta, D. L., 2017. Deep machine learning and neural networks: An overview. IAES Int. Jl. Art. Intel., 6(2), DOI: http://doi.org/10.11591/ijai.v6.i2.pp66-73

Nikam, V. B. and Meshram, B. B., 2013. Modeling rainfall prediction using data mining method: A bayesian approach. Proc. Inter. Conf. Comp. Intelligence, Modelling and Simulation, 132–136. https://doi.org/10.1109/CIMSIM.2013.29

Özbek, A. and Orcid, 2022. Daily Sea Water Temperature Forecasting Using Machine Learning Approaches.

Pathak, A. K., Kural, S., Singh, S., Kumar, L., Yadav, M., Gupta, M., Das, P. and Jain, G., 2024. Development of a robust and generalizable algorithm. Scientific Reports, 14(1), 1–11. https://doi.org/10.1038/s41598-024-66770-y

Radhika, Y. and Shashi, M., 2009. Atmospheric Temperature Prediction using Support Vector Machines. Int. Jl. Comp. Th. Eng., 55–58. https://doi.org/10.7763/IJCTE.2009.V1.9

Shrivastava, V. K., Shrivastava, A., Sharma, N., Mohanty, S. N. and Pattanaik, C. R., 2023. Deep learning model for temperature prediction: an empirical study. Model. Earth Sys. Env., 9(2), 2067-2080.

Singh, N., Chaturvedi, S. and Akhter, S., 2019. Weather Forecasting Using Machine Learning Algorithm. 2019 Int. Conf. Sig. Proc. Comm., ICSC 2019, 171–174. https://doi.org/10.1109/ICSC45622.2019.8938211

Utku, A. and Kaya, S. K., 2022. Multi-layer perceptron based transfer passenger flow prediction in Istanbul transportation system. Deci. Mak.: Appl. Manag. Eng., 5(1), 208–224. https://doi.org/10.31181/DMAME0315052022U

Verma, S., Bhatla, R., Shahi, N.K. and Mall, R.K., 2022. Regional Modulating behaviour of Indian summer monsoon rainfall in context of spatio-temporal variation of drought and flood events. Atm. Res., 264, 1-19.https://doi.org/10.1016/j.atmosres.2022.106201

Verma, A., Vishwakarma, A., Bist, S., Kumar, S. and Bhatla, R., 2023. A long-term drought assessment over India using CMIP6 framework: present and future perspectives. Mausam, 74(4), 963-972.

Zaytar, M., et al., 2016. Sequence to sequence weather forecasting with long short-term memory recurrent neural networks. Researchgate. NetMA Zaytar, C El Amrani Int. J. Computer Applications, 143(11), 975–8887. https://doi.org/10.5120/ijca2016910497

Zhang, H., Liu, Y., Zhang, C. and Li, N., 2025. Machine learning methods for weather forecasting: A survey. Atmosphere, 16(1), 82.

Received on: 18-07-2025; Revised on: 25-03-2026; Accepted on: 22-05-2026

J. Ind. Geophys. Union, 30(4) (2026), 276-289
https://doi.org/10.71122/JIGU.30(4)2026.0027

Magnetic investigation of structural controls on groundwater contamination and flow pathways along the Musi River, Ranga Reddy and Nalgonda districts, Telangana (India)

Udaya Laxmi G[1], Blessy Ganduri[1], Linga Swamy Jogu*[1] and Naveen Kumar Gardas[2]
[1]Department of Geophysics, Osmania University, Hyderabad-500 007, India.
[2]Department of Applied Geochemistry, Osmania University, Hyderabad-500 007, India.
*Corresponding author: lingaswamyjogugp@gmail.com

ABSTRACT

Magnetic investigations were conducted along the Musi River corridor between Peerzadhiguda and Valigonda areas, encompassing portion of the Ranga Reddy and Nalgonda districts in the state of Telangana, India, to delineate subsurface structural controls governing groundwater flow and contaminant migration. A total of 1,260 magnetic measurements were acquired along twelve traverses at 100 m station intervals and processed using magnetic anomaly mapping, Reduction to the Pole (RTP), and Analytical Signal (AS) techniques. The magnetic anomaly analysis identified seven prominent magnetic highs and four magnetic lows, indicating structurally controlled subsurface heterogeneity. Radial Average Power Spectrum (RAPS) analysis revealed three characteristic depth interfaces at approximately ~0.1 km, ~0.5 km, and ~1.6 km corresponding to weathered, semi-weathered and fractured granitic-gneissic basement. Two-dimensional magnetic modelling further constrained shallow structural bodies with depths ranging from ~0.12 – 0.22 km and lateral extents up to ~2 km, indicating broader and more complex fractured zones in the downstream sector. An integrated structural map revealed dominant NE–SW, NW–SE, and N–S lineament trends, with comparatively greater structural complexity in the downstream sector. The spatial correspondence between magnetic gradients, mapped geological structures, and modelled bodies indicates that faults, dykes, and fracture networks, act as preferential pathways of controlling groundwater flow and facilitating contaminant migration along the Musi River corridor.

Keywords: Magnetic anomaly; Reduction to the Pole; Radial Average Power Spectrum (RAPS); Analytical signal; Structural lineaments; Groundwater contamination; Musi River Basin (Telangana).

INTRODUCTION

The Musi River, flowing through the heart of the Hyderabad city in Telangana state, India, plays a critical role in sustaining urban and peri-urban communities. However, rapid urbanization, industrialization, and unregulated waste disposal have severely affected the river's hydrological and geochemical integrity (Phani and Rajendra Prasad, 2024). Numerous environmentalists, hydrologists, and geoscientists have investigated groundwater quality and pollution patterns within the Musi River basin, highlighting the urgent need for structural and geophysical investigations to understand subsurface contamination mechanisms. Early studies by Barker (1981) provided foundational insights into groundwater potential and resistivity characteristics in the Musi ayacut region. Subsequent investigations by the Andhra Pradesh State Ground Water Department (2002), enhanced our understanding of aquifer dynamics, recharge processes, and hydrogeological behavior. Later, Sekhar et al. (2005) documented the relationship between industrial activity and heavy metal contamination in the Musi River and adjoining aquifers.

In recent years, environmental geophysics has emerged as a vital interdisciplinary approach for delineating pollution pathways, mapping lithological variations, and characterizing structural controls influencing groundwater contamination (Akpa et al., 2023). Geophysical techniques such as magnetic, electrical resistivity, and electromagnetic methods, provide non-invasive means to detect subsurface anomalies associated with fractures, faults, shear zones, and intrusive dykes, which often govern groundwater flow and contaminant migration (Sharp, 2014; Jogu and Gardas, 2025). Magnetic investigations, in particular, offer a high-resolution tool for mapping near-surface structural heterogeneities, enabling correlation between magnetic anomalies and geological features within the hard rock terrains (Pazzi et al., 2016).

The present study undertakes an integrated qualitative and quantitative magnetic investigation of the Musi River segment between Peerzadhiguda and Valigonda areas, encompassing portion of the Ranga Reddy and Nalgonda districts in the state of Telangana, India. By combining magnetic anomaly, reduction to the pole (RTP), analytical signal (AS), radial average power spectrum (RAPS) analysis, and two-dimensional forward modelling, the study aims to delineate subsurface lineaments, fault zones, and depth interfaces that potentially facilitate pollutant transport.

LOCATION OF STUDY AREA

The study area extends between 17°20′ to 17°25′ N and 78°36′ to 79°02′ E, encompassing portions of the Ranga Reddy and Nalgonda districts in the state of Telangana, India. It is located approximately 20 km east of Hyderabad City in an approximate area of about 417 km² (Figure 1).

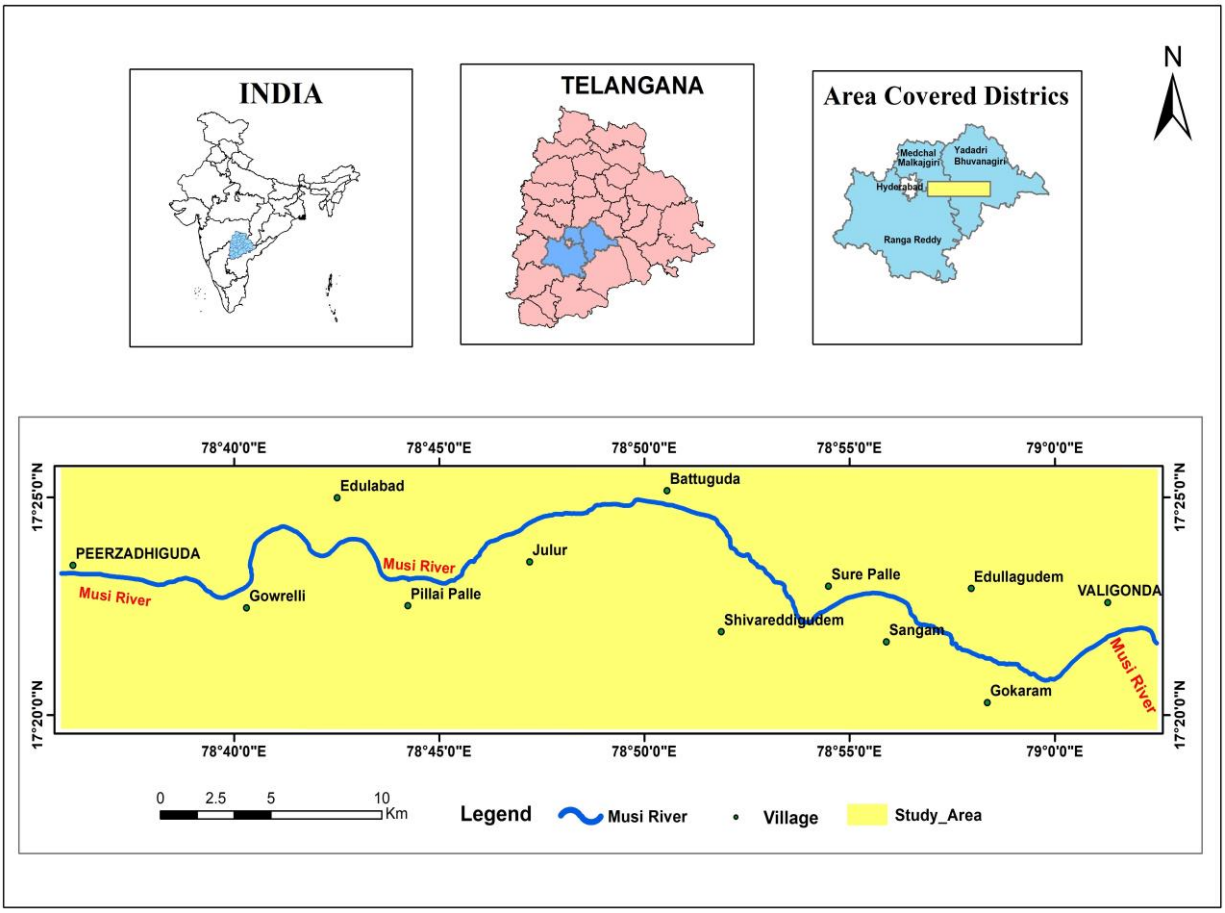

Figure 1. Location and key map of the study area showing studied Musi river course in Telangana state of India

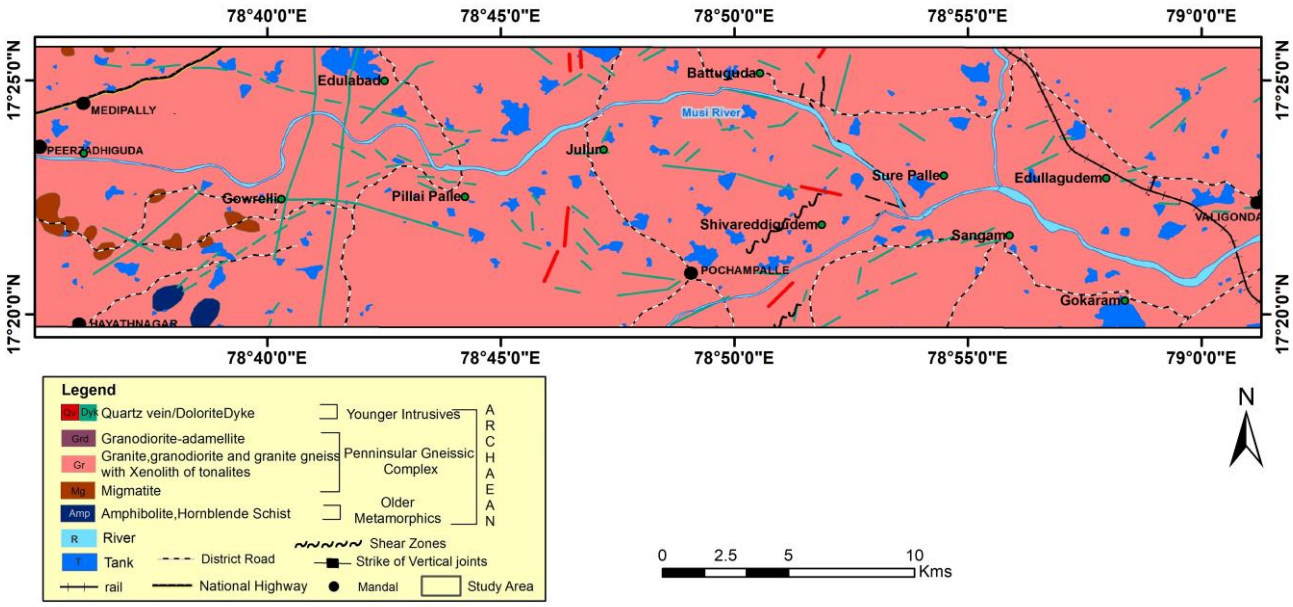

Figure 2. Geology map of the study region (Source: GSI, 2010)

The base data for this investigation were derived from Survey of India (SOI) topographical maps at scales of 1:50,000 and 1:250,000 (Topo Sheet Nos. 56 K, 56 K/11, and 56 K/15). These maps provided essential geospatial reference for field planning, mapping traverses, and correlating magnetic observations with geological features.

REGIONAL GEOLOGY

The study area (**Figure 2**) is predominantly composed of granitic-gneissic terrain, representing a variety of Archaean granitoids belonging to the Peninsular Gneissic Complex (PGC). These granitoids exhibit shades ranging from red to light pink and are interspersed with schistose units of older metamorphic origin. The rock formations are intruded by Proterozoic basic dykes, indicating multiple phases of magmatic activity and tectonic evolution. Based on field relationships and petrochemical characteristics, the granitoids of the region is classified into two major suites: Adamellite granodiorite and granite (Ramakrishnan, 2009). The granites are further subdivided into pink and gray series. The gray granites are typically medium- to fine-grained with low porosity and permeability, whereas the pink granites are medium- to coarse-grained, fractured, and fissured attributes that enhance their permeability and facilitate groundwater movement, including the infiltration of pollutants (Gugulothu et al., 2020; Kuntamalla and Saxena, 2021).

The granitoid suite is characterized by the presence of pegmatitic segregations and abundant aplite and quartz-feldspathic veins, reflecting late-stage magmatic differentiation. Numerous quartz veins traverse the area, which are often associated with minor shearing. The basic intrusives, including amphibolite, dolerite, gabbro, and pyroxenite, occur as dykes that crosscut all granitoid units. These dykes typically range from 7 to 50 meters in width, extending for several kilometers with occasional discontinuities, and are massive, compact, and dominantly doleritic in composition.

The geological configuration of the area, derived from the Geological Survey of India (GSI, 2010) District Resource Quadrangle Map, is illustrated in Figure 2, which depicts the distribution of lithological units and structural features that govern the hydrogeological regime of the Musi River basin.

METHODOLOGY

Magnetic observations were conducted using a Proton precession magnetometer (Model-600) along east–west traverses on both sides of the Musi River, covering its northern (upstream) and southern (downstream) banks. The traverses were designated as T1–T6 and T7–T12, respectively, extending from Peerzadhiguda to Valigonda village. The measurements were recorded at a station interval of 100 meters and a traverse spacing of 500 meters, ensuring a uniform distribution of magnetic readings across the 417 km² study area. A total of 1,260 magnetic observation stations were established (Figure 3). Although the Musi River generally follows an E–W course, the orientation of magnetic traverses was deliberately maintained in the E–W direction to intersect the dominant geological structures, which predominantly trend N–S, NE–SW, and NW–SE, as evidenced from the geological map (Figure 2). Since magnetic surveys are ideally conducted perpendicular to the principal structural trends to enhance anomaly resolution, the chosen traverse orientation, ensured effective delineation of dykes, shear zones, and fault-controlled features within the study area. The geospatial positions of all observation points were determined using a Global Positioning System (GPS) with a horizontal accuracy of ±1 meter. The magnetic readings were corrected for instrumental drift and diurnal variations, yielding an overall data accuracy of ±1 nT. Given the relatively compact extent of the surveyed region, the coordinates for each observation point were corrected for the International Geomagnetic Reference Field (IGRF-11, epoch 2010) using Geosoft, (2010). The geomagnetic field parameters over the area showed a declination from –0.5303° to –0.5157°, an inclination ranging from 23.9496° to 24.1314°, and a total magnetic field intensity between 42,994 nT and 43,455 nT. These corrected datasets were subsequently processed to delineate subsurface geological structures, including faults, shear zones, and intrusive boundaries, and to evaluate lithological variations within the study area (Jaques et al., 1997; Anak Mejus, 2014).

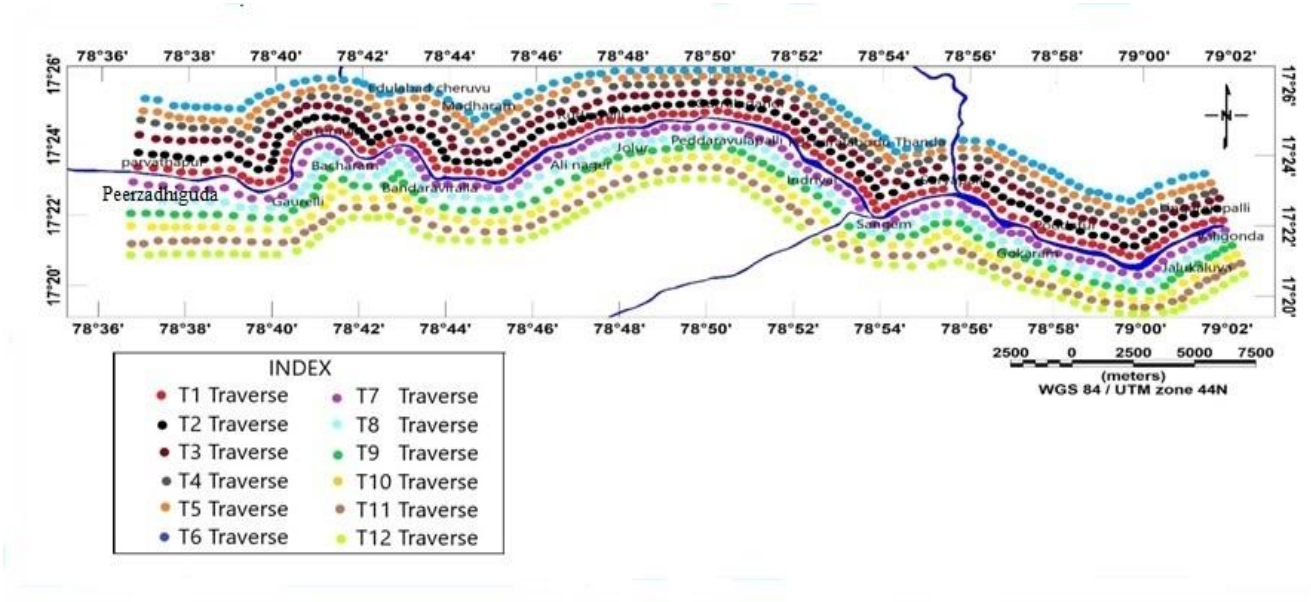

Figure 3. Map showing the layout of the magnetic observations

QUALITATIVE INTERPRETATION

Qualitative interpretation provides insights into the relative variations among different geological formations and their inferred structures (Gunn, 1997; Kamal et al., 2023; Akpa et al., 2023). The primary objective of qualitative magnetic analysis is to identify subsurface structures such as faults, dykes, and lithological boundaries by applying various derivatives and transformations of magnetic data, including filtering, reduction to the pole, and tilt derivative. These datasets were interpreted to delineate the trends of geological structures, including faults, intrusive dykes, and tectonically disturbed zones that significantly influence subsurface fluid movement and pollution pathways along the Musi River corridor.

Magnetic anomaly map

The magnetic anomaly map of the study area (Figure 4), contoured at 10 nT intervals, displays distinct patterns of magnetic highs and lows reflecting the bipolar nature of magnetic sources in low magnetic latitude regions (Ling et al., 2016). In the present study area, variations in the absolute geomagnetic field, inclination, and declination are relatively minor; therefore, the observed anomaly patterns primarily represent subsurface structural heterogeneities. A total of seven magnetic highs (H1–H7) and four magnetic lows (L1–L4) have been delineated to highlight structural variations across the study region. The prominent highs include: H1 northwest of Prathapa Singaram trending NW–SE; H2 southeast of Bacharam trending NNE–SSW; H3 northwest of Edulabad Cheruvu trending NNE–SSW; H4 north of Rudravelli trending NW–SE; H5 north of Gurraladandi trending NE–SW and gradually shifting to NW–SE; H6 northwest of Suryapalli trending NW–SE; and H7 north of Lingarajupalli striking NW–SE. These high-amplitude zones are predominantly concentrated in the northern, western, and central parts of the study area.

The identified magnetic lows include L1 northeast of Muthyalaguda trending NNW–SSE; L2 northeast to north–south of Bacharam trending NNE–SSW; L3 northwest of Banda Ravilara; and L4 southeast to northwest of Valigonda, abruptly changing to NNW–SSE. Several of these highs and lows occur as paired anomalies, representing different components of the same causative body due to the bipolar response of magnetic sources under the prevailing geomagnetic field conditions. The northern and southern sectors exhibit pronounced bipolar characteristics, with magnetic highs generally positioned toward the western side and corresponding lows toward the eastern side. Such configurations indicate structurally controlled magnetic bodies, including possible dyke intrusions, faulted contacts, and fractured zones within the studied region. These anomaly patterns, provide an initial framework for understanding subsurface structural complexity prior to RTP transformation and further quantitative analysis.

Reduction to the pole (RTP)

The observed magnetic anomaly pattern is influenced by the geometry of the causative body, its magnetization direction

(inclination), and its orientation relative to the Earth's magnetic field (declination). Under low magnetic latitude conditions, magnetic sources typically produce bipolar anomalies, complicating structural interpretation due to spatial displacement between anomaly peaks and their causative bodies. To simplify interpretation, the corrected magnetic field was transformed using the reduction to the pole (RTP) technique, which reorients magnetic anomalies as if the inducing field were vertical and aligned with the geographic north pole (Baranov and Naudy, 1964; Nabighian et al., 2005; Etman et al., 2025). This transformation minimizes dipolar asymmetry and places anomaly maxima approximately over their respective sources. The RTP contour map of the study area (Figure 5), generated with a contour interval of 50 nT, exhibits magnetic intensity values ranging from 142 nT to 542 nT, the RTP map presents a more symmetric and simplified anomaly distribution. The dominant anomaly trends are oriented NW–SE and NE–SW, consistent with the regional tectonic fabric of the Peninsular Gneissic Complex. In addition, several N–S trending anomalies correspond spatially with mapped dyke intrusions, suggesting structural control along fault-aligned intrusive pathways.

Structural discontinuities are delineated along zones of steep magnetic gradient that define anomaly boundaries. These gradient zones are interpreted as lithological contacts, dyke margins, or fault-controlled interfaces within the gneissic basement. The structural interpretation shown in Figure 5, distinguishes major structural lineaments and faults (solid lines) from inferred or subsidiary lineaments (dashed lines), as indicated in the map legend. Major lineaments coincide with the prominent magnetic gradients, whereas subsidiary features are inferred from subtle but coherent anomaly alignments. The potential influence of computational edge effects inherent to Fourier-based RTP transformation was carefully evaluated. Edge artifacts typically occur near grid margins due to abrupt truncation of data and often follow grid geometry. In the present study, however, the interpreted structural features are located within the interior portion of the dataset and do not align with grid boundaries. Moreover, the identified anomaly boundaries are consistently corroborated by corresponding maxima in the analytical signal map and are recognizable in the original magnetic anomaly map prior to RTP transformation. The persistence of these features across multiple independent datasets confirms that they represent genuine subsurface structural contacts rather than numerical artifacts generated during RTP processing. The RTP transformation therefore provides a reliable and structurally meaningful representation of magnetic sources in the study area, significantly enhancing the delineation of fault zones, intrusive bodies, and fracture-controlled domains that influence groundwater flow and contaminant migration.

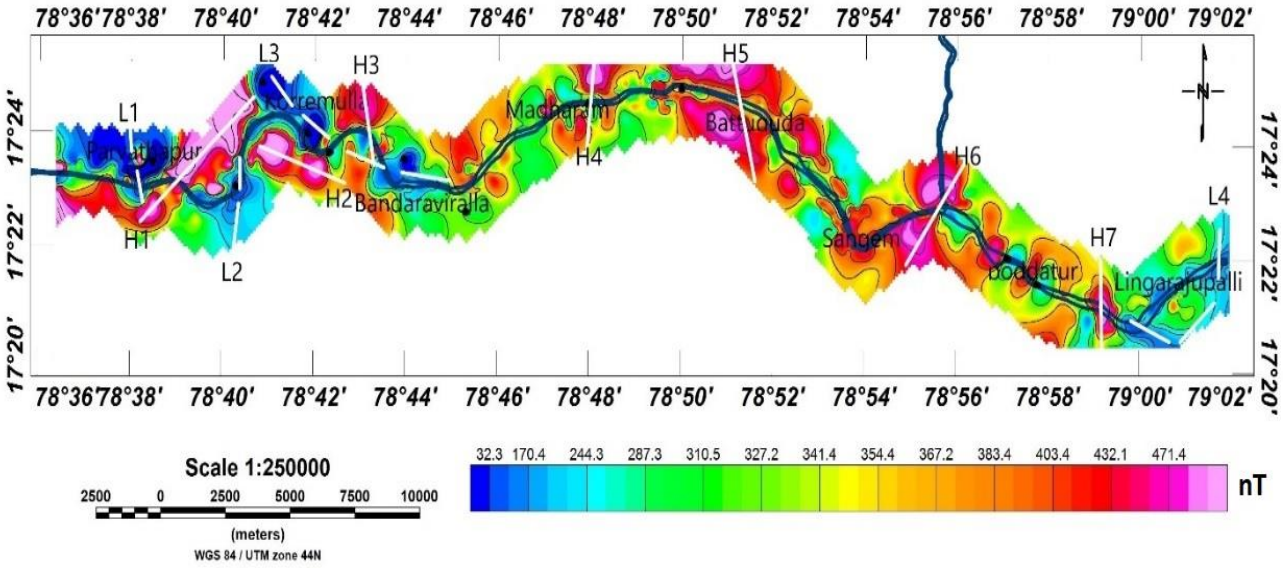

Figure 4. Magnetic anomaly map of the study area

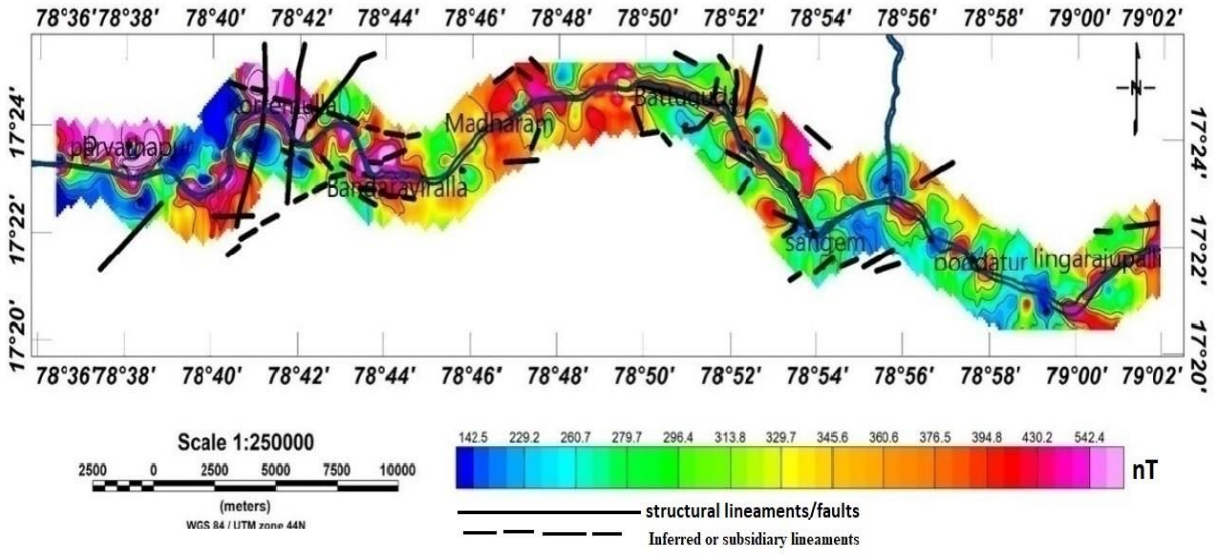

Figure 5. Reduction to the pole magnetic contour map of the study area

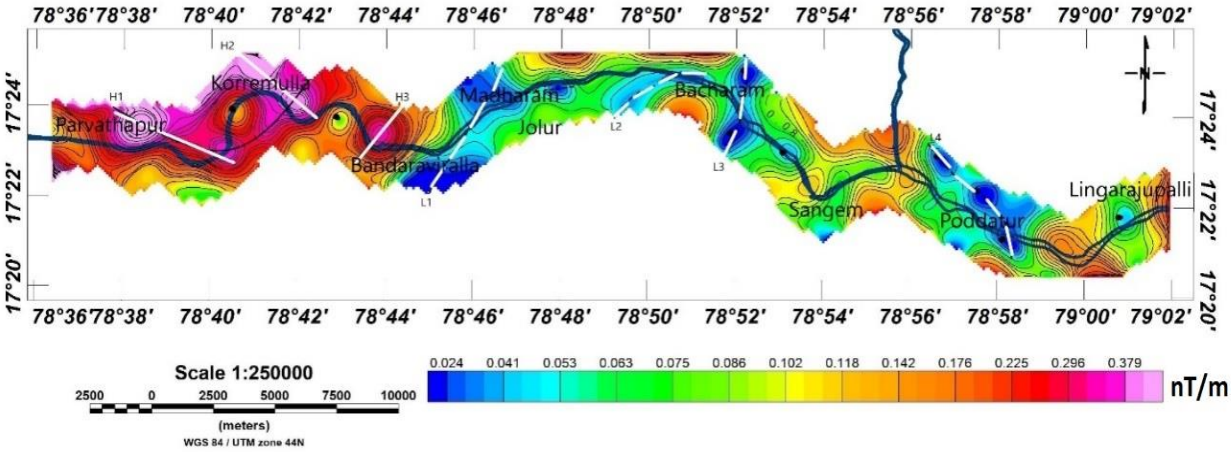

Figure 6. Analytical signal contour map of the study area.

Analytical signal map

The analytical signal (AS) technique provides a robust and direction-independent method for delineating structural boundaries and magnetic source contacts (Nabighian, 1988; Milligan and Gunn, 1997). The analytical signal amplitude represents the square root of the sum of the squares of the first-order derivatives of the magnetic field in the x, y, and z directions, and is expressed in nT/m. Because it is independent of magnetization direction, the analytical signal is particularly effective in low magnetic latitude regions, where conventional magnetic anomalies often exhibit significant dipolar asymmetry. The analytical signal contour map of the study area (Figure 6) which enhances shallow magnetic sources, clearly delineates structural discontinuities. Six prominent magnetic highs (H1–H6) and eight magnetic lows (L1–L8), have been identified. The dominant structural trends revealed by the AS map are, NE–SW and NW–SE, consistent with the patterns observed in the RTP map and regional tectonic fabric.

High-amplitude zones correspond to areas of steep magnetic gradient and are interpreted as shallow, high-susceptibility sources, such as doleritic dyke intrusions, faulted contacts, or structurally disturbed gneissic domains. In contrast, relatively low-amplitude regions are associated with zones of reduced magnetic contrast, which may represent weathered or fractured domains and possible tectonic disturbances. A prominent NE–SW trending structural discontinuity is inferred near longitude 78.73°, characterized by a sharp analytical signal gradient, indicating a probable lithological contact or a fault zone.

The western sector of the study area exhibits comparatively stronger analytical signal amplitudes, suggesting relatively shallow magnetic sources or increased structural complexity in the region. Importantly, the structural boundaries identified in the analytical signal map, spatially coincide with the anomaly trends observed in both the original magnetic anomaly and RTP maps. This consistency across independent magnetic transforms strengthens confidence in the interpreted contacts and confirms their geological origin. The analytical signal therefore provided a reliable delineation of subsurface structural elements, particularly fault zones, dyke margins, and fracture-controlled contacts that influence groundwater flow and contaminant migration within the study area.

QUANTITATIVE ANALYSIS

Quantitative estimation of the depth to intracrustal magnetic interfaces is a critical aspect of magnetic data interpretation. In the present study, the radial average power spectrum method was applied to the magnetic data to estimate source depths. Fourier spectral analysis, a widely used tool in both ground and aeromagnetic studies, enables quantitative evaluation by transforming spatial magnetic data into the frequency domain. This technique has been extensively applied in previous studies (Spector and Grant, 1970; Rao and Avasthi, 2006). The method involves removing a linear or planar regional field from the digital data, computing the Fourier transform, deriving the complex amplitude spectrum, and calculating the energy spectrum.

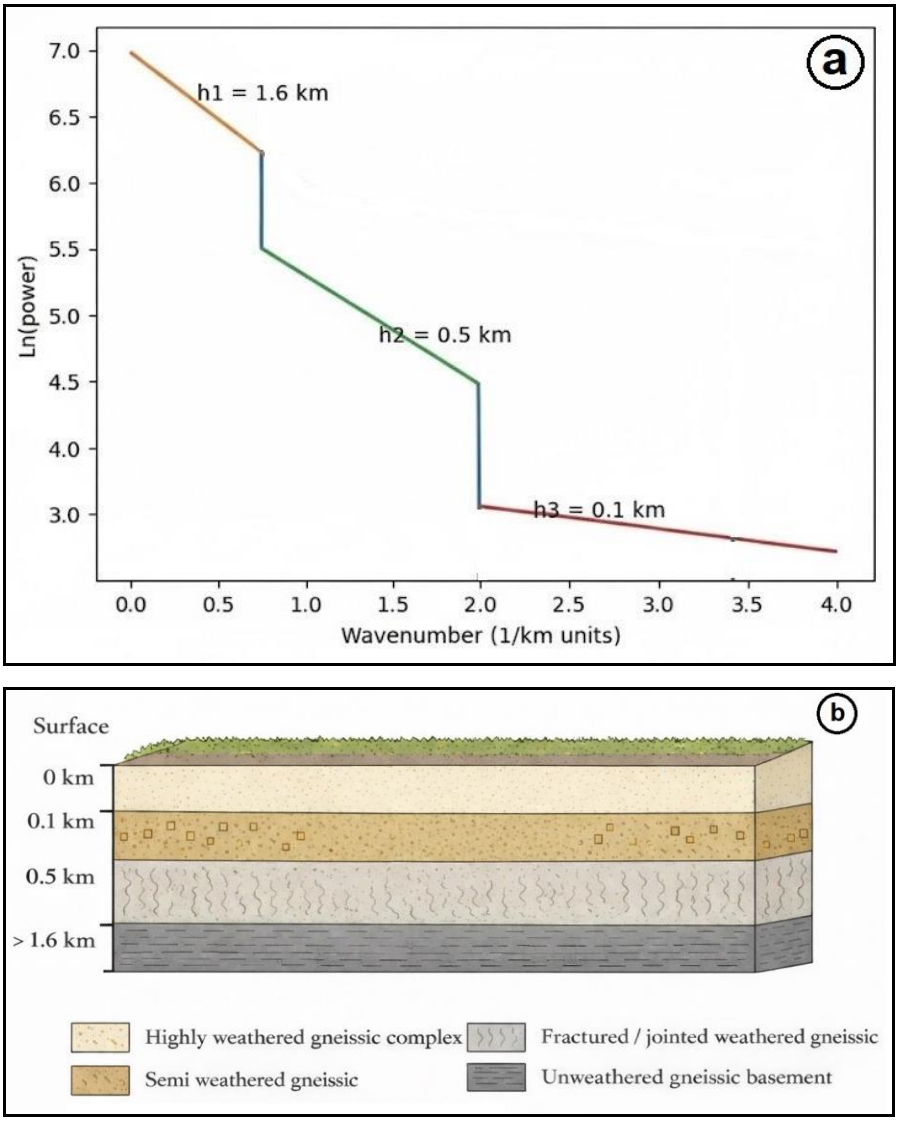

Figure 7. (a) Radial average power spectrum analysis of total study area, and **(b)** conceptual subsurface lithological diagram

For spectral computation, the magnetic data were gridded using minimum curvature interpolation with cell size compatible with the observation spacing. Radial average power spectra were computed using windowed grids confined to data-supported regions to avoid distortion from large no-data areas. Cosine tapering was applied at grid boundaries to minimize edge effects and spectral leakage. Zero-padding of large empty regions was avoided. The stability of spectral slopes was verified by comparing overlapping analysis windows. This approach ensures that the estimated depth interfaces are not significantly affected by padding-related FFT artifacts. The logarithm of energy is plotted against radial frequency (wave number), and the slope of the linear portion of the decay curve provides an estimate of the average source depth. Changes in slope indicate the presence of multiple sources at different characteristic depths, each requiring separate analysis (Spector and Grant, 1970). For the total study area, three depth interfaces were identified at approximately ~0.1 km, ~0.5 km, and ~1.6 km (Figure 7a). Based on these interfaces, a conceptual lithological diagram has been constructed (Figure 7b), illustrating four inferred subsurface units: (i) a highly weathered and fractured upper gneissic layer (0 to ~0.1 km), (ii) a semi-weathered granitoid zone (0.1 to ~0.5 km), (iii) a structurally disturbed and jointed gneissic domain influenced by dyke intrusions and shear zones (0.5 to ~1.6 km),, and (iv) a relatively unweathered gneissic basement at depths greater than ~1.6 km. This schematic representation integrates spectral depth estimates with geological interpretation to provide a comprehensive structural model.

Upstream and downstream segments

In order to evaluate spatial variations in depth distribution, the radial average power spectrum (RAPS) analysis was performed separately for the upstream (T1–T6) and downstream (T7–T12) datasets, similar to the total area analysis shown in Figure 7a and b. This sector-wise approach allows independent estimation of depth interfaces and facilitates comparison of structural layering between the two segments. The upstream segment (T1–T6) and the downstream segment (T7–T12) (Figures 8a and 9a). Separate radial average power spectrum (RAPS) analyses were performed for each sector to evaluate differences in depth distribution and structural configuration. For the upstream sector (T1–T6), three distinct depth interfaces were identified at approximately ~0.1 km, ~0.4 km, and ~0.79 km. These depth estimates suggest a relatively thin weathered zone near the surface (0 – ~0.1 km), underlain by a semi-weathered granitoid layer (~0.1– ~0.4 km), followed by a fractured and jointed gneissic domain extending to ~0.79 km depth. Below this level, the magnetic signature indicates a compact and less disturbed basement (Figure 8b).

In contrast, the downstream sector (T7–T12) exhibits depth interfaces at approximately ~0.1 km, ~0.39 km, and ~0.82 km (Figure 9b). While the shallow interface (~0.1 km) is comparable to that of the upstream region, subtle differences are observed in the intermediate and deeper interfaces. The slightly greater depth to the third interface (~0.82 km) in the downstream sector indicates marginal thickening of the fractured and structurally disturbed zone relative to the upstream segment.

Conceptual diagrams were constructed for both sectors to visually represent these lithological variations and structural contrasts. The downstream model suggests enhanced structural complexity, likely associated with intensified fracturing, dyke intrusions, and shear activity. This interpretation is supported by the qualitative magnetic analysis, which revealed higher-frequency and higher-amplitude oscillatory anomalies in the downstream region, compared to the smoother anomaly patterns observed upstream. The observed structural thickening and increased heterogeneity in the downstream sector may reflect localized tectonic reactivation or cumulative deformation along the Musi River corridor. Such structural disturbances can significantly enhance secondary porosity and permeability within the weathered and fractured gneissic units. Consequently, these zones may serve as preferential pathways for groundwater flow and contaminant migration. The integration of spectral depth estimation with qualitative magnetic interpretation therefore provides a coherent structural model, indicating that the downstream sector is characterized by comparatively stronger tectonic disturbance and structural heterogeneity. This finding has important implications for understanding groundwater vulnerability and pollutant transport mechanisms within the study area.

Two-dimensional magnetic modelling

To complement the spectral depth analysis and provide geometric constraints on individual magnetic sources, two-dimensional forward magnetic modelling was carried out for representative anomalies from both the upstream (T1–T6) and downstream (T7–T12) sectors (Figure 3). Two-dimensional forward modelling is commonly used in hydrogeological and near-surface studies to estimate the geometry, depth extent and magnetization contrasts of shallow sources (e.g., to delineate basement depth, dykes, and sedimentary cover) and to improve interpretation of structural controls on groundwater (Kebede et al., 2021).

Integrating 2-D forward models with spectral depth estimates and source-parameter imaging, increases confidence in depth and shape constraints for anomalies and helps link magnetic sources to hydrogeological features such as basement topography and faulted zones that control groundwater flow (El-Badrawy et al., 2024). While the radial average power spectrum method provides average depth estimates for ensembles of magnetic sources, it does not resolve the geometry or horizontal extent of specific structures. Therefore, the selected anomalies were chosen based on their amplitude, lateral continuity, structural significance inferred from RTP and analytical signal maps, and minimal influence from potential cultural noise. The magnetic anomalies were modelled using simple geometrical bodies consistent with the regional geological framework, where doleritic dykes, shear zones, and fault-controlled contacts are common.

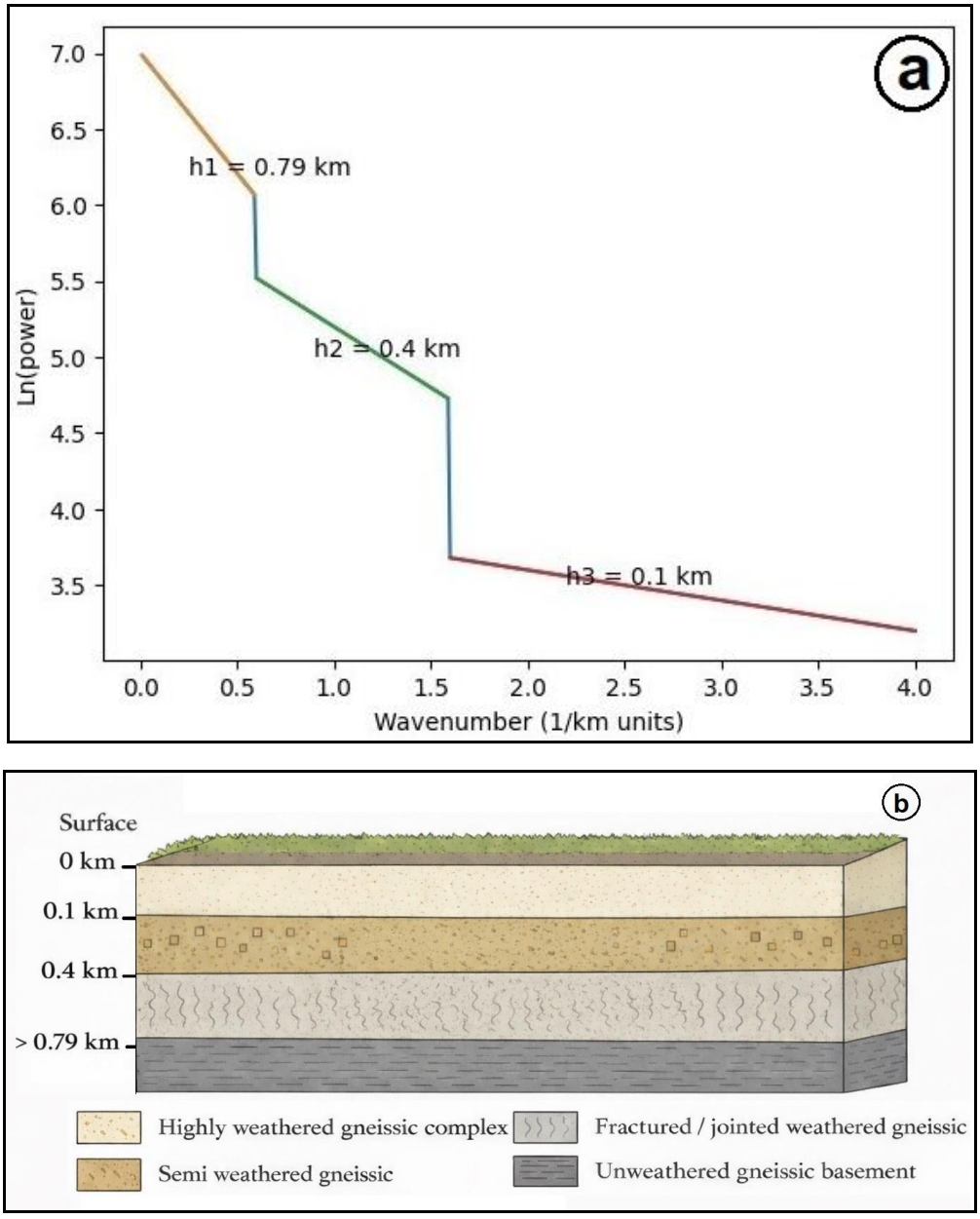

Figure 8. (a) Radial average power spectrum analysis of upstream study area, and **(b)** conceptual subsurface lithological diagram of upstream

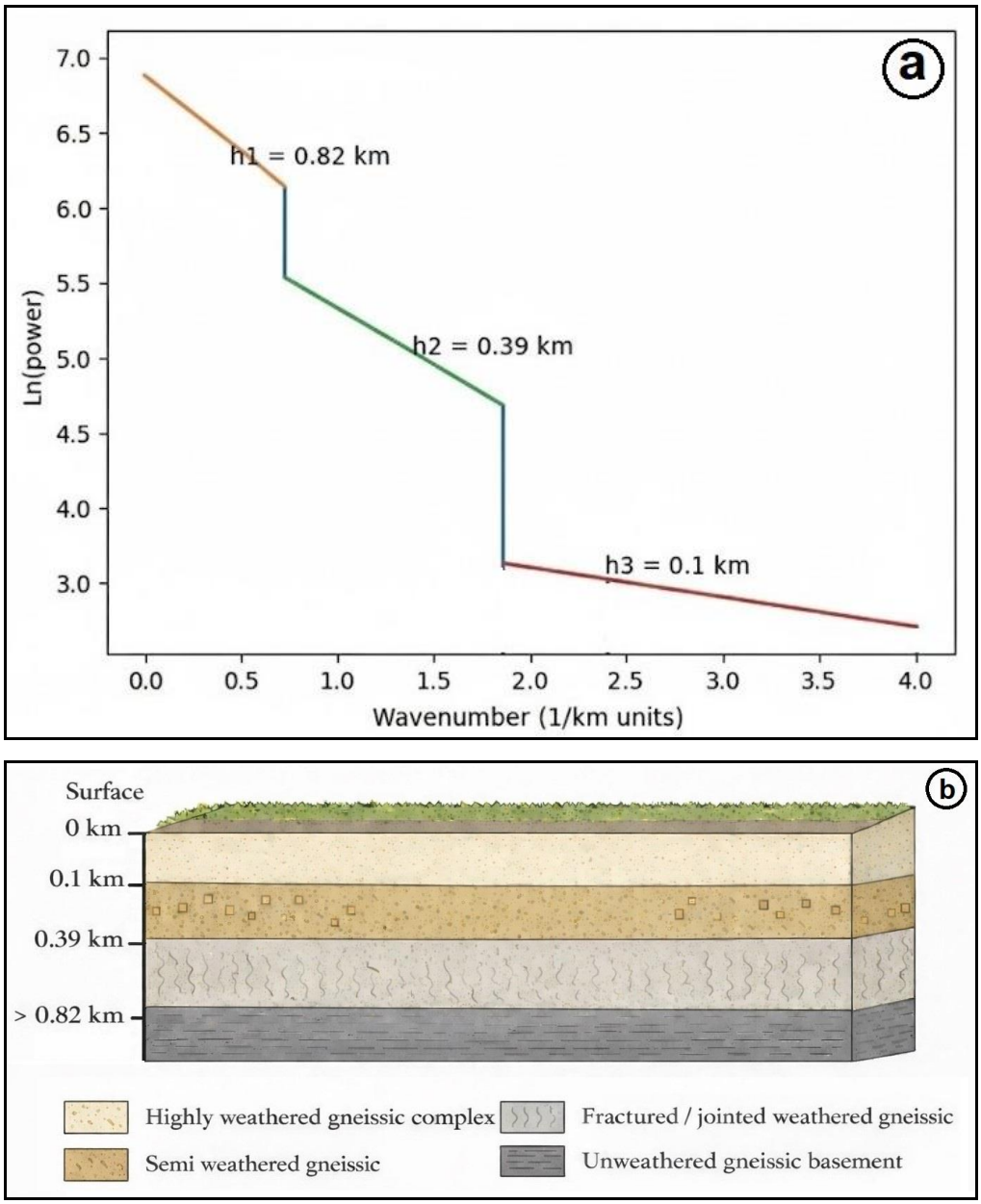

Figure 9. (a) Radial average power spectrum analysis of downstream study area, and **(b)** conceptual subsurface lithological diagram of downstream

Forward modelling was performed assuming induced magnetization under the local geomagnetic field parameters (inclination ~24° and declination ~ –0.5°). The anomalies were approximated using dyke-like or sheet-type bodies embedded within the gneissic basement. Model parameters, including depth to top, horizontal width, dip angle, and magnetic susceptibility contrast, were iteratively adjusted to achieve the best fit between observed and calculated magnetic responses. For the upstream sector, the anomaly was satisfactorily modelled by a moderately dipping dyke-like structure with a depth to top of approximately 0.12–0.18 km and a lateral extent of about 0.8–1.2 km. The susceptibility contrast required for fitting was moderate, consistent with localized dyke intrusion or fracture-controlled magnetization within semi-weathered granitoids (Figure 10).

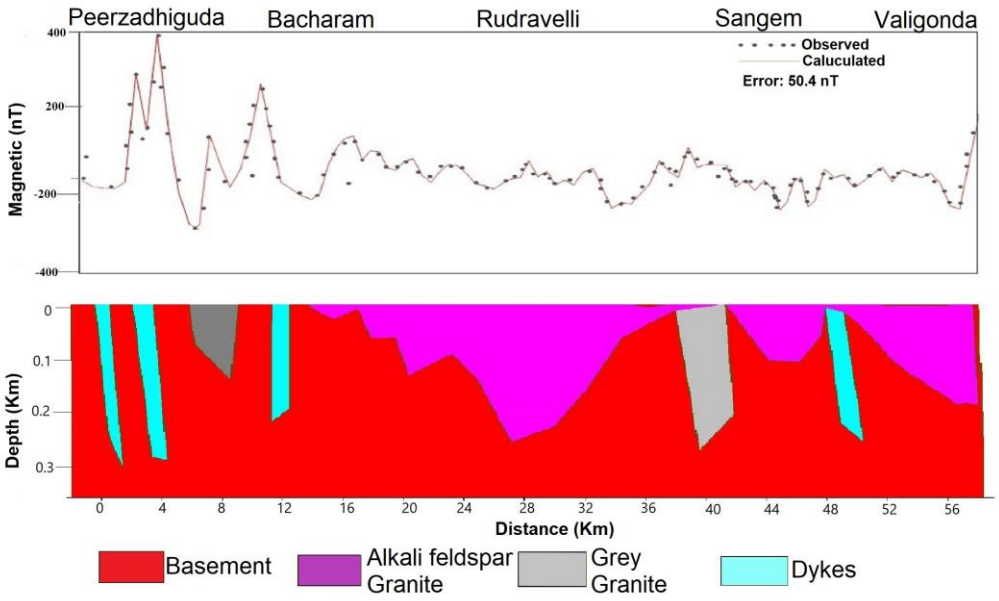

Figure 10. Magnetic model along the north traverse-(NT) upstream

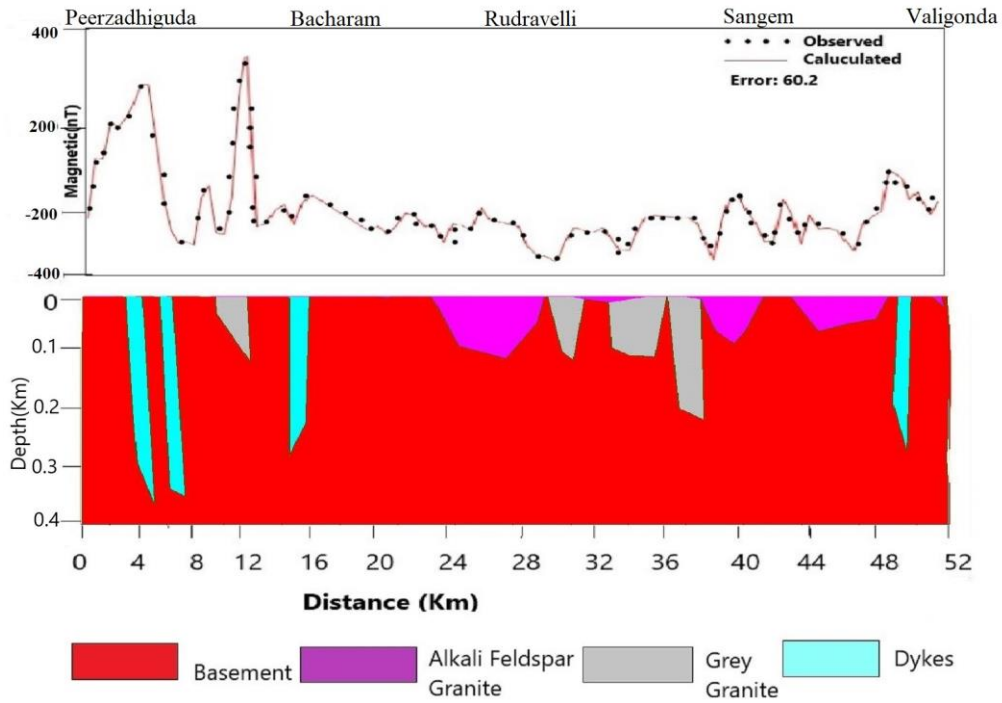

Figure 11. Magnetic model along the south traverse-(ST) downstream

In contrast, the downstream anomaly required a broader and slightly deeper source body to reproduce the observed higher-amplitude and more oscillatory magnetic pattern. The modelled depth to top ranged from approximately 0.15–0.22 km, with a horizontal extension of about 1.5–2.0 km, suggesting a thicker or more laterally extensive structurally disturbed zone. The increased width and susceptibility contrast indicate intensified fracturing, dyke intrusion, or shear activity in the downstream sector (Figure 11). These modelling results are consistent with the spectral depth estimates, particularly the shallow interface at ~0.1 km identified in both upstream and downstream sectors. Although the downstream RAPS analysis indicates a slightly deeper intermediate interface (~0.82 km), the modelled depths primarily constrain the shallow structural bodies within the upper fractured zone rather than the deeper

regional interfaces. The comparative modelling therefore supports the interpretation that the downstream segment of the Musi River corridor exhibits enhanced structural complexity and thicker fractured zones relative to the upstream sector. Such structural thickening and increased heterogeneity are likely to enhance secondary porosity and permeability, thereby facilitating groundwater movement and contaminant migration. The integration of forward modelling with spectral and qualitative magnetic interpretation provides more robust and quantitatively constrained subsurface structural framework for the study area.

Integrated structural map

To provide a comprehensive structural synthesis, the structural elements interpreted from the magnetic anomaly, reduction to pole (RTP), and analytical signal (AS) maps were integrated and superimposed onto the geological base map (Figure 12) (El-Badrawy et al., 2024; Khalifa et al., 2025). The integrated structural map combines magnetic lineaments derived from anomaly gradients, RTP symmetry enhancement, and analytical signal maxima with mapped geological features such as dykes, faults, migmatite/amphibolite bodies, and the Musi River channel. The magnetic anomaly-derived structures predominantly highlight bipolar responses associated with intrusive bodies and fault-controlled contacts. RTP-derived lineaments provide improved positional accuracy of causative bodies by minimizing dipolar displacement effects, thereby refining structural orientation (Olajide et al., 2025). The integrated structural map reveals dominant structural trends in NE–SW, NW–SE, N–S, and subordinate E–W directions. Several magnetic lineaments coincide spatially with mapped doleritic dykes and known fault traces, confirming their geological origin. In addition, multiple previously unmapped or subtle lineaments were identified from magnetic datasets, particularly in the downstream sector, indicating intensified structural deformation along the Musi River corridor.

The downstream region exhibits a higher density of intersecting magnetic lineaments compared to the upstream sector, suggesting enhanced tectonic disturbance and fracture development. The coincidence of magnetic lineaments with river course deviations and fault intersections indicates that the Musi River may be structurally guided in several segments. Such structurally controlled zones likely enhance secondary porosity and permeability, facilitating groundwater movement and contaminant migration pathways (El-Badrawy et al., 2024; Khalifa et al., 2025). This integrated structural framework provides a spatially coherent interpretation linking magnetic signatures with geological mapping and strengthens the structural control hypothesis proposed in this study.

DISCUSSION

The integrated magnetic investigation along the Musi River corridor reveals a structurally heterogeneous subsurface framework that exerts significant control on groundwater flow and contaminant migration. The combined interpretation of magnetic anomaly data, reduction to the pole (RTP), analytical signal (AS), spectral depth estimation, two-dimensional forward modelling, and integrated structural mapping, provides a multi-scale characterization of subsurface architecture within the studied region. A clear structural contrast is observed between the upstream and downstream sectors. The upstream region is comparatively stable, characterized by narrower intrusive bodies and moderately developed fracture systems. In contrast, the downstream sector exhibits greater structural complexity, reflected by a higher density of intersecting magnetic lineaments, stronger analytical signal gradients, and relatively thicker fractured domains. Spectral depth estimates and forward modelling collectively indicate slightly greater structural thickening and lateral continuity of magnetic bodies in the downstream region, supporting the interpretation of enhanced tectonic disturbance.

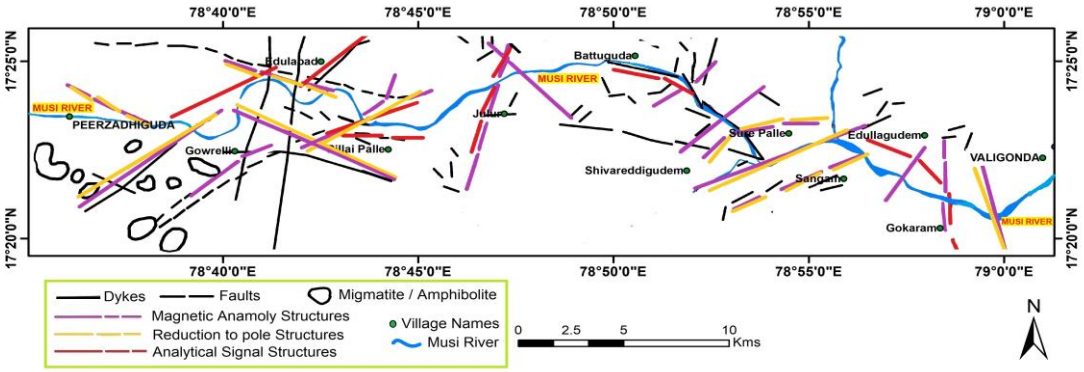

Figure 12. Integrated structural map of study area

Zones of steep magnetic gradient identified in the RTP and analytical signal maps consistently coincide with mapped doleritic dykes, fault traces, and structurally disturbed gneissic domains. The spatial agreement among independent magnetic transforms, strengthens confidence in the interpreted structural contacts and confirms their geological origin. The downstream sector, in particular, displays intensified structural heterogeneity, which is consistent with thicker fractured zones inferred from spectral analysis and broader modelled magnetic sources. Such structural complexity implies enhanced secondary porosity and permeability relative to the upstream segment. The integrated structural map further demonstrates that major magnetic lineaments align with mapped geological features and locally correspond with deviations in the Musi River course, suggesting partial structural control on river alignment. Intersecting lineaments and fault-controlled contacts likely act as preferential pathways for both vertical recharge and lateral groundwater movement. The presence of weathered and fractured gneissic layers overlying a comparatively competent basement creates permeability contrasts that facilitate fluid circulation within the hard rock terrain. Under such structurally controlled conditions, contaminants introduced through surface runoff, industrial discharge, or river infiltration may migrate downward through fracture networks and propagate laterally along fault-guided conduits.

CONCLUSIONS

This study demonstrates the effectiveness of integrated magnetic methods in delineating subsurface structural controls along the Musi River corridor between Peerzadhiguda and Valigonda areas, encompassing portion of the Ranga Reddy and Nalgonda districts in the state of Telangana, India. The combined application of magnetic anomaly mapping, reduction to the pole (RTP), analytical signal (AS), radial average power spectrum (RAPS) analysis, and two-dimensional forward modelling establishes a structurally heterogeneous framework comprising weathered zones, fractured gneissic domains, dyke intrusions, and basement interfaces. Sector-wise analysis reveals comparatively greater structural complexity in the downstream region, expressed by thicker fractured domains, broader magnetic source bodies, and a higher density of intersecting lineaments. The spatial correspondence between magnetic gradients, mapped geological structures, and modelled subsurface bodies confirms that fault zones, dyke margins, and fracture networks, exert primary control on groundwater movement within the study area. The integrated interpretation provides a structurally constrained hydrogeological model in which permeability contrasts between weathered, fractured, and competent basement units govern fluid circulation. Such structurally controlled pathways are likely to facilitate contaminant migration along the Musi River corridor.

Acknowledgements

The authors sincerely thank the anonymous reviewers for their constructive and insightful comments, which significantly improved the quality and clarity of the manuscript. The authors also gratefully acknowledge Dr. O.P. Pandey, Chief Editor of The Journal of Indian Geophysical Union (JIGU), for his critical evaluation and valuable suggestions.

Author credit statement

Udaya Laxmi G, Supervision, validation, interpretation of results, review and editing of the manuscript. Blessy Ganduri: Conceptualization, methodology development, data acquisition, data analysis, interpretation of results, and writing of the original draft. Linga Swamy Jogu: Methodology support, data acquisition, data analysis, interpretation, and manuscript review and editing. Naveen Kumar Gardas: Data acquisition, data analysis, and preparation of geological and thematic maps.

Data availability

The datasets generated and/or analysed during the current study are available from the corresponding author on reasonable request.

Compliance with ethical standards

There is no conflict of interest associated with this publication and authors adhere to copy right norms.

References

Akpa, C., Nnabo, P.N., Ani, C.C., Obasi, A.I., Obasi, P.N. and Nworie, C.D., 2023. Application of ground magnetic method for delineation subsurface structural control on sulphide ore deposit in Benue Trough; a case study of Ikenyi Izzi. Earth Sci. Malaysia, 7(1), 07-19.

Anak Mejus, L., 2014. Using multiple geophysical techniques for improved assessment of aquifer vulnerability. Lancaster University (UK, Unpublished Thesis).

Andhra Pradesh State Ground Water Department., 2002. Groundwater investigations and hydrogeological studies in Andhra Pradesh. Govt. of Andhra Pradesh.

Baranov, V. and Naudy, H., 1964. Numerical calculation of the formula of reduction to the magnetic pole. Geophys., 29(1), 67-79.

Barker, R. D., 1981. The offset system of electrical resistivity sounding and its use with multicore cables. Geophys. Prosp., 29(1), 128–143.

El-Badrawy, H.T., Abbas, A.M., Massoud, U., Abu-Alam, T., Alrefaee, H.A., Abo Khashaba, S.M. and Nagy, M., 2024. Integrated approach-based groundwater mapping in sohag governorate, upper Egypt, using remote sensing and aeromagnetic data. Front. Earth Sci., 12, p.1456055.

Etman, M.S., Mohamed, A.M.S., Saleh, S., Mohamed, S.A. and Fergawy, K.O., 2025. Geological Structures Assessment in Wadi Hagul, Northwestern Gulf of Suez, Egypt, Using Gravity and Magnetic Techniques. Jordan J. Earth & Envi. Sci., 16(2), 163-172.

Geosoft., 2010. Oasis Montaj V 8.4 – Integrated geophysical data processing and mapping system. Geosoft Inc.

GSI, 2010. Geological Survey of India. District Resource Map of Nalgonda and Ranga Reddy, Telangana. Geol. Survey of India Publications.

Gugulothu, S., Dhakate, R., Sreedhar, K., Ramesh, A. and Saxena, P.R., 2020. Geophysical and hydrochemical studies for sustainable development of groundwater resources in northwestern part of Telangana State, India. J. Earth System Sci., 129(1), 202, https://doi.org/10.1007/s12040-020-01452-7

Gunn, P.J., 1997. Application of aeromagnetic surveys to sedimentary basin studies. AGSO J. Australian Geol. and Geophys., 17, 133-144.

Jaques, A.L., Wellman, P., Whitaker, A. and Wyborn, D., 1997. High-resolution geophysics in modern geological mapping. AGSO J. Australian Geol. and Geophys., 17, 159-173.

Jogu, L.S. and Gardas, N.K., 2025. Prioritizing Groundwater Recharge Zones through Morphometric and Geospatial Analysis: A Case Study of the Musi River Basin, Telangana, India. Results in Earth Sci., 3, p.100136.

Kamal, M., Shen, J., Othman, A.A.A., Sultan Araffa, S.A., Tekin, H.O., Ene, A., Abdel-latief, A.S.A. and Zakaly, H.M., 2023. Integrated geophysical techniques applied for petroleum basins structural characterization in the central part of the Western Desert, Egypt. Open Chemistry, 21(1), p.20220293.

Kebede, H., Alemu, A., Nedaw, D. and Fisseha, S., 2021. Depth estimates of anomalous subsurface sources using 2D/3D modelling of potential field data: implications for groundwater dynamics in the Ziway-Shala Lakes Basin, Central Main Ethiopian Rift. Heliyon, 7(4), e06843.

Khalifa, M., Sharkawy, M.S., Mohamaden, M., Taha, A., Moneim, A.A., Zaki, S. and Masoud, A.M., 2025. Evaluation of groundwater resources in Wadi Qena, Egypt: a geophysical and hydrogeochemical perspective. Sci. Rep., 15, 43834.

Kuntamalla, S. and Saxena, P.R., 2021. Groundwater prospect detection using electrical sounding data in southwestern part of Telangana, India. Arab. J. Geosci., 14, 2640.

Ling, C., Xu, Q., Zhang, Q., Ran, J. and Lv, H., 2016. Application of electrical resistivity tomography for investigating the internal structure of a translational landslide and characterizing its groundwater circulation (Kualiangzi landslide, Southwest China). J. Appl. Geophy., 131, 154-162.

Milligan, P.R. and Gunn, P.J., 1997. Enhancement and presentation of airborne geophysical data. AGSO J. Australian Geol. and Geophys., 17(2), 63-75.

Nabighian, M.N. ed., 1988. Electromagnetic methods in applied geophysics: Voume 1, theory. Society of Exploration Geophysicists.

Nabighian, M. N., Grauch, V. J. S., Hansen, R. O., LaFehr, T. R., Li, Y., Peirce, J. W., Phillips, J. D. and Ruder, M. E., 2005. The historical development of the magnetic method in exploration. Geophys., 70(6), 33ND–61ND.

Olajide, T.A., Oladejo, O.P., Salaudeen, S.A., Adewunmi, H.I. and Sunmonu, L.A., 2025. High-resolution aeromagnetic mapping and 2d magnetic modelling for detailed depth profiling of subsurface magnetic sources in parts of the Nupe Basin, North-Central Nigeria. Dutse J. Pure and App. Sci., 11(3d), 336-349.

Pazzi, V., Tapete, D., Cappuccini, L. and Fanti, R., 2016. An electric and electromagnetic geophysical approach for subsurface investigation of anthropogenic mounds in an urban environment. Geomorphology, 273, 335-347.

Phani, P.R.C. and Rajendra Prasad, K., 2024. Geochemical Studies of Sediments and Waters of Musi River in Parts of Hyderabad City, Telangana, India. In Modern River Science for Watershed Management: GIS and Hydrogeological Application. Cham: Springer Nature Switzerland, pp. 505-523.

Ramakrishnan, M., 2009. Precambrian mafic magmatism in the western Dharwar craton, southern India. J. Geol. Soc. India, *73*(1), 101-116.

Rao, K.G.C. and Avasthi, D.N., 2006. Analysis of the Fourier spectrum of the gravity effect due to two-dimensional triangular prism. Geophys. Prosp., 21(3), 526-542.

Sekhar, C., Chary, N.S., Kamala, C.T., Shanker and Frank, H., 2005. Environmental pathway and risk assessment studies of the Musi River's heavy metal contamination-a case study. Human and Ecologi. Risk Asses., 11(6), 1217-1235.

Sharp, J.M. ed., 2014. Fractured rock hydrogeology (Vol. 490). Boca Raton, FL: CRC Press.

Spector, A. and Grant, F. S., 1970. Statistical models for interpreting aeromagnetic data. Geophys., 35(1), 293–302.

Received on: 03-12-2025; Revised on: 18-03-2026; Accepted on: 18-04-2026

J. Ind. Geophys. Union, 30(4) (2026), 290-304
https://doi.org/10.71122/JIGU.30(4)2026.0028

Hydrothermal origin of pyrite in the Zawar Pb-Zn deposit, Aravalli Craton: Insights from trace element geochemistry and supervised machine learning algorithms

Sima Gorai*, Bulusu Sreenivas and T. Vijaya Kumar
CSIR-National Geophysical Research Institute, Uppal Road, Hyderabad 500007, India.
Corresponding author: sima.geol90@gmail.com

ABSTRACT

The application of machine learning algorithms on geochemical datasets is emerging as a powerful tool for characterising ore deposits. In this work, we integrate the trace element geochemistry of different generations of pyrite with machine learning algorithms to understand the nature of ore deposition in the Zawar Pb–Zn deposit. Pyrites from Zawar have long been debated to have either sedimentary exhalative (SEDEX) or hydrothermal origins, making them ideal for testing classification approaches. We framed this as a binary classification problem and employed three ML algorithms, Random Forest (RF), Gradient Boosting (GB), and AdaBoost (AB), well-suited for recognising subtle geochemical patterns. A global dataset comprising 727 SEDEX and 577 hydrothermal pyrite samples, characterised by trace elements, such as Co, Ni, Cu, Zn, As, Ag, Sb, and the Co:Ni ratio, provided the training base for these models. Applying the trained models to in-situ Laser Ablation–Inductively Coupled Plasma–Mass Spectrometry (LA-ICP-MS) data from Zawar pyrites, yielded high accuracies: 97.24% for RF, 96.93% for GB, and 96.63% for AB. The classifications overwhelmingly support a hydrothermal origin, for the deposit. These results not only validate earlier geological interpretations but also demonstrate the integrated use of ore-geochemistry on machine learning for understanding the ore-forming processes, ultimately strengthening exploration techniques and mineral deposit models in economic geology

Keywords: Trace elements, Pyrite classification, Hydrothermal processes, Machine Learning, Zawar Pb-Zn deposits

INTRODUCTION

vein-type mineralization. Satellite imaging has since revealed hydrothermal alteration zones along major structures, Machine learning is increasingly applied across diverse branches of Earth Science, including geology, geophysics, hydrology, and atmospheric science, to analyze complex datasets, identify patterns, and improve predictions of natural processes and resource distribution (Gorai et al., 2025a, Dalai and Kumar, 2026). Geochemical exploration of mineral deposits evolved from limited data to handling large datasets, prompting the adoption of machine learning (ML), which has proven effective in classifying ore deposits in the reconnaissance stage of mineral exploration. Our current study uses machine learning to explore the long-debated origin of the Zawar deposit. This area is known for its complex ore formation, with theories pointing to both sedimentary exhalative (SEDEX) and hydrothermal origins. Early work by Ghosh (1957) and Mookherjee (1964) suggested a hydrothermal model supported by structural controls and high mineralization temperatures around 500°C . Later, Talluri et al. (2000) studied fluid inclusions in sphalerite-galena ores, showing temperatures from 320°C (vein-type) to 150°C (massive galena), consistent with hydrothermal deposition. Bhattacharya and Bull (2010) reported mixed features, both SEDEX-type bedding and structurally controlled especially near the Main Zawar Fold (Gorai et al., 2024). In a recent research low temperature hydrothermal Acanthite veins has been reported from the study area (Gorai et al., 2026).

Despite extensive research on the Zawar deposit, a definitive consensus on its genesis remains elusive due to the coexistence of SEDEX and hydrothermal features, leaving a critical need for objective, data-driven methods to distinguish between these processes across different mineralization stages. In this study, we apply three machine learning models, Random Forest, Gradient Boosting, and AdaBoost, to trace element data (Co, Ni, Cu, Zn, As, Ag, Sb, and Co:Ni ratio) from different pyrite generations: early framboidal pyrite (Py-1), euhedral pyrite (Py-2), and late-stage coarse pyrite (Py-3). These models classify whether each generation formed through SEDEX or hydrothermal processes, based on early published data sets. This approach helps clarify the genesis of the Zawar deposit using data-driven insights from pyrite geochemistry. This method may be useful in mineral exploration as a screening and support tool for interpreting pyrite trace element data from new samples. Once LA-ICP-MS data are obtained, the trained model can help provide a first-order indication of whether the pyrite geochemistry is more consistent with hydrothermal or SEDEX affinity.

GEOLOGICAL SETTING OF THE ZAWAR Pb-Zn DEPOSIT

The Zawar deposit lies within the highly mineralised Proterozoic Aravalli Supergroup in northwestern India (Deb et al., 1989). The Aravalli Craton stretches around 700 km in length along northwest India, is endowed with some of the country's most significant ore deposits, including Pb–Zn mineralisation at Zawar, Rajpura Dariba, and Rampura Agucha; copper deposits at Khetri and Neem Ka Thana; the phosphorite deposits of Jhamarkotra; and the gold deposits of Bhukia and many other economically significant ore deposits (Figure 1). The Aravalli Supergroup is subdivided into Lower-Middle

and Upper Aravalli Groups, defined by distinct lithological units separated by unconformities (Roy, 2000; McKenzie et al., 2013). The Lower Aravalli Group includes the Delwara Formation and the phosphorite-bearing Jhamarkotra Formation (~1.7 Ga; McKenzie et al., 2013). The Middle Aravalli Group comprises the Udaipur, Zawar, Bowa, and Tidi Formations, while the Upper Aravalli Group consists of the Debari and Jharol Formations. Zawar mineralisation, as reported by Mukherjee and Bhattacharya (2021), occurs within the Middle Aravalli Group, hosted in a siliciclastic-dolomitic carbonate sequence. The belt hosts substantial lead and zinc ore deposits, actively mined at various sites, like Balaria, Mochia Magra, Baroi Magra, and Zawar Mala. A geological map of the Zawar deposit, adapted from Roy (1995), is shown in Figure 2.

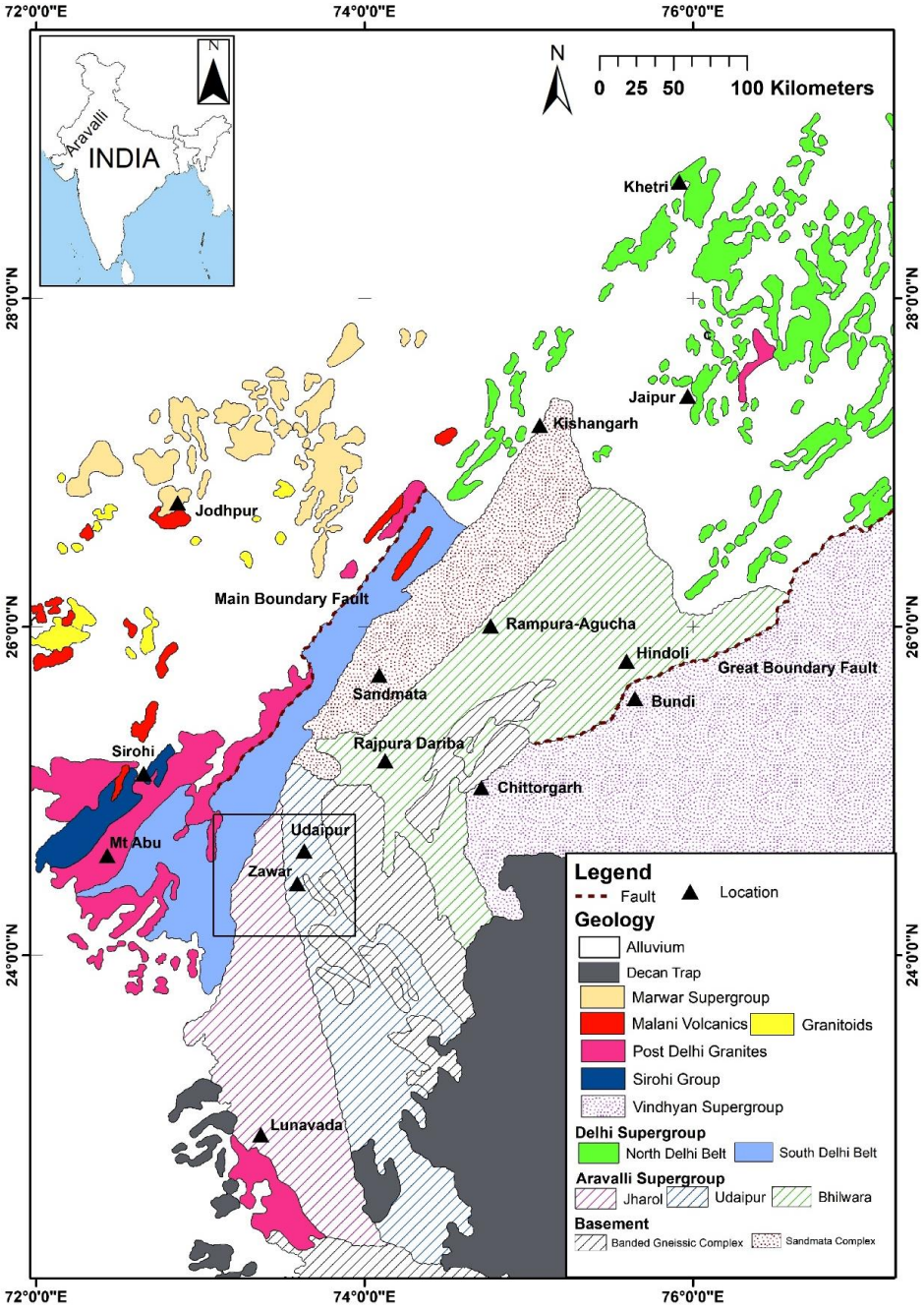

Figure 1. Geological map of The Aravalli Mountain Range representing the major ore deposits and the study area (After Roy et al., 1988).

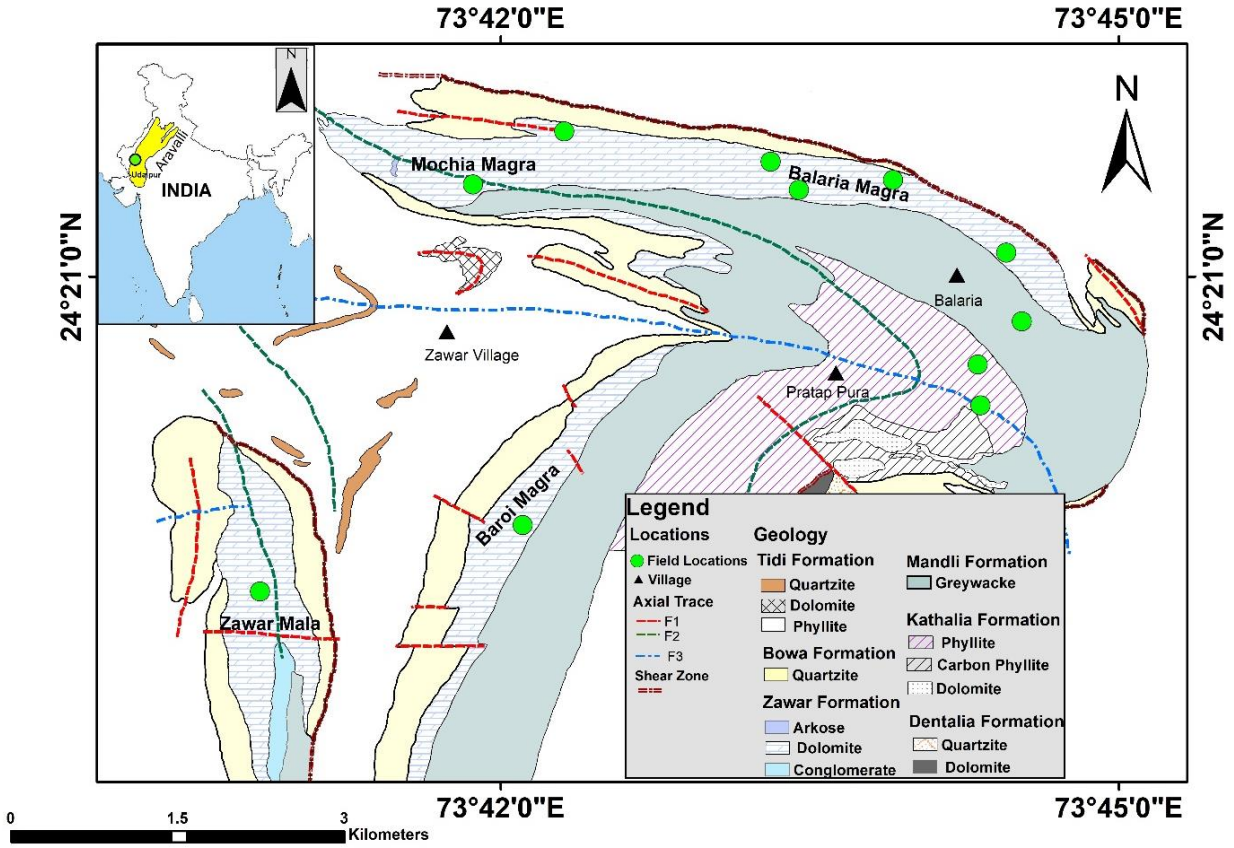

Figure 2. Geological map of the Zawar Pb-Zn deposit, Rajasthan, India (after Roy, 1995).

Pyrite mineralisation in Zawar

Pyrite occurs in the form of veins and disseminated patches in the dolomitic carbonates associated with the major Pb-Zn sulfide minerals like galena and sphalerite. Based on the mineral paragenetic history, three distinct phases of pyrite mineralisation have been observed from the samples collected from the different mines of the Zawar deposit. These are the first-generation rounded framboidal pyrite (Py-1), euhedral cubic pyrite (Py-2) formed before the deposition of sphalerite and galena, and the late-formed large crystals of pyrite (pentagonal in image) (Py-3), formed after the deposition of the main ore-bearing phases **(**Figure 3).

METHODOLOGY

To train the classification models, globally existing published data sets have been utilized (727 data for SEDEX deposits and 577 data for hydrothermal deposits) (Zhang et al, 2014; Gadd et al., 2016; Mukherjee and Large 2017; Grant et al., 2018; Liu et al., 2018; Song et al., 2019; Xiong et al., 2019; Knorsch et al., 2020; Xie et al., 2020; Wu et al., 2021; Zhao et al., 2021; Meng et al., 2022; Lin et al., 2022; Nie et al., 2023; Chao et al., 2023; Li et al., 2023). This data set is used to train machine learning models on trace element data to classify the deposit and test their predictive accuracy using 35 new pyrite samples from the Zawar deposit.

In situ LA-ICP-MS analysis

35 pyrite samples was analysed using LA–ICP–MS at the National Geophysical Research Institute (NGRI), Hyderabad, India. For sample preparation, small polished fragments of pyrite were mounted in one-inch epoxy resin discs. Analytical work was carried out on an Agilent 7800 quadrupole ICP–MS coupled with a 213 nm laser ablation system. Ablation conditions employed 10 Hz repetition rate, and a laser fluence of 10 J/cm², optimised for sulfide mineral analysis. External reference materials, including BCR-2G, NIST 610, and NIST 612, were used to ensure calibration and accuracy. These procedures provided high-precision trace element data, which form the foundation for distinguishing pyrite generations and constraining the ore-forming processes of the Zawar deposit. While preparing the data sets missing values or below detection limit values were completely removed for all elements to ensure consistency and reliability of model training in the next steps.

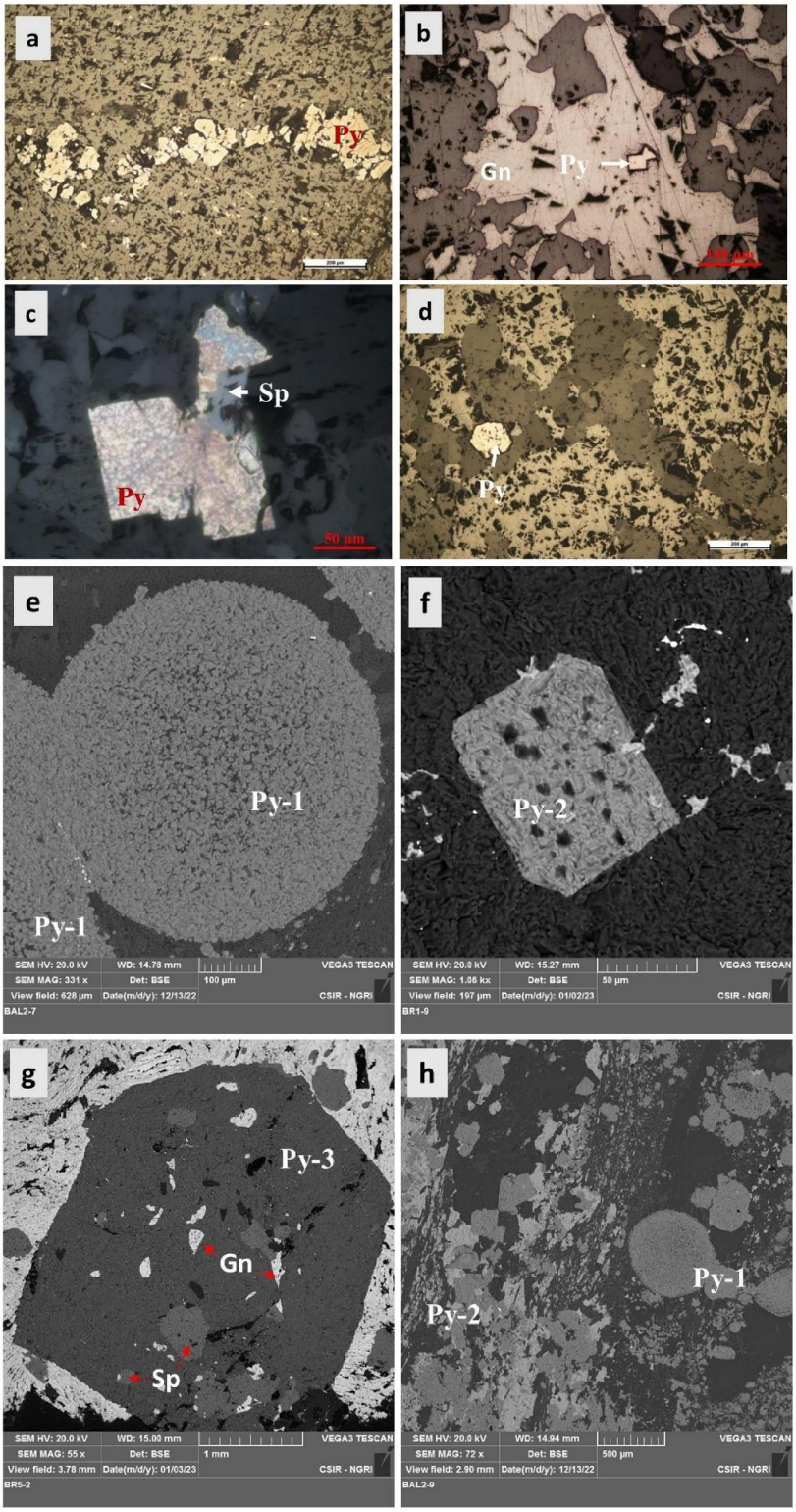

Figure 3. Ore petrographic images: **(a)** pyrite (Py) vein within host rock carbonate, **(b)** euhedral pyrite within galena (Gn), **(c)** an early-formed pyrite crystal is showing replacement by the late-formed sphalerite (Sp) at the corner, **(d)** euhedral pyrite with well-developed crystal outlines. Scanning Electron Microscopic Images of three varieties of pyrite: **(e)** large framboidal pyrite of first generation, **(f)** Sharp-edged, isolated euhedral pyrite crystal of second generation. **(g)** pyritohedral pyrite crystal of the last generation, showing pentagonal outline, and incorporation of the early formed sphalerite and galena, **(h)** mixed euhedral and framboidal pyrites with other mineral inclusions.

Algorithms used in the study

Random Forest (RF), Gradient Boosting (GB), and AdaBoost (AB), are the three machine learning algorithms, utilized in this study to construct predictive models for classification. The algorithms were deployed using Scikit-learn, a robust Python-based ML library recognised for its efficiency and ease of application. The choice of classifiers was guided by their demonstrated effectiveness in handling complex, multi-dimensional datasets, a capability crucial in geological studies that demand differentiation of minute geochemical variations. Collectively, these approaches enhance the reliability of classifying the Zawar deposit on the basis of pyrite trace element compositions.

Random Forest (RF)

Random Forest (RF), introduced by Breiman (2001), is an ensemble-based classification method that addresses the limitations of single decision trees, particularly their tendency to overfit. The algorithm constructs a large number of decision trees during training (Figure 4a), and the final prediction is derived from the majority vote of the individual tree outputs. The procedure involves bootstrap aggregation (bagging), where multiple subsets of the training dataset are generated, each used to train an independent decision tree. To enhance diversity among trees, a random subset of features is evaluated at each node to identify the optimal split. Once the ensemble of trees (DT-1, DT-2, …, DT-n) is constructed, their predictions (Result-1, Result-2, …, Result-n) are combined through majority voting, thereby reducing variance and improving generalization performance. An additional advantage of RF is the incorporation of Out-of-Bag (OOB) error estimation, which provides an unbiased measure of prediction accuracy without requiring a separate validation dataset. This is achieved by evaluating each tree on the samples excluded from its bootstrap training set ('out-of-bag' data). In applications such as ore deposit classification, for example distinguishing SEDEX from hydrothermal systems, the prediction for a given sample x can be formally expressed as the aggregated majority vote of all constituent decision trees.

$$RF^{class}(x) = mode\{T_b(x;\Theta_b)\}_{b=1}^{B} \quad (1)$$

Here *B* indicates the total number of trees, $T_b(x;\Theta_b)$ denotes the prediction made by the b-th tree for a given input sample x. The term Θ_b refers to the random parameters independently assigned to each tree, and 'mode' corresponds to the class level that appears most frequently across all three predictions. In this way the overall classification outcome (i.e., whether the deposit is classified as SEDEX or Hydrothermal) is determined by the majority voting principal applied to ensemble of decision trees.

Gradient Boosting (GB)

Gradient Boosting (GB), introduced by Friedman (2001), is an advanced machine learning approach primarily applied to classification problems. The model (Figure 4b) is built consecutively in a stage-wise manner, with each stage designed to correct the errors of the preceding model. The process begins with an initial model, *F0(x)*, which provides a baseline prediction, typically representing the most frequent or average outcome within the dataset. At each subsequent stage *t*, a new decision tree, *DTt (DT-1, DT-2, …, DT-n)* (Figure 4b), is fitted to the negative gradient of the loss function *L*, corresponding to the pseudo-residuals that quantify the misclassifications of the prior model. The contribution of each tree *DTt* is modulated by a weight *Wt* (e.g., *W1, W2, W3*, etc.), which controls the magnitude of the correction applied to the ensemble. The model is updated iteratively at each stage by incorporating these weighted corrections, ensuring that the ensemble progressively reduces the overall prediction error.

$$F_t(x) = F_{t-1}(x) + W_t . DT_t(x) \quad (2)$$

This iterative update signifies that the ensemble model $F(x)$ evolves by integrating the modifications suggested by each decision tree, thus:

$$F(x) = F_0(x) + \sum_{t=1}^{T} W_t . DT_t(x) \quad (3)$$

In our classification task of deposits into categories such as SEDEX or Hydrothermal, each decision tree DT_t precisely targets the segments of the data where the previous model $F_{t-1}(x)$ was less accurate. By doing so, Gradient Boosting fine-tunes the classification boundaries progressively with each stage, based on the calculated corrections from the trees *DT*-1, *DT*-2, ..., *DT*-n and their respective weights W1, W2, W3, etc. The final classification outcome for any sample is thus a cumulative result of all these adjustments, resulting in a refined decision that is reliable and effectively captures the complex distinctions between different types of geological deposits.

Ada Boost (AB)

AdaBoost, or Adaptive Boosting, introduced by Freund and Schapire (1997), is a classifier that strategically combines multiple weak classifiers designated as H1, H2, H3 in the diagram **(**Figure 4c**)** into a strong classifier. Each iteration of the algorithm fine-tunes the focus on the most challenging data samples by adjusting their weights. Initially, each data sample, such as Sample 1, Sample 2, through Sample n **(**Figure 4c**)**, is assigned an equal weight. As AdaBoost iterates through the training process, weights of samples incorrectly classified by the weak classifiers are increased, thereby emphasizing the more challenging cases in subsequent itera-

tions. This dynamic adjustment of sample weights is a defining characteristic of AdaBoost. At each iteration *t*, a weak classifier H_t is applied to the weighted training data. The performance of H_t is evaluated based on its error rate ϵ_t, which is computed as the sum of the weights of the samples that were incorrectly classified. The influence of each weak classifier in the final strong classifier is determined by a weight α_t, calculated using the relation:

$$\alpha_t = \frac{1}{2} log\left(\frac{1-\epsilon_t}{\epsilon_t}\right) \qquad (4)$$

This weight reflects the accuracy of H_t; classifiers that perform well are given more weight in the final decision process, while less accurate classifiers are assigned lesser weight. The final classification result is derived from a weighted majority vote among the outputs of all weak classifiers. The aggregate decision function for AdaBoost, after completing all iterations, is given by:

$$F(x) = sign\left(\sum_{t=1}^{T} \alpha_t H_t(x)\right) \qquad (5)$$

Here, T is the total number of iterations, and each $H_t(x)$ contributes to the final classification according to its computed weight α_t. This mechanism ensures that AdaBoost systematically targets the most challenging samples, progressively enhancing its accuracy, especially in complex classification tasks like distinguishing between different deposit classes.

Data Preparation

In this study, machine learning is applied to predict deposit types based on the trace element composition of pyrites from the Zawar deposit. Geological samples, detailed in the materials section, are compiled into a training dataset with key features including Co, Ni, Cu, Zn, As, Ag, Sb, and the Co:Ni ratio. The data undergoes pre-processing to remove incomplete entries and ensure consistency. Deposit type labels are converted to numerical form using label encoding, allowing compatibility with machine learning algorithms. The features are then normalized to ensure uniform scale, improving model stability and accuracy. The cleaned and standardized dataset is split into 75% for training and 25% for validation, allowing models to be evaluated on unseen data for reliable performance assessment. A complete workflow is provided in Figure 4d.

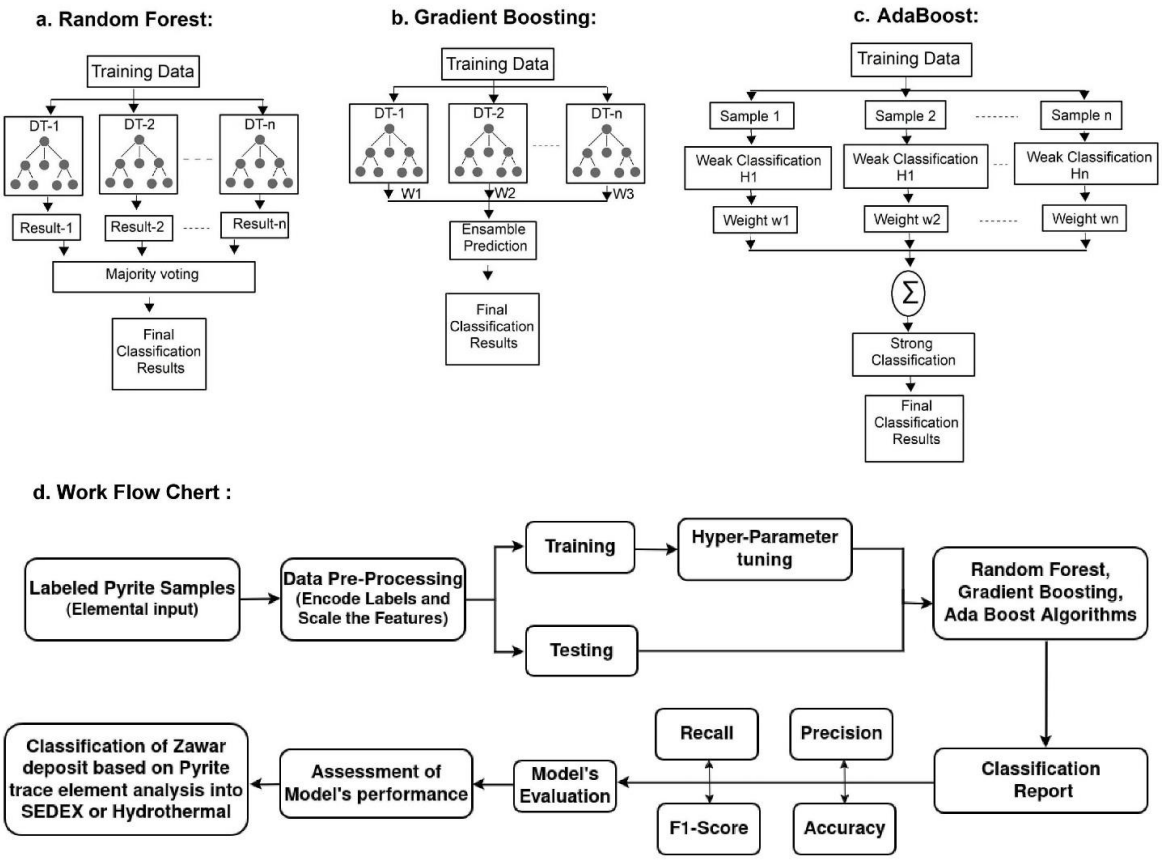

Figure 4. Methodologies of three different ML algorithms :**(a)** Random Forest **(b)** Gradient Boosting, **(c)** AdaBoost, **(d)** Workflow for classifying pyrite samples from the Zawar deposit.

RESULTS

Hyperparameter setting

We employed three machine learning algorithms to classify deposit types using pyrite trace element data, with Random Forest (RF) receiving detailed hyperparameter optimization. Initially, the model with 30 trees achieved 50.25% accuracy, which rose to 65.34% with 50 trees and reached a peak of 97.24% at 100 trees. Increasing the number of trees to 200 yielded only slight improvements, so 100 trees were selected as the optimal balance between accuracy and computational efficiency. Tree depths of 5, 10, and 15 were tested, with a depth of 10 offering the best compromise between capturing relevant patterns and avoiding overfitting. Between Gini impurity and entropy as splitting metrics, Gini performed better and was therefore adopted. Bootstrapping was enabled to improve model generalization by training each tree on random subsets of the data. Node-splitting parameters were further refined—requiring a minimum of two samples to split and at least one sample per leaf—and the number of features considered at each split was set to the square root of the total features. The final RF model, consisting of 100 trees, Gini impurity, bootstrapping, and optimized depth and split criteria, delivered strong performance and robustness.

Following RF optimization, Gradient Boosting (GB) and AdaBoost algorithms were implemented and fine-tuned to further enhance deposit type prediction. In Gradient Boosting, increasing the number of estimators from 50 to 100 raised accuracy from 85.62% to 96.93%. A learning rate of 0.5 provided an effective balance between fast convergence and accurate error correction, while a tree depth of 3 minimized overfitting while maintaining adequate model complexity. The model was trained on the full dataset (subsample rate = 1.0), ensuring stable learning, and employed a logarithmic loss function in combination with the 'Friedman mean squared error' criterion for reliable predictive performance.

For AdaBoost, expanding the number of weak learners from 50 to 100 improved accuracy from 85.12% to 96.63%, with negligible improvement beyond 100 learners. A learning rate of 0.5 ensured appropriate weighting of each learner's contribution, while simple decision stumps were used as weak classifiers to prevent overfitting. AdaBoost's adaptive weighting mechanism effectively emphasized misclassified samples, enhancing model accuracy across all classes. Overall, both ensemble models performed exceptionally well, with Gradient Boosting reaching 96.93% and AdaBoost achieving 96.63% accuracy, underscoring their reliability for predicting deposit types from pyrite trace element compositions.

Feature Correlation Matrix

After model parameterisation, we analysed inter-feature relationships using a Feature Correlation Matrix (Figure 5a) to understand how trace elements influence each other. Correlation coefficients range from -1.0 (strong negative) to 1.0 (strong positive), visualized with a diverging color scale. Notable positive correlations include Co-Ni (0.36), Ag-Sb (0.26), and As-Sb (0.22), suggesting shared geochemical behaviours or origins. A weak negative correlation between Cu and As (-0.04) hints at limited co-occurrence in mineralisation.

We then assessed feature importance (Figure 5b) to identify which elements most influence model predictions. In Random Forest, Ni emerged as the most significant, followed by As and Sb, indicating a balanced reliance on multiple features. Gradient Boosting heavily favoured Ni and Zn, highlighting their strong predictive roles. AdaBoost showed a more uniform feature distribution, slightly favouring Co and Zn, reflecting its ensemble nature. These differences underscore how each model interprets the data uniquely- Random Forest seeks optimal splits, Gradient Boosting corrects prior errors, and AdaBoost balances feature influence to improve classification accuracy.

Learning curves

We evaluated model training and reliability using learning curves (Figure 5c), generated through five-fold cross-validation to ensure robust performance estimates. The Random Forest model shows a high, stable training score with a steadily improving cross-validation score, indicating strong generalization and consistent performance on unseen data. Gradient Boosting starts with lower validation scores that improve significantly as more data is used, with training scores nearing perfection, indicating reduced overfitting and strong learning capacity. Similarly, AdaBoost displays lower initial validation scores that improve notably with additional data. While the training score climbs high, the cross-validation score shows some variability, suggesting sensitivity to data composition. Overall, the learning curves highlight strong performance and generalization in Random Forest and Gradient Boosting, while AdaBoost also demonstrates solid learning potential, particularly with larger datasets.

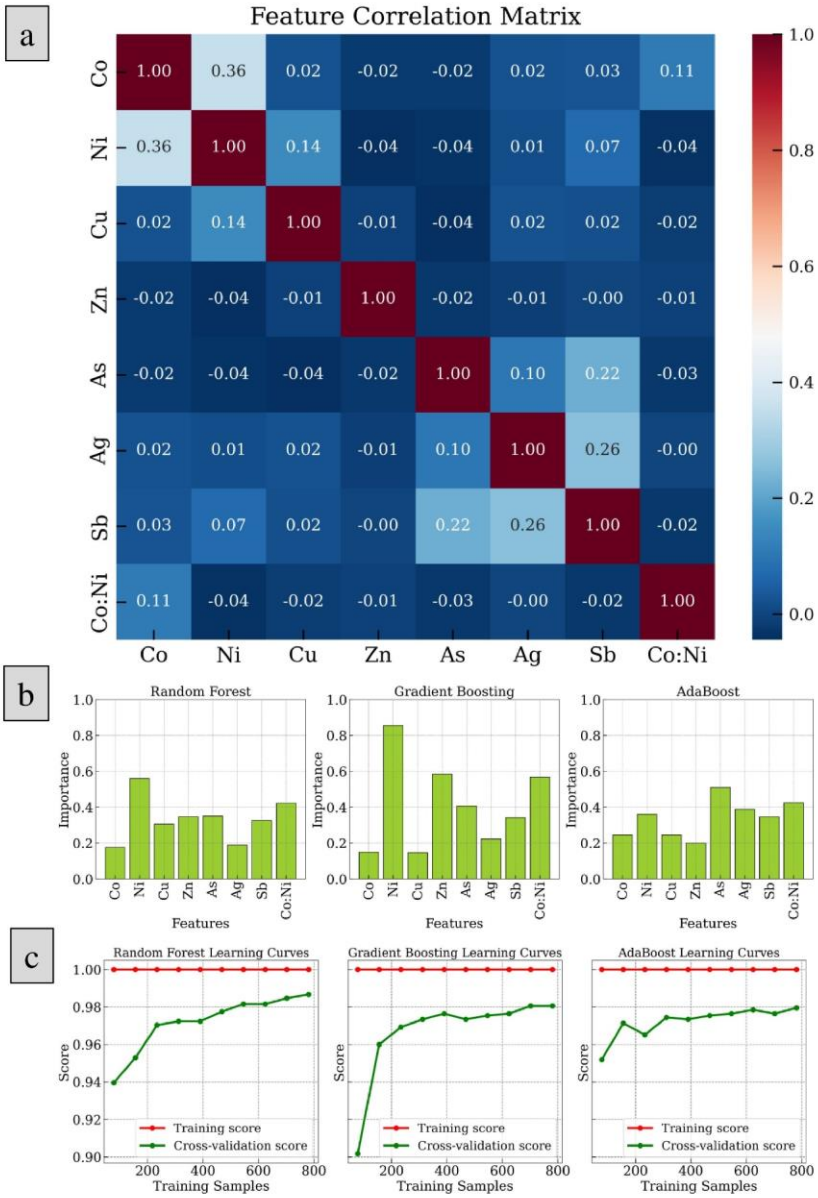

Figure 5. (a) Feature correlation heatmaps across different classification models. This set of heatmaps illustrates the correlation coefficients between various elemental features (Co, Ni, Cu, Zn, As, Ag, Sb, Co ratio), used in the classification of pyrite samples from Zawar deposit, using Random Forest, Gradient Boosting and AdaBoost algorithms. **(b)** Feature importance in machine learning models for pyrite classification. Graph illustrates the relative importance of each feature (e.g., Co, Ni, Cu, Zn, As, Ag, Sb, Co:Ni) in predicting pyrite origins using three machine learning algorithms: Random Forest, Gradient Boosting, and AdaBoost. Each panel highlights how different elements contribute variably to the model's decision-making process, with specific elements showing higher importance in certain algorithms, reflecting their unique handling of data features and model architecture. **(c)** learning curves showing improved training and validation accuracy with more data, indicating effective learning and minimal overfitting.

Performance evolution

After evaluating the models, we analyzed their confusion matrices (Figure 6a) to assess accuracy and error handling. The Random Forest model showed strong performance, correctly predicting 177 positives and 140 negatives, with only 4 false positives and 5 false negatives- highlighting its high reliability. Gradient Boosting improved slightly on true positives (178) but had 6 false positives and 4 false negatives, indicating strong detection capability, particularly for positives. AdaBoost closely followed, predicting 177 positives and 138 negatives, with 6 false positives and 5 false negatives, reflecting reliable classification.

These matrices confirm each model's skill in managing classification tasks, especially in identifying the positive class a

key factor in geological exploration where classifying a deposit can be costly.

We further quantified model performance using key metrics: precision, recall, F1 score, and AUC, all weighted to account for class imbalance. Random Forest showed high consistency with all metrics near 97.23% and accuracy at 97.24%. Gradient Boosting also performed well with precision, recall, and F1 score at 96.93%, AUC at 96.82%, and accuracy at 96.93%. AdaBoost yielded a precision and recall of 96.63%, F1 score of 96.62%, AUC of 96.54%, and accuracy of 96.63%. These results confirm all three models are highly effective in classifying deposit types based on trace element data.

The mentioned performance metrics are computed as follows:

$$\text{Precision: } P = \frac{TP}{TP+FP} \quad (6)$$

$$\text{Recall: } R = \frac{TP}{TP+FN} \quad (7)$$

$$\text{F1 Score: } F1 = 2 \times \frac{P \times R}{P+R} \quad (8)$$

$$\text{Accuracy: } A = \frac{TP+TN}{TP+TN+FP+FN} \quad (9)$$

where TP (True Positives) is the number of correct predictions that an instance is positive, TN (True Negatives) is the number of correct predictions that an instance is negative, FP (False Positives) is the number of incorrect predictions that an instance is positive, FN (False Negatives) is the number of incorrect predictions that an instance is negative.

t-distributed Stochastic Neighbour Embedding

After assessing the performance of all models, we applied t-SNE (t-distributed Stochastic Neighbour Embedding) to visualize the classification patterns by reducing the high-dimensional pyrite trace element data into two dimensions (Figure 6b). Prior to this, the features were normalized, and Principal Component Analysis (PCA) was performed to enhance stability and preserve the underlying data structure. This approach enabled clear visualization of inherent clusters and facilitated comparison between model-predicted and actual classifications.

As illustrated in Figure 6b, the training data (red/green) and model predictions (blue/magenta), exhibit strong correspondence across all three algorithms—Random Forest, Gradient Boosting, and AdaBoost- demonstrating their reliability in identifying hydrothermal deposits. Each model produced a unique clustering pattern. The Random Forest model exhibited compact and overlapping clusters between predicted and actual classes, reflecting its strong capability in feature learning. Gradient Boosting showed slightly better separation between classes, emphasizing its proficiency in capturing complex relationships through iterative refinement. AdaBoost also displayed well-defined clusters, though with minor instances of misclassification, indicating marginally higher variability. Overall, the t-SNE visualizations confirm that all three models effectively differentiate between SEDEX and hydrothermal deposit types, successfully capturing the distinct geochemical characteristics associated with pyrite mineralization, particularly within hydrothermal systems.

DISCUSSION

The major mineral phases encountered within the Zawar deposit comprise pyrite, galena, and sphalerite (Gorai et al., 2025 a, b). The host rock of this deposit is mainly dolomitic carbonate rock. Deposition of the Zawar sediments took place in the forearc basin regime (Absar and Sreenivas, 2015; Gorai et al., 2025a, b). Based on the low REE content and $\delta^{13}C$ values, Sachan (1993) suggested that the dolomitization process was linked to the infiltration of seawater driven by tidal pumping, indicative of a tidal flat environment. The mean positive $\delta^{13}C$ values (+1.4 to +4.32‰ PDB) reported by Sarker and Banerjee (2004) and the negative $\delta^{18}O$ values (-24.41 to -40.63‰) from Hoefs (1973) collectively point to a marine origin of the host dolomitic carbonates. The carbon isotope ($\delta^{13}C$) values from the Middle Proterozoic Zawar deposit are largely depleted, while the Balaria mine shows $\delta^{13}C$ values close to zero. The host carbonate rocks generally display a normal marine isotopic signature, but with depleted $\delta^{13}C$ values ranging from -3‰ to -9‰, suggesting significant hydrothermal alteration of marine carbonates (Fareeduddin et al., 2014). The $\delta^{18}O$ values vary between -10‰ and -17‰, clustering around -15‰, which aligns with isotopic patterns typical of Paleoproterozoic marine carbonates worldwide (Fareeduddin et al., 2014). Overall, the Zawar deposit, hosted in dolomitic carbonate rocks, provides isotopic evidence for seawater dolomitization, with $\delta^{13}C$ and $\delta^{18}O$ values confirming a marine origin that was later overprinted by hydrothermal activity in a forearc basin setting (Fareeduddin et al., 2014; Absar and Sreenivas, 2015). Fluid inclusion studies by Talluri et al. (2000) reveal the presence of low-salinity (4.3–14.7 wt.% NaCl equivalent) H_2O–NaCl fluids with a pH of 5.51, responsible for forming vein-type sulfide ores at trapping temperatures between 290°C and 395°C. The massive galena ores were deposited from H_2O–CO_2–NaCl fluids of lower salinity (3–4 wt.% NaCl equivalent) at 150–250°C and pH 4.25–4.31, indicating the influence of hydrothermal brines in the mineralization process (Talluri et al., 2000).

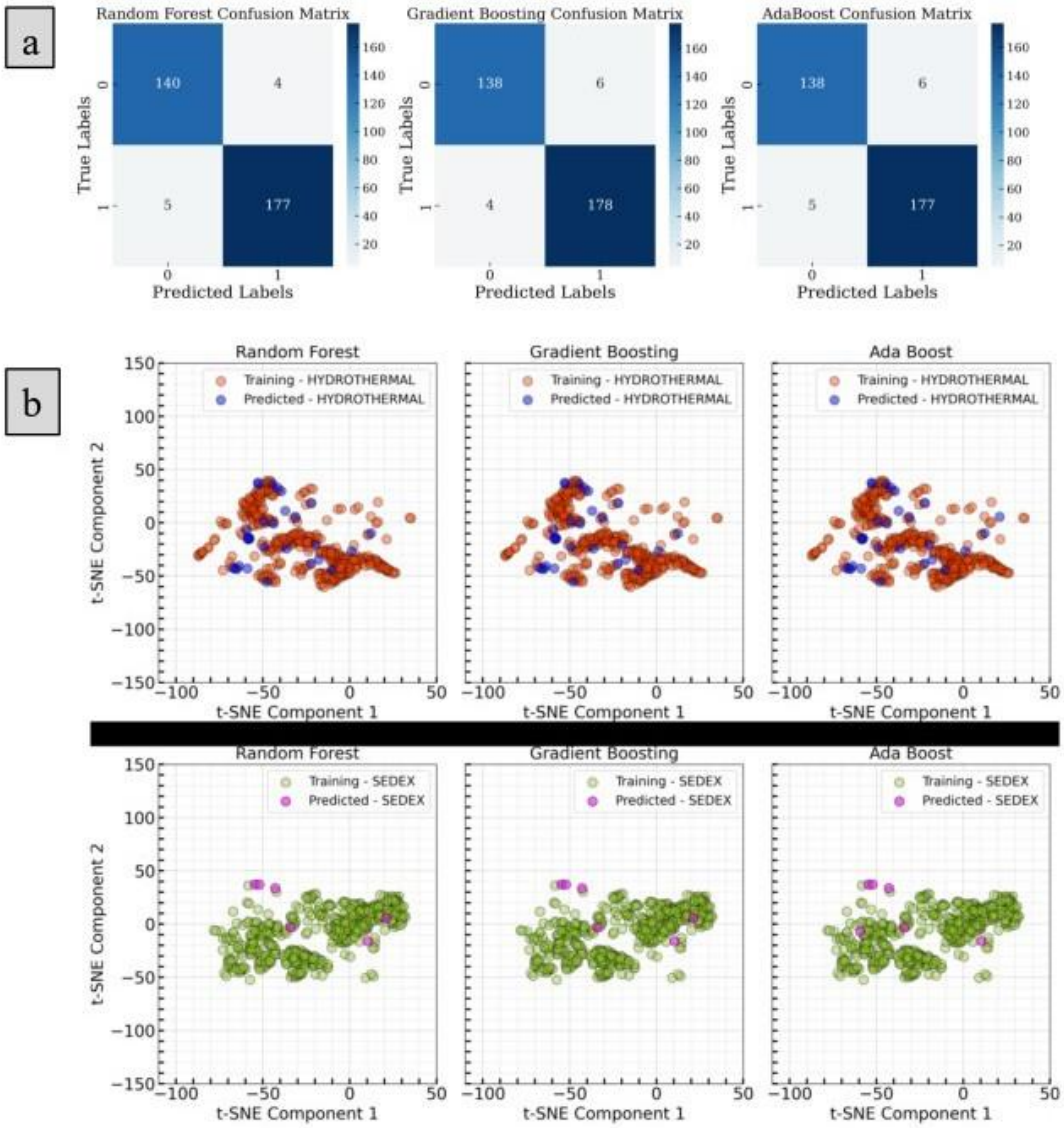

Figure 6. (a) Comparative evaluation of Random Forest, Gradient Boosting, and AdaBoost using Confusion Matrices. The matrices display true positives (TP), true negatives (TN), false positives (FP), and false negatives (FN) for each model. Random Forest shows high predictive accuracy with few errors, Gradient Boosting has slightly more errors, and AdaBoost demonstrates balanced misclassification. These matrices help evaluate each model's accuracy and specificity in classifying the dataset. **(b)** The scatter plot represents the t-SNE Visualization of Model Predictions for Pyrites, which reduces high-dimensional data to two components, for Random Forest, Gradient Boosting, and AdaBoost models. The colour-coded t-SNE visualizations compare training and predicted data points, showing how well each model predicts deposit types and discerns patterns in the geochemical data.

From the detailed petrographic observation, it is found that the Zawar deposit exhibits three phases of pyrite mineralisation, i.e. early formed (first generation) framboidal pyrite (Py-1), small crystals of euhedral cubic pyrite (second generation) (Py-2), and late-stage large pyrite crystals (third generation) (Py-3). Co, Ni, are the common iron-loving siderophile elements, and Cu, Zn, As, Ag, and Sb are some common sulfur-loving chalcophile elements present in trace amounts in pyrites (Goldschmidt, 1937; Debitius et al., 2008; Keith et al., 2018). Co and Ni tend to incorporate into the lattice structure of pyrite by stoichiometric lattice substitution (Jansson and Liu, 2020). Both Co^{+2} (0.74 Å) and Ni^{+2} (0.69 Å) can substitute for Fe^{+2}(0.74 Å) in the pyrite structure due to the similar ionic radius and charge. Cu, Zn, Ag and Sb mainly occurs as inclusions within the pyrite (Jansson and Liu, 2020). Cu^{+1}, and, Zn^{+2}, Ag and Sb can substitute Fe in the pyrite structure. Arsenic (As) is one of the most common elements to replace sulfur in the pyrite structure (Keith et al., 2018). As occurs in several oxidation states (including -I, +II, +III, +V) and can substitute (nonstoichiometric substitution)

into the pyrite lattice as either cation or anion (Huston et al., 1995; Reich et al., 2005; Qian et al., 2013; Deditius et al., 2014; Jansson and Liu, 2020). In reducing hydrothermal environment As^{-1} (2.22 Å) tends to substitute S^{-2} (1.84 Å) in pyrite lattice (Deditius et al., 2008). Arsenic (As) shows a wide range in the pyrites of the Zawar deposit.

Figure 7a summarizes the trace element concentrations (Co, Ni, Cu, Zn, As, Ag, Sb) in three types of pyrite (Py-1, Py-2, Py-3) from various samples. Py-1 generally exhibits higher trace element concentrations, particularly in elements like Co, Ni, As, and Sb, Py-2 has relatively lower concentrations but includes a strikingly high Zn content in one sample. Py-3 shows more variability, with notably high values of Co, Ni, and Zn in certain samples. Early-formed framboidal pyrite in hydrothermal systems tends to have higher trace element concentrations than late-formed pyrites, which may be due to several factors. Framboidal pyrite forms rapidly under low-temperature, early-stage conditions in metal-rich environments, allowing for greater trace element incorporation during crystallization. Early hydrothermal fluids are richer in trace metals, which decreases as the system progresses and minerals like sphalerite and galena precipitate. Additionally, the non-equilibrium growth conditions of framboidal pyrite can lead to more crystal defects, facilitating higher trace element content, whereas late-formed pyrites develop under more stable conditions, resulting in purer crystals with fewer trace elements.

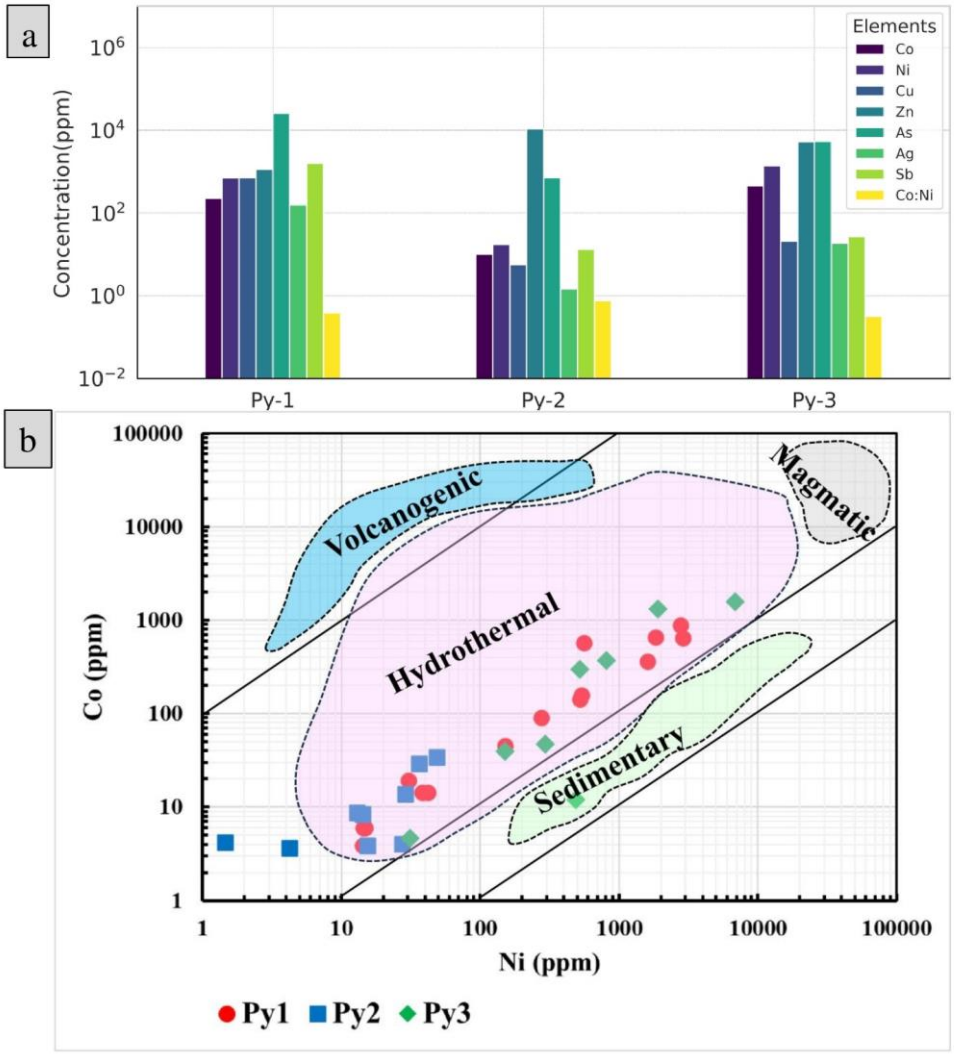

Figure 7. (a) The bar chart presents the elemental concentrations in parts per million (ppm) for three distinct generations of pyrite samples: Py-1, Py-2, and Py-3; **(b)** Co:Ni ratio plot of Zawar pyrites showing the Hydrothermal origin of the three generations of pyrites. (Fields of pyrite composition from Dora et al., 2020).

Table 1. Classification results and elemental compositions in ppm (Co, Ni, Cu, Zn, As, Ag, Sb, Co:Ni ratio) for Zawar deposit samples. Predictions are made using three machine learning models: Random Forest (RF), Gradient Boosting (GB), and Ada Boost (AB).

Sl No	Type	RF	GB	AB	Co	Ni	Cu	Zn	As	Ag	Sb	Co: Ni
1	Py-1	Hyd	Hyd	Hyd	575.38	554.96	351.33	235.13	31065.15	12.35	151.97	1.03
2	Py-1	Hyd	Hyd	Hyd	14.3	41.62	25.17	75.65	2908.97	24.98	313.75	0.34
3	Py-1	Hyd	Hyd	Hyd	91.2	274.08	153.43	178.88	20214.21	118.07	1664.89	0.33
4	Py-1	SEDEX	SEDEX	SEDEX	641.48	2864.08	1051.78	1290.93	98060.12	628.31	8425.34	
5	Py-1	SEDEX	SEDEX	SEDEX	891.88	2784.28	1189.38	1159.84	66556.84	524.94	3220.36	0.32
6	Py-1	Hyd	Hyd	Hyd	19.38	30.56	35.26	60.75	3855.71	29.53	230.55	0.63
7	Py-1	Hyd	Hyd	Hyd	157.73	535.47	450.7	1276.86	62007.27	377.36	3590.27	0.29
8	Py-1	Hyd	Hyd	Hyd	142.05	523.89	432.6	1152.73	58015.55	381.96	3420.26	0.27
9	Py-1	Hyd	Hyd	Hyd	3.89	14.22	11.42	10.91	956.22	5.9	93.66	0.27
10	Py-1	Hyd	Hyd	Hyd	6.07	14.33	14.55	17.28	962.59	6.48	97.09	0.42
11	Py-1	Hyd	Hyd	Hyd	6.03	14.71	15.20	20.67	968.63	7.10	96.58	0.40
12	Py-1	Hydl	Hyd	SEDEX	14.4	38.07	48.14	80.54	1995.67	21.06	222.26	0.37
13	Py-1	Hyd	Hyd	Hyd	5.97	14.46	26.6	19.58	993.7	9.3	101.96	0.41
14	Py-1	Hyd	Hyd	Hyd	45.12	150.34	143.12	301.84	9277.37	110.27	944.5	0.30
15	Py-1	SEDEX	SEDEX	SEDEX	654.82	1840.34	1873.15	6688.41	26880.75	110.43	1354.53	0.35
16	Py-1	SEDEX	SEDEX	SEDEX	363.68	1602.47	5564.29	5509.5	26515.5	173.4	1392.41	0.22
17	Py-2	Hyd	Hyd	Hyd	0.13	0.29	0.36	7134.87	34.1	0.26	1.71	0.44
18	Py-2	Hyd	Hyd	Hyd	0.25	0.52	1.01	4816.65	25.3	0.27	3.58	0.48
19	Py-2	Hyd	Hyd	Hyd	29.35	36.19	5.75	3739.56	1346.05	0.42	1.34	0.81
20	Py-2	Hyd	Hyd	Hyd	3.67	4.23	3.82	1649.47	265.33	0.065	0.46	0.86
21	Py-2	Hyd	Hyd	Hyd	4.02	27.16	14.28	93600.59	479.23	9.78	73.24	0.14
22	Py-2	Hyd	Hyd	Hyd	3.89	15.42	4.74	5143.23	415.44	3.79	53.79	0.25
23	Py-2	Hyd	Hyd	Hyd	13.71	28.89	8.69	363.75	1264.78	0.83	9.14	0.47
24	Py-2	Hyd	Hyd	Hyd	8.39	14.28	6.1	4.6	926.21	0.14	0.21	0.58
25	Py-2	Hyd	Hyd	Hyd	8.68	12.98	5	706.57	777.96	0.37	2.04	0.66
26	Py-2	Hyd	Hyd	Hyd	34.16	48.65	11.23	6.07	2211.06	0.14	0.16	0.70
27	Py-2	Hyd	Hyd	Hyd	4.23	1.45	0.66	422.53	92.35	0.032	0.68	2.91
28	Py-3	Hyd	Hyd	Hyd	39.23	150.67	1.82	4.48	300.48	0.033	0.087	0.26
29	Py-3	Hyd	Hyd	Hyd	47.3	294.02	1.34	3.72	173.67	0.03	0.089	0.16
30	Py-3	Hyd	Hyd	Hyd	1313.6	1916.73	5.48	12.86	5790.52	0.15	0.23	0.68
31	Py-3	Hyd	Hyd	Hyd	1585.45	6853.91	0.73	11485.23	14608.37	1.55	1.2	0.23
32	Py-3	SEDEX	SEDEX	Hyd	12.07	486.26	4.84	11.94	890.68	130.73	159.85	0.02
33	Py-3	Hyd	Hyd	Hyd	299.14	523.73	7.6	14.37	1036.34	0.12	0.3	0.57
34	Py-3	SEDEX	SEDEX	SEDEX	4.66	31.12	146.01	22231.42	419.94	14.83	53.57	0.14
35	Py-3	Hyd	Hyd	Hyd	373.82	805.8	0.18	8509.13	20091.28	0.55	0.55	0.46

Our machine-learning models utilize trace element signatures to classify the genesis of pyrite, using algorithms capable of selecting subtle patterns in complex datasets. Our analysis revealed that while the majority of samples from the Zawar deposit are consistently classified by all three models-mostly as hydrothermal in nature and a few as SEDEX- discrepancies occurred in two samples (Table 1).These inconsistencies may result from the unique geochemical signatures of these samples, which possibly exhibit characteristics of both hydrothermal and SEDEX deposits. These samples exhibited overlapping characteristics between SEDEX and hydrothermal deposits, suggesting they may possess transitional features. Such complexities arise from the natural variability and overlapping characteristics of geological formations, indicating that these samples might represent the nature of deposition with features characteristic of both the classes, placing them near the classification boundary. Figure 7b depicts a scatter plot of Co vs. Ni concentrations, with fields of volcanogenic, hydrothermal, magmatic and sedimentary settings (Dora et al., 2020**).** Our classification results are falling within the hydrothermal zone. This also confirms the validity of the machine learning approach and enhances its reliability in predicting complex geological phenomena. This integration highlights the predictive power of machine learning in geochemical classification, aligning well with known geological phenomena, and provides a subtle approach to understanding how specific geochemical environments influence the formation of mineral deposits. This capability enhances the geochemical models by adding a layer of predictive analytics that can dynamically adjust to new data, offering a refinement of our understanding of mineral genesis. The integration of geochemical analyses with machine learning techniques enhances our understanding of the Zawar region's mineralogical processes. By correlating empirical geological

data with analytical predictions, we hope that the application of machine learning in geology may aid in reliable explorations within this field.

CONCLUSIONS

This study aimed to investigate the geological origins of pyrite in the Zawar Pb-Zn deposit using machine learning on trace element data sets (Co, Ni, Cu, Zn, As, Ag, Sb) generated by *in-situ* LA-ICP-MS. The Zawar deposit exhibits three distinct phases of pyrite mineralization, with trace amounts of siderophile (Co, Ni) and chalcophile (Cu, Zn, As, Ag, Sb) elements incorporated into the pyrite structure through lattice substitutions or as inclusions. We applied three ML algorithms-Random Forest (RF), Gradient Boosting (GB), and AdaBoost (AB), to investigate these trace elements which demonstrated high accuracy in classifying the deposits' origins, achieving accuracies of 97.24%, 96.93%, and 96.63%, respectively. Notably, the majority of predictions from all three algorithms indicated a hydrothermal origin for the deposits, with a few samples classified as SEDEX. Our findings strengthen previous research and provide insights into the genesis of the Zawar deposits. The integration of ML-based methods with LA-ICP-MS data, provides insights into the origins of pyrite and demonstrates the potential of machine learning in geological exploration. Future studies could expand on this approach by incorporating additional geochemical data to refine the classification of ore genesis, and to more extent in mineral exploration.

Acknowledgements

We gratefully acknowledge Dr. Prakash Kumar, Director, CSIR–National Geophysical Research Institute (CSIR–NGRI), Hyderabad, for granting permission to undertake this work and for providing the requisite research facilities. We express our profound gratitude to Dr. Biswajit Mandal for his invaluable supervision, guidance, and encouragement throughout the course of this research. We are thankful to Dr. E.V.S.S.K. Babu for his kind assistance and for facilitating access to laboratory resources. We also extend our sincere thanks to Dr. A. Kasi Viswanadham (Vedanta Resources Limited) for his generous field guidance and support. We acknowledge the efforts of earlier researchers and the broader scientific community, whose contributions provided an essential foundation for the present study. Figures and plots were prepared using Matplotlib and ArcGIS.

Author Credit Statement

Sima Gorai: Conceptualization, methodology, data generation, writing original draft; Bulusu Sreenivas: Supervision, validation; review and editing; T Vijaya Kumar: Data acquisition.

Data Availability

Source of the training dataset used in this study is given in the manuscript, in the materials section, while data specific to the Zawar deposit is included in Table 1 of the manuscript. The models were trained and validated using the Scikit-Learn package (https://scikit-learn.org/; Pedregosa et al., 2011). Code for the Random Forest, Gradient Boosting, and AdaBoost algorithms employed in this study is available at https://scikit-learn.org/stable/api/sklearn.ensemble.html. The study-specific scripts used for model training and analysis are available from the corresponding author upon reasonable request.

Compliance with Ethical Standards

There is no conflict of interest associated with this publication and adhere to copyright norms.

REFERENCES

Absar, N. and Sreenivas, B., 2015. Petrology and geochemistry of greywackes of the~ 1.6 Ga Middle Aravalli Supergroup, northwest India: evidence for active margin processes. Int. Geol. Rev., 57(2), 134-158.

Bhattacharya, H. N. and, Bull, S., 2010. Tectono-sedimentary setting of the Paleoproterozoic Zawar Pb–Zn deposits, Rajasthan, India. Precamb. Res., 177(3-4), 323-338.

Breiman, L, 2001. Random forests. Machine learning, 45, 5-32.

Chao, W., Ye, H., Tang, X., Zhang, Z. and Wang, H., 2023. Textural, trace element, and sulfur isotope analyses of pyrite from the Yindongpo deposit, East Qinling Orogen: Implications for gold mineralization. Ore Geol. Rev., 105796.

Dalai, B. and Kumar, P., 2026. Detection and waveform-based source imaging of small-magnitude events using unsupervised machine learning and grouped time-reversals. Act. Geophys., 74(1), 71.

Deb, M., Thorpe, R. I., Cumming, G. L. and Wagner, P. A., 1989. Age, source and stratigraphic implications of Pb isotope data for conformable, sediment-hosted, base metal deposits in the Proterozoic Aravalli-Delhi orogenic belt, northwestern India. Precamb. Res., 43(1-2), 1-22.

Deditius, A. P., Utsunomiya, S., Renock, D., Ewing, R. C., Ramana, C. V., Becker, U. and Kesler, S. E., 2008. A proposed new type of arsenian pyrite: Composition, nanostructure and geological significance. Geochim. Cosmochim. Acta, 72(12), 2919-2933

Deditius, A. P., Reich, M., Kesler, S. E., Utsunomiya, S., Chryssoulis, S. L., Walshe, J. and Ewing, R. C., 2014. The coupled geochemistry of Au and As in pyrite from hydrothermal ore deposits. Geochim. Cosmochim. Acta, 140, 644-670. .

Dora, M. L., Upadhyay, D., Randive, K. R., Shareef, M., Baswani, S. R. and Ranjan, S., 2020. Trace element geochemistry of magnetite and pyrite and sulfur isotope geochemistry of pyrite and barite from the Thanewasna Cu-(Au) deposit, western Bastar Craton, central India: Implication for ore genesis. Ore Geol. Rev., 117, 103262.

Fareeduddin, Venkatesh, B. R., Hanumantha, R., Golani, P. R., Sharma, B. B. and Neogi, S., 2014. Petrology and stable isotope (S, C, O) studies of selected sedimenthosted basemetal

ore deposits in the proterozoic Aravalli-Delhi Fold Belt, Rajasthan. J. Geol. Soc. India., 83, 119-141.

Freund, Y. and Schapire, R. E., 1997. A decision-theoretic generalization of on-line learning and an application to boosting. J. Comp. Syst. Sci., 55(1), 119-139.

Friedman, J. H., 2001. Greedy Function Approximation: A Gradient Boosting Machine. The Annals of Statistics, 29(5), 1189-1232.

Gadd, M. G., Layton-Matthews, D., Peter, J. M. and Paradis, S. J., 2016. The world-class Howard's Pass SEDEX Zn-Pb district, Selwyn Basin, Yukon. Part I: trace element compositions of pyrite record input of hydrothermal, diagenetic, and metamorphic fluids to mineralization. Min. Dep., 51, 319-342.

Ghosh, S., 1957. Lead-zinc-silver mineralisation of Zawar, Rajasthan. Geol. Mining and Metallurgical Soc. Ind. Quarterly J., 29, 55-64.

Goldschmidt, V. M., 1937. The principles of distribution of chemical elements in minerals and rocks. The seventh Hugo Müller Lecture, delivered before the Chemical Society on March 17th, 1937. J. Chem. Soc. (Resumed), 655-673.

Gorai, S., Rani, N., Kumar, T. V. and Sreenivas, B., 2024. Integrated Remote Sensing and Petrographic Guide to Delineate the Hydrothermal Alteration Zones Along the Phyllites of the Main Zawar Fold, Rajasthan, India. J. Ind. Soc. Remote Sensing, 1-14.

Gorai, S., Dalai, B., Kumar, T. V. and, Sreenivas, B., 2025 a. Machine learning applications in trace element analysis: decoding the origin of galena in the Zawar Zn-Pb Deposit, India. Earth Sci. Informatics, 18(3), 1-19.

Gorai, S., Dalai, B., Vijaya Kumar, T., and, Sreenivas, B., 2025b. Integration of Machine Learning with In-Situ LA-ICP-MS Trace Element Analysis: Multi-Classification Approach Reveals the Hydrothermal Origin of Sphalerite in the Zawar Zn-Pb Deposit, Rajasthan, India. J. Geol. Soc. India., 101(8), 1235-1246.

Gorai, S., Sreenivas, B. and, Kumar T, V., 2026. Acanthite (Ag_2S) as an indicator of late-stage silver mineralization in the Zawar Pb─ Zn system, Rajasthan, India: Insights from Scanning Electron Microscopy (SEM) and Energy-Dispersive X-ray Spectroscopy (EDS) microtextural studies. J. Indian Geophy. Union, 30(2), 142-147.

Grant, H. L., Hannington, M. D., Petersen, S., Frische, M. and Fuchs, S. H., 2018. Constraints on the behavior of trace elements in the actively-forming TAG deposit, Mid-Atlantic Ridge, based on LA-ICP-MS analyses of pyrite. Chem. Geol., 498, 45-71.

Hoefs, J., 1973. A contribution on the isotope geochemistry of carbon in igneous rocks. Contributions to Min. and Petrology, 41, 277-300.

Huston, D. L., Sie, S. H., Suter, G. F., Cooke, D. R. and Both, R. A., 1995. Trace elements in sulfide minerals from eastern Australian volcanic-hosted massive sulfide deposits; Part I, Proton microprobe analyses of pyrite, chalcopyrite, and sphalerite, and Part II, Selenium levels in pyrite; comparison with delta 34 S values and implications for the source of sulfur in volcanogenic hydrothermal systems. Econ. Geol., 90(5), 1167-1196.

Jansson, N. F. and Liu, W., 2020. Controls on cobalt and nickel distribution in hydrothermal sulphide deposits in Bergslagen, Sweden-constraints from solubility modelling. Gff, 142(2), 87-95.

Keith, M., Smith, D. J., Jenkin, G. R., Holwell, D. A. and Dye, M. D., 2018. A review of Te and Se systematics in hydrothermal pyrite from precious metal deposits: Insights into ore-forming processes. Ore Geol. Rev., 96, 269-282.

Knorsch, M., Nadoll, P. and Klemd, R., 2020. Trace elements and textures of hydrothermal sphalerite and pyrite in Upper Permian (Zechstein) carbonates of the North German Basin. J. Geochem. Exp., 209, 106416.

Li, H., Zhu, D. P., Algeo, T. J., Li, M., Jiang, W. C., Chen, S. F. and Elatikpo, S. M., 2023. Pyrite trace element and S-Pb isotopic evidence for contrasting sources of metals and ligands during superimposed hydrothermal events in the Dongping gold deposit, North China. Min. Deposita, 58(2), 337-358.

Lin, H. T., Zhao, S. R., Gao, L. B. and Zhao, X. F., 2022. Geochronology, stable isotopes and pyrite chemistry of the Cangzhuyu gold deposit in the North China Craton: Implications for gold metallogeny of Xiaoqinling. Ore Geol. Rev., 144, 104812.

Liu, Z., Mao, X., Deng, H., Li, B., Zhang, S., Lai, J. and Shang, Q., 2018. Hydrothermal processes at the Axi epithermal Au deposit, western Tianshan: insights from geochemical effects of alteration, mineralization and trace elements in pyrite. Ore Geol. Rev., 102, 368-385.

McKenzie, N. R., Hughes, N. C., Myrow, P. M., Banerjee, D. M., Deb, M. and Planavsky, N. J., 2013. New age constraints for the Proterozoic Aravalli–Delhi successions of India and their implications. Precamb. Res., 238, 120-128.

Meng, L., Lan, C., Zhan, Q., Wu, Q. and Zhao, T., 2022. Origin of the Shanggong gold deposit, the southern margin of the North China Craton: Constraints from Rb-Sr ages of sericite, and trace elements and sulfur isotope of pyrite. Ore Geol. Rev., 142, 104728.

Mookherjee, A, 1964. The geology of the Zawar lead-zinc mine, Rajasthan, India. Econ. Geol., 59(4), 656-677.

Mukherjee, A. and Bhattacharya, H. N, 2021. Mixed siliciclastic–carbonate debrite–turbidite deposits in Paleoproterozoic Aravalli Supergroup, Zawar, Rajasthan, India: Implications on the Aravalli Basin evolution. J. Earth Syst. Sci., 130(3), 1-16.

Mukherjee, I. and Large, R., 2017. Application of pyrite trace element chemistry to exploration for SEDEX style Zn-Pb deposits: McArthur Basin, Northern Territory, Australia. Ore Geol. Rev., 81, 1249-1270.

Nie, X., Wan, Q., Hochella Jr, M. F., Luo, S., Yang, M., Li, S. and Yu, W., 2023. Interfacial adsorption of gold nanoparticles on arsenian pyrite: New insights for the transport and deposition of gold nanoparticles. Chem. Geol., 640, 121747.

Pedregosa, F., Varoquaux, G., Gramfort, A., Michel, V., Thirion, B., Grisel, O. and Duchesnay, É., 2011. Scikit-learn: Machine learning in Python. J. Machine Learning Res., 12(Oct), 2825-2830.

Qian, G., Brugger, J., Testemale, D., Skinner, W. and Pring, A., 2013. Formation of As (II)-pyrite during experimental replacement of magnetite under hydrothermal conditions. Geochim. Cosmochim. Acta, 100, 1-10.

Reich, M., Kesler, S. E., Utsunomiya, S., Palenik, C. S., Chryssoulis, S. L. and Ewing, R. C., 2005. Solubility of gold in arsenian pyrite. Geochim. Cosmochim. Acta, 69(11), 2781-2796.

Roy, A. B., 1995. Geometry and evolution of superposed folding in the Zawar lead-zinc mineralized belt, Rajasthan. Proceedings of the Indian Academy of Sciences-Earth and Planetary Sciences, 104(3), 349-37.

Roy, A. B., 2000. Geology of the Palaeoproterozoic Aravalli Supergroup of Rajasthan and northern Gujarat. Crustal evolution and metallogeny in the northwestern Indian shield, 87-114.

Roy, A. B., Paliwal, B. S., Shekhawat, S. S., Nagori, D. K., Golani, P. R. and Bejarniya, B. R., 1988. Stratigraphy of the Aravalli Sypergroup in the type area. Geol. Soc. Ind. Mem, 121-138

Sachan, H. K., 1993. Early-replacement dolomitization and deep-burial modification and stabilization: A case study from the late precambrian of the Zawar area, Rajasthan (India). Carbonates and evaporites, 8, 191-198.

Sarkar, S. C. and Banerjee, D., 2004. Carbonate-hosted lead-zinc deposits of Zawar, Rajasthan, in the context of the world scenario. Sediment-hosted lead-zinc sulphide deposits. Narosa Publishing House, New Delhi, India, 328-349.

Song, K. R., Tang, L., Zhang, S. T., Santosh, M., Spencer, C. J., Zhao, Y. and Sun, Y. Q., 2019. Genesis of the Bianjiadayuan Pb–Zn polymetallic deposit, Inner Mongolia, China: Constraints from in-situ sulfur isotope and trace element geochemistry of pyrite. Geosci. Front., 10(5), 1863-1877.

Talluri, J. K., Pandalai, H. S. and Jadhav G. N., 2000. Fluid chemistry and depositional mechanism of the epigenetic, discordant ores of the proterozoic, carbonate-hosted, Zawarmala Pb-Zn Deposit, Udaipur District, India. Econ. Geol., 95(7), 1505-1525.

Wu, Q., Zhao, T. P., Chen, W. T., Gao, X. Y., Meng, L. and Qiu, W. J., 2021. Origin of the Qiyugou gold deposit in the southern margin of the North China Craton: Insights from trace elements of pyrite and mineralogy of Bi-minerals. Ore Geol. Rev., 133, 104085.

Xie, J., Tang, D., Qian, L., Wang, Y. and Sun, W., 2020. Geochemistry of sulfide minerals from skarn Cu (Au) deposits in the Fenghuangshan ore field, Tongling, eastern China: Insights into ore-forming process. Ore Geol. Rev., 122, 103537.

Xiong, S. F., Jiang, S. Y., Zhao, K. D., Ma, Y., Chen, Q. Z and Jiang, M. R., 2019. Gold distribution and source of the J4 gold-bearing breccia pipe in the Qiyugou district, North China Craton: Constraints from ore mineralogy and in situ analysis of trace elements and S-Pb isotopes. Ore Geol. Rev., 105, 514-536.

Zhang, J., Deng, J., Chen, H. Y., Yang, L. Q., Cooke, D., Danyushevsky, L. and Gong, Q. J., 2014. LA-ICP-MS trace element analysis of pyrite from the Chang'an gold deposit, Sanjiang region, China: Implication for ore-forming process. Gond. Res., 26(2), 557-575.

Zhao, S. R., Li, Z. K., Zhao, X. F. and Li, J. W., 2021. Genesis of the Hongtuling Au-Mo deposit in the southern North China Craton revealed from pyrite trace element compositions and S-Pb isotopes. Ore Geol. Rev., 131, 104017.

Received on: 16-12-2025; Revised on: 17-05-2026; Accepted on: 25-05-2026

J. Ind. Geophys. Union, 30(4) (2026), 305-311
https://doi.org/10.71122/JIGU.30(4)2026.0029

Tree ring-width study of conifers from the western Himalaya (India) and its relationship with climate fluctuations

Somaru Ram[1*], N. Bharti[1], V.S. Parvathy[1], B. Preethi[1] and Manoj K. Srivastava[2]
[1]Centre for Climate Change Research, Indian Institute of Tropical Meteorology,
Ministry of Earth Sciences, Pune - 411008
[2] Department of Geophysics, Banaras Hindu University, Varanasi-221005, India
*Corresponding author: somaru@tropmet.res.in

ABSTRACT

Tree-ring width studies have been carried out in different locations of the western Himalayas in relation to climate variability. The significant relationship between tree ring chronology and monthly climate variable, indicates that rising potential evapotranspiration over the region, may lead to insufficient moisture supply, resulting in increased moisture stress conditions over the region for trees, whereas, increased rainfall and frequent wet day frequency may work as a booster to sufficient moisture supply which promotes tree growth during the subsequent growing season. The study highlights an important role of spring season moisture availability in the development of annual ring width. The analysis of the relationship between tree growth and climate shows that the potential evapotranspiration (PET) over the region, has a stronger limiting impact on the development of tree growth than the temperature.

Keywords: Western Himalaya, Tree ring-width, Temperature**,** Potential evapotranspiration, Rainfall, Wet day frequency

INTRODUCTION

The mountain ranges across the Himalayan region form the highest topography barrier on the earth, playing a crucial role in controlling the monsoon rainfall across the Asian region. This region shows the vast diversity of climate at short distances. Particularly in terms of rainfall, it showed high variability in rainfall due to complex and diverse mountainous terrain. In contrast, temperature pattern trend, indicates a strong spatial coherence across the region (Yadav et al., 1999)

However, to understand the long-term climate fluctuations across the Himalaya, several dendroclimatic studies have been performed in absence of observed climatic data over the region (Hughes, 1992; Pant et al., 1998; Borgaonkar et al., 1999; Chaudhary et al., 1999; Cook et al., 2003, 2010; Yadav et al., 2004; Ram and Borgaonkar, 2013, 2014, 2016, 2017; Singh et al., 2017; Shah et al. 2018; Ram et al., 2018, 2019, 2020, 2024). They showed that the tree growth from the western Himalayas, have a very good potential to extend the climatic data before the instrumental period, indicating the significant relationship of tree growth with various climatic parameters in the Himalayan region. Moreover, Borgaonkar et al. (2011) have shown that the warmth winter has significant role in boosting of soil moisture for the growth of the trees. Singh and Yadav (2000, 2005) have further revealed the strong relationship between tree growth and warmth winter. Similarly, Cook et al. (2010) reported that the trees growth is more influenced by the soil moisture availability.

Nevertheless, most of the dendroclimatic studies over the Himalaya have been concentrated based on rainfall and temperature relationship with tree growth. In the present study, an attempt is made to understand the influence of regional climate on tree growth across the mountainous region utilizing several meteorological parameters (e.g., rainfall, wet day frequency, temperature, and potential evapotranspiration) and examining their impacts on tree growth processes. This study could be useful in identifying the dominant climate that influences tree growth, providing a better understanding of climate affecting tree growth development.

METHODOLOGY

Tree ring-width data

Cedrus deodara tree ring-width data from the Bhairoghati (Ram, 2022) and Jangla, located in the western Himalaya near the Gangotri region (Borgaonkar et al., 2009; Ram et al., 2018), have been analysed to examine the relation with climate (Figure 1), which are sourced from International tree ring data bank (ITRDB), (http://www.ncdc. noaa.gov/paleo/ treering.html/). Dating errors in growth rings were verified using the standard cross-dating techniques with the help of specialized software (Stoke and Smiley, 1968; Holmes, 1983). Tree ring-width data were processed using the signal-free regional curve standardization technique (Cook et al., 2011) to preserve low- frequency climate signals in the series. The RCS_Sig Free software was used (Melvin and Briffia, 2008) to produce signal-free functions during standardizing. The resulting detrended series were averaged by using the bi-weight robust mean method to compute a site mean chronology. The Bhairoghati chronology extends to the period 1738-2004, while the Jangla chronology from 1538-2004 (Figure 1).

Climatic data

Due to the sparse distribution of meteorological stations in and around the sampling area, monthly data on rainfall, temperature, wet day frequency, and potential

evapotranspiration of Shimla region from 1901-2002, have been used to analyze climate fluctuations in the region. These data were obtained from the India Water Portal, as provided by India Meteorological Department (IMD). Mean monthly variation in temperature, potential evapotranspiration, rainfall, and wet day frequency over western Himalaya during 1901-2002 are presented in Figure 2. It is to be noted that, the complex hilly terrain in the studied region can introduce complications in the understanding of climate change and its variability.

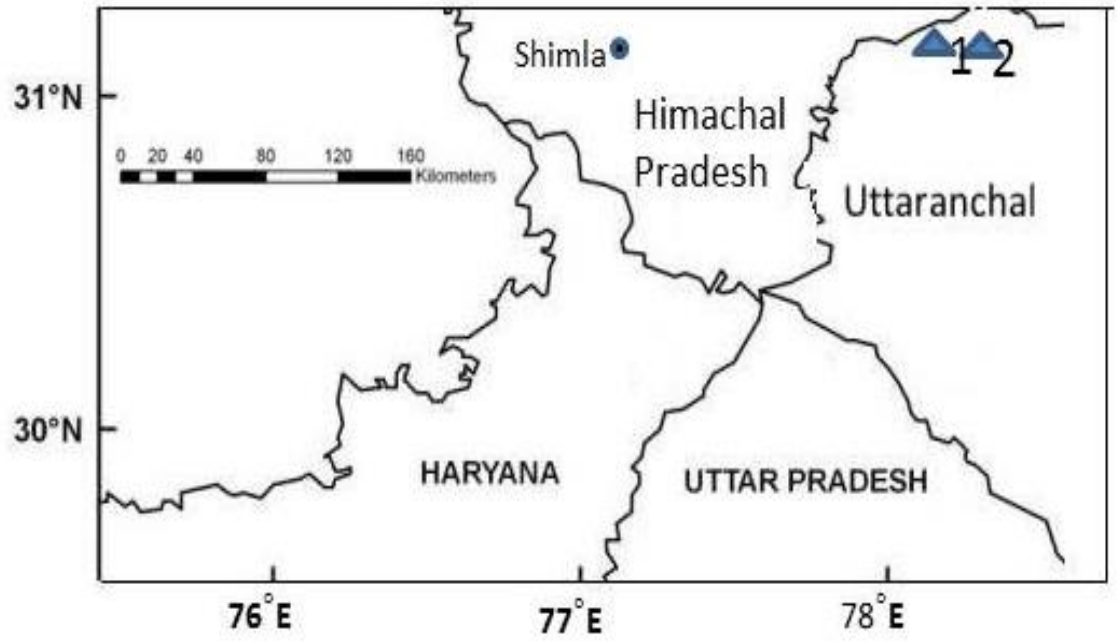

Figure 1. Map showing the sampling site in study area. ▲1: Bhairoghati; ▲2: Jangla. Location of Shimla district is also shown.

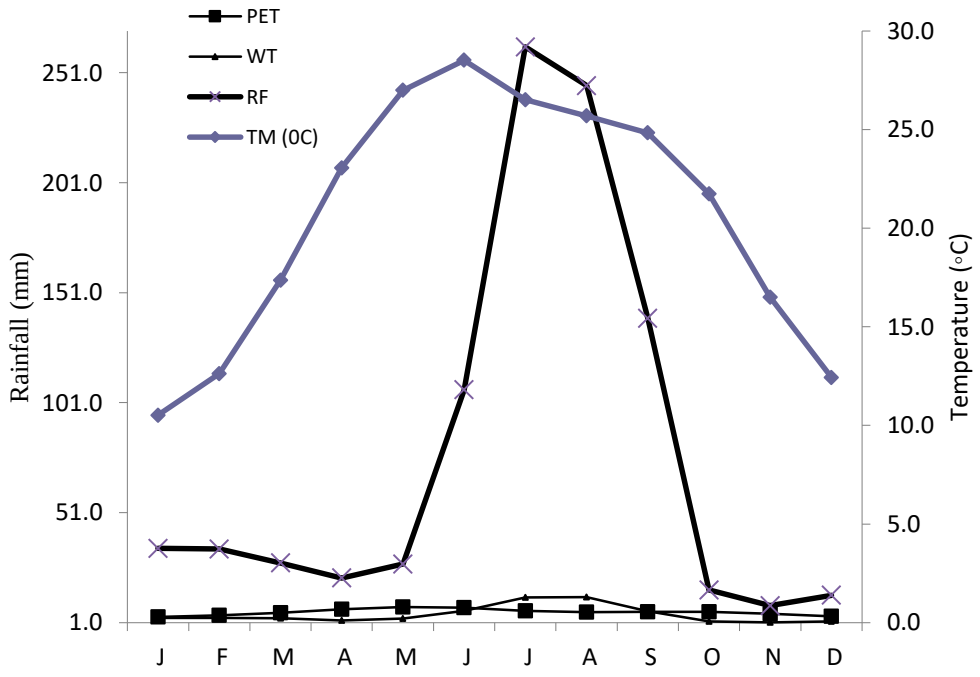

Figure 2. Mean monthly variations in temperature: TM(°C), potential evapotranspiration: PET (mm), rainfall: RF(mm), and wet day frequency: WT(per day) over the western Himalaya during 1901-2002.

RESULTS

Climatic data

Averaged monthly variations of rainfall (RF), mean temperature (TM), Potential evapotranspiration (PET), and wet day were shown are Figure 2. June is the hottest months with an average temperature 28.5°C, while July is the wettest time receiving 262.7 mm of precipitation (Figure 2). Similarly, the maximum wet day frequency occurs in the month of August.

The highest PET is observed in May, whereas the lowest occurs in January across the region.

Tree-ring chronology

Two sites (Jangla and Bhairoghati) chronologies along with tree core numbers are shown in Figure 3. They are highly correlated with each other. The correlation coefficient is 0.55 during 1738-2004.

The series correlation reveals good agreement of the site chronologies. Based on this strong correlation, a regional chronology has been developed by merging the two site chronologies, which exhibits the spatially coherence mode of variation, influenced by climate forcing (Figure 3, bottom)

Tree growth-climate relationships

Correlation analysis between ring-width index chronologies and climatic variables (monthly mean temperature, rainfall, potential evapotranspiration, and wed day frequency) is conducted on monthly basis, using DendroClim 2002 programme (Biondi and Waikul, 2004) that covers this period from 1901-2002 for each site and regional chronology. The windows start from previous year October (ending of growing season) to current year October (ceasing of growing season) are used to assess the impact of climate on tree growth. Dashed lines in the Figures (4a-d; 5a-d; 6a-d) show significance at the 5% level.

DISCUSSION AND CONCLUSIONS

To investigate the relationship between tree growth and the climate, the correlation analysis between tree ring-width index chronology and regional climate for the common period, was performed using the program DendroClim 2002 (Biondi and Waikul, 2004). A 13-month dendroclimatic window, extending from previous year October to current year October, was considered to evaluate tree growth-climate relationship (Figures 4a-d; 5a-d; and 6a-d). The dotted lines reveal the significant relationship between the tree growth and climate.

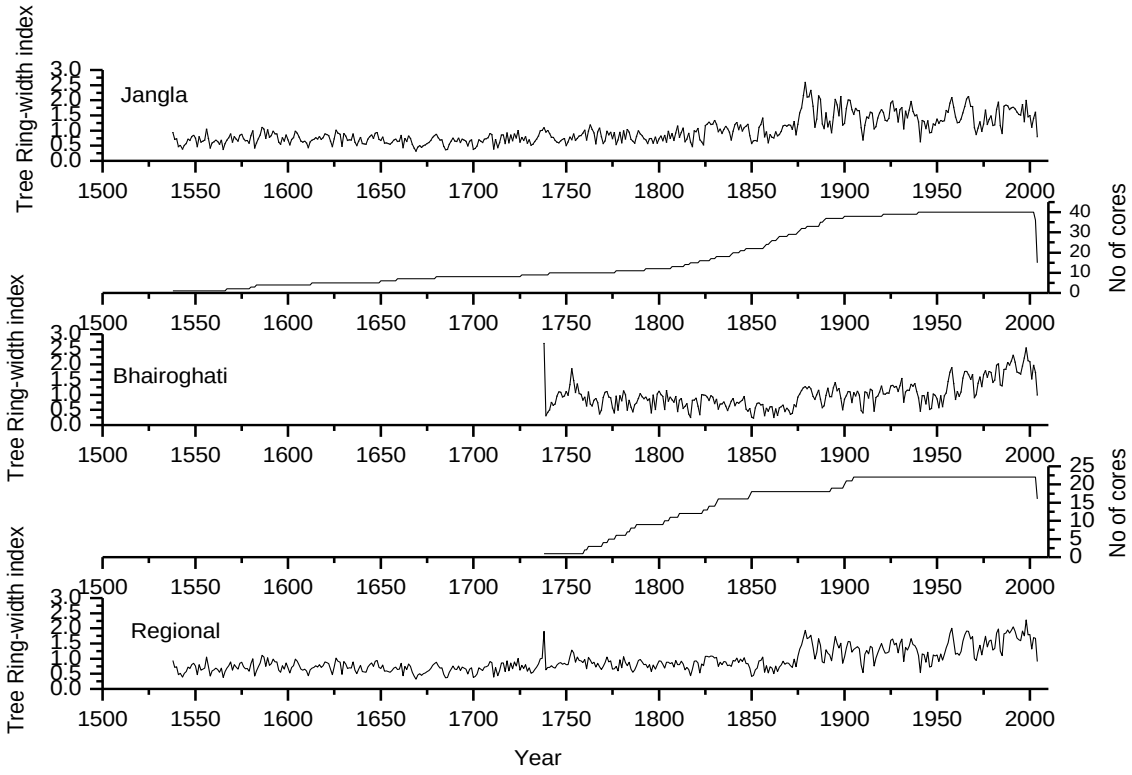

Figure 3. Tree ring-width index for different sites (Jangla, Bharioghati) and, regional chronology of the western Himalaya based on core sample studied.

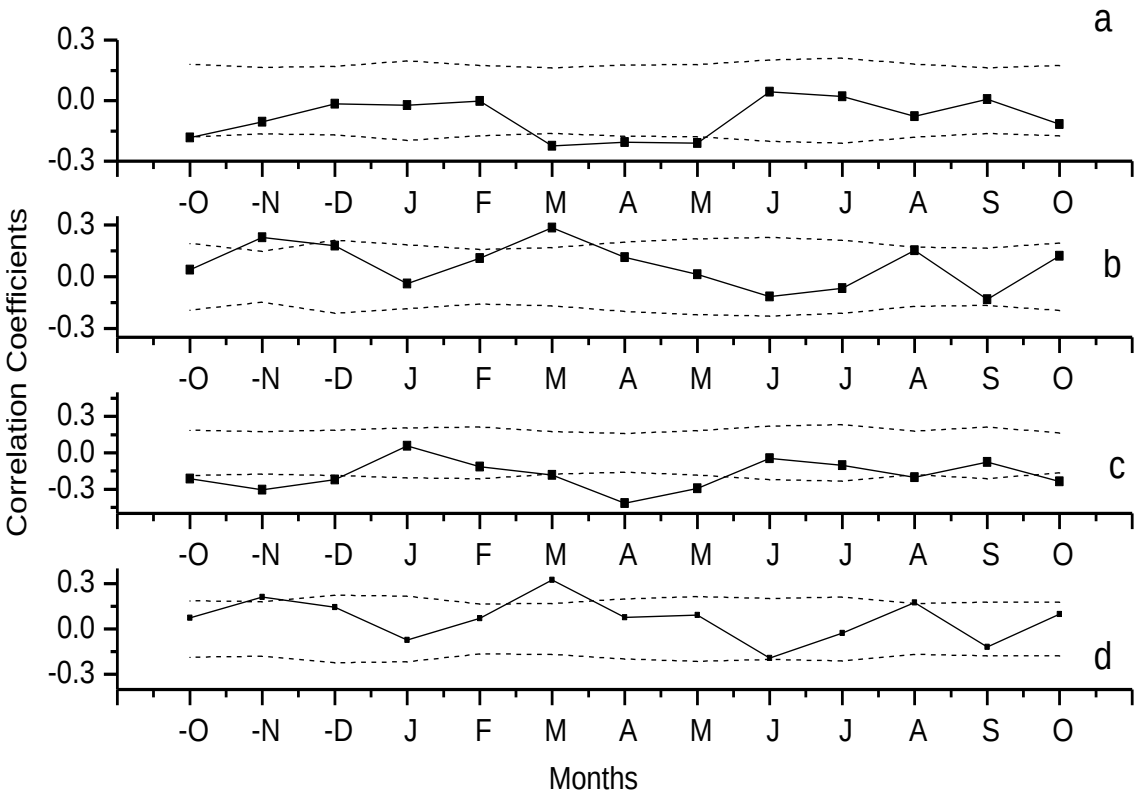

Figure 4. Correlation of tree ring chronology (Jangla) with (**a**) average monthly temperature, (**b**) rainfall, (**c**) potential evapotranspiration and, (**d**) wet day frequency. Dotted lines show the significance level at 5%.

At the Jangla site, the PET and temperature during spring season (March to May) were found to have significant negative influence on the tree growth (Figures 4a and 4c). This suggests that increasing PET and temperature over the region may have enhanced the transpiration and evaporation, which results into moisture stress condition that is not conducive to tree growth (Yadav et al., 1997, 2009; Borgaonkar et al., 1999; Ram et al., 2018). Furthermore, Ram and Borgaonkar (2014) also showed that the higher-temperatures above the normal during spring season, was harmful in developing of tree growth. In contrast, wet day frequency and rainfall during March month showed a significant relationship with tree growth (Figures 4b and 4d). These findings suggest that a slight increases in wet day frequency and rainfall prior to the starting of growing season, may work as booster in preserving soil moisture in the root zone of the tree and thereby promoting and enhancing development of tree growth in the region (Cook et al., 2010; Ram and Borgaonkar, 2016, 2017).

At the Bhairoghati site, PET during summer season from March to current year July, was found to have significant influence on the trees growth over the region (Figure 5c). The relationship indicates that increasing PET during summer and prior year October to November, may enhance the insufficient moisture supply to tree growth during growing season, which is consistence with finding of Ram and Borgaonkar (2014). But in case of the temperature, tree growth does not show a strong association like PET. PET is well associated with tree growth as compared to temperature (Figure 5c). PET is more reliable indicator of moisture that impacts tree growth. Ram and Borgaonkar (2016) reported that higher temperatures from March to May, may contribute inadequate moisture supply over the region, causing severe moisture stress condition for the tree growth development.

An increase in rainfall, and wet day frequency during early spring season (March to April) (Figures 5b and d), may help in promoting tree growth during the onset of growth as also evidenced by Borgaonkar et al. (1999). The relationship suggests that the moisture availability before the start of growing season, might woks as booster to the following year tree growth. In an earlier study, Pant and Borgaonkar (1983) also demonstrated that the preserved moisture before the start of growing plays a significant role during subsequent year tree growth.

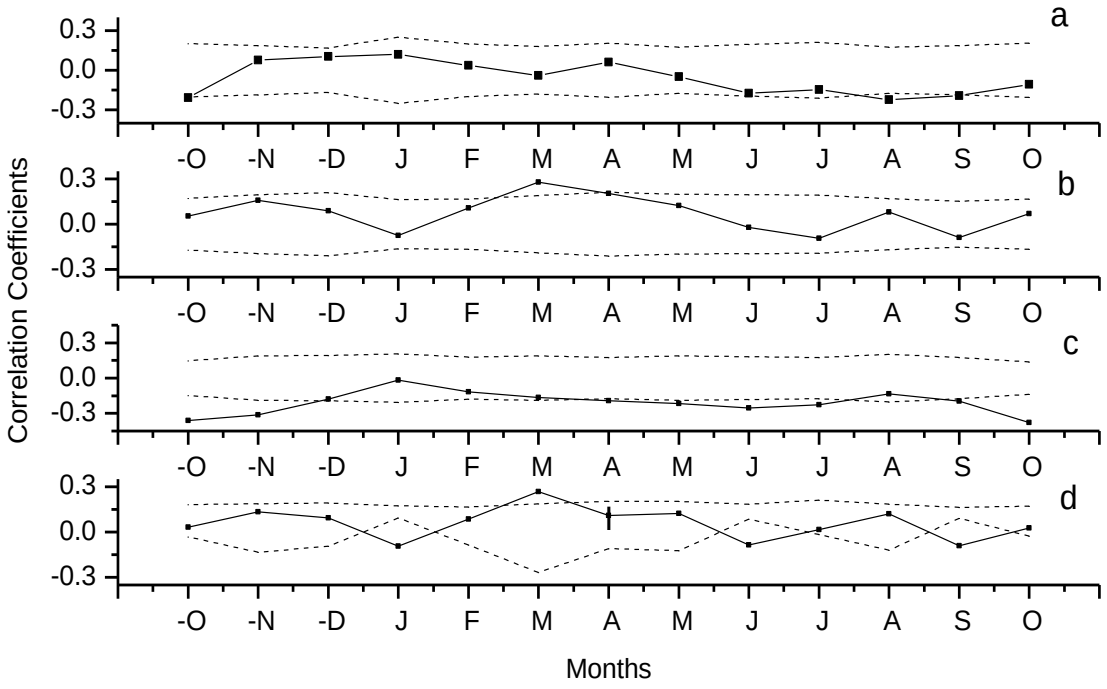

Figure 5. Correlation of tree ring chronology (Bhairoghati) with **(a**) average monthly temperature, (**b**) rainfall, (**c)** potential evapotranspiration and, (**d)** wet day frequency. Dotted lines show the significance level at 5%.

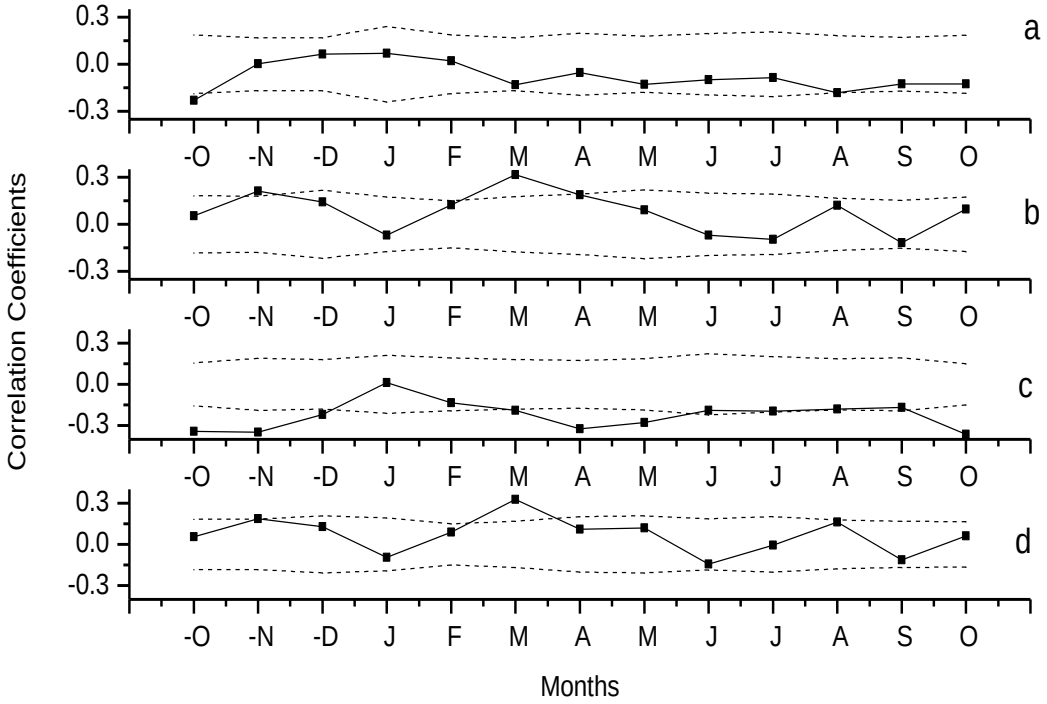

Figure 6. Correlation of regional tree ring chronology, with (**a**) average monthly temperature, (**b**) rainfall, (**c**) potential evapotranspiration and, (**d**) wet day frequency. Dotted lines show the significance level at 5%.

In case of regional chronology, PET from March to October and prior year October to November over the region shows the negative impact on tree growth, while PET during June to September is barely significant but negatively correlated with tree growth (Figure 6c**).** The significant correlation coefficients between tree ring chronology and monthly climate suggest that increased potential evapotranspiration during summer and prior year October to November over the studied region may turn insufficient moisture availability (Ram and Borgaonkar, 2014), leading to severe moisture stress condition at root zone of the trees. However, increasing rainfall and wet day frequency during spring season, may push moisture for the subsequent growing season of tree growth (Figures 6b and d). It indicates that the spring season moisture availability, plays an important role in developing of annual ring-width patterns, as also supported by Singh and Yadav (2005) and Ram and Borgaonkar (2017). Overall, this finding suggests that a spring season climate is more dominant in development of tree growth over the studied region.

The study has shown that the rainfall, temperature, potential evapotraspiration, and wet day frequency are found equally important in influencing of tree growth. In Particular, the climatic variables of PET and wet day frequency, appear to explain the variations in tree growth beyond the effects of rainfall and temperature. It suggests that the well distributed network of tree ring chronologies across the region may be used to reconstruct past PET and wet day frequency. Such reconstruction can improve our understanding of long-term climate variability / change over western Himalaya at both local and regional scale.

Further, this study highlights that the tree ring data from the Himalaya, has a significant potential for investigating the past climate variability / change. This study is valuable to the society, forest management, water resources, and estimating the wet and dry periods. Therefore, developing long-term climate proxy records from diverse locations of the Himalaya can greatly improve our understanding regarding climate variability / change at both local and regional scale over the past several centuries.

ACKNOWLEDGEMENTS

The authors are grateful to the Director of IITM, Pune for his kind support and providing the infrastructure facilities. We are thankful to India water portal (IWP) and ITRDB for making availability of the climate data and tree ring-width data respectively on the website. Author MKS is thankful to BHU IOE for the support.

Author Credit Statement

Somaru Ram prepared the manuscript with the help and discussion with Manoj K. Srivastava; N. Bharti: manuscript correction; V.S. Parvathy: Figure correction; B. Preethi: checking

Data availability

Data can be downloaded from India water Portal website. Data is available on request

Compliance with ethical standards

The author declare that they have no conflict of interest and adhere to copy right norms

References

Biondi, F. and Waikul, K., 2004. DENDROCLIM 2002: AC++ program for statistical calibration of climate signals in tree-ring chronologies. Comput. Geosci., 30, 303-311.

Borgaonkar, H.P., Pant, G.B. and Rupa Kumar, K., 1999. Tree-ring chronologies from western Himalaya and their dendroclimatic potential. IAWA, 20 (3), 295-309.

Borgaonkar, H.P., Ram, S. and Sikder, A. B., 2009. Assessment of tree-ring analysis of high- elevation Cedrus deodara D. Don from western Himalaya (India) in relation to climate and glacier fluctuations. Dendrochronologia, 27, 59-69.

Borgaonkar, H.P., Sikder, A.B. and Ram, S., 2011. High altitude forest sensitivity to the recent warming: A tree-ring analysis of conifers from western Himalaya. Quat. Int., 236, 158-166.

Chaudhary, V., Bhattacharyya, A. and Yadav, R.R., 1999. Tree-ring studies in eastern Himalaya. IAWA, 20, 317-324.

Cook, E.R., Krusic, P.J. and Jones, P.D., 2003. Dendroclimatic signal in long tree ring chronologies from Himalaya of Nepal. Int. J. Climatol., 23, 707-732.

Cook, E.R., Anchukaitis, K.J., Buckley, B.M., D'Arrigo, R.D., Jacoby, G.C. and Wright, W. E., 2010. Asian Monsoon failure and megadrought during the last millennium. Science, 328, 486-489.

Cook , E.R., Krusic, P.J., Holmes, R.H. and Peters, K., 2011. Program ARSTAN Ver.44a, www.ldeo.columbia.edu/tree-ring-laboratory.

Holmes, R.L., 1983. Computer assisted quality control in tree-ring dating and measurement. Tree-ring Bull., 44, 69-75.

Hughes, M.K., 1992. Dendroclimatic evidence from the western Himalaya. In: R.S. Bradley & P.D. Jones, editors, Climate since AD1500, London: Routledge

Melvin, T,M. and Briffia, K.R., 2008. A Signal free approach to dendroclimatic standardization. Dendrochronologia, 26, 71-86.

Pant, G.B. and Borgaonkar, H.P., 1983. Growth rings of teak trees and regional climatology. In: Environmental Management (Eds L.R. Singh RC Tiwari and RP Srivastava) The Allahabad Geographical Society Allahabad, India, 153-158.

Pant, G.B., Borgaonkar, H.P. and Rupakumar, K., 1998. Climatic signals from tree-rings: A dendroclimatic investigation of Himalayan spruce (*Picea smithiana*) Him. Geol., 19 **(**2), 65-73.

Ram, S., 2022. Dendroclimatic analysis of western Himalayan tree growth in India, Curr. Sci., 122, 769-771

Ram. S. and Borgaonkar, H.P., 2013. Growth response of conifer trees from high altitude region of Western Himalaya. Curr. Sci., 105 (2), 225-231.

Ram, S. and Borgaonkar, H.P., 2014. Tree-ring analysis over the western Himalaya and its long-term association with vapor pressure and potential evapotranspiration. Dendrochronologia, 32, 32-38.

Ram, S. and Borgaonkar, H.P., 2016. Reconstruction of heat index based on tree-ring width records of western Himalaya in India. Dendrochronologia, 40, 64-71.

Ram, S. and Borgaonkar, H.P., 2017. Moisture index during the last two centuries inferred from tree growth in the western Himalaya. Curr. Sci., 112 (12), 2453-2455.

Ram, S., Singh, H.N., Yadav, R.K. and Srivastava, M.K., 2018. Climatic response of Cedrus deodara tree-ring width records from Jangla region of western Himalaya in India: A case study. J. Indian Geophys. Union, 22, 6, 632-639.

Ram, S., Singh, H.N., Yadav, R.K. and Srivastava, M.K., 2019. Tree rings-width study of western Himalaya and their linkage with Boreal spring vapor pressure and wet day frequency. J. Ind. Acad. Wood Science https://doi.org/10.1007/s13196- 019-00243-y

Ram, S., Singh, H.N., Yadav, R.K., Nandargi, S.S. and Srivastava, M.K., 2020. Reconstruction of potential evapotranspiration over western Himalaya in India based on tree ring-width records. Quat. Int., 547, 145-151,

Ram S, Pandey, U. and Srivastava, M.K., 2024. Tree ring oxygen isotope ($\delta^{18}O$) variations from western Himalaya and it linkage with vapor pressure and runoff water in India. J. Ind. Acad. Wood Science, 21, 155-161, DOI:10.1007/s13196-024- 00340-7

Singh, J. and Yadav, R.R., 2000. Tree-ring indications of recent glacier fluctuations in Gangotri, western Himalaya. Curr. Sci., 79, 1598-1601.

Singh, J. and Yadav, R.R., 2005. Spring precipitation variations over the western Himalaya, India, since A.D. 1731 as deduced from tree-rings. J. Geophy. Res., 110, doi:10.1029/2004JD004855.

Singh, V., Yadav, R. R., Gupta, A.K., Kotlia, B.S., Singh, J., Yadav, A.K., Singh, A.K. and Misra, K.G., 2017. Tree-ring droughts records from Kishtwar, Jammu and Kashmir, northwest Himalaya, India. Quat. Int., 444, 53-64.

Shah, S.K., Pandey, U. and Mehrotra, N., 2018. Precipitation reconstruction for the Lidder Valley, Kashmir Himalaya using tree-rings of Cedrus deodara. Int. J. Climatol., 38, e758-e773.

Stokes, M.A. and Smiley, T.L., 1968. An introduction to tree-ring dating Univ Chicago Press Chicago.

Yadav, R.R., Park, W-K. and Bhattacharyya, A., 1997. Dendroclimatic Reconstruction of April-May temperature fluctuations in the western Himalaya of India since A.D. 1698. Quat. Res., 48, 187-191.

Yadav, R.R., Park, W.-K. and Bhattacharyya, A., 1999. Spring temperature variations in western Himalaya, India, as reconstructed from tree-rings: AD 1390-1987. Holocene 9, 85- 90.

Yadav, R.R., Park, W-K., Singh, J. and Dubey, B., 2004. Do the western Himalayas defy global warming? Geophys. Res. Lett., 31, L17201, doi:10.1029/2004GL020201

Yadav, R.R., Braeuning, A. and Singh, J., 2009. Tree ring inferred summer temperature variations over the last millennium in western Himalaya. Climate Dynamic, DOI 10.1007/s00382-009- 0719-0.

Received on: 27-9-2025; Revised on: 1-4-2026; Accepted on: 27-05-2026

J. Ind. Geophys. Union, 30(4) (2026), 312-321
https://doi.org/10.71122/JIGU.30(4)2026.0030

Study of air quality and aerosol over Indian region: A case study from COVID-19 period

Km Swarnima[1] and Sanjay Kumar[1&2*]
[1]Department of Physics, Nehru Gram Bharti University, Kotwa-Jamunipur-Dubawal, Prayagraj-221505, India
[2*]Department of Physics, Deen Dayal Upadhyaya Gorakhpur University, Gorakhpur-273009, India
[*]Corresponding author: sanjay.skitvns@gmail.com

ABSTRACT

Pandemic from CoronaVirus Disease 2019 (COVID-19, caused by SARS-CoV-19), remains a serious hazard to human health and life, which also led to significant economic losses across the world. In some cases, it resulted in loss of a large number of human life. The associated ambient air pollutants: (O_3), nitrogen dioxide (NO_2), sulphur dioxide (SO_2), and carbon monoxide (CO), black carbon (BC) and particulate matter (PM), are directly linked to the enhanced risk of stroke, heart disease, asthma, and lung cancer. In order to have quantitative estimate, a comparative study of these pollutants, aerosol optical depth (AOD), surface temperature, ozone, carbon monoxide (CO) and NO_2, aerosol size distribution over India, have been analysed for the months March- June during the lockdown period of 2020 which are compared with the averages during 2015-2019. The aerosol optical depth (AOD) from MODIS satellite, show a decrease in AOD during the lockdown period by 40% over the Indian region, compared to 5-year mean level (2015-2019), whereas the ground based AOD from AERONET (Aerosol Robotic Network), was reduced to 75 % at Kanpur, and 74 % at Gandhi College (Ballia) in India. The drop in AOD observed in lockdown, is a clear-cut indication of reduced level of air pollution. Peak of aerosol size distribution over Kanpur and Gandhi College, has also been analysed which show a reduction by 33% to 50 % from the average level. Enhancement in total ozone column of ~8% from the average level, is noticed during the lockdown period, which is attributed to the suppression in NO_2 and CO concentration that are supposed to destroy the formation of ozone through chemical reactions. The black carbon (BC) concentration during the lockdown period, also got reduced and found maximum at New Delhi (80%). The comparative analysis of other pollutants between all the three cities of India is also made. The decrease in temperature during the lockdown over New Delhi, was found to be greater than that observed over Kanpur and the Gandhi College in Ballia**.**

Keywords: Covid-19, Surface temperature, Air pollutants, Satellite and ground based measurements, Aerosol optical depth (AOD), Black carbon

INTRODUCTION

The coronavirus disease 2019, commonly known as COVID-19, was a global pandemic that emerged as a major health concern across the globe. It was first identified in Wuhan, China, in December 2019 (Bukhari and Jameel, 2020; Kanniah et al., 2020; Şahin, 2020). On January 30, 2020, the World Health Organization (WHO) declared the outbreak as a public health emergency of international concern. The virus rapidly spread across numerous countries, and on March 11, 2020, it was officially classified as a "pandemic."(Kumar, 2020; Ranjan et al., 2020; Usman et al., 2020). Due to very fast spread of COVID-19, it became a very serious matter for world, with around 17.77 million cases and a total death of 6,83389 people worldwide by the end of July 2020.

Recently, the World Health Organization (WHO) said that Covid-19, spread through aerosols in closed areas (Kumar, 2020; Ranjan et al., 2020). Air pollutants mainly include ozone (O_3), nitrogen dioxide (NO_2), sulphur dioxide (SO_2) and particulate matter (aerosol), which are directly associated with the risk of stroke, heart disease, asthma and lung cancer. The air pollution itself caused 3.7 million premature deaths worldwide in 2012. When these pollutants are inhaled, they first come into contact with the respiratory tract lining (RTLF). RTLF antioxidant levels have been shown to decrease with the presence of NO_2 and O_3, thereby weakening the body's defences against environmental oxidants. These also help fight tissues. Surprisingly, the presence of NO_2 and O_3 caused more damage than the combined effect of each pollutant alone. The solar EUV radiations, meteorological parameters and aerosol significantly affect the coronal transmission and its survival time in the air is around few hours (Gabbrielli et al., 2021; Wei et al., 2022). To date, understanding of the mechanisms by which this damage occurs is limited and quite complex. The government announced transportation closures, people's movement, and business restrictions in the country to prevent the spread of COVID-19. These activities were expected to reduce air pollution. Table 1 shows the duration of lockdown in India (https://en.wikipedia.org/wiki/COVID-19_pandemic_ lockdown_in_India).

The response of 2019-nCoV to air pollutants and aerosols, is currently a matter of investigation and the subject of international challenges (Dhaka et al., 2020; Bukhari and

Jameel, 2020; Ranjan et al., 2020: Usman et al., 2020; Goel et al., 2021). Most of the studies discussed above rely on data from relatively limited number of ground-based stations which may not be evenly distributed in local region or cities. In this study, both the ground and satellite-based measurements are used to study the influence of the lockdown at major cities of the India. The impact of the Met's parameters on the blow-out of Covid-19 in the India, during the global epidemic, is also examined. In this paper the influence of lockdown on the abundance of different pollutants over three major cities of India, namely Kanpur, Gandhi College (Ballia) and New Delhi have been analysed.

AOD AND POLLUTANTS DATA

Aerosol optical depth (AOD) log data are obtained from the MODIS GIOVANNI NASA website (https://giovanni.gsfc.nasa.gov/giovanni/). MODIS provides the daily AOD that we use for the Indian region at 1degree resolution. More details on MODIS data acquisition can be found elsewhere (Kumar et al., 2012, 2015,2023a). In this study, AOD at 550 nm (green band) from MODIS with resolution of 1˚× 1˚ available with better consistency, has been analysed (Lyapustin et al., 2018). The AOD data from March 1 to June 30 of the year 2020 has been compared to the mean values estimated for the same period from 2015 to 2019. Daily surface temperature (AIRS3STD_V06), having 1°×1° spatial resolution were obtained from NASA's GIOVANI. The daily CO concentration increase, expressed as mole fraction (ppv) in air, was obtained from the AIRS satellite with a resolution of 1°×1° (Parkinson, 2003).

The Total Ozone Mapping Spectrometer (TOMS), has been used to measure atmospheric ozone concentration. The total ozone column (TOC) is a parameter that represents concentration of ozone and daily data product of TOC with 1˚× 1˚spatial resolution from TOMS has been taken from https://giovanni.gsfc.nasa.gov/giovanni/. The information about tropospheric ozone can be obtained with the help of OMI satellite where OMI stands for Ozone Monitoring Instrument. The ozone is obtained by differentiating aerosols such as smoke, dust and sulphates and measuring air pressure coverage. Atmospheric ozone, NO_2 and the total column volume of lower atmospheric dust, smoke and other aerosols are measured by OMI and can be obtained from the website https://giovanni.gsfc.nasa.gov/giovanni/. The NO_2 total column ($1/cm^2$) with resolution of OMI 0.25°×0.25°and daily product are used for the present analysis.

Similarly, MERRA-2 that stands for Modern-Era Retrospective Analysis for Research and Applications, version 2, is a reanalysis dataset that includes black carbon (BC) and other $PM_{2.5}$ components. MERRA-2 model was used to reconstruct spatiotemporal distributions of $PM_{2.5}$ concentrations, BC, organic carbon, dust, sea salt, and sulphate (Li et al., 2024). MERRA-2 provides the spatial distribution of atmospheric BC concentration since 1980, with a spatial resolution of 0.5° × 0.625° and a temporal resolution of 1 h, 3 h and month. All products can be downloaded through the NASA Earth Science Data Website (https://earthdata.nasa.gov/). With the wide application of MERRA-2, many validations have been carried out on MERRA-2 model in various studies (Bali et al., 2017; Yan et al., 2022).

Ground based AERONET data

A network of ground sun-photometers stations is the Aerosol Robotic Network (AERONET). The AERONET is primarily used for aerosol studies (Holben et al., 1998) which measure direct sun and sky radiance in multiple channels to obtain aerosol parameters. In the present study, AERONET version 2, level 1.5 data for AOD at 500 nm have been used. In addition, aerosol volume size distribution (ASD) for 22 size bins from 0.05 to 15 μm radius, has also been taken from the website https://aeronet.gsfc.nasa.gov.

RESULTS

The daily new COVID cases along with relative humidity (RH) over India during 01 March 2020 to 30 June 2020, is shown in Figure 1.

As seen from the Figure 1, it is noticed that COVID cases are constantly increasing day-by-day during the lockdown period. To reduce the COVID cases and to avoid its spread the initiatives taken from government of India has been taken, like closure condition or lockdown. The details of lockdown in India are mentioned in Table 1. During lockdown period, the anthropogenic human activities which causes atmospheric pollution were reduced, which have several impacts on atmospheric pollutants. To quantify such impacts, the influence of environmental pollutant on COVID cases has been studied

Variation of AOD and with COVID-cases

Figure 2 shows the map of changes in AOD (550 nm) derived from MODIS for Indian regions from 01 March -30 June 2020 (bottom panel) and compared with mean estimated during 2015-2019 (top panel). The AOD map clearly shows that in the year 2020, it has decreased by up to 60%, compared to the mean during 2015-2019. Moreover, AOD maximization in the Indo Gangetic basin is noticed from 2015 to 2019. The decline in aerosol levels in 2020 is due to reduced anthropogenic activities because of closure condition in India. To further examine the influence of the closure/lockdownon on AOD, ground AOD data from

AERONET at two locations, Kanpur and Gandhi College (Ballia) in India were analysed, which is shown in Figure 3 a, b.

From this Figure, reduction in AOD at both the station started just after the public curfew which was held on 22 March 2020 in India. AOD during the lockdown period is smaller than the 05-year average values (2015-2019) and further started increasing after announcement of unlock phase I (01-30 June 2020) i.e. after 06 June 2020. Reduction in AOD was found ~75% over Kanpur and ~74 % over Gandhi College (ballia), which are quite higher than satellite observation from MODIS. Reduced level AOD as measured from both the ground and satellite observations, indicating low pollution level due to closure conditions

Surafce temperature variations

Variation of daily surface temperature as retrieved from AIRS satellite over Indian region in lockdown period from 01 March to 30 June 2020 and its comparison with mean estimated during 2015-2019, is shown in Figure 3(c). During the lockdown period fall in temperature is observed as compared to the 5-years average values with a maximum fall of ~ 4 ^{o} C. Anomaly in surface temperature (in %) is also computed. The anomaly in temperature varies from -15% to 5% during the lockdown period i.e. maximum fall about ~ 15 % from the average level was observed.

Response of envoronmental parameters

Variation of total ozone column (TOC), retrieved from TOMS satellite in lockdown period from 01 March to 30 June 2020 and mean estimated during the years from 2015 to 2019, is shown in Figure 3(d). TOC is amount of atmospheric ozone in a given column and normally expressed in Dobson unit (DU). As reflected from the Figure, TOC is increased from average value during the lockdown period varies from -3% to 8%. Thus, during the lockdown period, ozone layer depletion is reduced from the last five years average level (2015-2019). The observed enhancement in TOC is attributed to reduction in NO_2 and CO as reflected from Figure 3e, f. The ozone layer is not only important for human life but it also protects us from dangerous ultraviolet rays and significant changes in it are noticed during the lockdown period to avoid COVID-19 spread.

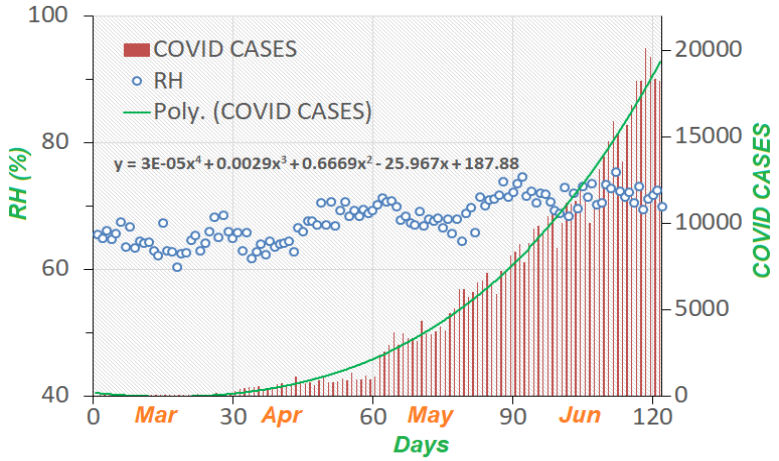

Figure 1. Daily new COVID cases along with relative humidity over India during 01 March 2020 to 30 June 2020.

Table 1. Lockdown period in India during 2020

No.	Lockdown phase	Period	Duration (in days)	Activities
1-	Public curfew	22 March	01 day	Announced by Prime Minister, Government of India
2-	Lockdown -1	25 March -14 April	21 days	Peoples are enforced to stay at their home. All transport services–road, air and rail–were suspended, with exceptions for transportation of essential goods, fire, police and emergency services.
3-	Lockdown -2	15 April- 03May	19 days	
4-	Lockdown -3	04 May-17 May	14 days	This lockdown was eased with several relaxations
5-	Lockdown -4	18 May- 31 May	14 days	More relaxation
6-	Unlock -1	01 June- 30 June	30 days	Most of activities are permitted
7-	Unlock -2	01 July- 31 July	31 days	Most of activities are permitted

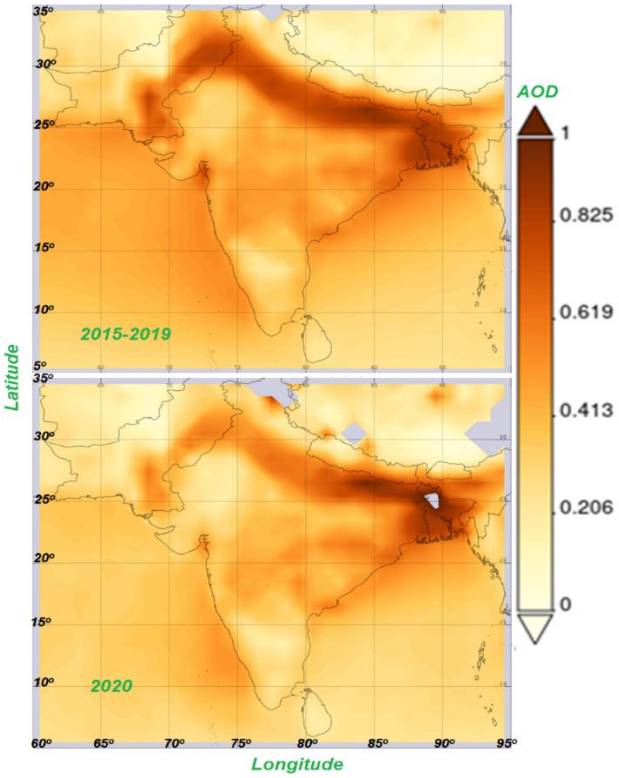

Figure 2. Variation of AOD (550 nm) from MODIS over the Indian region in lockdown period from 01 March- 30 June during 2015-2020.

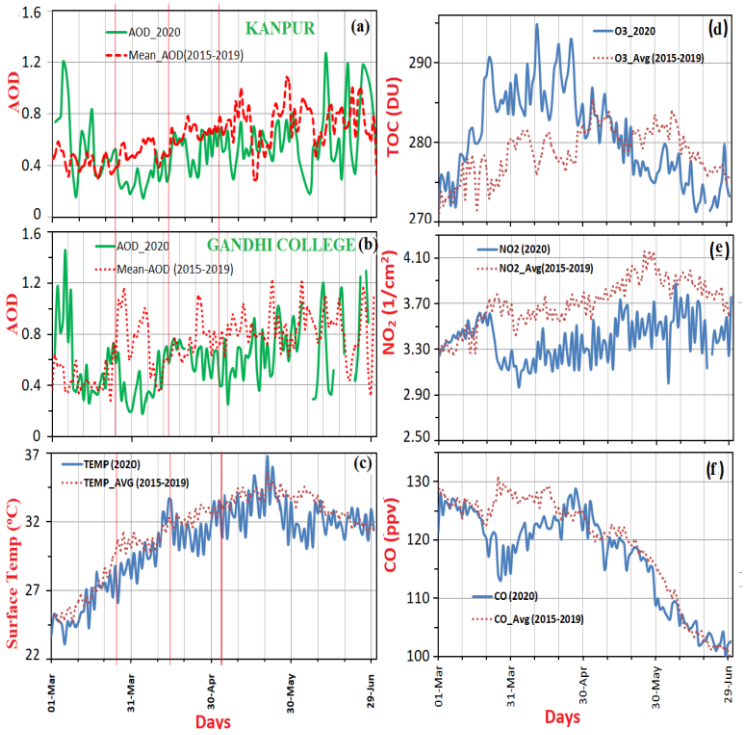

Figure 3. Variation of environmental parameter during lockdown period from 01 March – 30 June, 2020 including **(a)** atmospheric aerosol optical depth (AOD) from AERONET over Kanpur, **(b)** aerosol optical depth at Gandhi College, Ballia **(c)** Variation of daily surface temperature derived from AIRS satellite over Indian region, (**d)** Variation of daily surface total ozone column derived from AIRS satellite over Indian region, **(e)** Variation of daily NO_2 column derived from AIRS satellite over Indian region and **(f)** CO mole fraction (ppv)

Variation of CO

The concentration of CO (carbon monoxide), is measured as a mole fraction in air, expressed in parts per volume (ppv). CO data is obtained from the AIRS satellite with a spatial resolution of 1˚ × 1˚. For this study, CO measurements during the closed period from March 1 to June 30, 2020, have been analysed and compared with 05 years mean level (2015-2019). The results, shown in Figure 3f, indicate that the CO levels during this period, were lower than the 5-year average level. The variation in CO concentration ranged from a decline of -14% to an increase of +4%, with the lowest reduction being around 14% compared to the 5-year average estimate. This decrease in CO levels is believed to have contributed to the ozone formation, as evidenced by the higher levels of TOC observed during the same period in 2020 (Figure 3d).

Variation of NO_2

The total NO_2 column, measured by the OMI satellite over the Indian region at a resolution of 0.25° × 0.25°, is analysed during the lockdown period and compared with the 05 years average level (2015 to 2019), as shown in Figure **3(e)**. The data suggests a noticeable decrease in NO_2 concentrations during the lockdown period. This reduction is linked to the lockdown measures, implemented by the Government of India to curb the spread of COVID-19. During the lockdown, the NO_2 levels fluctuated between -24% and +6%, with a general decline observed compared to the 05-year average level. This decrease in NO_2 is expected to impact ozone formation, as reflected by the rise in Total Ozone Column (TOC) concentrations (Figure 3d). Beyond its atmospheric effects, nitrogen dioxide also has serious implications for human health. Breathing air with elevated levels of NO_2 can lead to respiratory issues. Short-term exposure, in particular, can worsen conditions such as asthma, causing symptoms like coughing, wheezing, and shortness of breath. In severe cases, this may result in hospitalizations and emergency room visits.

Black carbon (BC)

The impacts of lockdown on BC mass density from MERRA-2 model over Indian region, have been analysed and compared with 05 year mean (2015-2019) as shown in Figure 4. From the map, a clear-cut reduction in BC concentration is noticed in the Indian region during the COVID period 2020 when compared with the 05 year mean value (2015-2019). The quantitative analysis is carried out at three different cities of India. The analysis of black carbon, particulate matter ($PM_{2.5}$) and other pollutants over three different cities are also carried out. The quantitative estimate in the drop of these parameters during the lockdown condition is mentioned in Table 2. The drop in BC and $PM_{2.5}$ during the lockdown period is noticed at all the three cities with the maximum at New Delhi (~ 80% BC, 66% $PM_{2.5}$).

Particulate matter ($PM_{2.5}$)

Particulate matter are solid particles that include ash, dust, or even animal wastes and are also released during fossil fuels burning. The $PM_{2.5}$ refers to the fine particle of size less than 2.5 μm and PM_{10} for the coarse particle of size less than 10 μm and significantly changes due to crop residual burning and festival such as Diwali (Dhaka et al., 2020; Kumar, 2020; Chandu et al., 2023). The burning during the Diwali festival not only degrades the air quality but also impose the serious problems on human health which was recently reported over New Delhi (Rani and Kulshrestha, 2026). The impacts of lockdown on particulate matter ($PM_{2.5}$) have been analysed over Indian region during 01 March – 30 June 2020. For this, satellite-based data from MERRA-2 model during lockdown period has been compared with 05 year mean (2015-2019) and shown in Figure 5. From this figure, it is clearly seen that the black carbon and $PM_{2.5}$ both are significantly reduced during the lockdown period.

Table 2. Perturbation in atmospheric parameters from 5 years mean value during lockdown period from 01 March to 30 June over three cities of India.

Atmospheric parameters/ pollutants	Data taken from	Perturbation in pollutants		
		Kanpur	Gandhi College	New Delhi
Temperature	AIRS satellite	-27%	-22%	-30%
Aerosol	AERONET	-48%	-50%	-42%
Ozone	TOMS	18%	22%	14%
Black carbon	MERRA-2 model	-72%	-70%	-80%
Particulate matter ($PM_{2.5}$)	MERRA-2 model	-53%	-50%	-66%
Carbon mono oxide (CO)	AIRS satellite	11%	14%	16%

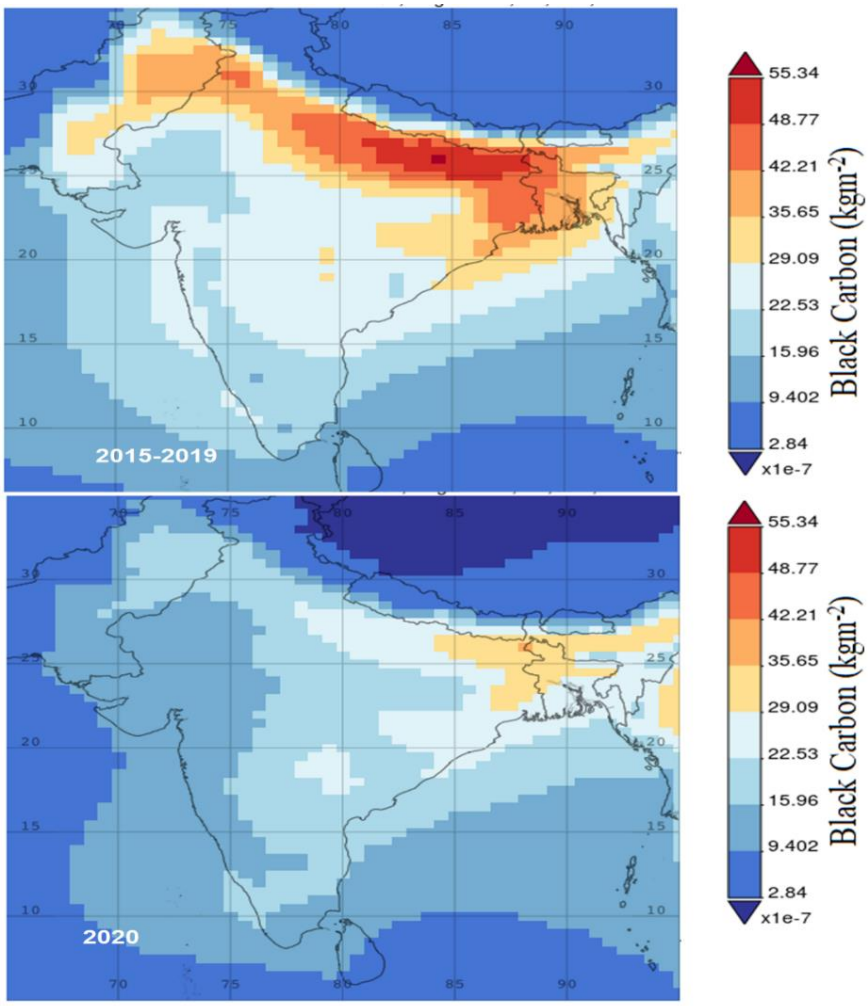

Figure 4. Time average map showing the spatial variation of particulate matter black carbon (BC) mass density (kg m^{-2}) during the lockdown period of 2020 (bottom panel) along with 05 year mean level (top panel). The BC are reduced significantly during the lockdown period of 2020 when compared to mean level estimate of 2015-2019.

DISCUSSION

As seen from the results discussed above, the lockdown restriction in India, significantly affected the pollution level. Using satellite-based AOD of MODIS between 25 March and 15 May 2020, Ranjan et al. (2020) have shown that the AOD level in the Indian region decreased by approximately 45% during the lockdown period, in comparison to the average AOD level estimated from 2000 to 2019. In addition, using AOD values obtained from Himawari-8, Kanniah et al. (2020) reported a decrease (about 40% to 70%) during the March-April of the year 2020 in Malaysia compared to the same months of the years 2018 and 2019.

Similarly, a drop-in air pollution of ~ 50% was noticed during the quarantine/lockdown in Barcelona, Spain. NO_2 concentration and BC was reduced by 45-51%, whereas O_3 levels increased between 33% and 57% during the lockdown period (Tobías et al., 2020). The study in China indicated carbon emissions dropped by 25% during lockdown, that is, approximately 1 million tons less as compared to the same period of last year (Wang and Su, 2020). The lockdown restriction during COVID-19 period, implemented by the governments of different countries, definitely restricted to the human activities, which resulted into significant reduction of air pollution at global and local scale (Kumar et al., 2015; Bauwens et al., 2020; Nakada and Urban, 2020; Kumar, 2025). The drop-in air pollution observed during the lockdown may have definitely influenced the climate change and global warming. Many workers have reported reduction in the Earth's temperature during the lockdown (Kumar, 2025). The results further indicate a reduction in air temperature during the lockdown period in the top 3 countries of the world: USA, Brazil and India. The environmental impacts of COVID-19 over Brazil and USA are more severe than that of India.

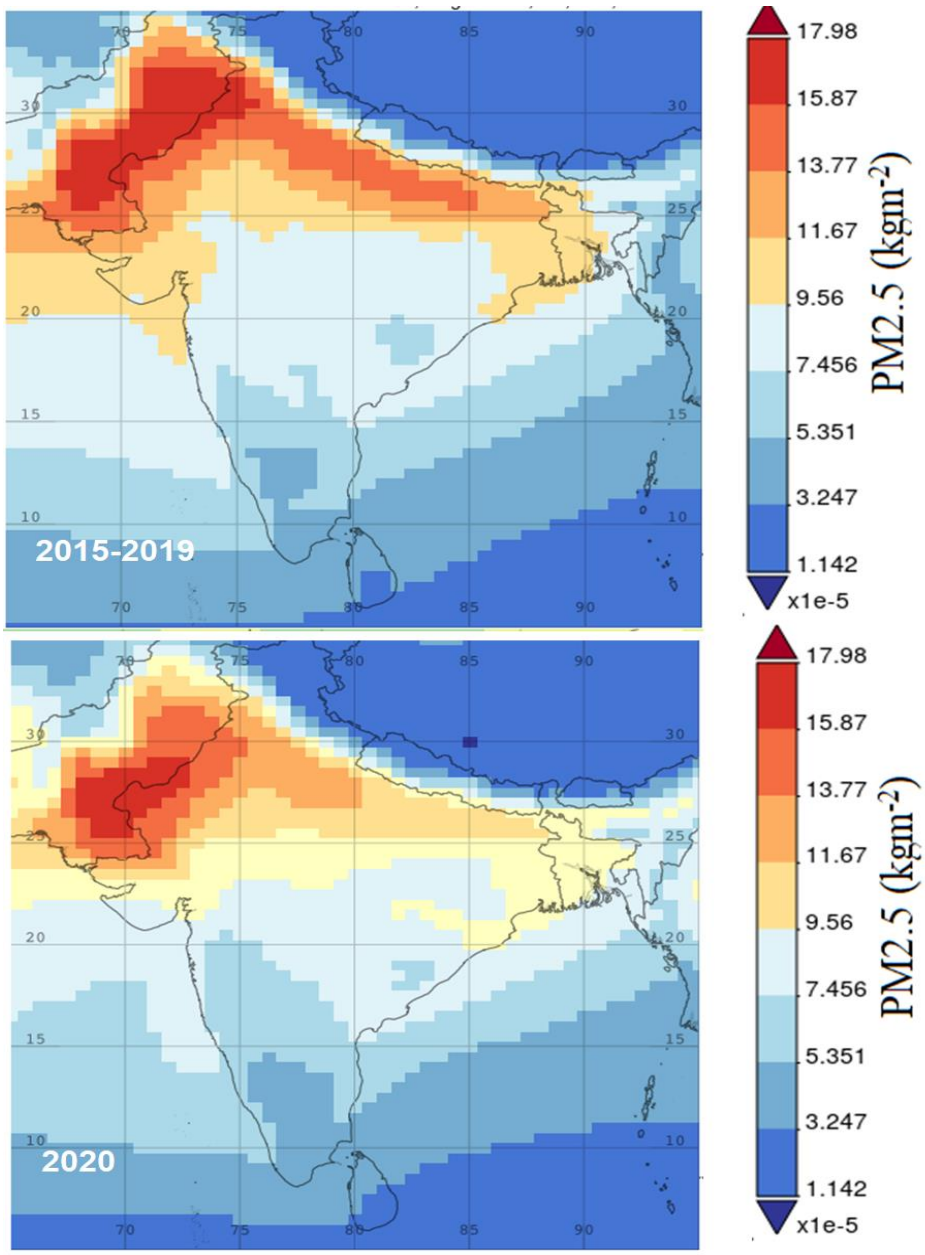

Figure 5. Time average map showing the spatial variation of particulate matter ($PM_{2.5}$) during the lockdown period of 2020 (bottom panel) along with 05 year mean level (top panel). The PM**2.5** are reduced significantly during the lockdown period of 2020 when compared to mean level estimate of 2015-2019.

However, the implications of carbon monoxide extend beyond its role in indoor environments. CO, whether indoors or outdoors, can disrupt the transportation of oxygen in the bloodstream, leading to symptoms such as chest pain and heart-related issues. Additionally, CO contributes to the formation of tropospheric ozone, another harmful pollutant with significant health risks. While CO itself does not directly drive climate change, its presence in the atmosphere can influence the concentrations of other greenhouse gases, such as methane and carbon dioxide. This in turn affects the overall greenhouse effect, contributing to climate change and global warming by altering Earth's surface temperature.

Nitrogen dioxide is also a critical compound both in the stratosphere, where it affects ozone chemistry, and in the troposphere, where it acts as a precursor to ozone formation. NO_2 is primarily produced through various combustion processes and during storms or lightning (Christian et al., 2003). The concentration of NO_2 serves as a key indicator of air pollution and plays a significant role in the chemistry of ozone (O_3) and hydroxyl radicals (OH) in the troposphere

through chemical reactions (Rohrer and Berresheim, 2006; Siingh et al., 2015). Additionally, nitrogen oxides (NOx) produced by lightning is 6.5 ± 4.7 times more effective in ozone formation than other sources (Finney et al., 2016). Beyond its atmospheric effects, nitrogen dioxide also has serious implications for human health. Breathing air with elevated levels of NO_2, can lead to respiratory issues. Short-term exposure, in particular, can worsen conditions such as asthma, causing symptoms like coughing, wheezing, and shortness of breath.

Similar to other diseases, air pollution levels influenced the spread of COVID-19 and promoted the community transmission/transmission of COVID-19 as stage 3 transmission (Bashir et al., 2020; Kumar, 2020; Usman et al., 2020; Sanghatawatana et al., 2023; Kumar, 2025). Previous studies have also found significant association between the poor air quality and COVID-19 (Bashir et al., 2020; Şahin, 2020; Marwah and Agrawala, 2022). Recently, Bashir et al. (2020) reported that poor air quality increased the extent of transmission COVID-19 in New York City. Similarly, Zhu et al. (2020) found that $PM_{2.5}$, PM_{10}, CO, NO_2, and O_3 were all associated with the spread of COVID-19, while SO_2 was negatively associated with the spread of COVID-19 in Turkey and China. As per Kerimray et al. (2020), the effects of preventing air pollution in Almaty, Kazakhstan, resulted in $PM_{2.5,}$ CO, and NO_2 reduction by approximately 21%, 49%, and 35%, respectively during lockdown condition as compared to the same period in 2018 and 2019. Bashir et al. (2020) too reported that lockdowns in Malaysia led to a 30% reduction in air pollution, while mobility was controlled by approximately 90%. Therefore, the COVID-19 control situation played an important role in global climate control by affecting the concentration of atmospheric pollutants. This suggests that there is room for our environment and nature to recover from pollution. Recently, Chandrakala et al. (2024) has reported reduction in the BC along with aerosol parameters over semi urban region Vijayawada in the India during 2006-2021. They have shown 30% reduction in the BC level during the COVID-19 lockdown period.

The suppression in the pollution level as seen in BC data is noticed to be maximum at New Delhi (~80 %) in the IG basin region attributed to the most populated as well as industrial region (Kumar et al., 2015). Our result agrees with those reported by Goel et al (2021) who have shown reduction in BC at New Delhi is ~78% during the lockdown period. It is important to notice that in addition to the lockdown restrictions other restriction/policy such as odd-even scheme in New Delhi significantly affect the $PM_{2.5}/PM_{10}$ values (Kumar et al., 2023b).

CONCLUSIONS

Based on our study following conclusions can be drawn.

(1) Mean surface temperature analysis during the lockdown period over Indian regions shows reduction from the 5 year mean level (2015-2019) with the maximum fall of ~ 4 ^{o}C (~15 %).

(2) Aerosol optical depth (AOD) from MODIS satellite in Indian region is reduced by 40% during the lockdown period, compared to 5-year mean level, whereas ground based AOD from AERONET reduced to 75 % at Kanpur, and 74 % at Gandhi College in Ballia.

(3) Lockdown conditions also affected the width and peaks of aerosol size distribution (ASD) and reduction in peak of ASD by 33% at Kanpur and 50% at Ballia.

(4) The enhancement in ozone concentration (TOC) ~ 8% is observed during the lockdown period, which is an indicator of fall in ozone depletion that are harmful for human health and affects climate as well. Moreover, ozone enhancement during the lockdown period is attributed to the reduction in NO_2 and CO which are expected to affect the ozone formation through chemical reactions.

(5). The analysis of met parameters during lockdown, reveals a fall in temperature, which is larger over the New Delhi than that for Kanpur and Gandhi College (Ballia).

(6) Quantitative analysis of black carbon (BC) and particulate matter ($PM_{2.5}$) during the lockdown period is found to have the maximum reduction in BC (~80%) and $PM_{2.5}$ (~66%) at the New Delhi.

Acknowledgements

Authors thank to the anonymous reviewers for their constructive comments/suggestions which helped to improve the MS quality.

Author credit statement

Km Swarnima analysed the data and wrote the MS. S. K. supervised the analysis and involved in the discussion.

Data availability

Authors are thankful to GIOVANNI, NASA team for providing the satellite data for surface temperature, AOD, NO2, O3, CO, BC, PM2.5, and Temperature (https://giovanni.gsfc.nasa.gov/giovanni/). Authors also thank to NASA team for supporting operation of Kanpur, New Delhi, and Gandhi College AERONET sites (https://aeronet.gsfc.nasa.gov/)

Compliance with Ethical Standards

The authors declare that they have no conflict of interest and adhere to the copyright norms.

REFERENCES

Bali, K., Mishra, A.K. and Singh, S., 2017. Impact of anomalous forest fire on aerosol radiative forcing and snow cover over Himalayan region. Atmos. Environ., 150, 264–275.

Bashir, M.F., Ma, B., Bilal, Komal, B., Bashir, M.A., Tan, D. and Bashir, M., 2020. Correlation between climate indicators and COVID-19 pandemic in New York, USA. Sci. Total Environ., 728, 138835.

Bauwens, M., Compernolle, S., Stavrakou, T., Müller, J.F., van Gent, J., Eskes, H., Levelt, P.F., van der A, R., Veefkind, J.P., Vlietinck, J., Yu, H. and Zehner, C., 2020. Impact of Coronavirus Outbreak on NO2 Pollution Assessed Using TROPOMI and OMI Observations. Geophys. Res. Lett. 47, e2020GL087978.

Bukhari, Q. and Jameel, Y. 2020. Will Coronavirus Pandemic Diminish by Summer? SSRN Electronic J., doi:10.2139/ssrn.3556998

Chandrakala, M., Nandan, R., Ratnam, M. V. and Bhaskara Rao, S. V. 2024. Source apportionment of black carbon and the impact of COVID-19 lockdown over a semi-urban location in India. Atmospheric Environ., X, 21, 100243.

Chandu, K., Raju, A.D., Kumar, S.V.J. and Mahendra, N., 2023. Spatial variations in PM2. 5/PM10 over time in Andhra Pradesh, India. J. Indian. Geophys. Union, 27(3), 211-220.

Christian, H. J., Blakeslee, R. J., Boccippio, D. J., Boeck, W. L., Buechler, D. E., Driscoll, K .T., Goodman, S. J., Hall, J. M., Koshak, W. J., Mach, D.M. and Stewart, M. F., 2003. J. Geophys. Res. Atmos. 108, ACL 4

Dhaka, S. K., Chetna, Kumar, V., Panwar, V., Dimri, A. P., Singh, N., Patra, P. K., Matsumi, Y., Takigawa, M., Nakayama, T., Yamaji, K., Kajino, M., Misra, P. and Hayashida, S., 2020. PM2.5 diminution and haze events over Delhi during the COVID-19 lockdown period: an interplay between the baseline pollution and meteorology. Sci. Reports 2020 10:1, 10(1), 13442-.

Finney, D.L., Doherty, R.M., Wild, O., Young, P.J. and Butler, A., 2016. Response of lightning NOx emissions and ozone production to climate change: insights from the atmospheric chemistry and climate model intercomparison project. Geophys. Res. Lett., 43, 5492–5500.

Gabbrielli, M., Gandolfo, C., Anichini, G., Candelori, T., Benvenuti, M., Savellini, G.G., Cusi, M.G., 2021. How long can SARS-CoV-2 persist in human corpses? Int. J. Infect Dis. 106, 1-2.

Goel, V., Hazarika, N., Kumar, M., Singh, V., Thamban, N.M. and Tripathi, S.N., 2021. Variations in Black Carbon concentration and sources during COVID-19 lockdown in Delhi. Chemosphere 270, 129435.

Holben, B.N., Eck, T.F., Slutsker, I., Tanré, D., Buis, J.P., Setzer, A., Vermote, E., Reagan, J.A., Kaufman, Y.J., Nakajima, T., Lavenu, F., Jankowiak, I. and Smirnov, A., 1998. AERONET—A Federated Instrument Network and Data Archive for Aerosol Characterization. Remote Sens. Environ. 66, 1–16.

Kanniah, K.D., Kamarul Zaman, N.A.F., Kaskaoutis, D.G. and Latif, M.T., 2020. COVID-19's impact on the atmospheric environment in the Southeast Asia region. Science of The Total Environment 736, 139658.

Kerimray, A., Baimatova, N., Ibragimova, O.P., Bukenov, B., Kenessov, B., Plotitsyn, P. and Karaca, F., 2020. Assessing air quality changes in large cities during COVID-19 lockdowns: The impacts of traffic-free urban conditions in Almaty, Kazakhstan. Sci. Total Environ. 730.

Kumar, S., 2020. Effect of meteorological parameters on spread of COVID-19 in India and air quality during lockdown. Science of The Total Environment 745, 141021.

Kumar, S., 2025. Effect of lockdown due to COVID-19 on environmental pollutant: a comparative study between top three countries of the world. Indian J. Physics, 99(3), 883-892.

Kumar, S., Kumar, S., Singh, A.K., and Singh, R.P., 2012. Seasonal variability of atmospheric aerosol over the North Indian region during 2005–2009. Adv. Space Res., 50, 1220–1230

Kumar, S., Kumar, S, Kaskaoutis, D.G., Singh, R.P., Singh, R.K., Mishra, A.K., Srivastava, M.K. and Singh, A.K. 2015. Meteorological, atmospheric and climatic perturbations during major dust storms over Indo-Gangetic Basin. Aeolian Res. 17, 15–31.

Kumar, S., Singh, N., Singh, R.P. and Siingh, D. 2023a. Variability of air quality and aerosol over Indian region during 2003–2012. Indian J. Phys., 97, 17-23.

Kumar, K., Kulshrestha, M.J., and Singh, S., 2023b. Influence and distribution pattern of n-Alkanes in PM2.5 and PM10 during odd- even scheme in Delhi, India. J. Indian Geophys. Union, 27(3), 174-184.

Li, W., Wang, Y., Yi, Z., Guo, B., Chen, W., Che, H. and Zhang, X. 2024. Evaluation of MERRA-2 and CAMS reanalysis for black carbon aerosol in China. Environmental Pollution 343, 123182.

Lyapustin, A., Wang, Y., Korkin, S. and Huang, D., 2018. MODIS Collection 6 MAIAC algorithm. Atmos. Meas. Tech. 11, 5741–5765.

Marwah, M. and Agrawala, P. K. 2022. COVID-19 lockdown and environmental pollution: an Indian multi-state investigation. Environ. Monit. Assess. 194, 49.

Nakada, L.Y.K. and Urban, R.C., 2020. COVID-19 pandemic: Impacts on the air quality during the partial lockdown in São Paulo state, Brazil. Science of The Total Environment 730, 139087.

Parkinson, C.L., 2003. Aqua: an earth-observing satellite mission to examine water and other climate variables. IEEE Transact. on Geosci. Remote Sensing, 41, 173–183

Rani, N. and Kulshrestha, M.J., 2026. Abundance, distribution pattern and health risk assessment of polycyclic aromatic hydrocarbons in size-segregated aerosols during Diwali festival in Delhi (India). J. Indian Geophys. Union, 30(2), 114-121

Ranjan, A.K., Patra, A.K. and Gorai, A.K., 2020. Effect of lockdown due to SARS COVID-19 on aerosol optical depth (AOD) over urban and mining regions in India. Science of The Total Environment 745, 141024.

Rohrer, F. and Berresheim, H., 2006. Strong correlation between levels of tropospheric hydroxyl radicals and solar ultraviolet radiation. Nature, 442, 184–187.

Şahin, M., 2020. Impact of weather on COVID-19 pandemic in Turkey. Science of The Total Environment 728, 138810.

Sanghatawatana, P., Thaithatkul, P., Anuchitchanchai, O., Liang, J. and Chalermpong, S., 2023. The effect of COVID-19 lockdown on particulate matters concentration: Case of land use regression difference modeling in Bangkok, Thailand. City and Environment Interactions 20, 100125.

Siingh, D., Singh, R.P., Kumar, S., Dharmaraj, T., Singh, A.K., Singh, A. K., Patil, M.N. and Singh, S. 2015. Lightning and middle atmospheric discharges in the atmosphere. J. Atmos. Sol. Terr. Phys., 134, 78–101.

Tobías, A., Carnerero, C., Reche, C., Massagué, J., Via, M., Minguillón, M.C., Alastuey, A. and Querol, X., 2020. Changes in air quality during the lockdown in Barcelona (Spain) one month into the SARS-CoV-2 epidemic. Science of The Total Environment, 726, 138540.

Usman, M., Farooq, M. and Hanna, K., 2020. Environmental side effects of the injudicious use of antimicrobials in the era of COVID-19. Science of the Total Environment, 745, 141053.

Wang, Q. and Su, M., 2020. A preliminary assessment of the impact of COVID-19 on environment – A case study of China. Science of The Total Environment, 728, 138915.

Wei, Y., Dong, Z., Fan, W., Xu, K., Tang, S., Wang, Y. and Wu, F., 2022. A narrative review on the role of temperature and humidity in COVID-19: Transmission, persistence, and epidemiological evidence. Eco-Environment & Health. 1(2), 73–85.

Yan, G., Yu, H., Li, M., Zheng, X., Li, S., Yao, D., Liu, M. and Hu, P., 2022. Pollution characteristics of black carbon based on MERRA-2 reanalysis data in core city of Central Plains Economic Zone, China: Historical trend and potential sources. Front. Environ. Sci., 10, 1028572.

Zhu, Y., Xie, J., Huang, F. and Cao, L., 2020. Association between short-term exposure to air pollution and COVID-19 infection: Evidence from China. Science of The Total Environment, 727, 138704.

Received on: 29-08-2025; Revised on: 28-05-2026; Accepted on: 29-05-2026

J. Ind. Geophys. Union, 30(4) (2026), 322-325
https://doi.org/10.71122/JIGU.30(4)2026.0031

Impact related deformation within and around the proposed Kaveri Crater, southern India.

K. R. Subrahmanya
A701, Century Central Apartments, Kanakapura Main Road, Bengaluru- 560111, India.
Corresponding author: kavericrater@gmail.com

ABSTRACT

Occurrence of an extraterrestrial impact crater, named as Kaveri crater, has been proposed from the southern Indian peninsula. This crater, with a diameter of about 120 km, could be the fourth largest on the surface of the Earth. Initial findings regarding this crater have already been published (Subrahmanya and Prakash Narasimha, 2017). In the present work, we provide additional primary and supporting evidences. Shatter cones are observed within the crater, while the radial and concentric fractures are present outside the crater rim. Besides, Planar Deformation Features are found to be present in quartz and plagioclase. Indirect evidences point its formation around Neoproterozoic – Cambrian boundary.

Key words: Kaveri crater (South India), Impact structure, Deformation, Shatter cone, Planar Deformation Features.

INTRODUCTION

Southern Indian terrain predominantly consists of Precambrian schists, gneisses and granulites. Within this terrain, there is a circular depression, bound by a mountainous terrain. All the hill ranges around this structure, have a steep slope facing the depression and a gentle slope in the other direction. Subrahmanya (2007) suggested that this physiographic anomaly to the east of the Palghat Gap, could have been resulted due to an extraterrestrial impact. Subsequent field and laboratory investigations too provide supporting evidences (Subrahmanya and Prakash Narasimha, 2017). The present paper provides additional significant structural evidences in the support of impact origin of this crater.

STRUCTURE

South of Anaimalai–Palani–Kodaikanal hill range, there is a major break in the gradient. This is a part of the Karur–Kambam-Painavu-Trichur shear zone (KKPTSZ). Northwest of Nilgiris, there is a similar break. These two regions indicated by arcs in Figure 1, are listric faults and apparent rim of the proposed crater. Reddy et al. (2003) who have made detailed geophysical investigations of the region, have expressed the view that the Nilgiris and Kodaikanal granulite massifs, have undergone uplift during the Phanerozoic period. Apparent rim and listric faults are not prominent to the north, northeast and east of the crater, because the radial fractures dominate in this region.

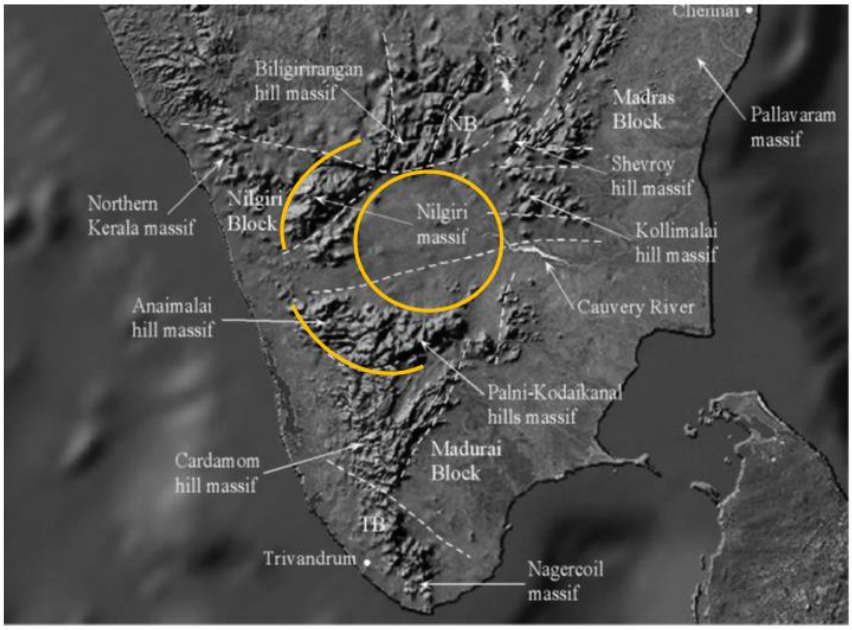

Figure 1. Shaded relief map of the proposed Kaveri crater (yellow circle). Yellow arcs south of Anaimalai Hill Massif and north-west of Nilgiri massif, represent apparent rim and listric fault. Dashed lines indicate fractures/faults/shear zones which radiate from the crater (Modified from Rajesh and Santosh, 2004).

MESOSTRUCTURES

Shatter cones are meso-structures which are one of the definitive indicators of the crater formed due to impact. The pressure range required for its formation is 2 to 30 GPa. (Osinski and Ferriere, 2016). In the Kaveri crater, shatter cone (Figure 2) is observed on the top of a granite body, near Konganar Siddar Temple, Uthiyur Hills, which is close to the centre of the crater. Length of the cone is about 70 cm and the width at the base is nearly 45 cm.

Micro deformation structures in quartz

Ferrière et al. (2009) and French and Koeberl (2010), have discussed in detail about the convincing identification of impact structures. Among these, undisputable evidences are Planar Deformation Feature and Planar Fracture in quartz. One of the quartz grains that has well-developed planar features as shown in Figure 3, was investigated using Universal Stage. The quartz grain has one set of Planar Deformation Feature trending NW and one set of prominent Planar Fracture trending NE. The second set of Planar Fracture is parallel to the Planar Deformation Feature. In some places, the NE trending Planar Fracture has been displaced along the Planar Deformation Feature planes, thereby indicating that the Planar Fracture developed first. Some of the Planar Deformation Feature planes have undergone annealing. Measurement of the angle between the c-axis and the poles perpendicular to Plane/s of Planar Deformation Feature is 21°.

Figure 2. Shatter cone in granite (front and base view) location being near the Konganar Siddar Temple, Uthiyur hills, Uthiyur, Tamil Nadu. Scale of the pen: 15 cm.

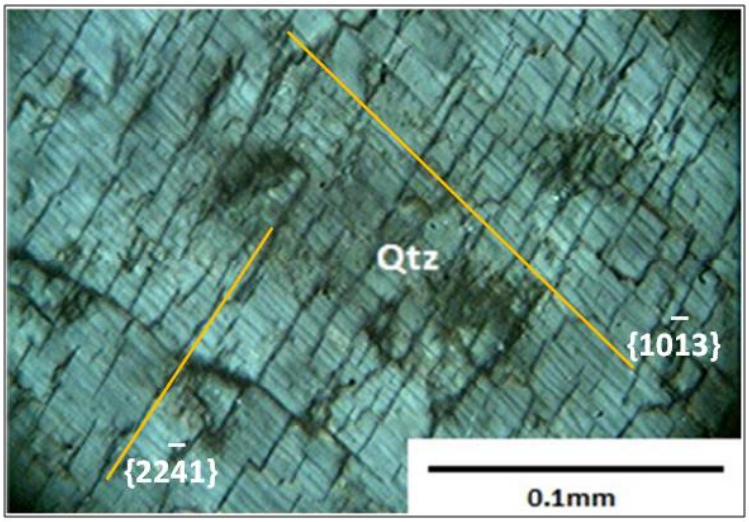

Figure 3. Planar Deformation Feature {10$\underline{1}$3} and Planar Fracture {22$\underline{4}$1} in quartz, as indicated by NW and NE trending yellow lines respectively. A second set of Planar Fracture parallel to {10$\underline{1}$3} is also present.

This indicates that plane of the Planar Deformation Feature is {10$\underline{1}$3}. The interpolar angle between the c-axis and NE trending Planar Fracture is 77^o, which indicates {22$\underline{4}$1} as the Planar Fracture plane.

Micro deformation structures in feldspar

Plagioclase minerals from Oddanchatram anorthosite have developed checkerboard pattern with three sets of intersecting Planar Deformation Feature in N-S, NNW-SSE, WNW- ESE directions. Besides, there is a Planar Fracture, trending in ENE WSW direction. The mineral has lower transparency in PPL (Figure 4). The XPL image (not shown here), indicates lack of twinning and lower birefringence. Dikes with sooty clouded feldspars have been recorded close to the northern rim of the crater (Halls et al., 2007). Figure 5 a, shows one such clouded feldspar just to the north of the crater. Figure 5 b, which is a part of the Figure 5 a, has two Planar Deformation Feature planes in NE and NW directions. These have been partially annealed and decorated.

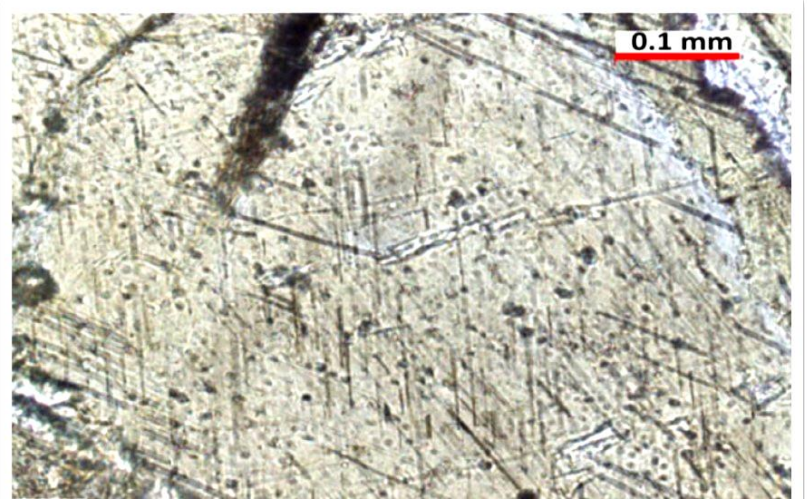

Figure 4. PPL image of Planar Deformation Feature / Planar Fracture in clouded plagioclase grain from Oddanchatram anorthosite, partly occupied by Fe–Ti oxide needles oriented in N-S, NNW-SSE, WNW-ESE, ENE-WSW directions (Soumya et al, 2017).

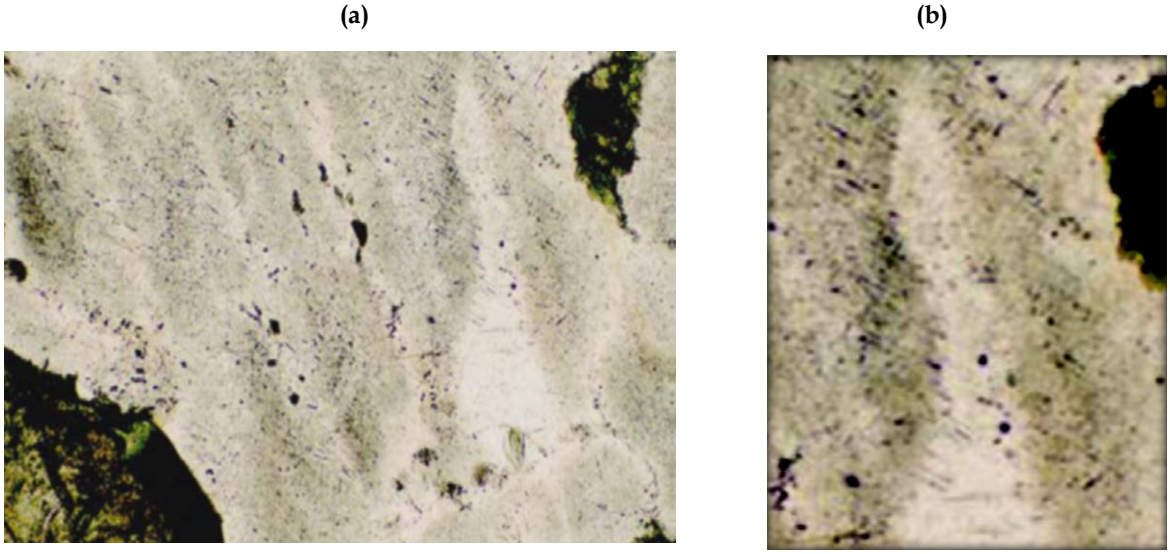

Figure 5. (a) Sooty clouded plagioclase (PPL). Width of the image is 1.2 mm. (Halls et al., 2007). **(b)** Magnified image of the north-eastern part of the Fig. 5 (a), with enhanced contrast. Two sets of Planar Deformation Feature trending NW (prominent) and NE are intersecting with each other. Planar Deformation Feature area shows decoration and partial annealing.

DISCUSSION AND CONCLUSIONS

Rock types in the circular depression is dominantly granitic gneisses/migmatites. This is surrounded by charnockite hills. Quartz and plagioclase show the presence of Planar Deformation Feature and Planar Fracture, which are one of the definitive evidence of extraterrestrial impact. Shatter cone; Planar Deformation Feature and Planar Fracture in quartz and plagioclase; taken together, indicate that the hypervelocity impact pressure was in the range of 2 to 30 GPa. Geophysical analysis gives supportive evidences (Subrahmanya and Prakash Narasimha, 2017). All these evidences, taken together substantiate the earlier study that the Kaveri crater may be an extraterrestrial hypervelocity impact. Available geochronological data (Yellappa and Mallikharjuna Rao, 2018; Nathan and Gopalakrishnan, 2022) provide a narrow window on the timing of impact. Sivanmalai syenite whose age of emplacement is 623 $\pm$ 21 Ma has quartz and pegmatite veins. Quartz in these, have developed Planar Deformation Feature and Planar Fracture, indicating that impact is younger than 623 Ma. Oddanchatram anorthosite whose age of intrusion is 560 $\pm$ 12 Ma (Nathan and Gopalakrishnan, 2022), has Planar Deformation Feature developed in plagioclase. A huge impact normally creates large quantity of melt. It has been seen that within the crater and also adjacent to crater rim, there are innumerable emplacements of granitic bodies. Ages of these ranges from 580 Ma to 510 Ma with a mean of 545 Ma. Metamorphic age of Paleoproterozoic rocks (~2.5 Ga) within and close to the crater, range in age from 576 Ma to 512 Ma with a mean of 548 Ma. These age data indicates that the impact could have occurred at the Proterozoic – Paleozoic boundary.

Acknowledgment

The very first field work for the investigations on Kaveri crater was carried out under the guidance of Prof. (Late) B Mahabaleshwar. The author expresses his homage. Universal Stage measurements were carried out under the guidance of Prof. C. E. Nehru, Emeritus Professor, City University of New York. This was made possible by the Geological Society of India, which conducted a workshop at the Savitribai Phule Pune University during January 2020. Dr P Krishnamurthy and Prof R A Duraiswami facilitated attending the Workshop, as a participant and also as a resource person. The host University was generous in providing travel grants and local hospitality. Prof. Prakash Narasimha is thanked for sharing field data, rock samples and thin sections. Sandeep helped in the preparation of figures.

Author credit statement:

K. R. Subrahmanya: Visualization, investigation, formal analysis, writing the paper.

Data availability: Data is presented in the article.

Compliance with ethical standards

The author declares that there is no conflict of interest and adhere to copyright norms.

REFERENCES

Ferrière L., Morrow J. R., Amgaa T. and Koeberl, C., 2009. Systematic study of universal-stage measurements of planar deformation features in shocked quartz: Implications for statistical significance and representation of results. Meteoritics & Planet. Sci., 44 (6), 925–940.

French, B.M. and Koeberl, C., 2010. The Convincing Identification of Terrestrial Meteorite Impact Structures: What Works, What Doesn't and Why. Earth Sci. Rev., 98, 123-170. http://dx.doi.org/10.1016/j.earscirev.2009.10.009

Halls, H.C., Kumar, A., Srinivasan, R and Hamilton M.A., 2007. Paleomagnetism and U–Pb geochronology of easterly trending dykes in the Dharwar craton, India: feldspar clouding, radiating dyke swarms and the position of India at 2.37 Ga. Precamb. Res., 155, 47-68.

Nathan N. P. and Gopalakrishnan K., 2022. Geology and Mineral Resources of Tamil Nadu and Puducherry, ISBN, 978-93-80998-44-2, The Geological Society of India, book series.

Osinski, G. R. and Ferriere, L., 2016. Shatter cones: (Mis)understood? Science Advances 2(8):e1600616-e1600616 DOI: 10.1126/sciadv.1600616

Rajesh, H.M. and Santosh, M., 2004. Charnockitic magmatism in southern India. J. Earth Syst. Sci., 113, 565–585.

Reddy, P.R., Rajendra Prasad, B., Vijaya Rao, V., Kalachand Sain, Prasada Rao, P., Prakash Khare and Reddy, M.S., 2003. Deep Seismic Reflection and Refraction/Wide-angle Reflection Studies along Kuppam-Palani Transect in the Southern Granulite Terrain of India, In: M. Ramakrishnan (Ed.), Tectonics of Southern Granulite Terrain, Kuppam-Palani Geotransect. Mem. Geol. Soc. India, no.50, pp.79-106.

Soumya, G. S., Mohamed Asanulla, R., and Radhakrishna, T. 2017. Rockmagnetism in relation to magnetic mineralogy of anorthosites in the southern granulite region of the Indian shield. Geophys. J. Int. 209, 1768–1778. doi: 10.1093/gji/ggx134.

Subrahmanya, K.R., 2007. Kaveri Crater - A probable impact structure in the Precambrian Terrain of Southern India. National Seminar on PGE and IX Convention of the MSI, NGRI Hyderabad, 19-20 July, 2007, pp.120.

Subrahmanya, K. R. and Prakash Narasimha, K. N., 2017. Kaveri Crater – An Impact Structure in the Precambrian Terrain of Southern India. J. Geol. Soc. Ind., 90 (4), 387-395

Yellappa T. and Mallikharjuna Rao J., 2018. Geochemical characteristics of Proterozoic granite magmatism from Southern Granulite Terrain, India: Implications for Gondwana, J. Earth Syst. Sci. 127, 22

Received on: 16-12-2025; Revised on: 29-03-2026; Accepted on: 12-04-2026

J. Ind. Geophys. Union, 30(4) (2026), 326-329
https://doi.org/10.71122/JIGU.30(4)2026.0032

SHORT NOTE

The 24 June 2026 Venezuela earthquake sequence in the context of major earthquake doublets and complex strike-slip ruptures

D. Shashidhar*, K. Mallika and B. Laxman
CSIR-National Geophysical Research Institute, Hyderabad 500007, Telangana, India
*Corresponding author: shashidhar.ngri@csir.res.in

The *24 June 2026 Venezuela earthquake sequence* has renewed interest in one of the longstanding questions in earthquake source physics: under what conditions do large strike-slip earthquakes occur as independent but mechanically linked events, rather than a single continuous rupture? At 22:04:33 UTC, an Mw 7.2 earthquake occurred in Yaracuy State, approximately 160 km west of Caracas, the capital city of Venezuela at a focal depth of about 22 km. Only 39 s later, a second and larger Mw 7.5 earthquake nucleated nearby, 6.2 km apart from each other, at a depth of approximately 10 km, producing widespread strong ground shaking across the north-central Venezuela. Preliminary focal mechanism solutions indicate predominantly right-lateral strike-slip mechanism, consistent with the rupture along the Caribbean–South American plate boundary system along the San Sebastian fault system, which extends along the northern coast of Venezuela (USGS, 2026).

Although the 24 June 2026 Venezuela earthquake sequence has attracted worldwide attention because of the occurrence of two major strike-slip earthquakes within only 39 s, it may not represent an isolated phenomenon. Historical accounts of the 1812 Caracas earthquake, suggest a complex multi-event rupture, while the region recently experienced a doublet in September 2025, consisting of an M 6.2 and an M 6.3 earthquake WSW of the present 2026 earthquake sequence. Together, these sequences raise the possibility that closely spaced, mechanically linked ruptures, may recur within the strike-slip fault systems, accommodating deformation along the Caribbean–South American plate boundary. The 2026 sequence therefore provides an opportunity to place Venezuelan seismicity in the broader context of large earthquake doublets and complex strike-slip ruptures.

Earthquake doublets are generally defined as two earthquakes of comparable magnitude occurring close together in space and time, usually on adjacent or mechanically connected fault segments. Unlike ordinary mainshock - aftershock sequences, in which the largest aftershock is typically about 1.2 magnitude units smaller than the mainshock according to Bath's law (Bath, 1965), both earthquakes in a doublet are principal ruptures, capable of generating widespread ground shaking and releasing comparable amounts of seismic moment. Such sequences provide valuable natural laboratories for investigating multi-fault rupture, Coulomb stress transfer, dynamic triggering, and cascading fault failure (King et al., 1994; Harris, 1998).

Among the modern examples (Figure 1), the *2012 Indian Ocean earthquake sequence*, remains the largest strike-slip earthquake sequence ever instrumentally recorded. The Mw 8.6 earthquake and the Mw 8.2 event that followed approximately two hours later, ruptured multiple conjugate strike-slip faults within the Indo-Australian Plate. Finite-fault inversions, seismic waveform modelling, and geodetic observations demonstrated that rupture propagated through an exceptionally complex fault network, illustrating how accumulated intraplate stresses can be released through cascading multi-fault failure (Meng et al., 2012; Duputel et al., 2012).

The *2023 Türkiye–Syria earthquake sequence*, provides perhaps the clearest modern example of a continental strike-slip earthquake doublet. The Mw 7.8 rupture on the East Anatolian Fault was followed approximately nine hours later by a Mw 7.5–7.7 earthquake on the adjacent Surgu–Çardak fault system. Because both earthquakes were similar in size and ruptured different fault segments, the sequence differs fundamentally from a conventional aftershock sequence. Independent finite-fault inversions, InSAR observations, GNSS measurements, and Coulomb stress modelling, consistently indicate that the first rupture substantially increased stresses on neighbouring fault segments, promoting nucleation of the second earthquake (Jia et al., 2023; Melgar et al., 2023; Milliner et al., 2023; Wallace et al. 2018). Consequently, this sequence has become a benchmark case for understanding cascading rupture, multi-fault faulting, and static stress triggering in continental transform environments.

Not all large strike-slip earthquakes, however, evolve as earthquake doublets. The *2025 Myanmar (Mandalay) earthquake*, illustrates that rupture complexity alone is insufficient evidence for classifying an earthquake sequence as a doublet. The Mw 7.7 earthquake ruptured approximately 470–535 km of the Sagaing Fault during a single rupture episode lasting nearly 90 s, making it one of the longest continental strike-slip ruptures, recorded instrumentally.

Seismic and geodetic observations indicate bilateral rupture initiation, followed by sustained super-shear propagation over much of the southern fault segment through the Burridge–Andrews transition mechanism. Although the rupture exhibited pronounced heterogeneity, multiple asperities, variable rupture velocity, and multi-segment faulting, these complexities occurred within a single evolving rupture, rather than through two independently nucleated earthquakes. The Myanmar event therefore provides an important counterexample, demonstrating that super-shear propagation and rupture complexity do not necessarily imply an earthquake doublet (He et al., 2025; USGS, 2025). Other important examples include the *2002 Denali Fault earthquake*, in which rupture propagated across several connected fault systems over approximately 340 km, and the *2013 Balochistan earthquake*, where rupture extended for more than 200 km with pronounced spatial heterogeneity (Eberhart-Phillips et al. 2003; Jolivet et al. 2014). Similar observations following the *2016* Mw *7.8 Kaikoura earthquake*, where widespread triggered slow slip and after slip occurred on the southern Hikurangi subduction zone (Wallace et al., 2018). These earthquakes illustrate that rupture can jump between geometrically connected fault segments, while remaining part of one evolving earthquake.

Other well-documented examples further illustrate the diversity of earthquake doublets. The *2006–2007 Kuril Islands earthquake sequence* consisted of a Mw 8.3 megathrust earthquake, followed approximately two months later by a Mw 8.1 outer-rise normal-fault earthquake. Although the two earthquakes involved contrasting faulting mechanisms, they are widely regarded as a classic "doublet couple" because stress redistribution following the megathrust rupture promoted failure within the down going Pacific Plate (Ammon et al., 2008; Lay et al., 2009). Additional continental examples include the *1987 Superstition Hills* sequence in California and the *1997 Umbria–Marche* sequence in Italy, both of which remain important case studies for understanding fault interaction and static stress transfer between neighbouring fault segments (Stein et al., 1992; Chiaraluce et al., 2003).

An interesting historical perspective is further provided by the *26 March 1812 Caracas earthquake*, one of the most destructive earthquakes in South American history. Contemporary historical accounts suggest that the catastrophe may have consisted of two or possibly three large sub-events affecting different parts of northern Venezuela, within a relatively short period. Early eyewitness descriptions refer to two principal shocks separated by approximately 30 min, with the first devastating Caracas and La Guaira and a subsequent event causing severe destruction farther southwest toward Mérida.

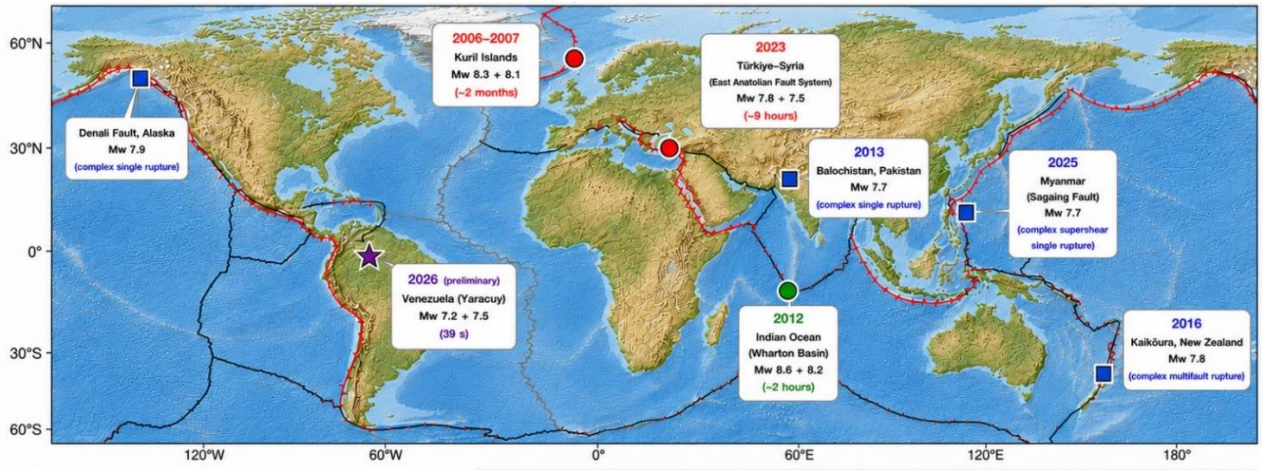

No.	Earthquake Sequence	Year	Magnitude (*Mw*)	Inter-event Time	Classification	Tectonic Setting
■	Denali Fault, Alaska	2002	7.9	—	Complex single rupture	Continental strike–slip
●	Kuril Islands	2006–2007	8.3 + 8.1	~2 months	Earthquake doublet	Subduction (megathrust–outer rise)
●	Indian Ocean (Wharton Basin)	2012	8.6 + 8.2	~2 hours	Earthquake doublet	Oceanic intraplate strike–slip
■	Balochistan, Pakistan	2013	7.7	—	Complex single rupture	Continental strike–slip
■	Kaikōura, New Zealand	2016	7.8	—	Complex multifault rupture	Oblique plate boundary
●	Türkiye–Syria (East Anatolian Fault System)	2023	7.8 + 7.5	~9 hours	Earthquake doublet	Continental strike–slip
■	Myanmar (Sagaing Fault)	2025	7.7	—	Complex supershear single rupture	Continental strike–slip
★	Venezuela (Yaracuy)	2026	7.2 + 7.5	39 s	Possible earthquake doublet / rapid cascading rupture*	Continental strike–slip

Figure 1. Global distribution of major earthquake doublets and complex strike-slip ruptures during 1900 – 2026 with Mw ≥ 7.0, instrumentally recorded events.

Subsequent macroseismic re-evaluations, together with paleoseismological investigations, suggest that the 1812 disaster may have involved rupture of multiple segments of the Bocono–San Sebastian fault system, including a Mw ~7.4 rupture on the north-eastern Bocono Fault and a Mw ~7.1 rupture on the offshore San Sebastian Fault, although the precise rupture chronology remains uncertain because no instrumental observations were available (Altez, 2010; Choy et al., 2010; Pousse-Beltran et al., 2018). Consequently, the 1812 Caracas earthquake is best interpreted as a complex historical earthquake sequence rather than a confirmed earthquake doublet.

Taken together, these examples indicate that the large strike-slip earthquakes, may evolve through two fundamentally different rupture styles: (i) rupture remains continuous despite considerable spatial complexity, heterogeneous slip, and variable rupture velocity, as illustrated by the Myanmar earthquake; (ii) rupture occurs as two distinct, but mechanically linked principal earthquakes, forming a true earthquake doublet, as demonstrated by the Indian Ocean and Türkiye sequences and potentially, by the preliminary observations from the recent Venezuela sequence. Distinguishing between these rupture styles, is essential for understanding rupture segmentation, dynamic triggering, stress transfer, and the seismic hazard posed by interconnected fault systems.

Acknowledgements

We are thankful to Dr. Prakash Kumar, Director, CSIR-National Geophysical Research Institute (CSIR-NGRI), Hyderabad, for his constant encouragement and permission to carry out this research work. Our sincere thanks to Dr. O.P. Pandey, Chief Editor, for his valuable suggestions in improving this article.

Author Credit Statements

All authors contributed towards the projected idea in the paper

Data Availability

Available on reasonable request from the corresponding author

Complience with the Ethical standard

No conflict of interest and authors adhere to copyright norms

References

Altez, R., 2010. New interpretations of the social and material impacts of the 1812 earthquake in Caracas, Venezuela. Ancient Earthquakes. Geological Society of America Special Paper, 471**,** 47–58. https://doi.org/10.1130/2010.2471(05)

Ammon, C.J., Kanamori, H. and Lay, T., 2008. A great earthquake doublet and seismic stress transfer cycle in the central Kuril Islands. Nature, 451(7178), 561–565. https://doi.org/10.1038/nature06521

Bath, M., 1965. Lateral inhomogeneities of the upper mantle. Tectonophysics, 2(6), 483–514. https://doi.org/10.1016/0040-1951(65)90003-X

Chiaraluce, L., Ellsworth, W.L., Chiarabba, C. and Cocco, M., 2003. Imaging the complexity of an active normal fault system: The 1997 Umbria–Marche (central Italy) earthquake sequence. Bull. Seismological Soc. America, 93(4), 1418–1434. https://doi.org/10.1785/0120020052

Choy, J.E., Palme, C., Guada, C. and Klarica, S., 2010. Macroseismic interpretation of the 1812 earthquakes in Venezuela using intensity uncertainties and a priori fault-strike information. Bull. Seismological Soc. America, 100**(**1), 241–255. https://doi.org/10.1785/0120090105

Duputel, Z., Rivera, L., Kanamori, H., Hayes, G.P., Hirshorn, B. and Weinstein, S.A., 2012. The 2012 Wharton Basin earthquake sequence: Complex rupture and source process. Geophys. Res. Lett**.,** 39, L21304. https://doi.org/10.1029/2012GL053955

Eberhart-Phillips, D., Haeussler, P.J., Freymueller, J.T., Meyer, R.P., Fletcher, H., Allen, M., Pancha, A., Friberg, P., Michael, A.J., Mooney, W.D., Ratchkovski, N.A. and Sieh, K., 2003. The 2002 Denali fault earthquake, Alaska: A large magnitude, slip-partitioned event. Science, 300(5622), 1113–1118. https://doi.org/10.1126/science.1082703

Harris, R.A., 1998. Introduction to special section: Stress triggers, stress shadows, and implications for seismic hazard. J. Geophys. Res. Solid Earth, 103(B10), 24347–24358. https://doi.org/10.1029/98JB01576

He, Z., Zhang, Z., Wang, X. and Wang, R., 2025. Rupture dynamics of the 2025 Mw 7.7 Myanmar earthquake: A bilateral supershear rupture on unusually long fault superhighway. Geophys. Res. Lett., 53(1), e2025GL118023. https://doi.org/10.1029/2025GL118023

Jia, Z., Jin, Z., Marchandon, M., Ulrich, T., Gabriel, A.-A., Fan, W., Shearer, P., Zou, X., Rekoske, J., Bulut, F. and Fialko, Y., 2023. The complex dynamics of the 2023 Kahramanmaraş, Türkiye, *Mw* 7.8–7.7 earthquake doublet. Science, 381(6661), 985–990. https://doi.org/10.1126/science.adi0685

Jolivet, R., Cattin, R., Chamot-Rooke, N., Lasserre, C., Peltzer, G., Doin, M.-P. and Avouac, J.-P., 2014. The 2013 Balochistan earthquake: Coseismic slip distribution and rupture characteristics. J. Geophys. Res. Solid Earth, 119(9), 7305–7320. https://doi.org/10.1002/2014JB011370

King, G.C.P., Stein, R.S. and Lin, J., 1994. Static stress changes and the triggering of earthquakes. Bull. Seismological Soc. America, 84(3), 935–953. https://doi.org/10.1785/BSSA0840030935

Lay, T., Kanamori, H., Ammon, C.J., Hutko, A.R., Furlong, K. and Rivera, L., 2009. The 2006–2007 Kuril Islands great earthquake sequence. J. Geophys. Res. Solid Earth, 114**,** B11308. https://doi.org/10.1029/2008JB006280

Melgar, D., Taymaz, T., Yolsal-Çevikbilen, S., Crowell, B.W., Owen, S.E. and Goldberg, D.E., 2023. Rupture kinematics of the 2023 Kahramanmaraş earthquake sequence. Science, 381(6661), 1350–1355. https://doi.org/10.1126/science.adi0685

Meng, L., Ampuero, J.-P., Sladen, A. and Rendon, H., 2012. Complex rupture of the 2012 Indian Ocean earthquake sequence. Nature, 490(7419), 245–249. https://doi.org/10.1038/nature11452

Milliner, C.W.D., Dolan, J.F., Hollingsworth, J., Çakir, Z., Landgraf, A., Tiberti, M.M., Basili, R. and Owen, L.A., 2023. The multifault rupture of the 2023 Türkiye earthquake sequence. Science Advances, 9**(**39), eadi0685. https://doi.org/10.1126/sciadv.adi0685

Pousse-Beltran, L., Audemard, F.A., Pathier, E., Jouanne, F., Nocquet, J.-M. and Van Welden, A., 2018. Earthquake geology of the last millennium along the Boconó Fault, Venezuela. Tectonophysics, 747–748**,** 40–53. https://doi.org/10.1016/j.tecto.2018.09.010

Stein, R.S., King, G.C.P. and Lin, J., 1992. Change in failure stress on the southern San Andreas fault system caused by the 1992 magnitude = 7.4 Landers earthquake. Science, 258(5086), 1328–1332. https://doi.org/10.1126/science.258.5086.1328

USGS, 2025. Preliminary finite-fault model and moment tensor solutions for the 2025 Myanmar (Mandalay) earthquake. U.S. Geological Survey, Earthquake Hazards Program. Available at: https://earthquake.usgs.gov/earthquakes/eventpage/us7000pn9s/executive

USGS, 2026. Preliminary earthquake source information for the 24 June 2026 Venezuela earthquake sequence. U.S. Geological Survey, Earthquake Hazards Program. Available at: https://earthquake.usgs.gov/earthquakes/ eventpage/us6000t7zp/executive

Wallace, L.M., Hreinsdóttir, S., Ellis, S., Hamling, I., D'Anastasio, E. and Denys, P., 2018. Triggered slow slip and afterslip on the southern Hikurangi subduction zone following the Kaikōura earthquake. Geophys. Res. Lett., 45**,** 4716–4724. https://doi.org/10.1029/2018GL077385

Received: 26-06-2026; Revised: 27-06-2026; Accepted: 27-06-2026

J. Ind. Geophys. Union, 30(4) (2026), 330
https://doi.org/10.71122/JIGU.30(4)2026.0033

Prof. V. V. Jagannadha Sarma

It is with profound sorrow that we record the passing of Prof. V. V. Jagannadha Sarma, an eminent geophysicist, hydrologist, teacher, researcher, and institution builder.

Prof. Sarma served as Head of the Department of Geophysics at Andhra University, where he devoted several decades to teaching, research, and the advancement of Earth and water sciences. He was widely recognized for his pioneering contributions to hydrology, groundwater studies, rainfall analysis, and water-resource management. Through his scholarly work, publications, and mentorship, he inspired generations of students and researchers.

A visionary academic, Prof. Sarma was the Founder of the Association of Hydrologists of India, established in 1982 to promote research and collaboration in hydrological sciences in India. His leadership played a pivotal role in creating a national platform for hydrologists, geologists, geophysicists, engineers, and environmental scientists.

He served as President of the Association of Hydrologists of India and edited several important publications and conference proceedings that contributed significantly to the development of hydrological research in the country.

Prof. V. V. Jagannadha Sarma will be remembered not only for his academic excellence and scientific contributions but also for his humility, mentorship, and dedication to nurturing young scientists. His passing is a great loss to the geoscience community, Andhra University, and the nation.

We pay our heartfelt tributes to Prof. V. V. Jagannadha Sarma and pray that his soul rests in eternal peace. His legacy will continue to inspire future generations of geoscientists and hydrologists

GUIDE FOR AUTHORS

The Journal of Indian Geophysical Union (JIGU), a SCI Journal published bimonthly by the Indian Geophysical Union (JIGU), is an inter disciplinary journal from India that publishes high-quality research in earth sciences with special emphasis on the topics pertaining to the Indian subcontinent and the surrounding Indian Ocean region. The journal covers several scientific disciplines related to the Earth sciences such as solid Earth Geophysics, geology and geochemistry, apart from marine, atmosphere space and planetary sciences. J-IGU welcomes contributions under the following categories :

*Research articles, short notes and students section reporting new findings, results, etc.

*Review articles providing comprehensive overview of a significant research field.

In addition, JIGU also welcomes short communications, after communications and report on scientific activity, book reviews, news and views, etc.

The manuscript should be submitted electronically as a single word format (.doc file) including the main text, figures, tables, and any other supplementary information along with the signed "Declaration Letter". The manuscript should be submitted by email (jigul1963@ gmail.com) to the Chief Editor.

After acceptance of the manuscript the corresponding author would be required to submit all source files (text and Tables in word format) and figure in high resolution standard (*.jpg, *.tiff, *.bmp) format. These files may be submitted to JIGU as a single *.zip file along with the "Copyright Transfer Statement".

IMPORTANT INFORMATION

Ethics in publishing; J-IGU is committed to ensuring ethics in publication and takes a serious view of plagiarism including self-plagiarism in manuscripts submitted to the journal, Authors are advised to ensure ethical values by submitting only their original work and due acknowledgement to the work of others used in the manuscript. Authors must also refrain from submitting the same manuscript to more than one journal concurrently, or publish the same piece of research work in more than one journal, which is unethical and unacceptable. Editor of JIGU is committed to make every reasonable effort to investigate any allegations of plagiarism brought to his attention, as well as instances that come up during the peer review process and has full authority to retract any plagiarized publication from the journal and take appropriate action against such authors if it is proven that such a misconduct was intentional.

Similarly, Editor and Reviewers are also expected to follow ethical norms of publishing by ensuring that they don't use any unpublished information, communicated to them for editorial or review purpose, in their own research without the explicit written consent of the author. They are also expected to keep manuscript' data/ observations/ any other information related to the peer review confidential to protect the interest of the authors. Reviewers should refrain from reviewing the manuscripts in which they have conflicts of interest resulting from competitive, collaborative, or other relationships or connections with any of the authors, companies, or institutions connected to the manuscript.

Conflict of interest

All authors are requested to disclose any actual or potential conflict of interest including any financial, personal or other relationships with other people or organizations within three years of beginning the submitted nor that could inappropriately influence, or be perceived to influence, their work.

Submission declaration

Submission of a manuscript implies that the work has not been published previously and it is not under consideration for publication elsewhere, and that if accepted it will not be published elsewhere in the same or any other form, in English or in any other language, without the written consent of the publishers. It also implies that the authors have taken necessary approval from the competent authority of the institute/organization where the work was carried out.

Copyright

After acceptance of the manuscript the corresponding author would be required to sign and submit the "Copyright Transfer Statement".

MANUSCRIPT PREPARATION

The corresponding author should be identified (include E-mail address, Phone/Mobile number). Full affiliation and postal address must be given for all co-authors.

Abstract:

An abstract of not more than 300 words must be included.

Text:

The manuscript should be structured to include a front page containing the title, Author(s) name, affiliation and address of the institute, where the work was carried out, and 5-to-6 Key words. Author(s) present address, if different from the above mentioned address, may be given in the footnote. The corresponding author should be identified with an asterisk and his/her email ID should be provided. This page should be followed by the main text consisting of Abstract, Introduction, Methods/ Techniques/ Area description, Results, Discussion, Conclusions, Acknowledgements, and References. Tables and Figures with captions should be inserted at the end of main text. It should not be inserted in the body of the text.

Figures/ Illustrations:

figures should be provided in camera-ready form, suitable for reproduction (which may include reduction) without retouching. Figures in high-resolution (at least 300 dpi) standard formats (*.jpg, * tiff, *.bmp) are acceptable. Figures should be numbered according to their sequence in the text. References should be made in the text to each figure. Each figure should have a suitable caption.

Tables:

Authors should take note of the limitations set by the size and layout of the journal. Table should not exceed the printed area of the page. They should be typed on separate sheets and details about the tables should be given in the text. Heading should be brief. Large tables should be avoided and may be provided as supplementary information, if required.

Equations:

Equations should be numbered sequentially with Arabic numerals and cited in the text. Subscripts and Superscripts should be set off clearly.

Equation writing software that presents each equation as an object in MS Word will be accepted. Style and convention adopted for the equations should be uniform throughout the paper.

References:

All references to publications cited in the main text should be presented as a list of references in order following the text and all references in the list must be cited in the text. References should be arranged chronologically, in the text. The list of references should be arranged alphabetically at the end of the paper.

References should be given in the following form:

Kaila, K.L., Reddy PR., Mall D.M., Venkateswarlu, N., Krishna V.G. and Prasad, A.S.S.S.R.S., 1992, Crustal structure of the west Bengal el eon deep seismic sounding investigations. Geophys. J. Int., 1,45-66.

REVIEW PROCESS:

All manuscripts submitted to the journal are peer-reviewed. It is advisable to send the contact details of 4 potential reviewers along with the manuscript to expedite the review process. Editor has the option to select reviewers from the list or choose different reviewers. The review process usually takes about 3 months. All enquiries regarding the manuscript may be addressed to the Chief Editor.

GALLEY PROOF:

Technical editing of manuscripts is performed by the editorial board. The author is asked to check the galley proof for typographical errors and to answer queries from the editor. Authors are requested to return the corrected proof within two days of its receipt to ensure uninterrupted proceedings The editor will not accept new material in proof unless permission from the editorial board has been obtained for the addition of a "note added in proof". Authors are liable to be charged for excessive alterations to galley proof.

PUBLICATION CHARGES:

There are no page charges for publication. The corresponding author will receive a soft copy (pdf format) of his/her published article. Should the author desire to purchase reprints of his/her publication, he/she must send the duly signed Reprint Order Form (accompanies the galley proof and contains price details) along with the corrected galley proof to the Editor. The reprint charges must be paid within one month of sending the Reprint Order Form.

Any payment related to printing or purchase of reprints should be made in the form of a Demand Draft in the name of Treasurer, Indian Geophysical Union, payable at Hyderabad.

You may download the pdf file from:
http://iguonline.in/journal/instructions.php